Irradiation Induced Phase Change in Low Enriched Uranium-Molybdenum Fuel as it Relates to Microstructure

A Dissertation

Presented in Partial Fulfillment of the Requirements for the

Degree of Doctor of Philosophy

with a

Major in Nuclear Engineering

in the

College of Graduate Studies

University of Idaho

by

Kelley M. Verner

Approved by:

Major Professor: R. A. Borrelli, Ph.D.

Committee Members: Dennis Keiser, Jr., Ph.D.; Indrajit Charit, Ph.D.; Dakota Roberson, Ph.D.

Department Administrator: Indrajit Charit, Ph.D.

December, 2021

Abstract

Uranium-Molybdenum (U-Mo) is a metallic fuel studied for decades for use in research and test reactors to replace the currently used highly enriched uranium (HEU) with low enriched uranium (LEU). As part of the Material Management and Minimization (M^3) program, all civilian sources of HEU must be replaced with materials enriched to less than 20% ^{235}U. The combined effort of computational and experimental work is required to make this goal a reality. Herein, the current gaps in knowledge and empirical data necessary for computational model improvement are highlighted, collected, and analyzed. To complement this data collection, an experiment measuring the elastic modulus of U-Mo is designed using the Resonant Ultrasonic Spectroscopy - Laser (RUSL) measurement technique, and the results are predicted. Based on a novel use of molecular dynamics (MD) calculated radiation diffusion and the theory of a critical fission rate where phase reversion occurs, the change in the current phases in U-Mo will happen in the ongoing Transient Reactor Test Facility (TREAT) experiment. This experiment will relate changes in the material elastic modulus to crystallographic phase change and inform computational methods by providing unique data to these studies.

Acknowledgements

I would first like to thank my committee members for their expertise and guidance throughout the doctoral research process, especially to Dr. Robert Borrelli and Dr. Dennis Keiser for giving me a unique opportunity to work with this university and the Idaho National Laboratory.

Thank you to the United States High Performance Research Reactor (USHPRR) team of computational researchers at Idaho National Laboratory, Argonne National Laboratory, Pacific Northwest National Laboratory, North Carolina State University, Purdue University, and the University of Wisconsin - Madison for their insight and expertise on microstructure modeling needs for computational improvement included in this work. I'd like to extend a special thank you to Dr. Benjamin Beeler for his guidance and expertise on microstructure computational research on the included work.

Additionally, thank you to the aLEU-RUSL team of researchers and scientists at the Idaho National Laboratory for making the RUSL experiment possible and bringing it to fruition.

Lastly, thank you to my fellow students, colleagues, and mentors at the University of Idaho, American Nuclear Society, Los Alamos National Laboratory, and Idaho National Laboratory for the support and encouragement throughout this time and for helping me to learn and grow as an engineer and researcher.

Dedication

This dissertation is dedicated to my large and fantastic family, without whom I would not be the person I am today. Thank you to my parents, Alice and Eric, for always supporting and believing in me no matter what my goals are. And thank you, Chris, for encouraging me and keeping me sane throughout this crazy time.

Table of Contents

List of Tables

List of Figures

List of Acronyms

AFIP ATR Full size plate In center flux trap Position

AFIP6-MkII ATR Full size plate In center flux trap Position Mark II

ANCOVA analysis of covariance

ANOVA analysis of variance

ASTM American Society for Testing Materials

ATR Advanced Test Reactor

BCC body centered cubic

BSE back-scattered electron

BUSTER Broad Use Specimen Transient Experiment Rig

DPA displacements per atom

ECAR engineering calculations and analysis report

EBSD electron backscatter diffraction

EDM electrical discharge machining

FCC face-centered cubic

FGB fission gas bubbles

FGP-GUI fission gas pore graphical user interface

HEU highly enriched uranium

HFIR High Flux Isotope Reactor

HIP hot-isostatic pressing

IL interaction layer

INL Idaho National Laboratory

JMAK Johnson-Mehl-Avrami-Kolmogorov

LEU low enriched uranium

M^3 Material Management and Minimization

MCNP Monte Carlo N-Particle Transport Code

MD molecular dynamics

MM microstructural modeling

MP Mini-Plate

NED neutron equivalent device

NNSA National Nuclear Security Administration

ODE ordinary differential equation

OM optical microscopy

PIE post-irradiation examination

PCF power coupling factor

PDF probability density function

PKA primary knock-on atom

RED Radiation Enhanced Diffusion

RERTR Reduced Enrichment of Research and Test Reactors

RUS resonant ultrasound spectroscopy

RUSL Resonant Ultrasonic Spectroscopy - Laser

SEM scanning electron microscope

TEM transmission electron microscope

TREAT Transient Reactor Test Facility

U-Mo Uranium-Molybdenum

USHPRR United States High Performance Research Reactor

U-Zr uranium-zirconium

WDS wavelength dispersive X-ray

XRD X-ray diffraction

Statement of Contribution

The information herein was completed with the assistance of the USHPRR and aLEU-RUSL research team at Idaho National Laboratory. Chapter 2 was prepared and written by myself with edits and input from Dr. Robert Borrelli, Dr. Benjamin Beeler, and Dr. Dennis Keiser. Ongoing work is underway to publish this information as a journal article.

Chapter 3 is a summary conglomeration of two Idaho National Laboratory (INL) reports titled ”Quantitative Image Analysis of AFIP6-MkII and RERTR-12 Fresh Fuel and Irradiated Fuel Fission Gas Bubble and Recrystallized Fraction” and ”AFIP6-MkII and RERTR-12 Porosity Data Collection and Analysis for Modeling and Simulation”. The first report I was a co-author on, and my contribution included collecting historical data from the two experiments and summarizing the fabrication and PIE differences. The analysis and final writing of the report were performed by Dr. Dennis Keiser and Dr. Jan-Fong Jue. In the second report, I was the first author. In this report, I compiled the data from SEM image analysis performed by Dr. Charlyne Smith and Dr. Assel Aitkaliyeva at the University of Florida, along with other data from past INL reports. I developed the included data analysis and methodology as well as writing and compiling the report.

In Chapter 4 the work included was performed by me as the co-principal investigator for the aLEU-RUSL project. However, the final neutronics and thermal analysis were performed by researchers Dr. Joshua Fischler and Mr. Clint Wilson to meet the required safety and internal requirements. The final design of the RUSL holder was done as a whole design team with input from thermal and neutronics models as well as mechanical design finalized and drafted by INL researchers. My contribution included designing the experiment, leading the team in experiment planning, and giving advisement and expertise on the requirements for the investigation based on my research contained within.

Chapter 1: Introduction

The study of nuclear fuels is complex in that to qualify or ready a fuel for real-world applications, the studies of nuclear physics and materials engineering are combined. As nuclear science has progressed, so have the difficulties and requirements for the fuels used in it. Varying types of nuclear reactors exist, each with differing requirements of the fuel used. For example, commercial reactors used for making electricity use much lower quantities of the fissile ^{235}U necessary for creating a sustained chain reaction, whereas research reactors used for testing and developing new types of materials that may undergo extreme environments require much higher quantities of ^{235}U to produce the necessary neutrons to damage the tested materials. Metallic fuels like Uranium-Molybdenum (U-Mo) have been proposed and studied for decades to create the extreme environments used in research and test reactors. Developing these types of fuels for use in research reactors and other extreme environments requires many levels of scientific study to encapsulate and predict their behavior fully. Experimental techniques measure the mechanical and microstructural behavior before and after irradiation, and computational work focuses on understanding the material's behavior at these same levels while employing physical models and simulations.

Early work for this dissertation began with connecting the starting microstructure and swelling performance of U-Mo fuels from past Reduced Enrichment of Research and Test Reactors (RERTR)-12 and Advanced Test Reactor (ATR) Full size plate In center flux trap Position Mark II (AFIP6-MkII) fuel campaigns. The purpose is to understand how the starting form of the material may affect its performance inside the reactor. From there, the data collected from the pre-and post-irradiation examination (PIE) was used to quantify microstructure qualities of the U-Mo fuels for computational scientists of the United States High Performance Research Reactor (USHPRR) group, where the current fuel data is lacking or not readily available. Newer fuel campaign data was collected from micrograph imaging and stitching of Mini-Plate (MP)-1 experiments designed to homogenize monolithic U-Mo fuels and standardize the fuel fabrication techniques. Data collected by Ms. Tammy Trowbridge and Dr. Fidelma Di Lemma was analyzed and collected for computational scientists in the USHPRR group. Analysis of swelling data was also performed on ATR Full size plate In center flux trap Position (AFIP)-7 plates studied using profilometry, a measurement technique that scans a piece of material to measure the thickness. The fission density (fissions/cm^3) and post-irradiation swelling were mapped and processed to make a large amount of data more manageable for the scientists and engineers to analyze further. Parallel work on the phase transformation of the same U-Mo fuels included the beginning development of a measurement technique using the electrical resistivity of a sample material inside a reactor during an actual radiation experiment. However, a more established method of measuring elastic tensor constants was developed and found before further exploration of the resistivity method. This resonant ultrasound spectroscopy (RUS) method uses fiberoptic lasers to excite and measure the subsequent vibrations of a U-Mo beam to measure the frequency of these vibrations and deduce the elastic constants from the

measurement. In theory, a material's elastic modulus depends on the crystallographic structure present; therefore, if a polymorphic material changes solid phases due to some outside causative factor, the elastic constant will change, as will the vibrational frequency.

1.0.1 Motivation and research question

The work herein connects the two overarching themes of the work performed over the last several years, data collection for computational research and phase transformation detection methods using the RUS technique, all for U-Mo that meet data needs laid out by computational scientists. To fully qualify the fuels, both areas of science must complement each other to produce reliable and easily manufactured fuels. Computational methods are performed more quickly and with less expense compared to physical experiments and inform experimental work with their results. The reverse of this is also true; experimental data is required by computational modeling and simulation to validate and inform the results. Together, the development of an iterative process is possible. This process will increase the speed and effectiveness of the research to create a usable metallic fuel for research reactor applications. The work herein connects the many levels of studying the U-Mo fuels by focusing on the microstructure behavior and how it is related to computational science and the physical experiments used to more carefully understand the material properties and advance the understanding of U-Mo metallic fuels for research reactor applications. By collecting past microstructure data, the gaps in what is available for computational improvements will be found, and a new method of measuring the microstructure phase changes is developed to see if the phase change in U-Mo metallic fuels can be measured during irradiation. This collected information will be included in the data used by computational scientists.

1.1 Background of metallic fuel

Research reactors are unique compared to more common commercial nuclear power plants due to the more extreme and complex neutronic environment required by the research applications. Power densities are nearly 17 $\mathrm{kW/cm^3}$ and fission densities are between $3–6\times10^{21}$ $\mathrm{fissions/cm^3}$ [1,2]. This is compared to the 5 $\mathrm{kW/cm^3}$ power density of a commercial, pressurized water reactor [1]. In the research reactors, temperatures are near 250°C at the centerline of the fuels [2], compared to the centerline temperature near 1400°C in commercial UO_2 fuel [3]. This low temperature, high power environment puts a high demand on the fuels used in these reactors. However, another restriction of these research reactor fuels comes from the Material Management and Minimization (M^3) program under the National Nuclear Security Administration (NNSA) [4,5]. The M^3 program was previously started as the RERTR program in the 1970s to remove all civilian sources of highly enriched uranium (HEU) (> 93% ^{235}U) and replace them with low enriched uranium (LEU) (< 20% ^{235}U) [4–9]. Current HEU fuels used in test reactors like ATR and High Flux Isotope Reactor (HFIR) are enriched to far above the maximum LEU enrichment of 20% ^{235}U.

Due to the lower enrichment requirement of the new LEU fuels, more dense material is required to achieve the same high power and fluxes [2, 6]. With the denser material, the fissile ^{235}U atoms are closer together and may sustain a chain reaction with the high power and fluences necessary for material testing and production. Metallic fuels can meet these requirements and have been studied extensively for research reactors around the world [10, 11].

To create the metallic fuels required for research reactor applications, alloying elements are combined with uranium to create a dense, reliable, and stable fuel. Pure uranium metal exhibits poor resistance to corrosion, dimensional stability, and mechanical properties; however, adding the alloy to the uranium improves these issues [2, 12–14]. Alloying elements include molybdenum, zirconium, and niobium, to name a few [2, 14–16]. By creating a binary alloy, the high density of the fuel is maintained while stabilizing the ideal crystal structure of the uranium. The following subsection will elaborate on the existing uranium crystal structures and exactly how the alloys improve the performance of the fuel.

1.1.1 Alloy functions and fuel improvements

Pure uranium metal exists in three main polymorphic forms, α, β, and γ. α uranium is an orthorhombic crystal structure existing up to 665 °C before it transforms into the tetragonal β phase. The final, high-temperature phase occurs at 771 °C and is the body centered cubic (BCC) γ phase [17]. Examples of the forms of the uranium lattice structures are in Figure 1.1. Included are the geometries of the three measurements to show how each shape differs from one another. α uranium undergoes anisotropic swelling during irradiation that causes the material to be dimensionally unstable, which can lead to deformation and uneven strains throughout the material [18]. As the crystal undergoes thermal expansion, the α phase will expand in two directions, [100] and [001], but will shrink linearly along the [010] direction [19]. This uneven growth that occurs as the temperature increases negatively affects the material by causing these uneven strains.The symmetric shape of the γ phase, however, prevents uneven swelling and allows the shape to swell isotropically.

The BCC structure of the γ is more open, i.e., there is more room between atoms in the crystal lattice than the atoms in an orthorhombic α phase and allows for interstitial movement without increasing the volume of the crystal [18, 20]. This is obvious when comparing the α crystal in Figure 1.2 to the BCC crystal in Figure 1.1. The α uranium structure is more complex than the simple orthorhombic structure shown previously and is more closely packed than the γ. This final γ phase undergoes isotropic swelling due to the even dimension in all directions and is the most stable and is, therefore, the most desirable form of uranium [12, 21].Therefore, the goal is to maintain the γ phase while maintaining the high uranium density, which is achieved by adding an additional metal to the uranium.

Firstly, alloying the uranium with another metal allows the formation of a solid solution with the uranium and can hinder the movement of interstitials and vacancies created during the irradiation of the material [18]. This

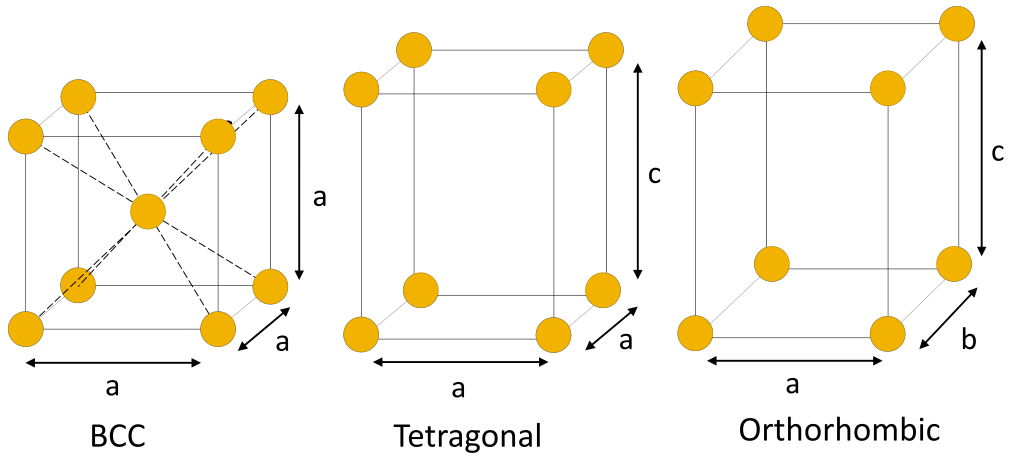

Figure (1.1) Basic crystal structure of the BCC, simple orthorhombic, and simple tetragonal lattices showing the dimensional differences in the basic lattice shapes.

prevents a change in volume due to void creation [18]. Secondly, the creation of an alloy will stabilize the γ phase to a metastable phase that exists at low temperatures [2, 6]. Transition metals between groups V and VIII and periods 4 and 5 work the best for nuclear fuel alloys due to the binding of uranium's "s" and "p" orbitals with the transition metal "d" orbitals via hybridization [21]. Therefore, a solid solution forms between these two types of metals. Finally, the atomic size is essential to choosing an alloying metal [21]. The smaller the atom, the more soluble it is with uranium but does not form strong compounds, and larger atoms form strong bonds but are not very soluble in the solution [21]. The alloying metal will occupy the center location in the uranium cubic cell, as Figure 1.3 shows with a molybdenum alloy, and this alloy atom stabilizes the cubic structure [23].

Molybdenum has both good solubility and bond strength with uranium and has been studied since the 1950s as a possible binary fuel alloy [21,24]. In addition, U-Mo alloy fuels have high uranium density, long-lived γ stability, and good mechanical properties [12, 21]. Molybdenum alloyed fuels are able to retain the γ structure while still having a high ^{235}U density. It is soluble up to 17 to 20wt% Mo in γ uranium [12, 15]. However, common weight percents tested are between 7 and 12wt% Mo, and the results show that U-10wt% Mo is one of the most promising compositions because it is more resistant to stress corrosion cracking than U-7wt% Mo and more ductile than U-12wt% Mo [25]. From these positive qualities, the study of U-10wt% Mo continues as a possible candidate to meet the goals of the M^3 conversion program. Therefore, this work moves U-Mo fuels forward as a possible candidate for use in research reactors and aims to further the field of study on this particular fuel type.

1.1.2 Types of U-Mo fuel

Two types of metallic fuel exist, monolithic and dispersion; both are illustrated in Figure 1.4. Monolithic fuels are made of the ingot of U-Mo fuel meat and surrounded by an aluminum cladding, or a zirconium diffusion barrier

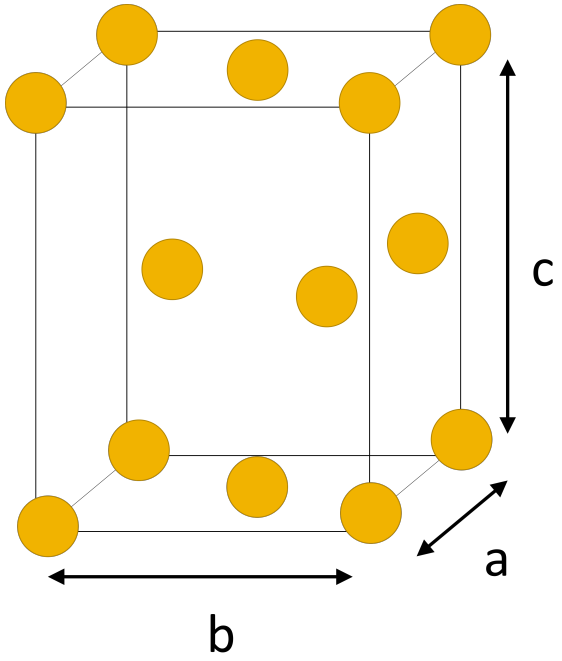

Figure (1.2) α uranium crystal structure with the dimensions of a = 0.285 nm, b = 0.586 nm, and c =0.496 nm [22].

with the aluminum cladding [2,9,15]. Dispersion fuel consists of small, U-Mo particles suspended in an aluminum or aluminum-silicon matrix, surrounded by aluminum cladding [2]. Uranium density of the two types are 6-8 gU/cm^3 and $\sim$ 16 gU/cm^3 for dispersion and monolithic fuels, respectively [11]. Additionally, dispersion fuels have undesirable interactions between the fuel particles and the matrix where an amorphous interaction layer (IL) forms that leads to increased swelling and possible fission gas releases at very high fission rates (fissions/cm^{3}s) [9,11,26]. To address this issue, monolithic fuels have been proposed [11]. Monolithic fuels are more easily used in the extreme reactor environment due to this higher density of the ^{235}U [27,28]. In more recent years, monolithic fuels have become the focus of the NNSA for their high uranium density and less severe interaction between the cladding and fuel meat [29]. Therefore, the primary focus here is on monolithic fuels that consist of 10wt% molybdenum with the LEU.

1.1.3 Problems with U-Mo alloy fuel

Despite the advantageous characteristics of the U-Mo fuel, swelling of the fuel is still a concern because it decreases the thermal conductivity and makes the structures containing the fuel less stable, and may lead to fuel failure [20, 30]. In addition, fission gas bubbles (FGB) produced during irradiation as gaseous fission products lead to swelling [18, 31]. In some studies, swelling is observed as a volumetric increase as high as 76% in some samples [32]. Anisotropic swelling is also still a concern in the fabricated U-Mo fuels. This is due to phase decomposition that occurs during the fabrication of the fuel as it is exposed to high temperatures that may lead

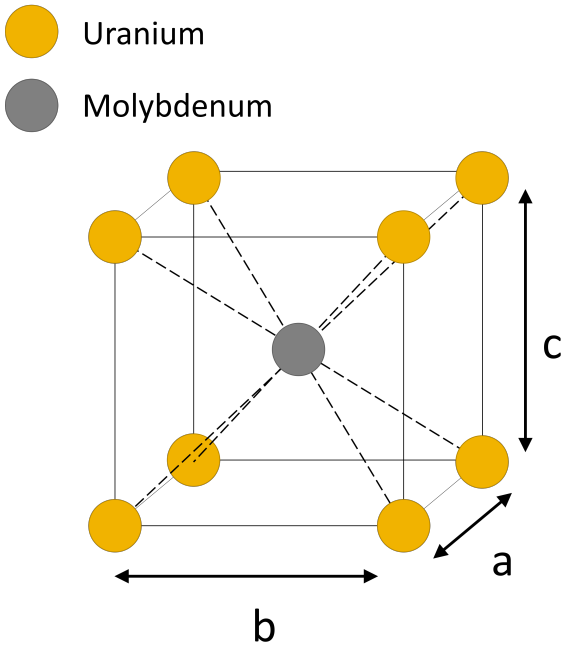

Figure (1.3) BCC structure of U-Mo alloy showing the center atom place occupied by the alloying element

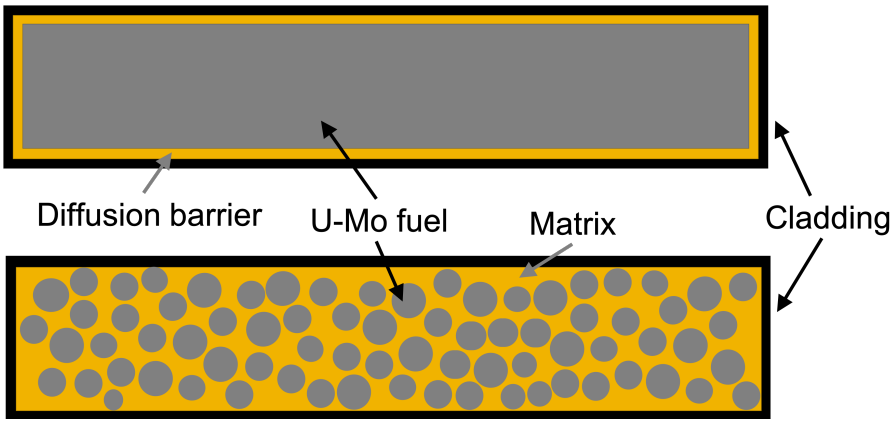

Figure (1.4) Monolithic (top image) and dispersion (bottom image) fuel type examples showing the large fuel piece in the monolithic fuel type and the particle fuel in dispersion fuels. Both are surrounded by cladding preventing contamination of the reactor.

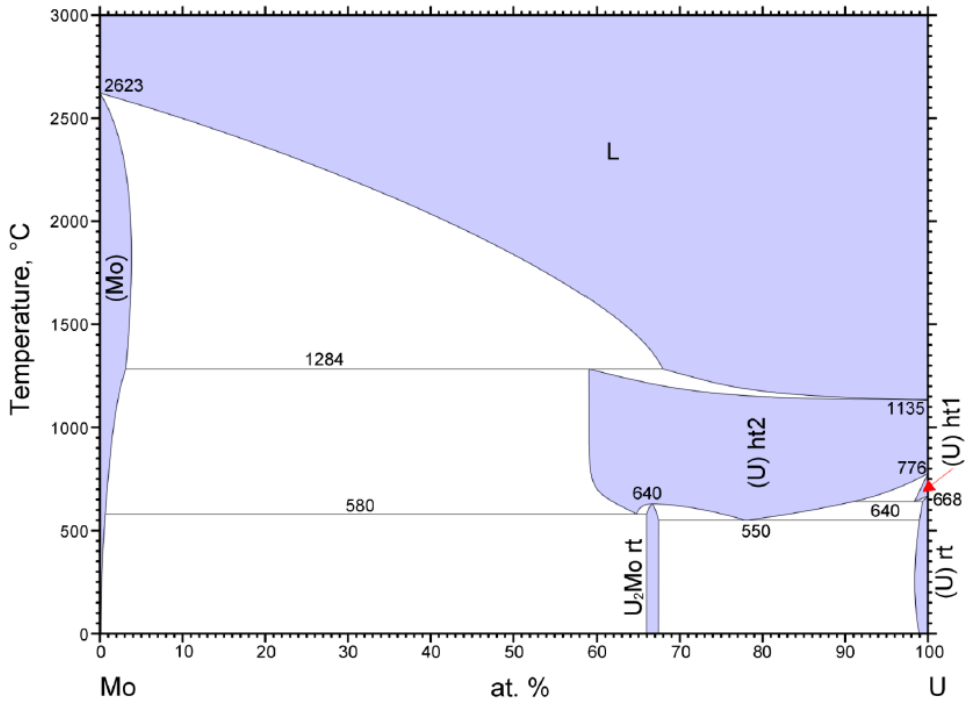

Figure (1.5) U-Mo phase diagram; adapted from [35].

to cellular transformation and discontinuous precipitation that cause the loss of the γ phase [33, 34]. As shown in Figure 1.5, in U-10wt% Mo, the material is at the stable α phase until 550°C, and above that temperature, the transformation to γ occurs. However, during fabrication, the γ phase is maintained and remains metastable at lower temperatures. The term "metastable" γ indicates the crystal structure in this form is not entirely stable at temperatures below the eutectoid point or the point where the γ phase decomposes to the $\alpha + \gamma'$ phase. If another phase is present and exists at lower energy, a change to that lower energy phase may begin [18, 21]. Therefore, the γ phase created during fabrication can decompose to an $\alpha + \gamma'$ phase that will cause non-ideal behavior of the fuel in the reactor.

1.1.4 U-Mo phase reversion

Another interesting behavior of U-Mo phases is the phenomenon of phase reversion. Reversion is essentially the opposite of the phase decomposition; an $\alpha + \gamma'$ phase will change back to the γ phase under irradiation [12, 36–38]. During the irradiation of the material, enough damage and energy are imparted to the structures that this phase change occurs at much lower temperatures than the eutectoid temperature, where the change is regularly observed. Thus, by changing the less stable decomposed phase back to the ideal BCC structure, the fuel may be made more stable.

Many methods are used to retain the γ phase for as long as possible to improve the phase stability and fuel performance. For example, pretreatments and fabrication methods ensure the most stable swelling behavior by controlling the starting microstructure [2, 7, 8, 22, 25, 30, 39–47]. However, decomposition is still observed in the fuel after fabrication [33, 46–49]. Therefore, one possible method of retaining the BCC phase and preventing negative repercussions from phase decomposition from occurring is to encourage phase reversion during irradiation [12, 36–38]. The retention of the γ phase is dependent on the fission rate or flux environment in the reactor [36–38]. It is expected this is from the energy imparted to the material from the irradiation environments. However, the temperature and fission conditions where the reversion occurs are not well quantified. This work will address how best to predict and quantify when these conditions are met to intentionally cause phase reversion.

1.2 Goals of research

Between the FGB swelling and the anisotropic behavior of the decomposed phase, challenges still exist before U-Mo can be fully implemented in research reactors like ATR or HFIR. One of the most challenging aspects of fixing these problems is quantifying the causative factors impacting the unstable fuel behavior. The mechanical, or macroscale, material behavior depends on multiple smaller scales of physical phenomena. To understand the swelling of the fuel during irradiation, the smaller microstructure level relationships must be quantified—for example, the impacts of phase decomposition on the fuel performance. The work herein takes the approach of understanding the fuel behavior by looking at the microstructure level characteristics of U-Mo fuels as a whole, then focusing in on one specific microstructure behavior, phase reversion. The primary goal is to show how interconnected all of these parameters are while quantifying the available microstructure data for use by scientists. In order to expand the current body of experimental data for computational methods, novel research will be done to design an irradiation experiment for measuring phase transformations that may affect fuel swelling and longevity.

1.3 Microstructure data needs

Material science studies exist at four primary levels; mechanical scale, microstructure scale, atomic scale, and subatomic scale [19]. From the bottom down approach, these are all related, as Figure 1.6 illustrates. The microstructure performance impacts the mechanical performance observed. The atomic and subatomic scales affect the microstructure. Therefore, understanding the behavior of one makes the other predictable. Modeling and simulation of these smaller-scale characteristics allow for larger-scale fuel performance predictions. By creating accurate computational methods of fuel behavior, experiments are made less costly and more reliable. Conversely, quantifying experimental data for use in models makes more accurate models and simulations.

This work informs microstructure modeling data requirements while also focusing on one particular microstructure characteristic to understand the changes in material properties in the reactor environment. Models of subatomic

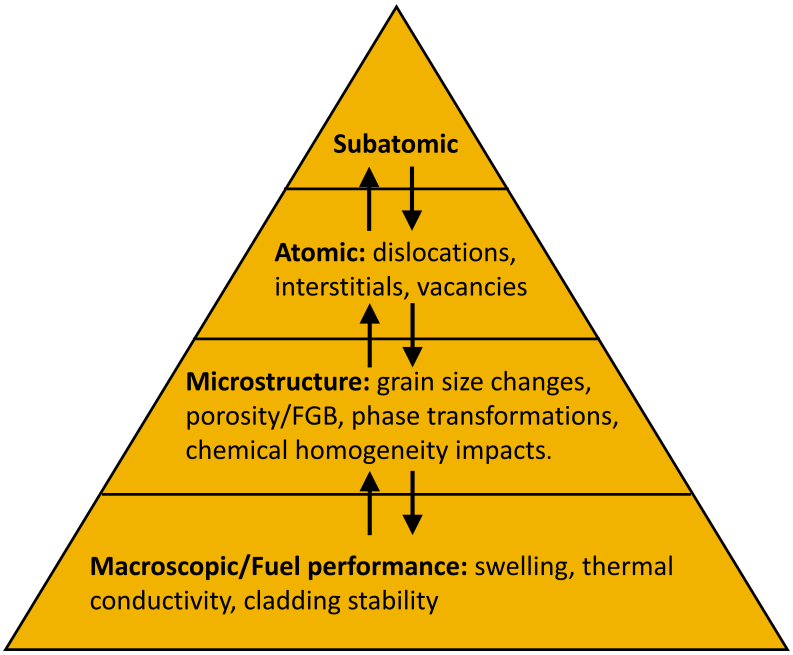

Figure (1.6) Four main levels of material science shown as interconnecting topics; each influences the other and will determine how the material behaves as a whole.

and atomic behavior inform the microstructural performance of the fuel. The microstructural performance then impacts the macroscopic or mechanical behavior of the material. Of the fuel performance parameters affected most heavily during irradiation, swelling is one of the most consequential. Microstructural changes increase the fuel volume that may lead to rupture of the fuel cladding, decrease in thermal conductivity, and ultimately fuel failure. The microstructural characteristics impacting this observed swelling are the primary focus of the data collection of computational modeling improvements. Subatomic or atomic models may predict the microstructure behavior that will lead to this fuel failure. Combining the computational and experimental aspects of the U-Mo work is an iterative process that requires data from experiments to validate models and models to understand the kinetics and physical phenomena determining the experimentally observed results. The data requirements outlined in Chapter 2 were collaboratively determined by a team of USHPRR computational scientists from several universities and national laboratories. For this work, historical data from RERTR and AFIP experiments were collected. After synthesizing the literature data and past experimental data, a new data analysis method was performed and included below. This is the early process of improving data collection and forming a library of U-Mo microstructure data; therefore, the importance was placed on what data is currently available and where are there missing data.

1.3.1 Microstructure data collection plan

From the diagram in the microstructure section of the pyramid are numerous characteristics of the materials. The most important relations to the swelling and fuel performance are included in Figure 1.7. During irradia-

tion, the grain size, phase composition, chemical composition (homogeneity), and porosity will change. These are interdependent, and one change in the property will impact another. The arrows in the figure indicate these complicated relationships and how they ultimately return to the macrostructure, swelling performance of the fuel. These connections between microstructures are highlighted and further explained in Chapter 2 of this document. The importance of highlighting this diagram here is that the early work contained within was performed on quantifying these microstructure features from past work. The overwhelming amount of data and possible areas of study that could be collected on microstructure required a more narrowly focused approach to provide new and unique data to the computational efforts. Therefore, the focus turned to one microstructure, in particular, phase reversion during irradiation. The phases present in the fuel impact the possible anisotropic swelling, the amount of grain refinement, and the overall longevity of the fuel.

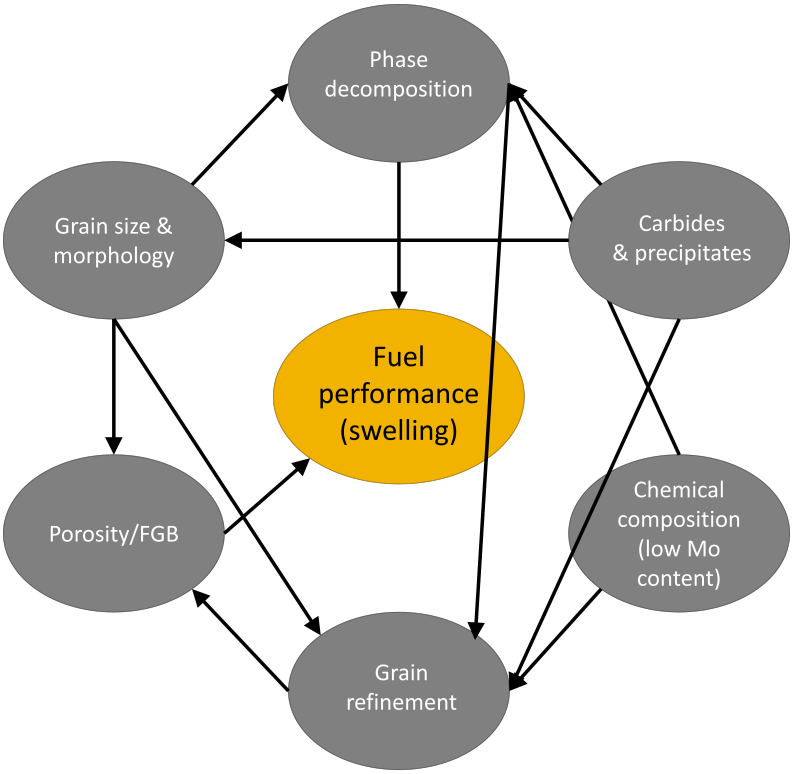

Figure (1.7) Microstructure components and how all are related to the swelling behavior of the fuel. Each aspect will impact the fuel performance either directly like the FGB that cause gaseous swelling or indirectly, like the grain refinement that increases the number of FGB and therefore indirectly impacts the swelling. Each microstructure impacts another, and for full fuel qualification, the relationships must be quantified.

1.4 Resonant Ultrasonic Spectroscopy - Laser (RUSL) phase transformation measurements

To measure the phase reversion in-pile, the RUSL measurement technique developed by Hurley et al. [50] is applied. This RUS method uses a laser to measure the flexural frequency of a vibrating beam of material to determine changes in microstructure by relating the frequency changes to the elastic modulus of the material [50–53]. The elastic tensor stiffness relates to the elastic modulus, and any changes detected indicate some change to the material's properties. The elastic modulus relates to the crystallographic phases present in the material and will change with a phase change. For example, the elastic modulus of α U-Mo is 187.4 GPa and 58.6 to 97.0 GPa for γ [54]. Additionally, finding the frequency of a vibrating beam requires the elastic modulus values based on the relationship between beam properties and measured vibrational frequency explored in Chapter 4. Therefore, measuring the frequency of a U-Mo beam during irradiation will determine any changes in the material elastic constants that occur. This idea was successfully tested in measuring the elastic modulus of U-8wt% Mo specimens between 25 and 660 °C by Steiner et al. [52].

However, this method has only been used for a fuel specimen under controlled temperatures in a furnace due to the complicated and expensive nature of performing irradiation experiments. Willard and Schmitt studied these phase reversions occurring under irradiation in U-Mo fuels. In their work, they proposed the use of a critical fission rate where the energy from the irradiation environment imparted on the fuel was sufficient to retain the γ phase and revert the $\alpha + \gamma'$ back [37]. There is not currently a method of measuring this critical fission rate or at what temperature and fission rate the phase reversion occurs during an irradiation experiment. To understand the changes in a U-Mo fuel under irradiation, this RUSL method will be used to determine where changes in the elastic modulus occur during irradiation and if those relate back to the expected phase changes.

The RUSL holder first developed at the Idaho National Laboratory (INL) will be used to test a U-Mo specimen in the Transient Reactor Test Facility (TREAT) [51, 55]. TREAT is a graphite-moderated reactor used for short, powerful transient testing of materials. By using this reactor, the U-Mo specimens are exposed to the proper fission rates to test if and when phase reversion occurs in the material. By measuring this, the proposed methods for determining when the critical fission rate and temperatures exist that will retain the γ phase material and improve the performance of U-Mo fuels.

1.5 RUSL experimental design plan

The as-fabricated phase decomposition has been studied for U-Mo in PIE work for many U-Mo experiments. Phase reversion to the fully γ phase has also been observed. However, the actual temperature and fission conditions

it occurs under are not. By using an approach proposed by Newell et al. [56], the fraction of the decomposed phase is calculated in this work for the proposed RUSL experiment. To calculate the Johnson-Mehl-Avrami-Kolmogorov (JMAK) and dissolution-based volume transformation, the diffusion and required fission rates for reversion are needed [56–59]. Chapter 4 uses an updated diffusion-based method to calculate the Radiation Enhanced Diffusion (RED) and the required fission rate for phase reversion, the critical fission rate, to gather the information required to predict the amount of phase reversion possible from the MP-1 experiment samples to be irradiated in TREAT. The steps required for this outcome are as follows,

- Calculate the critical fission rate based on historical data and equations from Willard and Schmitt [37]
- Design the TREAT power transient using thermal and neutronic analysis to match the critical fission rate values and temperatures
- Calculate the radiation dependent diffusion coefficients with the fission rates and temperatures determined by the neutronic and thermal analysis
- Calculate the estimated decomposition reversion for the RUSL experiments from the diffusion and power transients

Using this method of estimating the phase reversion of the fuels gives a baseline of where changes in the RUSL measurements may be detected. After the irradiation in TREAT, the comparisons between the expected phase reversion conditions and the actual phase reversion conditions can be made. These measurements also relate to the required computational data by providing the elastic modulus measurements of a sample while it is irradiated. The mechanical changes of the material will relate to the microstructure changes and inform future models and experiments of the expected fuel behavior.

1.6 Connecting microstructure to the phase detection experiment

The work herein is similar to the four levels of material science. It starts from a larger perspective on the microstructure of the U-Mo fuels and then focuses on the phase transformations observed after irradiation of these fuel types. By understanding the broadest level of the U-Mo microstructure and its interconnected characteristics, the computational data collection, a more complete perspective of the fuel as a whole is achieved. Then choosing narrowing in on one gap in existing data, the phase transformation, a more complete prescriptive approach to the experimental design is applied. The phase reversion in the fuel will impact the other microstructure evolution observed in the fuel which in turn impacts the macro level fuel performance. Therefore, the most comprehensive level of the work is in Chapter 2, and is a critical literature review focused on the available microstructure data that aligns with the requirements outlined by the USHPRR group of computational scientists. Chapter 3 then magnifies the needs for data further by looking at the analysis methods used on the data after it is collected. This work is performed using porosity data collected by the University of Florida to standardize the microstructure data collection and analysis methods to compliment the microstructure data needs and improve the data collection.

Finally, the most niche area of the research is condensed down to the RUSL experiment design used to measured phase changes in the fuel that will impact the other larger aspects discussed in the earlier chapters. Chapter 4 includes the work performed to design and analyze a TREAT experiment of phase reversion measurement technique RUSL to give specific phase change data and elastic modulus measurements to the computational science group. To summarize and expand on the current scope, Chapter 5 outlines future work that expands the current efforts to gather more data on phase transformation mechanisms and fuel performance in a reactor environment.

Chapter 2: Critical Literature Review

2.1 Introduction

The driving force of the M^3 program mission, formerly the RERTR program, is to convert civilian sources of HEU to LEU [4, 5]. LEU is a nuclear fuel or material enriched to less than 20% ^{235}U [5, 8, 9]. Metallic nuclear fuels have been explored as an option for research reactor purposes for decades [5]. To meet the very high peak power densities and neutron flux demands of research reactors, the LEU material must be have a very high ^{235}U density [5,14]. Pure uranium metal is far too unreliable, exhibiting poor corrosion resistance, easy oxidization, poor hardness, and dimensional instability when irradiated [14]. Alloying uranium with other heavy metals improves fuel reliability and performance [18, 21]. U-Mo fuels are an option for replacing current HEU fuel with LEU alternatives. U-Mo fuel has good corrosion resistance, high ^{235}U density, and stable behavior required of a metallic fuel for flux environments as severe as research reactors such as ATR and HFIR [18,21,60]. However, it can exhibit severe swelling under irradiation. Ideal fuel candidates are dimensionally stable and retain all fission products within the material [8]. Various techniques used to stabilize the fuel behavior and control the swelling include fabrication methods, pre-treatments, and material selection [2, 7, 8, 22, 25, 30, 39–47]. Ultimately, all of these ideas for stabilizing fuel depend on the microstructure behavior. The microstructure is complex and made up of interlinking characteristics that are impossible to separate from one another. Experiments and models must quantify these interlinking factors to understand and predict the U-Mo alloys behavior. While significant modeling and testing have been performed on U-Mo fuels, there is a disconnect between the two interlinking areas of interest.

2.1.1 Motivation and objectives

Models along with experiments facilitate a more robust understanding of the mechanisms controlling the microstructure of materials. Together they inform future experiments and provide insight into the material mechanisms at work causing the unwanted behavior. Reliable, consistent data is needed to create robust models. However, there is a lack of consistency in data collection and processing methods. Many studies have called attention to the need for better-prescribed data collection and more accurate property data to improve models [28,61–65]. Recent studies by Anjantiwalay et al. [65] have focused on summarizing and collecting data for U-Mo fuels as well. This work looks to expand on this information by publicizing a list of microstructure modeling data needs while collecting the available data related to the needs outlined in Table 2.1. There has been little work published explicitly outlining the data required for the validation and improvement of the U-Mo alloy fuel modeling.

This work collates available data on U-Mo microstructure using modeling requirements developed by a team of scientists and engineers involved with the USHPRR fuel qualification efforts. The information herein is collected to

provide an accessible reference for modelers to find current data and highlight areas where U-Mo microstructural data is inconsistent or missing between research methods. The researchers will discuss how various conditions and microstructures impact each other. These parameters must then be quantitatively understood and recorded for model validation and creation. The sections of the paper will follow thus; Section 2.2 will discuss the need for the modeling data, Section 2.3 will discuss how each of the microstructure features impact swelling or each other, and lastly, the summarized microstructure data currently available in the literature will be presented in Section 2.5 and the ongoing needs and work of this will follow in Section 2.6. This investigation will not be able to fulfill all the microstructure modeling needs. However, it acts as a starting point to find and aggregate the available data and reveal gaps in current data exists needed to meet material modeling goals.

2.2 Modeling needs for microstructure data

Nuclear material testing and data availability is unique compared to the ubiquitous material databases of other fields. A combination approach of simulations and experiments is required due to the scarcity of irradiated fuel characterization data. The modeling and material characterization components must work simultaneously to inform each other. Tonks et al. [66] proposed using a combination of simulations performed at atomistic and mesoscale length scales with experiments to improve microstructure models and, ultimately, macroscale, fuel models. PIE data is difficult to come by because of the time, cost, and safety precautions required for irradiation experiments. Models fill in the gaps of information needed to inform material design and performance while creating predictive experiments. However, a model's prediction accuracy depends on the reliability of the material parameters on which it is based. Therefore, the model is sensitive to the accuracy of the data used [61, 62]. Depending on the model, the data type provided may vary. Correlations of the existing data are often used [63, 67, 68], as are averages of data [63, 69, 70], and data distributions [61, 62, 71]. These data are not only model inputs but necessary for the validation of model results [61, 66, 72]. By comparing the model to the characterized fuel, the physical data validate that the model performs as the real-world material did. Validating the model with experimental data requires a representative dataset in the proper form. For example, validation of models is often more reliable when using a size distribution than a sample mean that does not fully encapsulate the overall population, of fuel plate behavior [61, 62]. Often fitted values are used, predicted averages based on other known material factors [63]. Future data collection must be targeted in how the information is presented, i.e., correlations, data distributions, or averages, and focused on microstructural features necessary for qualifying nuclear fuels for implementation in reactors.

2.2.1 Microstructure Modeling Needs

Table 2.1 shows the required information for microstructure modeling improvements. Thirteen microstructural modeling (MM) tasks or properties were determined by the USHPRR microstructure modeling research team as essential areas of interest where U-Mo microstructure data is lacking or unavailable. Currently, some of these aspects of material characterization and PIE work are already collected as a regular part of fuel qualification procedures [73–76]. One challenging aspect is the data presentation and its accessibility. Often data is not readily available and is presented in internal laboratory reports and communications or as averaged data points without the context of the data shape or distribution.

Table (2.1) Microstructure Modeling (MM) Needs

MM task	Target information	Details
MM1	Volume fractions of different phases before and after irradiation.	a. Fraction of α and γ in as fabricated condition and post-irradiation. b. Carbide distribution before and after irradiation
MM2	Features (dislocation, grain boundary, carbide, etc.) type, size, and density before and after irradiation.	a. Grain boundary size and aspect ratio before & after (B&A) irradiation. In refined grain zone and in non-refined grain zone. b. Dislocation density B&A irradiation. Emphasis decomposed regions.
MM3	molybdenum concentration inhomogeneity before and after irradiation	molybdenum concentration profiles B&A irradiation, including regions of bulk and regions of grain boundaries, defects, precipitates and phase decomposed areas
MM4	Grain boundary bubble size distribution as a function of burnup.	Inside and outside grain refinement region.
MM5	U10wt% Mo refined grain volume fraction as a function of burnup and initial grain size.	
MM6	Gas density within bubbles at a given burnup.	Multiple bubble sampling to determine gas pressure inside bubbles.
MM7	Defect diffusion (self-diffusion and Xe diffusion).	a. Preferably both irradiation enhanced and thermal b. Diffusivity (U and Xe) on grain boundaries c. Effect of pressure on defect diffusivity and formation energy
MM8	Grain boundary denuded zone width.	a. Thickness of region around grain boundaries with no fission gas bubbles b. Variation with irradiation condition (flux and temperature)
MM9	UMo/Zr interdiffusion region	a. Characterization of phases b. molybdenum concentration profile c. Gas bubble density, gas bubble size, and gas bubble distribution as a function of burnup d. Mechanical properties: elastic constant, yield strength
MM10	Effect of gas bubble structures on mechanical properties (stress strain curves)	
MM11	Elastic constants and Yield stress of U-Mo single crystal and polycrystal, before and after irradiation	
MM12	Interstitial loop stability in U-Mo matrix with gas bubble superlattice	
MM13	As-fabricated grain size distributions in RERTR-12 archive plates.	

Of the 13 MM needs, some are overlapping in their topic areas; they can be broken up into the following topics:

- Mechanical properties: MM11 and technically all microstructure will relate back to this
- Porosity and FGB: MM4, MM6, MM8, MM10, and MM12

- Grain morphology: MM13, MM2a, and MM8
- Grain refinement: MM5
- Molybdenum homogeneity: MM3
- Phase decomposition: MM1a
- Interdiffusion zone: MM9
- Atomistic data: MM7, MM2b, MM12

Separating the requirements into these fields will illuminate the importance of each microstructure characteristic and how it relates to fuel modeling and performance.

Inside the list of MM needs, there are two main areas of interest; as-fabricated microstructure and irradiated microstructure. The as-fabricated, or starting, microstructure will impact the irradiation performance and must therefore be quantified to compare to the final irradiated specimens [25, 62, 77, 78]. PIE data is more challenging to obtain due to the difficulties in irradiating experiments and performing characterization on the irradiated material. Paradoxically, to make more predictive models that eliminate the need for complicated irradiation experiments, irradiation experiments are required.

A tiered approach to data collection should be implemented to mitigate irradiation experiment difficulties and use irradiated experimental data to the fullest. Easily obtainable data or already existing data should be gathered first. Following this step, work currently being performed may fit into the MM requirements and fill an important niche outside the intended benefits of the work. Lastly, the more complex microstructure data can be explicitly obtained to meet the MM goals. For example, the atomistic data required for MM2, MM7, and MM12 demands specific equipment and expertise in elucidating the information from material samples. Data currently available will only meet the needs of a few of MM tasks. The available data is explained and outlined in the following.

To complete the first tier of those suggested, first, each microstructural component listed in Table 2.1 is related to fuel performance and each other in Section 2.3. And Section 2.5 summarizes the existing data of some of the MM requirements. Lastly, the existing data is analyzed and discussed to improve upon the overall data and to see where the needs of the U-Mo models are not met.

2.3 Microstructure behavior background

Two primary types of metallic, LEU U-Mo fuels have been developed over the course of the RERTR program - dispersion and monolithic fuels. When looking at the history of U-Mo fuels in the RERTR efforts, the early focus was on dispersion fuels [5, 20]. These are made of ground or atomized powders of U-Mo mixed with a matrix material, often aluminum, and pressed to combine. Following this, they are rolled into a flat fuel foil [2, 9, 79]. In the literature, much of the data available pertain to this fuel type, opposed to its monolithic counterpart

[20, 26, 67, 80–83]. Monolithic fuel is made of an ingot of U-Mo fuel that is rolled with a zirconium diffusion barrier, and aluminum cladding [2, 9, 44, 84]. More recently, monolithic fuels are the focus for U-Mo fuels due to the complications of the formation of an interaction layer between the dispersion fuel meat and matrix that may lead to early fuel failure [2, 9, 26, 27, 29, 85]. Of the two types of metallic fuels, monolithic have the highest ^{235}U density near 15.5 gU/cm^3 compared to the approximate 8.5 gU/cm^3 in dispersion fuels [15, 86, 87]. Because of the high ^{235}U density, monolithic fuels are ideal for use in research and test reactors that require much higher neutron flux environments than LEU, dispersion fuels can produce [14, 29]. Despite their differences, there are microstructural similarities between the two fuel types. Data from dispersion fuel is often used when studying monolithic fuels due to their similarities or lack of data of monolithic materials [20].

2.3.1 Fuel behavior and microstructure

Each MM need presented will have an impact on the swelling. Swelling of the fuel is impacted by almost all of the microstructural components, either directly or indirectly. For example, FGB filled with gaseous fission products will expand and fill voids or nucleate bubbles together to grow and pressurize the material. Thereby increasing the volume, or swelling, of the material [18, 31, 88, 89]. An indirect example is the irradiation-induced grain refinement of the material. It increases the surface area of the grain boundaries where FGB are the most impactful on the swelling of the material [90]. As the grain refinement increases, so does the grain boundary surface area, giving FGB areas to grow and increase the swelling of the fuel [20, 30, 90]. This is why the MM tasks are all outlined in this work - to gather information on characteristics of the fuels to understand the impacts these structures have on the overall fuel stability. Models and experiments aim to understand this microstructure evolution during irradiation more fully to predict and prevent fuel failure. The following subsections will illustrate the connections between each MM task and the overall fuel behavior.

2.3.2 Porosity

Of all the required MM tasks, the study of the FGB and porosity are the most numerous, six of the 13 MMs involve pore or FGB data. The production of fission gases during irradiation, Kr and Xe, create FGB throughout the fuel and have the most notable impact on the swelling behavior. As fission events occur, solid and gaseous fission products form. These fission gas atoms are not soluble in the fuel matrix and therefore congregate at lattice sites or in bubbles [72]. Vacancies and gas atom numbers increase with the fission density and fill the voids and spaces created by fission damage events, which creates the volume changes observed [18, 31, 88, 89]. At low fission densities, below 2.5×10^{21} f/cm^{3}s, few FGB are produced [20], and swelling has a linear relationship with fission density, where solid fission products impact the volume change more than gaseous fission products [26, 81, 91, 92]. As the fission density increases, so do the effects of FGB on the material [26, 91]. This increase in the swelling rate is

shown in Figure 2.1 as a piecewise linear interpolation of the RERTR and AFIP data [92]. Between $2.5-3.5 \times 10^{21}$ f/cm^{3}s, the FGB begin nucleating and growing, therefore the swelling increases [20].

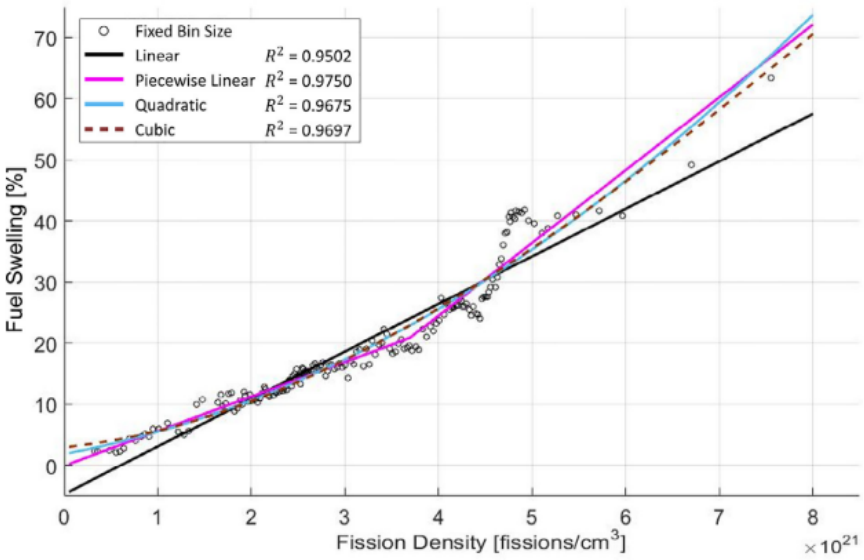

Figure (2.1) Binned swelling measurements from RERTR and AFIP experiments based on fission density. Four fitted models are displayed here and illustrate the benefits of a piecewise function to describe the change in swelling near 3.5x10^{21} f/cm^3. Reproduced from Robinson et al. [92]

Two pore types exist in the material inter-and intragranular [2,20]. Intergranular FGB exist at grain boundaries and are most responsible for fission gas swelling in the material [2,26,30,61,90,91,93,94]. Figure 2.2 illustrates what these intergranular FGB look like along the grains of U-7wt% Mo dispersion fuel sample R2R040 [77]. Intragranular FGB are contained inside the grain and are smaller compared to the intergranular bubbles, normally on the nanometer scale [26,45,81,91]. Figure 2.3 from Gan et al. [91] shows a transmission electron microscope (TEM) image of a U-7wt% Mo particle containing these intragranular FGB.

Quantifying the size, shape (eccentricity), and volume fraction of the FGB is vital to understand the behavior of the fuel. This morphology of the bubbles and the amount of FGB swelling is measurable by studying the pores left behind by the FGB [20]. Pores are observable under various microscopy methods and may be measured and counted to estimate the amount of gaseous swelling experienced by the fuel. Fission density, temperature, fabrication methods, and the fuel type will determine this FGB, or pore, morphology [31]. Measuring and quantifying the size and number of FGB will help determine the amount of swelling occurring and if the fission gases will escape and cause fuel failure [18,31].

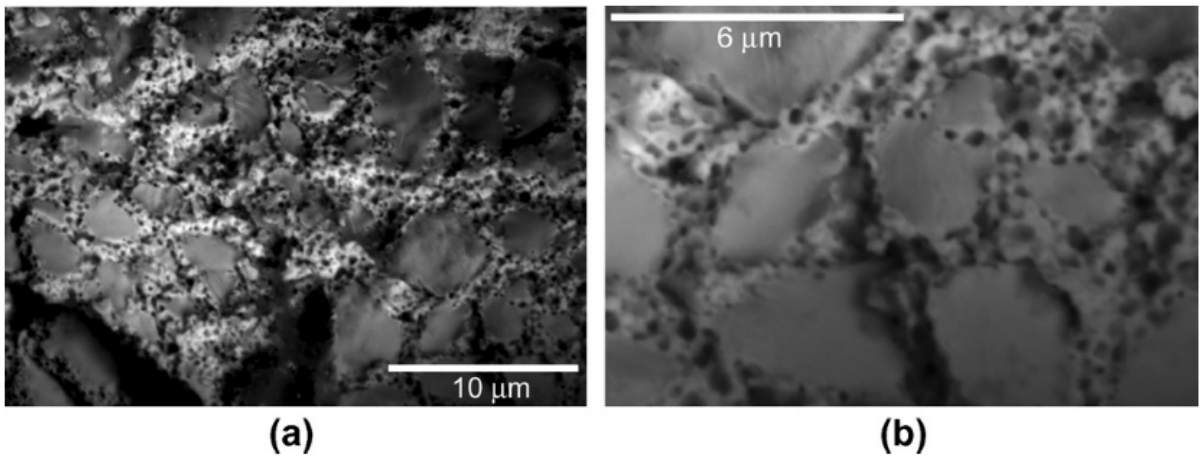

Figure (2.2) scanning electron microscope (SEM) image of Sample R2R040 dispersion fuel showing the intergranular FGB that decorated the grain boundaries of the microstructure at two magnifications. Reproduced from Keiser et al. [77]

2.3.2.1 Intergranular bubble size

MM4 is concerned with intergranular bubbles related to the fuel burnup or fission density, specifically in the form of size distributions. As highlighted by Rest et al. [61] and Kim et al. [30] the size distributions of data and FGB create more reliable model validation as opposed to average data values. Bubbles will nucleate at sinks, like the grain boundaries. The grain boundaries act as a sink for interstitials in the material that leaves behind vacancies [95]. Vacancies and gas atoms near the grain boundary are more mobile and therefore form more readily than the intragranular bubbles do [89]. The grain size is essential to the properties of the intergranular FGB as the larger the grain boundary surface area, the larger the gas bubble size, density, and content will be [69]. The more surface area the FGB have to grow on, the more bubbles will occur and induce more swelling. If there is an increase in the grain boundary area, there is an increase in intergranular FGB numbers and size. Grain refinement or the formation of smaller grains observed in the material will cause this phenomenon to occur [14, 20, 30, 96, 97]. Section 2.3.3.1 will further explain the grain refinement microstructure. As MM4 states in Table 2.1 the porosity before and after irradiation is important because the starting grain size will impact the amount of intergranular pore swelling. Moreover, the intergranular pores will evolve with the increase in fission density as the grain size changes.

2.3.2.2 Gas density within FGB

MM6 focuses on the gas density and internal pressure within FGB. As FGB expand and grow, the pressure inside each bubble will also increase. Models by Jian et al. [98] predicted a bubble pressure of 500 MPa before grain refinement occurs and relieves that pressure. This pressure will impact the normal stresses in the material as

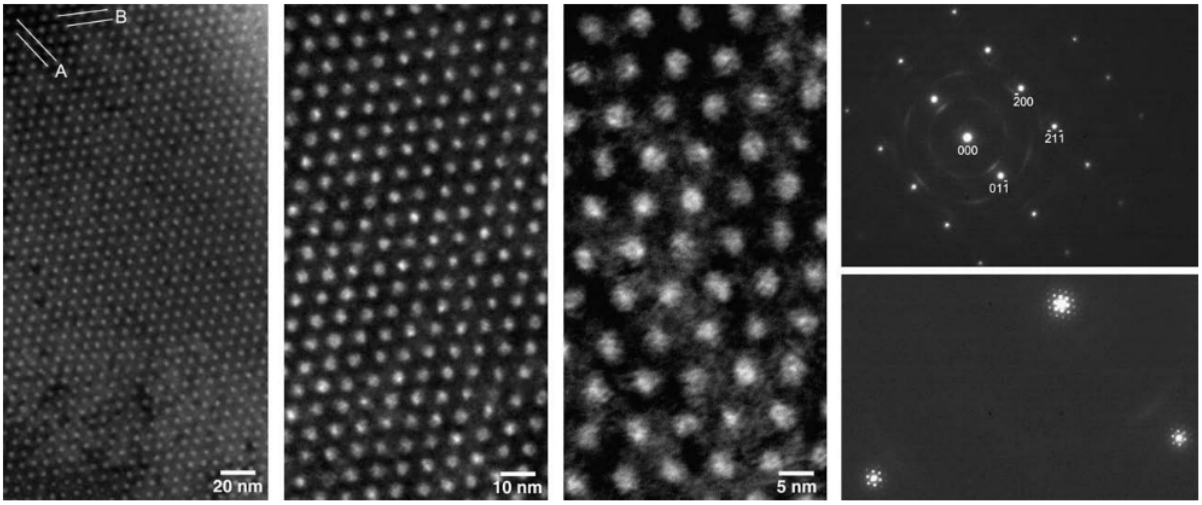

Figure (2.3) TEM images from U-7wt% Mo grain interior of intragranular FGB superlattice at several magnifications and the selected-area diffraction pattern. Reproduced from Gan et al. [91]

well as the microstructure evolution [31, 99]. The importance of this is the prevention of interstitial loop growth by the over-pressurized intragranular FGB which will delay the onset of grain refinement [70]. However, as pressure increases, dislocations in the system will encourage grain refinement [100, 101]. There is a fine line between the internal bubble pressure stabilizing the fuel and pressure causing drastic microstructural changes.

For modeling purposes, the internal bubble pressure is needed to accurately model the onset of grain refinement, the production of dislocations in the system, and the overall stresses in the fuel. This type of experimental data is not very prolific in the literature, nor is it easily produced. For this work, no data was obtained relating to the pressure inside FGB. This falls under the second or third level of the previously proposed tiered approach to data collection. In future experimental planning, bubble pressure measurements may be planned for and supported after obtaining the more easily accessible data types.

2.3.2.3 Bubble superlattice related MM behaviors

Intragranular pores often form a structure called a fission gas superlattice made of small nanosized FGB that arrange themselves into an face-centered cubic (FCC) lattice network within the BCC U-Mo structure [2, 26, 30, 69, 81, 83, 91]. The FCC allows for the accommodation of fission gases in the grains without causing a great deal of swelling, stabilizing the fuel temporarily [45, 81, 83, 91]. The superlattice starts forming around 10% burnup at grain boundaries [102]. As the burnup or fission density increases, the nanobubble lattice moves inwards from the grain boundaries until, at the highest burnup observed (25% ^{235}U), the lattice collapses along the grain boundary, most likely from the grain refinement, and the superlattice only fills the middle of the grain [102]. MM8 involves these denuded zones found along grain boundaries created by the movement of intragranular bubbles to the grain

boundaries at high fission densities burnup (25% ^{235}U) that leave an area devoid of FGB [102].

This superlattice structure is a sink for defects, so interstitial loop movement pauses until the grain refinement begins and the lattice collapses [103]. The interstitial loop stability with the superlattice is of interest in MM12 because of this. Interstitial loops caused by irradiation initiate the grain refinement; these add strain to the material from lattice displacements [97]. However, the increase of interstitial movement is paused by the intragranular bubbles that are over-pressurized in coarse grains [70]. Up to approximately $4x10^{21}$ f/cm^3 fission density, the superlattice is stable [2, 30]. At fission density levels above this, grain refinement destroys the lattice [20, 72, 83, 103]. The observed linear dependence of FGB swelling on fission density found at low burnups (Figure 2.1) proves to no longer be true at higher burnups [72, 92]. The swelling increases non-linearly at the higher fission densities. After this fission density, the superlattice collapses, and intragranular bubbles coalesce and move to grain boundaries where they merge with or become intergranular FGB. This increases in the number and size of intergranular FGB [20, 30, 44, 83, 104]. Due to the onset of grain refinement and the collapse of the superlattice, and the movement of intragranular FGB, the swelling rate of the material quickly increases.

2.3.2.4 Interaction layer FGB

All of the previously discussed properties or features of porosity are needed, specifically at the interdiffusion or interaction region of the fuel, as stated by MM9c. In dispersion fuels, the fuel particles and the matrix interact with each other to form new phases of the two metals that weaken the overall structure of the fuel. The interaction layer forms around the fuel particles and grows in thickness as the fission rate increases [105]. The increase of the interaction layer weakens the matrix while gases are produced, and porosity further weakens the matrix structure [105]. Additionally, voids fill with gas and cause pillowing at the interaction layers causing them to pull apart [26]. Similarly, monolithic fuels develop unique metallic phases between the cladding, or diffusion barrier, and fuel matrix. When pores or bubbles form in these layers, the bonding strength between the materials weakens and becomes a possible area of fuel debonding and failure. Keiser et al. [8] observed this porosity and debonding of the cladding interface in monolithic fuels. When a zirconium diffusion barrier is present, the U-Mo/Zr interface exhibits higher levels of porosity as well; this is detrimental to the fuel performance [45]. The amount of porosity at these interaction layers will weaken the bond of the cladding to the fuel and increase the likelihood of failure. As with the pure U-Mo section of the fuel, the pressure of the FGB will increase tensile stresses at the cladding interface [98]. Modeling and predicting fuel failure will require pore size, volume fraction, and pressure at these interaction layers to correctly predict premature fuel failure.

2.3.2.5 Porosity impacts on mechanical behavior

Porosity in nuclear fuels will have more impacts than just on the volume change of the fuel. FGB reduce thermal conductivity [89, 106], the microhardness of the material decreases with the increase of porosity [18], or bubble volume fraction increases with an increase of the material creep coefficient [98, 107]. Predictions of the material's experimental modulus can be made with the amount of porosity present in the material [94]. This is why MM10 is concerned with the structure of various FGB and how each relates to the mechanical properties. Quantifying pore structures post-irradiation allow connections between porosity and mechanical behavior to be drawn. However, to improve the predictability of each, less uncertainty in the experimental values of the FGB and mechanical properties are needed [94, 106].

2.3.3 Grain size material impacts

This section focuses on the three MM sections that relate to the grain size of the U-Mo system, MM2a, MM5, and MM13. MM2a deals with the grain size and aspect ratio of the material before and after irradiation. MM5 asks for the amount of material volume fraction that has undergone grain refinement, and MM13 only asks for the as-fabricated microstructure of the samples from RERTR-12 and AFIP6-MkII. These are two fuel campaigns performed to improve the fabrication and qualification of metallic fuels for the M^3 programmatic goals.

Grains in U-Mo determine the evolution of several other microstructure features produced during fabrication and irradiation. Phase decomposition nucleates at grain boundaries [21], defects congregate at the grain boundaries as they act as sinks in the material [108], grain refinement begins at grain boundaries [30, 61, 96] and grain boundaries often are depleted of molybdenum and therefore have a different elemental composition the rest of the fuel [69, 78, 109]. These other microstructures impact the performance of the fuel during irradiation, and the grain boundaries directly impact each of the features. Through these various mechanisms, the grains indirectly increase swelling and can cause poor irradiation performance. So the modeling information and data provided here is twofold, 1) the starting grain size will impact the amount of intergranular FGB and what amount and speed the material willfully undergo grain refinement, and 2) the final grain size can indicate how much swelling occurred or help understand how much of the swelling was due to the FGB and grain refinement. Knowing these features of the material allows for optimization of the starting grain size and understanding how to limit the congregation of FGB at the boundaries.

2.3.3.1 Grain refinement

During irradiation, grains will restructure and form much smaller grains. As more dislocation and interstitial loops form during irradiation and stress is added from fission gas production, the grains will begin to subdivide [70,

81, 97]. The grains change from a micron-scale diameters to submicron sizes [26, 97]. To describe the mechanism of grain subdivision, it is hypothesized that polygonization occurs as defects annihilate and restructure the material [65, 78]. Previously, recrystallization was the term used to describe this phenomenon, but it's been observed that the new grains exhibit low angle grain boundaries [65, 78, 110]. These low-angle grain boundaries are an indication of the polygonization process, not recrystallization [18]. For the purposes of this work, "grain refinement" will be used to describe this creation of small subgrains during irradiation.

Grain refinement results in a higher surface area to volume ratio of the grains. As Section 2.3.2 explains, gas bubbles nucleate more easily at grain boundaries due to the trapping of gas atoms and the addition of vacancies along them [89]. The radiation enhanced diffusion of the material causes atoms to diffuse more quickly at the grain boundaries as well [63]. These new smaller grains create a shorter path for the diffusion of atoms within the grain to reach the grain boundary [69]. As the grains divided, the surface area of grain boundaries creates more locations for the FGB to easily grow, and the enhanced diffusion and shortened diffusion length all work together to increase the size and number of FGB in the material. Therefore, intergranular FGB will increase in number and size from the creation of these new grain boundaries as the fission density increases [20, 30, 90]. Intragranular FGB contribute to the increase in fission gases when the grain refinement spreads to the interior of the grain and the FGB superlattice collapses. The previously contained gases spread to the newly created grain boundaries and combine to become larger bubbles [20, 81, 83, 102–104].

While FGB cause the direct swelling and expansion of the material as the intergranular pores increase in size and pressure, and the intragranular FGB collapse that feed this growth, the amount of grain boundaries area available for bubble growth will determine the number of bubbles and how much they grow during irradiation [20, 30, 96]. The nonlinear increase in the swelling rate is due to this restructuring of the grains, and the increase of FGB swelling [92]. In other words, the grain refinement will have a direct impact on the gas and bubble growth responsible for fuel swelling. Therefore, modelers must understand the amount of grain refinement in relation to the fission density and temperature to accurately model grain size, porosity, and fission gas swelling.

2.3.3.2 Starting grain size and structure

Due to the importance of grain refinement on FGB growth and swelling, recording the grain size before and after irradiation is critical to know what changes occur in the material. Grain size at the beginning of the fuel life will affect the grain refinement, gas bubble formation, therefore, impacting the swelling [69]. Grain refinement begins at grain boundaries, so if the surface area of the number of starting grain boundaries is reduced the grain refinement can be as well, i.e. larger grains [30, 72, 97, 100, 111]. U-Mo alloy performs best with equiaxed, large grains [112]. Small grains, with a low aspect ratio in an irradiation environment will increase the swelling of the fuel more drastically than large grains since smaller grains allow for more large FGB to be made [44, 69].

Beginning grain size will have many impacts on the material besides the grain refinement, as shown in the next subsections. The amount of phase decomposition observed in the fuel can be traced back to the grain size of the material. Larger grains means lower surface area of the grain boundary where the transformation products nucleate [30, 41]. Frazier et al. [112] annealed U-Mo samples at temperatures between 700 and 900°C for up to 24 hours to observe the grain size and size distribution of the material using electron backscatter diffraction (EBSD). The observed grain growth kinetics impacted the "phase transformation kinetics" and how the fuel performed when irradiated [112]. This is because of the dependence of the phase decomposition on the starting grain size [46]. Transformation from the γ to $\alpha + \gamma'$ phase begins at the grain boundaries of the previous γ phase [46]. Large grain samples exhibit the smallest eutectoid transformation, volume fraction [46]. Much like the porosity growth, the less grain boundary surface area will results in less area for the phase transition to occur [46]. The phase decomposition or reversion of the γ phase will cause changes to the grain size this means the phase change will impact grain size then FGB nucleation [93].

Knowing the starting grain size and microstructure is required to model the changes in the microstructure observed after irradiation. The grain size, grain refinement, FGB, and fuel stability are all interrelated. One type of data can predict the results or another and vice versa.

2.3.4 Phases and precipitates

Various types of phases exist in the U-Mo fuel as a result of fabrication techniques and elemental fuel composition. Crystallographic phases and carbide precipitates present in the material are features important to fuel qualification. MM1 and 9a require information on the phase composition of material before and after irradiation. The starting microstructure includes the amount of phase decomposition present and the number of second phases, like carbides, that are both results of fabrication methods used [69]. Therefore, measuring the phases before irradiation allows for a better understanding of how the fuel changes during use. Furthermore, measuring the phases after irradiation helps explain how the overall structure behaved and how these phase discontinuities in the material microstructure will impact other microstructures and irradiation behavior.

2.3.4.1 Phase decomposition

Ideally, uranium-based nuclear fuels exist in a metastable γ, BCC, crystallographic phase [2, 18, 21, 60]. It is the most stable phase during irradiation of the material compared to the orthorhombic α phase exhibited at lower temperatures [18, 21, 24, 36, 113]. Molybdenum is used as an alloying metal with uranium to stabilize the γ phase by preventing the movement of interstitials and vacancies while preventing dislocation loops from forming [18, 60, 114]. Of the many U-Mo compositions studied, U-10wt% Mo is the most stable while still retaining the high density required of a metallic fuel [2, 60]. However, the γ phase will undergo eutectoid decomposition to $\alpha + \gamma$'

(U_2Mo) structure over time [18, 24, 36, 54, 60, 115–121]. As shown in the phase diagram of Figure 2.4 at 550°C and above, this eutectoid transformation of $\alpha + \gamma$' to γ will occur in U-10wt% Mo (or 22at%) [35]. Below this temperature, the preferred γ phase will undergo phase decomposition. Conversely, $\alpha + \gamma$' phase may revert to the γ phase during irradiation at temperatures well below the eutectoid point shown in the phase diagram [2, 24, 37, 38].

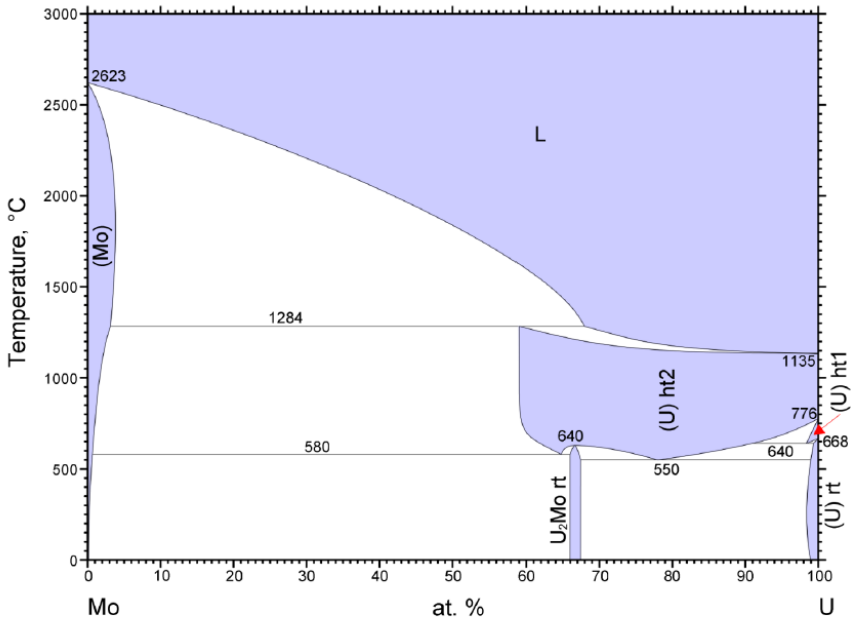

Figure (2.4) U-Mo phase diagram illustrating the 550°C eutectoid point of U-10wt% Mo where the γ phase will decompose to $\alpha + \gamma$' phase [35]

Much like grain refinement, the decomposition begins at grain boundaries and is dependent on the starting grain size of the material [21, 41, 46]. The phase decomposition is detrimental to the fuel stability because the α phase undergoes anisotropic swelling leading to unequal strains between grains and possible fuel deformation [2, 18]. Figure 2.5 shows a decomposed region in a monolithic fuel sample as long, "plate-shaped" phases along grain boundaries [122]. From the figure it is clear how different this phase is from the intact grains next to the decomposed area. Decomposed, $\alpha + \gamma$', regions are prone to earlier grain refinement compared to the γ phase at lower fission densities [2, 49, 69, 93, 109]. This early grain refinement is due to the fact that during the reversion process, smaller grains are expected to form allowing for early grain refinement, changing the microstructure during irradiation and leading to further FGB swelling [2, 49, 93]. Additionally, the decomposed phase contains lower percents of molybdenum which will also lead to grain refinement more readily [2, 69, 109]. As stated previously, the amount of grain refinement impacts the FGB formation behavior, and ultimately the swelling observed. To accurately model the swelling, grain refinement, and FGB, the starting amount of phase decomposition of the material is essential data to obtain.

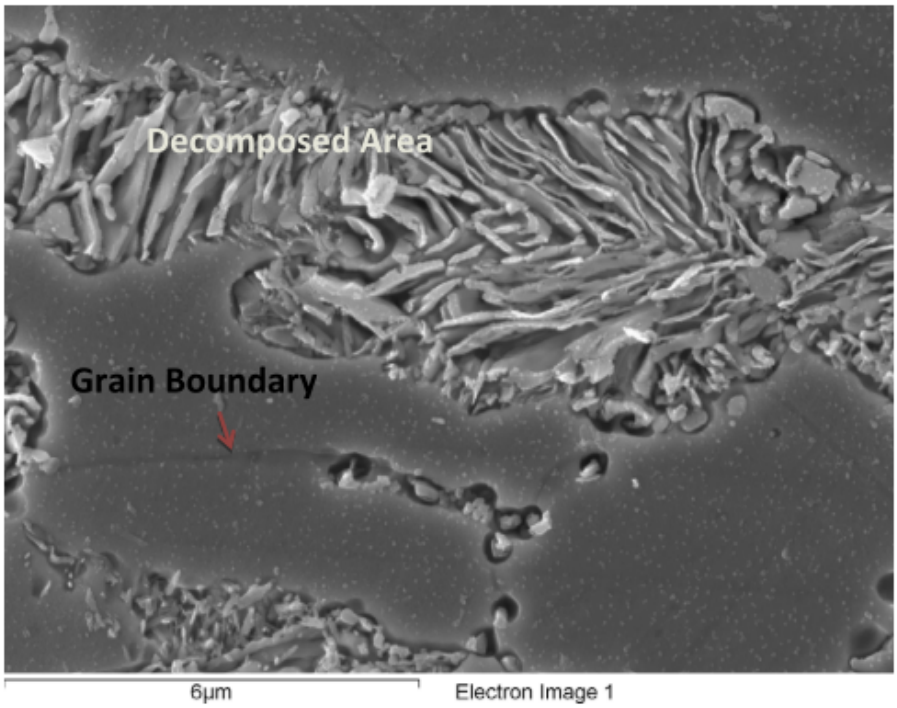

Figure (2.5) Decomposed region of a longitudinal SEM, U-Mo sample with low molybdenum content. Reproduced from Jue et al. [122]

2.3.4.2 Carbides

Carbon is present in the starting U-Mo material and during fabrication will precipitate out of the U-Mo matrix into larger precipitates called carbides [45]. Figure 2.6 shows some of these second phase particles in an optical microscopy (OM) images. The grain boundaries of the material are indicated. The challenge with these carbide features is that they may act as a nucleation site for other microstructure formation [29, 123]. Specifically, phase decomposition is susceptible to forming at these inclusions [29]. Interfaces between two grains weaken with these types of second phases [74, 123]. This weakening effect is especially problematic at interaction layers [74, 122]. They also may create a pinning effect on the movement of dislocations and strengthen the material [43]. Grain boundary movement may also be hindered by a carbide blockage [112]. If carbides are present in the material, it is important to quantify the number and size of the particles to accurately portray the grain boundary and dislocation movement or phase decomposition in simulations.

2.3.5 Chemical homogeneity

The homogeneity of the two elements, uranium and molybdenum, will impact the overall performance of the fuel. Heterogeneous chemical makeup leads to more phase decomposition, varying grain sizes, and increased FGB volume [62, 80, 109]. In previous studies, phase decomposition was present in samples exposed to fabrication tem-

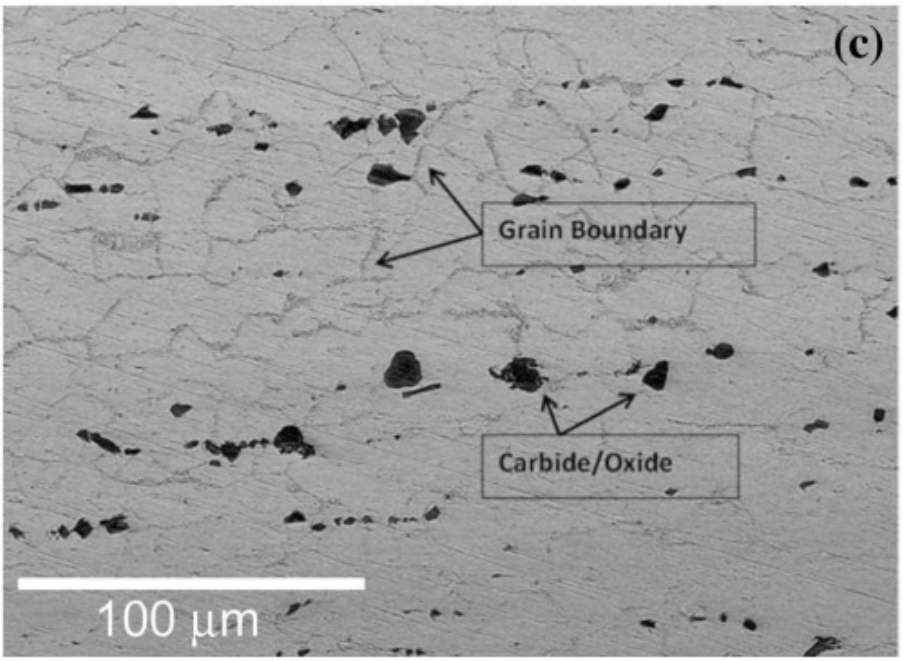

Figure (2.6) Optical microscopy image of grain boundaries and second phases present in fabricated monolithic fuel sample. Reproduced from Keiser et al. [45]

peratures that would not indicate any transformation should occur based on the molybdenum alloy content. In other words, the fabrication temperatures were above the 550˚C eutectoid temperature existing at the 10wt% Mo, and phase decomposition still existed. A non-uniform chemical composition will cause the unexpected decomposition because of the variation of molybdenum content across the sample. Molybdenum is alloyed with ^{235}U to prevent unwanted phase decomposition and stabilize the γ BCC phase. However, as indicated by the U-Mo phase diagram, areas with low molybdenum content will decompose at a higher temperature than a more homogeneous material with higher, more even molybdenum distribution [74].

Quantifying the existing chemical composition is necessary because it will impact many microstructure characteristics during irradiation. If the amount of phase decomposition and chemical composition is known, material swelling may be predicted [63]. Therefore, MM3 includes the need formolybdenum concentration profiles before and after irradiation, as doesMM9b at the interdiffusion regions of monolithic fuels.

During fabrication of the material, various techniques can cause the segregation of molybdenum from the uranium. Stripes or “bands” of alternating metals appear across the monolithic fuels plates [47, 74]. Figure 2.7 shows the alternating dark and light sections of the U-Mo fuel plate, often termed ”chemical banding” that is a result of the starting fuel material composition or the fabrication methods employed [25, 29, 69]. Monolithic fuels begin as an ingot of U-Mo metal and are rolled and machined into flat foils. The starting ingot may not have the two elements evenly homogenized. Therefore, when the fuels are rolled flat, the banding is present [25, 62, 109]. In one

example of this chemical banding in a U10wt% Mo monolithic fuel, molybdenum concentrations vary between 8.5 to 11.5wt% in AFIP6-MkII samples and are nearly 100 μm long [74].

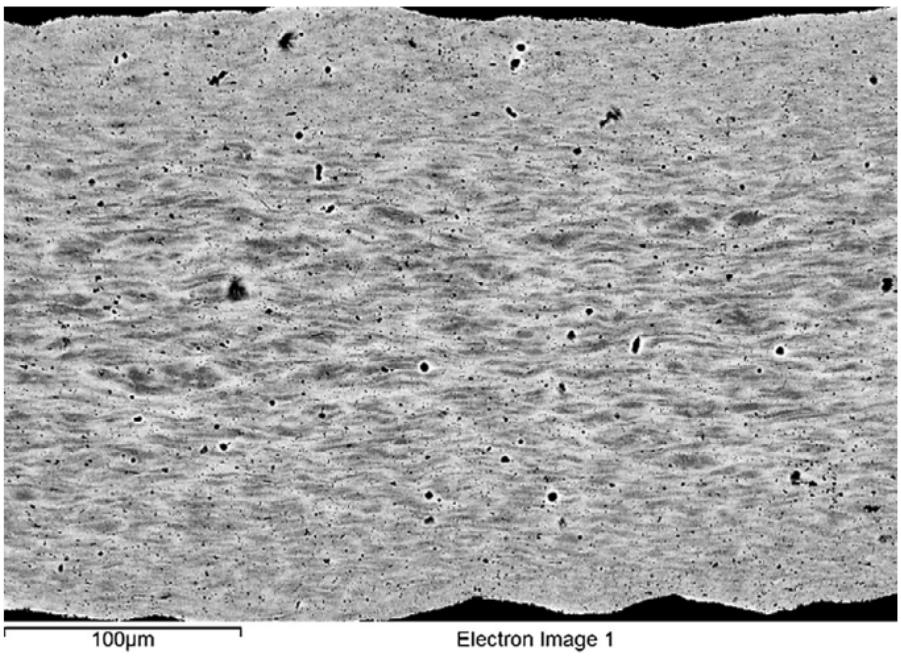

Figure (2.7) Chemical banding present in a U-Mo monolithic fuel foil as seen under SEM analysis after a cold-rolling, fabrciation treatment. Dark bands are high in Mo. Reproduced from Jue et al. [124]

Molybdenum will deplete at grain boundaries in the fuel [69,78,109]. This counteracts the stabilizing properties of the alloying metal and α uranium is likely to form [78]. Due to the high interfacial energies of molybdenum compared to BCC uranium, the molybdenum will migrate away from grain boundaries to the grain center to lower the energy of the system [41, 109]. These areas will act more like a lower weight percentage fuel instead of the design alloying composition [78]. Hot spots of higher fission densities are possible in these low molybdenum areas due to the higher amount of ^{235}U [69, 74]. It has been deemed the increase in the fission density of these areas is not significant to the swelling, however it may heavily impact other microstrucutral behaviors that impact swelling [69]. Depletion of the molybdenum at the grain boundary causes earlier onset of grain refinement and phase decomposition [60, 62, 69, 78]. Section 2.3.4.1 explains the phase decomposition of the material will act as an areas of nucleation for grain refinement.

As the grain refinement increases, the amount of FGB swelling will also increase. Additionally, smaller grains exist in lower molybdenum weight materials. Therefore intergranular FGB growth is made easier, and the grain refinement will occur and complete sooner [20,44]. Therefore, the lower content molybdenum alloys have a higher swelling rate from the more significant bubble growth rate, and the coalescence of the superlattice bubbles [80,99]. At the interdiffusion area of U-Mo and zirconium, an increase in the porosity occurs at the area of low molybdenum

concentration [45]. Fabrication methods used should prevent the depletion of molybdenum at grain boundaries to prevent premature grain refinement, decomposition, and ultimately swelling [109]; i.e., a more homogeneous fuel will reduce microstructural behaviors that are deleterious to the fuel swelling and performance. High-temperature annealing may be used to control the chemical composition and improve the fuel performance [29,41,43,61,74,82, 109]. By controlling the chemical homogeneity during fabrication, the phase decomposition and grain refinement may also be controlled [2, 82].

2.4 Data selection methods

Understanding the current state of data available for U-Mo microstructure modeling is complicated due to the number and variation of studies exploring this metallic fuel. Several experimental campaigns have been performed under the M^3 program. These include the most recent MP-1 experiments and previous RERTR-1 to -12 and AFIP-1 to -7 experiments. Therefore, data from M^3 fuel campaigns are the focus of the following sections. This limits differences in fabrication methods and fuel materials, and makes the comparison of separate samples and experiments more feasible. Additionally, this work focused on finding data in the format and types required for model improvement. For example, data distributions are preferred to averaged values. Also, not every experiment in these campaigns used metallic, U-Mo fuels. These non-U-Mo samples will not be included in this analysis.

Recently, the RERTR program has moved fuel development towards monolithic fuels designs and away from dispersion fuels [84]. Therefore, the focus is on newer, monolithic studies such as RERTR-12, AFIP6-MkII, and MP-1. All of these samples are fabricated in similar methods and are all monolithic fuels. However, some microstructure characteristics are limited in what is available for monolithic fuels. Therefore, dispersion fuel data is included where appropriate or where monolithic fuel data is unavailable.

Similarly, fabrication data that relates to each irradiated sample is limited. Often, a sister plate is kept as an archive of the fabricated microstructure [47,49] and few studies were found characterizing these fabricated samples as rigorously as the irradiated samples. Ideally, both pre- and post-irradiation microstructure for monolithic fuels would be included, but much of the necessary data is not available currently, and substitutions of the required data must be used instead.

Selected M^3, U-Mo experiments that included MM data are provided below in Table 2.2. Fuel type (dispersion or monolithic), fabrication methods, characterization methods, and material composition in the table highlight the differences between samples. Each experiment and reference provides needed MM information on the microstructure of U-Mo fuels. The following sections elaborate on the specific microstructure data collected from each sample and for each microstructure characteristic and if the data fulfills the needs of the USHPRR modeling goals or if further information must be acquired.

Table (2.2) Irradiated U-Mo M^3 microstructure data experiments and samples including fabrication and characterization methods.

Experiment	Sample ID	Fabrication	Characterization	^{235}U %	Mo wt%	Source
AFIP-1	1B5	D(rb)	OM, SEM	19.5	U-7Mo/Al	[63, 125]
	1T2	D	OM	19.9	U-7Mo/Al	[77]
	1TT	D(rb)	OM, SEM		U-7Mo/Al-2Si	[125]
	JJ-652	D	EBSD		U-7Mo/Al	[78]
	KGT-2141	D	EBSD		U-7Mo/Al	[78]
AFIP-2	2BZ	M(fb)	OM, SEM		U-10Mo	[125]
	2TT	M(fb)*	OM, SEM		U-10Mo	[125]
	3BZ	M(h)	OM, SEM	19.75	U-10Mo	[125]
AFIP-3	3BZ TE 3	M(h)	SEM	19.75	U-10Mo	[126]
	3BZ TE 4	M(h)	SEM	19.75	U-10Mo	[126]
	3BZ TE 5	M(h)	SEM	19.75	U-10Mo	[126]
	3BZ TE 6	M(h)	SEM	19.75	U-10Mo	[126]
	3BZ TE 7	M(h)	SEM	19.75	U-10Mo	[126]
	3TT	M(h)*	OM, SEM	19.75	U-10Mo	[125]
AFIP6-MkII	CB1131	M(h)	OM, SEM	40	U-10Mo	[47, 49]
	6II-1	M(h)	EBSD	40	U-10Mo	[110]
	96A	M(h)	OM, SEM	40	U-10Mo	[49, 127]
	97A	M(h)	OM, SEM	40	U-10Mo	[49, 127]
	KGT2763	M(h)	OM, SEM	40	U-10Mo	[49, 127]
	342-1-1	M(h)	EBSD	40	U-10Mo	[110]
AFIP-7		M(h)	GUI-VIB	40	U-10Mo	[128]
RERTR-1	A003	D(g)	SEM	19.5	U–10Mo	[20, 30, 61, 129]
	V002	D(a)	SEM	19.5	U–10Mo	[20, 30, 61, 129]
RERTR-2	A005	D(g)	SEM	19.5	U–10Mo	[30]
	B004	D(g)	SEM	19.5	U–8Mo	[30]
	C003	D(g)	SEM	19.5	U–6Mo	[30]
	D005	D(g)	SEM	19.5	U–4Mo	[20, 30]
	V003	D(a)	SEM	19.5	U–10Mo	[30]
RERTR-3	A10	D(g)	SEM	19.5	U–10Mo	[30]
	S03	D(a)	SEM	19.5	U–6Mo	[20, 30, 61, 129]
	V03	D(a)	SEM	19.5	U–10Mo	[20, 30, 61, 129]
	V07	D(a)	SEM	19.5	U–10Mo	[20, 30, 61, 129]
	Y01	D(g)	TEM, SEM	19.5	U–10Mo	[20, 30, 61, 129]
	Z03	D(a)	TEM, SEM	19.5	U–10Mo	[20, 30, 61, 129]
RERTR-4	A6002H	D(g)	TEM, SEM	19.5	U–10Mo	[20, 30]
	V6001M	D(a)	TEM, SEM	19.5	U–10Mo	[20, 30]
	V6022M	D (a)	TEM, SEM	19.5	U–10Mo	[20, 30]
RERTR-5	A6008H	D(a)	TEM, SEM	19.6	U–10Mo	[20, 30, 61, 129]
	A8002L	D(g)	TEM, SEM	19.6	U–10Mo	[20, 30, 61, 129]
	R6007F	D(a)	TEM, SEM	19.5	U–7Mo	[20, 30, 61, 129]
	V6018G	D(a)	TEM, SEM	19.5	U–10Mo/Al	[20, 30, 61, 63, 71, 129, 130]
	V6019G	D(a)	TEM, SEM	19.5	U–10Mo/Al	[20, 30, 61, 63, 71, 129, 130]
	V8005B	D(a)	TEM, SEM	19.5	U–10Mo	[20, 61, 129]
	V8005G	D(a)	SEM	19.5	U-10Mo/Al	[63, 71, 130]
RERTR-6	L1F040	M(fb)	TEM, SEM	19.7	U–10Mo	[20, 28, 30]
	L1F100	M(fb)	TEM, SEM	19.7	U–10Mo	[20, 30]
	L2F030	M(fb)	TEM, SEM	19.7	U–10Mo	[20, 30]
	R1R010	D(a)	OM, SEM	19.5	U-7Mo/Al-1Si	[71, 130]
	R2R010	D(a)	OM, SEM	19.4	U-7Mo/Al-2SI	[77]
	R2R020	D(a)	OM, SEM	19.4	U-7Mo/Al-2Si	[71, 77, 130]
	R2R030	D(a)	SEM	19.1	U-7Mo/Al-5Si	[77]
	R5R020	D(a)	SEM	19.1	U-7Mo/Al-0.2Si	[71, 130]
RERTR-7	H1F020	M(fb)		58	U-12Mo	[28, 85]
	L1F120	M(fb)	TEM, SEM	58.2	U–10Mo	[20]
	L1F140	M(fb)	TEM, SEM	58.2	U–10Mo	[20, 28, 30]
	L2F040	M(fb)	TEM, SEM	58.3	U–10Mo	[20, 30]
	R2R040	D(a)	OM, SEM, FIB	58.2	U-7Mo/Al-2Si	[77, 104]
	R2R050	D(a)	OM	58.2	U-7Mo/Al-2Si	[77, 130]
	R3R040	D(a)		58.3	U-7Mo/Al-5Si	[130]

	R3R050	D(a)	SEM, FIB	58	U-7Mo/Al	[104]
RERTR-8	H1P010	M(h)	TEM, SEM	57.5	U–12Mo	[20, 30]
	L1P020	M		SEM	U-10Mo	[76]
	R9R010 C	D(a)	SEM, FIB	58	U-7Mo/Mg	[104]
RERTR-9	R6R018	D		58.1	U-7Mo/Al-3.5Si	[130]
RERTR-9A	L1F26C	M(fb)	TEM, SEM	57.5	U–10Mo	[20, 30]
	L1F32C	M(fb)	TEM, SEM	57.8	U–10Mo	[20, 30]
	L1P04A	M(h)	TEM, SEM	58.3	U–10Mo	[20, 28, 30]
	R2R078	D(a)	OM	44.4	U-7Mo/Al-2SI	[77]
	R4R018	D(a)	OM	44.4	U-7Mo/Al-2Si	[77]
RERTR-9B	L1F34T	M(fb)	TEM, SEM	58.8	U–10Mo	[20, 28, 30]
	L1P05A	M(h)	TEM, SEM	58.3	U–10Mo	[20, 28, 30]
	L1P09T	M(h)	TEM, SEM	58.8	U–10Mo	[20, 30]
	R2R088	D(a)	OM	58.1	U-7Mo/Al-2Si	[77, 130]
	R2R118	D(a)	OM	58.1	U-7Mo/Al-2Si	[77]
RERTR-10	L1P12Z	M(h)	SEM	67	U-10Mo	[30]
RERTR-12	JJ1031	M(h)	SEM, OM	70	U-10Mo	[47, 49]
	L1P462	M(h)	SEM	40	U-10Mo	[76]
	L1P482	M(h)	SEM	40	U-10Mo	[76]
	L1P754	M(h)	SEM	70	U-10Mo	[76]
	L1P755	M(h)	SEM, EBSD	70	U-10Mo	[49, 110, 127, 128]
	L1P757	M(h)	EBSD	70	U-10Mo	[110]
	L1P758	M(h)	SEM	70	U-10Mo	[76]
	L1P759	M(h)	SEM	70	U-10Mo	[76]
	L1P776	M(h)	SEM	70	U-10Mo	[76]
	L1P784	M(h)	SEM	70	U-10Mo	[76]
	L1P7A0	M(h)	SEM	70	U-10Mo	[76]
	L2P499	M(h)	SEM	40	U-10Mo	[76]
	LIP773	M(h)	SEM	70	U-10Mo	[49]

2.5 Currently available M^3 U-Mo microstructure data

Previously, the connections between the different data types that were found in the literature and explained in Section 2.3. In the following section the actual data for each of the microstructure data will be presented. From the many M^3 experiment results of irradiated data are presented with either fission density or fission rate, but not always both. Where available both values for the same sample are given. Data is presented as it appeared in the references from which it is extracted. For example, some references presented the PIE results in reference to a fission density and others used fission rate, therefore several data sets only have one or the other. If data distributions are available they are included, however distributions of data are often not readily available. Additionally, data that is too large to add to the report is available from the authors.

2.5.1 Porosity data

Porosity data includes several aspects of the FGB or pores present in irradiated fuel. In the criteria presented in Table 2.1, the information needed is the FGB per area of the fuel, the pore volume fraction (defined as porosity for this work), pore size, and eccentricity in relation to the fission density. Pore size is the diameter or area of the pore. Eccentricity is a value representing the roundness of the pores. A value of 1 indicates the pore is a perfect circle or sphere. As the eccentricity decreases away from 1 toward 0, the pores are more elongated.

The most desirable format of the pore information is a size distribution, opposed to an averaged value. A critical report to the current data available of FGB distributions and bubble density is an Argonne National Laboratory reports by Kim et al. [129]. Many studies use this data as the basis for model validation and inputs [20,30,61,131]. While this report is very informative to the available porosity data, it analyzes only dispersion RERTR experiments. Monolithic fuel plates do not have nearly the same concerns about porosity or reaction of the fuel particles and the matrix as is true in dispersion fuels [20].

Table (2.3) FGB density related to the pore diameter for irradiated samples

Experiment	Sample ID	Fission density (10^{21} f/cm^3)	Fission Rate (10^{14} f/cm^{3}s)	FGB per area (b/μm^2)	Pore diameter (μm)	Source
RERTR-1	A003	3	3.3	1.06	0.18	[20,30]
	V002	2.9	3.2	0.68	0.15	[20,30]
RERTR-3	S03	2.9	6.8	0.79	0.18	[20,30]
	V03	2.6	6.1	0.96	0.16	[20,30]
	V07	2	4.9	0.13	0.13	[20,30]
	Y01	2		0.35	0.09	[20]
	Z03	2.2		0.31	0.09	[20]
RERTR-5	A6008H	3.1		1.19	0.17	[20]
	A8002L	3		1.26	0.18	[20]
	R6007F	2.5		0.8	0.16	[20]
	V6018G	2.4		0.67	0.14	[20]
	V6019G	3.1		1	0.16	[20]
	V8005B	2.5		0.61	0.16	[20]

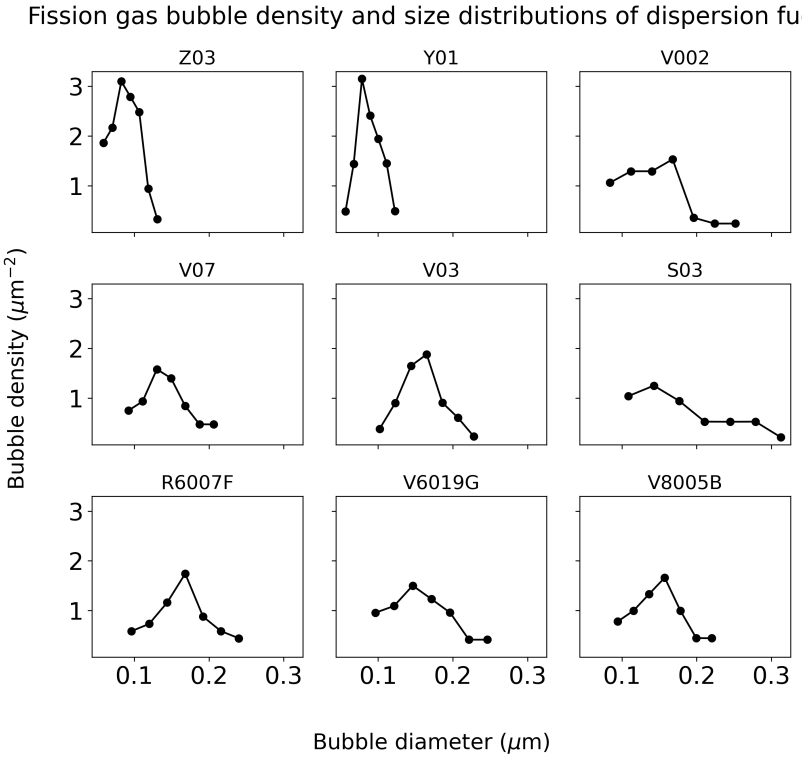

Figure (2.8) Bubble size and density distributions of dispersion fuels recreated from graphs and data in [129] and [61].

Data from Kim et al. [129] and Rest et al. [61] exists in the form of pore size distribution and bubble density distributions. However, the samples illustrated by Figure 2.8 are only for dispersion samples from RERTR-1, 3, and 5. More recent distributions of monolithic samples are unavailable. The bubble density per cross sectional area and the bubble diameter are used to calculate the overall porosity of the fuel [61, 129]. Or the pore volume fraction may be measured directly as a percent of the total area of the samples [104]. This is why not all sources report both bubbles per area and porosity. Table 2.3 shows the pore diameter and pore density per area of several dispersion samples collected by Kim et al. [20]. Aside from this data, no other sources were found that presented the FGB density as a unit of cross sectional area.

Table (2.4) FGB size, porosity, and eccentricity data in relation to the irradiation conditions

Experiment	Sample ID	Fission density (10^{21} f/cm^3)	Fission Rate (10^{14} f/cm^{3}s)	Porosity (% vol)	Pore diameter (μm)	Pore area (μm^2)	Eccentricity	Source
AFIP6-MkII	96A	4.24		15.04	0.38	0.15	0.69	[127]
	96A	4.74		16.5				[49]
	97A	3.91		15.49	0.35	0.12	0.64	[127]
	97A	4.74		27.2				[49]
	KGT2763	4.74		11.8				[49]
	KGT2763	4.14		24.24	0.47	0.27	0.63	[127]
AFIP-7		1.16	2.50	3.27	0.27	0.07	0.61	[128]
RERTR-1	A003		3.80	2.7	0.18			[129]
	V002	3.10	3.80	1.2	0.15			[129]
	V002	3.10	3.80		0.15			[129]
RERTR-3	S03	2.90	7	2	0.18			[129]
	V03	2.60	6.30		0.16			[129]
	V07	2.10	5.10		0.13			[129]
	Y01	2.00	4.80		0.09			[129]
	Z03	2.20	5.30	0.2	0.09			[129]
RERTR-4	A6002H	5.70		11				[20]
	V6001M	4.80		8				[20]
	V6022M	5.50		10				[20]
RERTR-5	A6008H	3.10	3.10		0.17			[129]
	A8002L	3.00	2.90		0.18			[129]
	R6007F	2.40	2.40	1.6	0.16			[129]
	V6018G	2.30	2.30		0.14			[129]
	V6019G	3.00	2.90	2	0.16			[129]
	V8005B	2.40	2.40		0.16			[129]
RERTR-7	R2R040 E	6.30	8.10	18.418	0.323	0.112	0.69	[104]
	R3R050 A	5.20	6.60	12.485	0.164	0.4	0.651	[104]
	R3R050 B	5.20	6.60	11.331	0.173	0.036	0.698	[104]
RERTR-8	L1P020	5.95		25				[76]
	R9R010 C	5.50	11	7.684	0.118	0.016	0.745	[104]
	R9R010 D	5.50	11.00	7.482	0.116	0.015	0.736	[104]
RERTR-12	L1P462	3.34		10				[76]
	L1P755	7.56	5.86	15.42	0.3	0.09	0.64	[128]
	L1P755	5.18		13.3				[49]
	L1P755	5.21		25	0.5	0.25	0.62	[127]
	L1P759	8.72		27				[76]
	L1P784	6.31		35				[76]
	L1P7A0	7.71		36				[76]
	L2P499	2.48		4				[76]
	LIP773	3.45		13.7				[49]

As is shown in Table 2.4 more references present the data in the form of pore size and volume fraction of the pores. The porosity shown from other studies in Table 2.4 aligns with the expected fission densities where fission gas swelling increases. Samples with the highest porosity and grain diameter are exposed to higher fission densities, over 4×10^{21} f/cm^3. Some of the literature presented the pore size in the area as opposed to diameter. Area and eccentricity of the bubbles may be more representative of the shape and size due to the elongated nature of some of the measured pores. The lack of consistency in the collection of data on porosity, or FGB, makes using the data difficult when modeling these types of fuel behavior. Ideally, porosity data would include size distributions and density as a function of burnup or fission density.

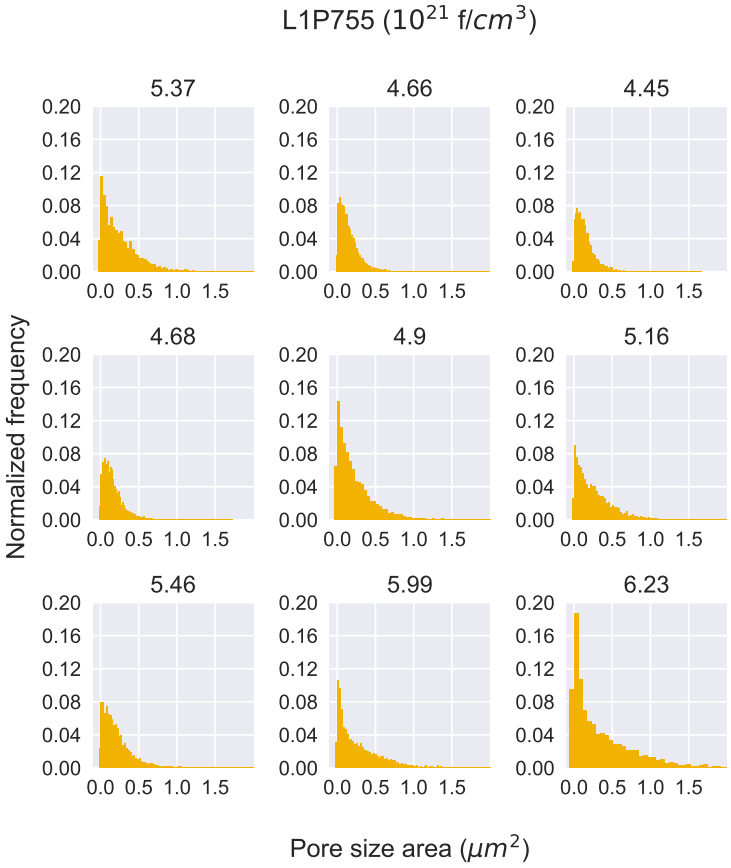

Figure (2.9) L1P755 pore size area normalized frequency distributions in relation to the are specific fission density. Reproduced from Verner et al. [127]

More recently, FGB and pore data was collected from RERTR-12 and AFIP6-MkII samples and analyzed using a standardized image analysis technique developed by Smith et al. [127, 128]. Figure 2.9 underscores the relationships between FGB and fission density and shows the pore size area size distribution for RERTR-12 sample,

L1P755. Fission densities are shown above each histogram of the pore size normalized frequency. This same data is analyzed and presented by Smith et al. in several references [128, 132]. Porosity volume fraction, pore diameter, and eccentricity are all also included in this research. The data distributions were analyzed and summarized in Table 2.4. The data distributions are added to the data library compiled for the MM outlined previously. This is by far the largest and most complete data collected specifically to meet the MM modeling needs. By collecting data in this manner in the future more statistically rigorous analysis may be performed and the usefulness for models increased. Future work will focus on using the same method and quantity of data for microstructures outside of the porosity data.

2.5.2 Grain size data

Metrics of grain size data differ, similarly to those pertaining to FGB. Grains are described with grain diameter, grain area, grain number, and aspect ratio. Different methods exist to measure these characteristics. An average grain diameter may be quantified by measuring the grains in four directions and calculating the mean from each micrograph or in some methods a lineal intercept is used [129], or as done by Di Lemma et al. [133] on MP-1 samples, a point counting method measures the grain size number, not the grain diameter. The grain aspect ratio gives the shape of the grains as well. More advanced techniques such as EBSD may be used to understand the grain size or shape [110]. While all these techniques will give reliable values, the variation in the methods makes comparing data from study to study difficult.

Unlike FGB characteristics, grain size must be measured before and after irradiation. As discussed in Section 2.3.3, grain refinement causes grains to become much smaller after irradiation depending on the fission density. Therefore, the collected grain size data is presented in the following sections in the as-fabricated and irradiated grain size characteristics.

2.5.2.1 As-fabricated grain sizes

More recent fuel campaigns focus on producing a large sample size of materials characteristics to study, as was done in the MP-1 efforts. Large quantities of plates were fabricated using slightly different methods to standardize the fuel fabrication techniques and understand how fabrication affects the irradiation behavior. In the analysis of these samples, the grain size was measured and reported as the American Society for Testing Materials (ASTM) standard grain number, which is inversely proportional to the grain diameter [133]. As Figure 2.10 shows, the smaller grain size samples came from the cold rolling technique, and samples encased in the zirconium diffusion barrier were slightly larger. Large sized grains, outlying data points in the as-cast samples are shown in the figure as well. This is possibly due to measurement errors created by deformation in the sample, the standard deviation is much higher in these samples and the deformation leads to fewer counts along the plate [133]. The raw data

Figure 2.10 was produced from can be found in reference [133]. MP-1 pre-irradiation characterization shows how important fabrication techniques are to the microstructure and how varied the starting microstructure is from sample to sample.

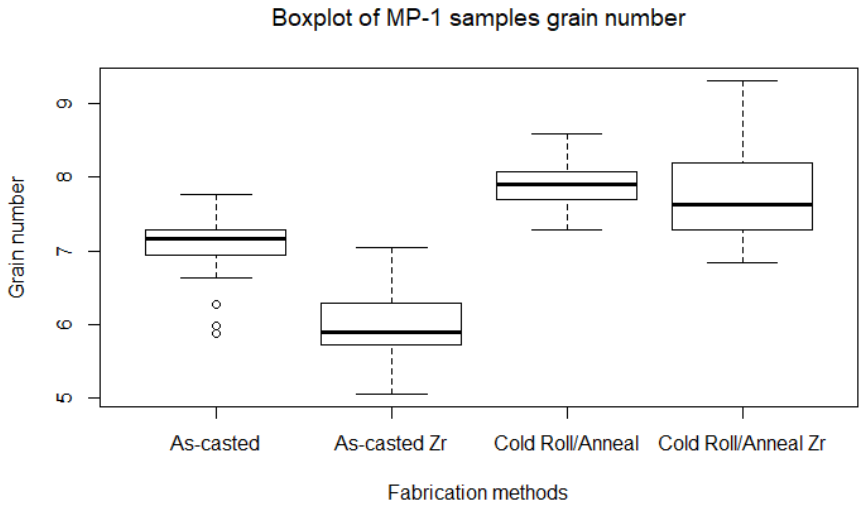

Figure (2.10) Boxplot of the as-fabricated grain numbers from the MP-1 experiments currently being studied as part of the M^3 program. Some samples were characterized as they are cast during production, after cold-rolling, and two types were covered by a zirconium diffusion barrier. Adapted from Di Lemma et al. [133]

Twenty-four samples were analyzed in the MP-1 study and from each sample six locations were used for the image analysis. The large amount of produced data in this analysis of MP-1 is useful to increasing the reliability of data and improving data statistics. However, most data sources present the information in a more limited manner. As-fabricated monolithic grain sizes data are presented in Table 2.5. As seen in the table, Keiser et al. [47] presents the as-fabricated grain size as an area, opposed to the diameter measured from the other two references. From [110] et al., the grain diameter is measured to be about 7 to 9 μm. This measurement is larger than the starting diameter presented by [78] who also used EBSD to measure the grains. Also, the measurements collected by Di Lemma, [110] have large standard deviations. The discrepancy in the grain sizes may be due to the low grain aspect ratio measured in the materials [110]. AFIP6-MkII plates also had a large range of grain sizes. The average grain size was 11.4±7.4 μm, and some grains were elongated up to 25 μm [74]. From other studies the starting grain size ranges from as low as 2 μm [129] to nearly 16 μm [41, 46]. However, these studies do not focus on the monolithic fuels and only present a mean size from several tests and are therefore not compared to the other AFIP6-MkII and RERTR-12 work.

The importance of recording grain size and aspect ratios comes from the need to know the starting sizes and understand the shapes of the grains. If two samples have similar grain diameters but different aspect ratios, they will behave differently. Knowing this level of detail is critical to modeling how the starting material will evolve

Table (2.5) Grain size and aspect ratio of monolithic, as-fabricated fuel samples.

Experiment	Sample ID	Grain diameter (μm)	Grain area (μm^2)	Aspect ratio	Source
AFIP-1	JJ-652	4			[78]
AFIP6-MkII	CB1131		68		[47]
	UM0-342-1-1	7.6 ± 4.5		0.33 ± 0.14	[110]
RERTR-12	JJ1031		54.13		[47]
	L1P757	9.3 ± 4.4		0.29 ± 0.10	[110]

as it is irradiated. Currently, there is a lack of data on the starting grain aspect ratios and starting grain size of U-Mo fuels. Further work must be done to increase the available grain size data for as-fabricated U-Mo for use in computational research.

2.5.2.2 Grain refinement and irradiated grain size

Grain refinement is not measured by the new grain size of the material but by the volume fraction of the material made up of the new smaller grains. The volume fraction of refined grains is heavily dependent on the fission density. Presented in Table 2.6, the fission density or fission rate associated with various samples shows how at the highest fission densities, samples may be 100% changed. However, at lower fission densities, the amount of refinement may be significantly lower. Both the post-irradiation grain size and volume fraction of grain refinement are included as data requirements in Table 2.1. They are related because the area with the smaller grains constitutes the area where grain refinement occurs. Quantifying the size of the grains with the amount of grain refinement will inform how much swelling may be taking place or how much the material has changed.

As is seen in Tables 2.7 and 2.8, the grain diameter decreases after irradiation compared to the starting grain sizes in Table 2.5. However, in Table 2.8 the grain sizes are not nearly as small as those seen in Table 2.7 because of the lower fission densities of the samples. Grain refinement is expected to begin near $3.5 \text{x} 10^{21}$ f/cm^3 [2,20,62] and grain refinement is expected to be complete near $5 \text{x} 10^{21}$ f/cm^3 [30]. Larger grains observed in irradiated samples also belong to the samples with the lowest about of grain refinement, shown in Table 2.6. The samples with the smallest overall grain diameters are nearly fully refined. As the volume fraction of the grain refinement increases, the average grain size will decrease. However, grain refinement is often not presented with the corresponding grain size in the affected areas. The lack of overlap in the samples in Tables 2.7 and 2.8 and Table 2.6 highlight the differences in data collected. More grain refinement data is available than the irradiated grain size data. Measuring both parts of the grain refinement is more useful in presenting a complete picture of the irradiation microstructure and understanding the microstructure behavior.

Table (2.6) Grain refinement volume fraction of M^3 experiments in relation to fission density or rate

Experiment	Sample ID	Fission density (10^{21} f/cm^3)	Fission Rate (10^{14} f/cm^{3}s)	Refinement vol fraction (%)	Source
AFIP-3	AFIP-3BZ TE 3	4.32		62.5	[126]
	AFIP-3BZ TE 4	4.32		75.4	[126]
	AFIP-3BZ TE 5	4.32		68.6	[126]
	AFIP-3BZ TE 6	4.32		63.7	[126]
	AFIP-3BZ TE 7	4.32		53	[126]
AFIP6-MkII	96A	4.74		88.6	[49]
	97A	4.74		97.2	[49]
	KGT2763	4.74		77.7	[49]
RERTR-1	A003	3	3.30	26	[20, 30]
	V002	2.90	3.20	9	[20, 30]
RERTR-2	A005	4.80	2.40	100	[30]
	B004	5.10	2.50	100	[30]
	C003	5.10	2.50	100	[30]
	D005	5.50	2.70	100	[20, 30]
	V003	4.90	2.40	54	[30]
RERTR-3	A10	2.50	6.10	34	[30]
	S03	2.90	6.80	57	[20, 30]
	V03	2.60	6.10	10	[20, 30]
	V07	2	4.90	0	[20, 30]
RERTR-4	A6002H		2.60	100	[30]
	V6001M		2.10	65	[30]
	V6022M		2.50	100	[30]
RERTR-5	A6008H		3.20	29	[30]
	A8002L		3.10	28	[30]
	R6007F			11	[30]
	V6018G		2.50	7	[30]
	V6019G		3.10	7	[30]
	V8005B		2.60	6	[30]
RERTR-8	L1P020	5.95		75	[76]
RERTR-12	L1P462	3.34		72	[76]
	L1P755	5.18		89.4	[49]
	L1P759	8.72		91	[76]
	L1P784	6.31		89	[76]
	L1P7A0	7.71		93	[76]
	L2P499	2.48		37	[76]
	LIP773	3.45		74.9	[49]

2.5.3 Phase composition

Information exploring the volume fraction of phase decomposition for fabricated monolithic fuels is available from RERTR, AFIP, and MP-1 experiments. Fabricated volume fraction of the decomposed areas in RERTR-12 and AFIP6-MkII are given in Table 2.9. The amount of decomposition in JJ1031 (RERTR-12) is about half that of CB1131 (AFIP6-MkII). Indicating the amount of decomposition in AFIP6-MkII plates is much higher. Therefore, the effects of the phases present in AFIP6-MkII are expected to be more significant than in RERTR-12. These decomposition values may be used to predict or understand the post-irradiation behaviour of the samples.

In more recent research, MP-1 experiments qualify if phase decomposition is present in the fabricated samples but does not measure the volume fraction of the decomposed areas [133]. Of all the MP-1 samples where decomposition was studied, all exhibited some amount of phase decomposition [133]. One of the goals of the MP-1

Table (2.7) Irradiated RERTR-12 and AFIP6-MkII sample grain size data

Experiment	Sample ID	Fission density (10^{21} f/cm^3)	Grain diameter (μm)	Grain area (μm^2)	Aspect ratio	Source
AFIP-1	KGT-2141	5.3	0.3			[78]
AFIP6-MkII	6II-1	2.4	0.55	0.61	0.33 ± 0.15	[110]
	6II-1	4.9	0.35	0.1	0.49 ± 0.12	[110]
RERTR-12	L1P755	5.2	0.45 ± 0.25		0.46 ± 0.12	[110]

Table (2.8) Grain size of irradiated dispersion fuel samples using lineal intercept method and four measurement average (adapted from [61, 129])

Experiment	Sample ID	Fission density (10^{21} f/cm^3)	Fission Rate (10^{14} f/cm^{3}s)	Grain diameter (μm)	Grain diameter* (μm)	Source
RERTR-1	A003	2.70	3.80		3.2	[61,129]
	V002	3.10	3.80	6.3	4.9	[129]
RERTR-3	S03	2.90	7		3.6	[129]
	V03	2.60	6.30		7.3	[129]
	V07	2.10	5.10		6.5	[129]
	Y01	2	4.80		10.1	[61,129]
	Z03	2.10	5.10	24.4	23.6	[61,129]
RERTR-5	A6008H	3.30	3.30	5.3	6.2	[61,129]
	A8002L	3.20	3.20	3.9		[61,129]
	R6007F	2.60	2.60		6.2	[61,129]
	V6018G	2.30	2.30	4.9	5.2	[61,129]
	V6019G	3.30	3.30	8.5	7.6	[61,129]
	V8005B	2.50	2.50	8.1		[61,129]

*Lineal intercept method

fuel campaign was to measure the amount of decomposition and secondary phases in the samples to mitigate the negative effects on the behavior that the decomposed phases has [133]. However, the volume fraction of the decomposed regions, or the amount of decomposition, is not yet available and therefore is difficult to apply in model development work.

Table (2.9) Phase decomposition volume fraction of of RERTR-12 and AFIP6-MkII fabricated, archival samples.

Experiment	Sample ID	Decomposition (%)	Source
AFIP6-MkII	CB1131	14.18	[47]
	CB1131	18.0±6.1	[49]
RERTR-12	JJ1031	7.4±3.6	[49]
	JJ1031	7.63	[47]

Table (2.10) Carbide volume fraction of RERTR-12 and AFIP6-MkII fabricated and irradiated samples.

Experiment	Sample ID	Fission density (10^{21} f/cm^3)	Carbide vol. fraction (%)	Source
AFIP6-MkII	CB1131	Fabricated	3.95	[47]
	KGT2763	4.74	1	[49]
	96A	4.74	0.93	[49]
	97A	4.74	0.77	[49]
RERTR-12	JJ1031	Fabricated	2.44	[47]
	L1P755	5.18	0.0043	[49]
	LIP773	3.45	0.0097	[49]

2.5.3.1 Carbide data

Pre- and post-irradiation volume fractions of carbides are presented in only a few references. Table 2.10 contains the starting carbide volume fraction of RERTR-12 and AFIP6-MkII and the irradiated carbide volume fraction measured [47, 123]. There is a decrease in the volume fraction of the carbides in the material after irradiation. Therefore, it is important to understand the destruction of these second-phase particles in the fuel and their impacts on the fuel behavior. Modeling may help to illustrate and explain the destruction of these second-phase carbide particles.

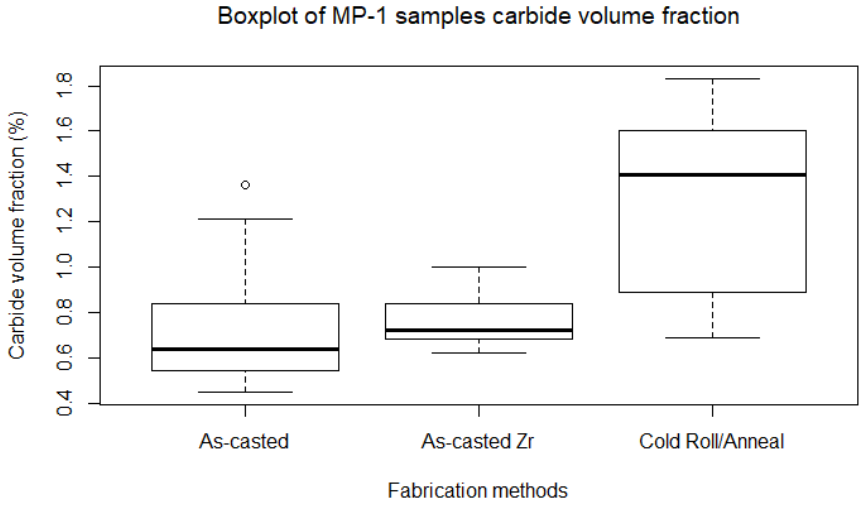

Figure (2.11) Boxplot of the as-fabricated carbide volume fractions from the MP-1 experiments currently being studied as part of the M^3 program. Some samples were characterized as they are cast during production, after cold-rolling, and one type was covered by a zirconium diffusion barrier. Adapted from Di Lemma et al. [133].

Additionally, MP-1 data in Figure 2.11 show the summarized volume of carbides in the most recent fuel fabrication efforts. The volume fraction of carbides is lower than in values from Table 2.10. The lower carbide values may indicate that the efforts of the MP-1 fuel campaign were successful in homogenizing the material and preventing unwanted phases from forming. Further exploration into the fabrication methods and irradiation performance of these samples is required to understand and quantify the carbide effects fully.

Table (2.11) Mo variation across fabricated RERTR-12 and AFIP6-MkII archival plates

Experiment	Sample ID	Banding (%)	Light/dark phase (%)	Mo variation (wt%)	Source
RERTR-12	JJ1031	88	59/41	7–13	[47, 49, 74]
AFIP-6MkII	CB1131	100	60.17/39.83	8.5 –11.5	[47, 49, 74]

2.5.4 Mo concentration

The availability of molybdenum distributions throughout the fuel is also limited and performed using differing approaches, much like the previous microstructure information. For example, chemical banding is presented in Table 2.11 and was measured to estimate the fluctuating molybdenum amount across the RERTR-12 and AFIP6-MkII plates. The area fraction, or percent, of the material that is banded shows that the chemical composition is heterogeneous across 100% and 88% of the RERTR-12 and AFIP6-MkII plates, respectively. Banding is then further broken into Mo-rich, dark phases and Mo-depleted, light phases [47, 74]. The amount of light to dark amounts are almost identical between the two samples. Lastly, techniques such as wavelength dispersive X-ray (WDS) analysis are used with SEM imaging to measure the molybdenum variation across the plate. Data from the two previous plates are provided in Table 2.11 from Jue et al. [74, 122] on the archival, fabricated plates. Molybdenum weight percent variation was slightly higher for the RERTR-12 plates. This variation is expected to come from the faster cooling methods used while fabricating the RERTR-12 plates compared to the AFIP6-MkII samples [74]. The two samples are reasonably similar in the chemical homogeneity measured despite the differences in the molybdenum weight variation. Studies from other AFIP and RERTR experiments that included data on the molybdenum variation were not available. Therefore, further exploration into the chemical composition of past experiments would help understand the fuel behavior.

The MP-1 molybdenum distribution is available, as well [133]. Figure 2.12 shows the comparisons of the different fabrication methods and the molybdenum distribution. The weight percent between 9.5 and 11wt% Mo is more similar to those of AFIP6-MkII than RERTR-12 samples in Table 2.11. This data gives a limited amount of information as to where molybdenum depletion exists in the material. molybdenum variation along the grain boundaries and in more exact locations of the low molybdenum concentration areas are needed for precise modeling of the effects of higher ^{235}U. Measurements of chemical variation maps have not been found for U-Mo in the M^3 experimental data that may help inform microstructure modeling efforts.

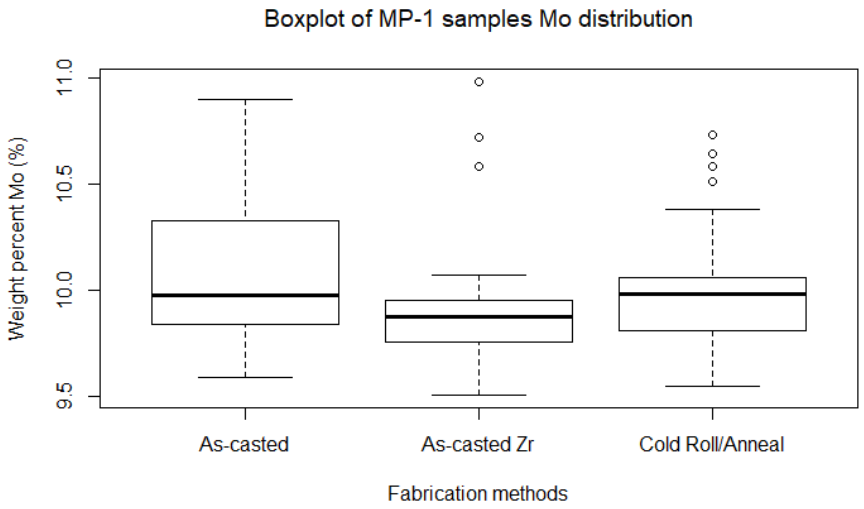

Figure (2.12) Boxplot of the as-fabricated molybdenum weight percent across a sample from the MP-1 experiments currently being studied as part of the M^3 program. Some samples were characterized as they are cast during production, after cold-rolling, and one type was covered by a zirconium diffusion barrier. Adapted from Di Lemma et al. [133]

2.6 Critical analysis of available data

From Table 2.2 the number of samples and studies involving U-Mo fuels are numerous. This table explains the differences in fuel type and composition to inform those using the data if these are comparable or to warn how the samples are different. When comparing the microstructure of the various experiments, knowing the starting differences of each sample is critical. For example, comparing the porosity of a dispersion sample to a monolithic sample is not advisable due to the important differences in the fabrication methods and starting microstructure. However, as is seen in the other sections on the available microstructure data, information on certain MM topics is not available for both fuel types. All of the samples are highlighted to provide modelers with an array of available data. Additionally, the data presented underscores the areas of the MM needs where data is lacking.

2.6.1 Pore data

The amount of data found on fuel porosity and FGB is by far the most widely available for the fuel campaigns included. FGB, or the gaseous fission products that cause pores contribute directly to the swelling observed in the material. Therefore, this phenomenon is studied the most abundantly. Of the numerous works, few studies included the pore size distribution that is most useful for modeling purposes [30, 61, 62]. Due to the significant differences in FGB size and population throughout the fuel, using an averaged data point is less telling of the actual microstructure than the entire dataset or distribution of the FGB. Moreover, of the studies on FGB pores, none were

found to include the gas density inside of those bubbles required by MM6. From this summary and collection of FGB and porosity data, there are undoubtedly many results of M^3 experimental porosity studies, but the complete datasets are necessary for the use in models and not readily obtainable.

2.6.2 Grain behavior

Grain size data irregularity is problematic for model validation and usage indicated by MM2a. For example, grain characteristics are given in the forms of grain size area [47], grain number [133], and grain diameter [72, 112, 129]. Methods used to collect the data also may differ between different studies [65]. Some grain size-related MM2a data needs, like grain aspect ratios, are not as prevalent in the literature as grain diameter measurements. While all of these grain characteristics are related and may be deduced from the other, a standardized approach is required to make the data more consistently comparable.

Grain refinement volume fractions in Table 2.6 are presented to meet the needs in MM2 and 5. Literature containing this grain refinement data often presents the information only as the amount of refinement as a function of fission density, not grain refinement and grain size. However, MM5 requires the inclusion of the starting grain size with this analysis. Starting grain size in the material will control how much grain refinement occurs and how soon it will initialize during irradiation. MM2a is the need for the final grain size inside the refined areas. Data connecting the starting and post-irradiation grain morphology are uncommon. Few sources present the fabricated and irradiated grain size along with the grain refinement observed. To improve data collection methods, the starting grain size must be available along with the PIE information. Additionally, the amount of grain refinement is must be presented with the grain size and grain morphology. Few studies contain all of the required grain information. Therefore, it is difficult and inadvisable to compare all the various information from the M^3 experiments.

Data on RERTR-12 specifically are asked for in MM13. Table 2.5 and 2.7 show the most recent results on the grain size of archival and irradiated fuel plates for this experiment and AFIP6-MkII. For the first time, Di Lemma et al. [110] used EBSD to measure texture, grain size, and grain aspect ratio of the fabricated and irradiated fuel samples. While this new use of EBSD informs the grain boundary angles present and the change of grain size after grain refinement, a full grain size distribution is still not available in the literature. Grain size distributions from multiple experiment samples will provide a more thorough representation of the grain microstructure and are required to meet the modeling needs.

2.6.3 Phase volume and chemical composition data

Phase volume fractions and molybdenum distribution from MM1 and 3 are explored in fuel characterization and PIE studies, but qualitatively. Few studies of M^3 experiments reported on these characteristics of fabricated or irradiated specimens. And the ones that did do not give exact phase volume fractions or measurements. To meet

the MM needs, more work must be done to quantify these fuel microstructures for multiple samples.

As is shown in the previous sections, much work has been done to study U-Mo fuels. However, it is summarized or qualitative information. More recent studies on RERTR, AFIP6-MkII, and MP-1 fuel campaigns have expanded to include much of the information required to improve models as indicated in Table 2.1 [127, 132–134]. However, a more targeted, quantitative approach is needed when providing data for specific purposes like model validation and inputs. All the MM experimental data gathered in this work is inconsistent in its characterization methods and metrics and is not always available as fabricated and irradiated samples. Directly comparing the before and after microstructure is not advisable unless the samples use the same characterization techniques or materials. More standardized data collection and analysis approaches are needed to answer the questions and needs presented above fully. Understanding exactly how the microstructure has changed during irradiation will allow for more precise modeling and quantification of how irradiation conditions impact the material.

2.7 Conclusions

The overall conclusion from collecting the U-Mo data available in the literature, is there is a need for more complete and standard microstructure data production and publication. Modeling efforts require experimental data for validation and model inputs. However, the current data is lacking in consistency in what metrics and methods are used to measure the microstructure characteristics. Additionally, many of the MM needs included here are not being studied or are not found in large quantities as part of the M^3 fuel qualification efforts.

Standardized methods such as those developed by Smith et al. [128] in porosity image analysis are necessary to make comparable data between experiments. Errors and differences in the related microstructure results may be attributed to differences in characterization techniques or an underlying physical trait of the material. Separating experimental and physical differences is impossible without knowing every aspect of the characterization and analysis used to obtain the experimental values. If two studies used different analysis techniques, the comparison of the data must be done carefully and with understanding that the information may not be comparable due to experimental differences.

The data currently available for model improvement from the M^3 experiments meets some of the MM needs, but many aspects require further study and data collection. This work is a starting point for communicating modeling needs to other U-Mo researching entities. Using the MM as a guide for future experiments will allow for more prescriptive data collection as well as better communication between the experimentalists and modelers working towards the implementation of U-Mo fuels in research and test reactor environments. Both parties may inform the work of each other to improve fuel qualification techniques and methods.

2.8 Future work

While the amount of materials data on monolithic U-Mo fuels may be limited, experiments may be performed or planned using the data needs explained in Table 2.1. Current, work is underway that will meet these data requirements, but the information must be shared in an easily attainable format with the microstructure modeling researchers. Clear communication between modelers and experimentalists is key to bridging the gap of experimental data and modeling needs. By using the MM needs outlined in this work as a guide for future experiments or future data collection, U-Mo material models can be made more precise and reliable, while also providing useful information for designing irradiation experiments and planning future fuel qualification work. Current work is underway to obtain MM data from ongoing experiments and to assist in planning future M^3 U-Mo fuels work.

Chapter 3: Historic data collection and data analysis methods development

3.1 Introduction to RERTR and AFIP6-MkII

The purpose of this chapter is to explain the work performed on the RERTR-12 and AFIP6-MkII samples to better understand the differences in performance of the two experiments. Chapter 2 highlighted the data needs required to improve modeling capabilities. In an attempt to collect more data and improve the reliability of that data, two internal INL reports were produced for this work and the statistical analysis of the collected porosity and microstructure data are explained in the following sections. INL/LTD-18-51296 [47] is focused on the image analysis of AFIP6-MkII and RERTR-12 before and after irradiation. For the purposes of this work the contributions are in collecting data from past INL reports and analyzing connections between starting microstructure and the PIE data. Specifically, the focus is on data of as-fabricated fuel while studying the grain refinement and porosity of the material in a standardized method. INL/EXT-20-60135 [127] extends this work of attempting to standardize data collection and analysis methods for the use in computational material science. It focuses on how experimental conditions and pore, FGB, data are collected and analyzed for modeling improvements. Porosity data was collected by researchers at the University of Florida and the work herein takes the large datasets of porosity results and analyzes them in a repeatable manner necessary for reliable data collection.

3.2 Purpose of studying past experiments

Swelling is a primary concern of the performance of metallic fuels; grain refinement, FGB, and the decomposition of phases all will influence the volume change observed. All the explored microstructural features are interdependent and must be quantified to understand the relationships these have fully. The fabricated microstructure will impact the irradiation behavior of the material, and the evolution of one characteristic may influence another. RERTR-12 and AFIP6-MkII are unique cases of U-Mo fuels that were similar in fabrication and were expected to swell similarly but did not. Understanding how the as-fabricated microstructure affects the two experiments' swelling and irradiated structure differences is performed first. In the second portion, pore size data is collected using a new image analysis technique developed by Smith et al. [128], and the work herein analyzes the results to quantify the relationship between fission density and FGB growth. As the fission rate or density increases, the size and number of FGB is also expected to increase. However, as is shown that this relationship is more complicated than a purely linear relationship. Below, a new data analysis method is developed to demonstrate the benefits and needs of collecting more comprehensive data for modeling purposes.

3.3 RERTR-12 and AFIP6-MkII history

In the effort to qualify an effective LEU fuel for research and test reactors, two experimental campaigns were undertaken, the RERTR-12 tests and AFIP6-MkII tests. These two irradiation experiments on U-10wt% Mo, monolithic fuels were expected to behave similarly. However, PIE results were dissimilar, despite the same material fabrication and preparation methods [73]. The swelling behavior of the two plates was drastically different with respect to the amount of swelling and the fission densities experienced in the experiment. As shown in Figure 3.1, AFIP6-MkII exhibited approximately 15% higher swelling than the samples of RERTR-12 [75, 76]. From this graph, it is also clear there were more RERTR-12 samples tested than AFIP6-MkII. But there is also a peak in the AFIP6-MkII swelling between 4.5×10^{21} and 6×10^{21} f/cm^3, much higher than the RERTR-12 measurements. This discrepancy is the subject of this section to try to understand what microstructure differences exist that may explain this behavior.

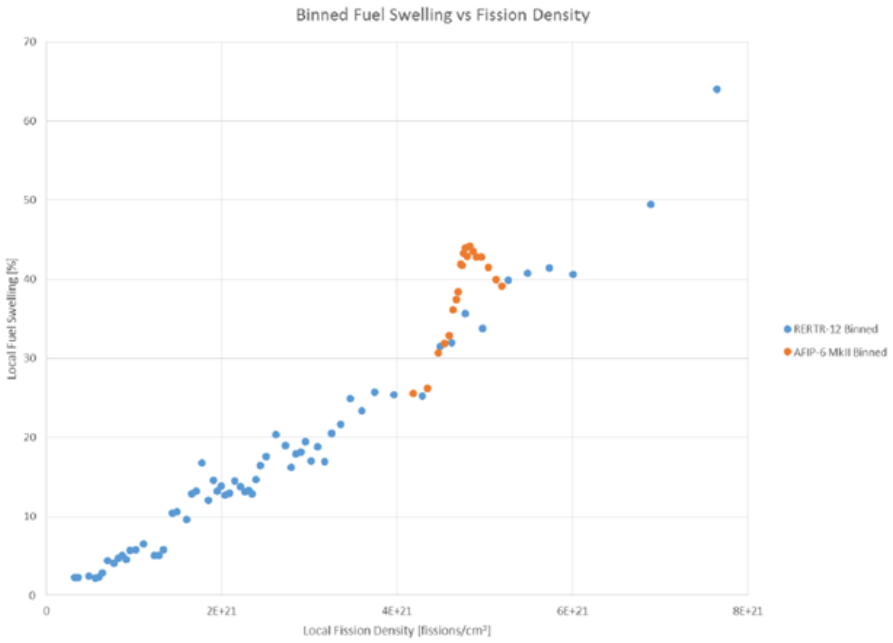

Figure (3.1) Swelling volume percents based on binned data points for RERTR-12 and AFIP6-MkII experiments collected and analyzed by Robinson et al. [49]. Orange, AFIP6-MkII swelling measurements are between 10 and 15% higher at similar fission densities despite the similar fuel structures.

For RERTR-12, 56 mini-plates were made and tested. Whereas, AFIP6-MkII consisted of two plates, which matched the dimensions of a full-sized ATR plate [135, 136].The material composition of both experiments is U-10%Mo fuel meat, surrounded by a zirconium diffusion barrier with an Al cladding. The samples were hot-rolled, annealed, then cold-rolled to achieve the proper thickness [135, 136]. The zirconium diffusion barrier was added using a hot-isostatic pressing (HIP) treatment [73]. Table 3.1 provides more details on the samples explored in this

Table (3.1) Dimensions and characteristics of RERTR-12 and AFIP6-MkII archival and sister plates [135, 136]

Experiment	Dimension	Composition (wt%)	As-fab samples	Irradiated samples
RERTR-12	2.54 cm × 10.16 cm × 0.1397 cm	70% ^{235}U, 10wt% Mo	JJ1031	L1P755, L1P773
AFIP6-MkII	5.69 cm × 114.3 cm × 0.132 cm	40% ^{235}U, 9.84wt% Mo	CB1131	AFIP6

work. RERTR-12 samples are enriched to 70% ^{235}U, whereas AFIP6-MkII have 40% enrichment. Sample names in the table will be referred to throughout this chapter.

3.4 Fuel fabrication

Fabrication techniques are explored to elucidate differences between as-fabricated microstructure of the two experiments. Below, each fabrication step is explained in detail, and differences are highlighted to understand possible irradiation effects from the samples.

3.4.1 Foil preparation

The U-Mo foils are created from cast fuel coupons produced at Y-12 [73]. Alloy coupons are treated with 30% nitric acid, deionized water, and ethanol and wiped clean to remove any current oxidation. The zirconium foils are cleaned with a lint-free cloth, and the outer sides are polished with a 30-μm diamond polish and rinsed with ethanol, DI water, and wiped down for RERTR-12. However, the AFIP6-MkII outer zirconium surfaces are cleaned only with acetone. After the cleaning step was complete, a 100°C 10 minutes, Neolube treatment is applied outside the zirconium foils. Next, the fuel coupon is placed within low carbon steel frames, and zirconium foils are placed over both open faces of the steel frame, covering the fuel coupon. The zirconium foils are slightly larger than the inside of the frame and held in place before spot welding the zirconium to the outside of the frame. Steel plates then cover both surfaces of zirconium and are welded around the entire setup [135, 136].

3.4.2 Hot rolling

Next, the samples are hot rolled and annealed. Both experiments are preheated for 30 minutes in a box furnace at 650°C. For RERTR-12, the mill rolls are preheated before the rolling occurred. AFIP6-MkII undergo three passes. These passes consist of three reduction passes and single passes and are reheated every five minutes. On the first reduction pass, the sample is cross-rolled with a 20% reduction to widen the plate. After 12 total passes, the final thickness was 0.072 in [135].

Hot-rolling the RERTR-12 samples is much different, due to the number of mini-plates produced and the varying

thickness of the starting samples. Of the 56 plates, the number of rolling passesis between 9 and 27, resulting in a thickness reduction of 20 to 40% per pass. L1P755 undergoes ten hot passes for a 40% thickness reduction and a final thickness of 0.015 inches. The thickness of L1P773 is reduced by 40% to 0.016 inches eight hot passes. JJ1031 undergoes a reduction of 40% in nine passes and ended with a thickness of 0.015 inches [136]. After the samples were rolled to the proper thickness, they are annealed for 45 minutes at 650˚C.

3.4.3 Cold rolling

Following the annealing and hot rolling is the cold rolling step where the plates are again put through a mill roll but in an unheated environment. RERTR-12 plates are cold rolled in three, four, and four passes for L1P755, L1P773, and JJ1031, respectively. The thickness reduction is between 20 and 25% for a final foil thickness of 0.012 inches. The cold rolling caused warping to occur in some samples; this includes L1P755 and L1P773. L1P773 is annealed at 650˚C a second time to flatten out [136]. AFIP6-MkII6 cold rolling reduction is about 40% in 14 to 16 rolling sets. Each set includes three passes, so the total number of actual cold roll passes was 42 to 48. The final thickness of the plates is 0.015 in [135]. After the cold rolling work is complete, the samples then undergo HIP processing.

3.4.4 HIP fuel fabrication

HIP is a method for manufacturing materials by placing an item in a highly pressurized and heated environment to bond materials. In the case of monolithic nuclear fuels, the pressure and temperature conditions bond the aluminum (Al-6061) cladding to the zirconium coated U-Mo fuel [137]. One of the cladding sheets has a recessed area to lay the U-Mo in and then is covered with the second sheet [135, 136]. RERTR-12 plates are clad with an Al-6061-T6, 0.040-inch sheet. The sheets are prepared for HIP by degreasing the material with acetone or ethanol, etched with a 2M NaOH solution. The sheets are then pickled in a 30% acid solution, rinsed with water followed by a hot rinsed, wiped down before vacuum sealing the apparatus [136]. Similarly, the AFIP6-MkII plates are prepared; however, a pickling step using hydrofluoric acid and deionized water is also employed [135].

After this preparation, steel plates are placed on the outsides of the fuel plates to ensure even pressure during HIP steps. The plates are then welded shut and vacuum sealed. RERTR-12 is processed for 3 hours at 315˚C and AFIP6-MkII is done for 2.75 hours at 321˚C. HIP-ing is then performed at 560˚C at 15 ksi pressure for 90 and 95 minutes [135, 136].

3.4.5 Final processing

The final steps used in fabricating the two experimental plates ensure the reliability and quality of the fuel. Ultrasonic testing and blister annealing inspect the foil placement and thickness. These two inspections also check for debonded locations between the cladding and fuel. Boehmite processing prevents corrosion of the outer material

by creating a film of boehmite during an autoclave step at 185°C for eight to 18 hours [8, 135, 136, 138]. Lastly, bend and fuel-out-of-zone testing ensure the fuel does not delaminate when bent and checks the lamination. Fuel-out-of-zone checks that the fuel meat is in the proper location and size [135, 136].

Table (3.2) Comparison of RERTR-12 and AFIP6-MkII fabrication methods, highlighted in red are the most notable differences between the two. Reproduced from [74].

	JJ1031 (Alloy 328-2, RERTR-12, plate ID L1P757, HIP 58-4)	JJ1028-F2, JJ1028-F4 and CB1131-F8 (Alloy342-1-1, AFIP-6MKII, plate ID UM0-342-1-1)
Feed stock	INL HEU	Y-12 HEU (coupon 3G60-C7-PA24)
Casting	INL are melting	Y-12, vacuum casting, no in-mold annealing
Enrichment	70%	40%
Foil thickness, including Zr (mil)	12	14.9
Hot rolling passes	9	12
Max hot rolling reduction (%)	40	20
Total hot rolling reduction (%)	85	84
Total hot rolling time at 650°C	80 min	80 min
Post hot rolling annealing at 650°C	45 min	45 min
Cold rolling passes	4 (aggressive)	44
Total cold rolling reduction (%)	20	40
Flattening at 650°C/lhour	No	No
Total time at 650°C	125 min	125 min
Foil characteristic	Wavy (after cold rolling)	Flat (after cold rolling)
HIP run temperature (°C)	560	560
HIP run pressure (psi)	15000	15000
HIP run ramp rate (°C/hour)	280	Used a slower ramp rate
HIP bonding time at 560°C (minutes)	90	95
HIP run variables	Six plates per HIP can	Two plates per HIP pack, thicker cladding, without top strong-back
Note	Miniplate benchmark, RERTR-12 first insertion, Carbon less than 400ppm	Carbon 692ppm, Iron 80ppm

3.4.6 Fabrication differences

From the comparison of the two archival plates of the previously outlined fabrication steps, the biggest differences are in the number of cold rolling passes and the ramp rate used in the HIP process [47, 135, 136]. Table 3.2 was prepared by Jue et al. [74] in earlier characterization efforts to highlight the startling differences in the AFIP6-MkII and RERTR-12 plates. AFIP6-MkII historical sample, CB1131 underwent 44 cold rolling passes and was reduced by 40% whereas the RERTR-12 sample, JJ1031 underwent a 20% reduction in only four passes [47, 49, 74]. The

slower HIP ramp rate in AFIP6-MkII results in a larger amount of phase decomposition present than in RERTR-12 [47]. The γ phase decomposes to the lamellar, $\alpha + \gamma$' phase from the longer time exposed to the heat and slow cooling. The next section further characterizes the fuel microstructure used to explore any other microstructural differences between the two experiments.

3.5 Characterization and image analysis methods

In [47] an early version of a standardized, automated process was developed by researchers at the University of Florida and demonstrated in that work. The image analysis used a combination of MATLAB and ImageJ software to measure grains, carbides, phase transformation, grain refinement, and pores with OM. Further details on this process can be found in Ref. [47]. However, this technique has been improved upon in newer work by Smith et al. [128]. The automated process is more reliable and easily used than previous manual measurement processes. This is outside the scope of this dissertation work due to the methodology being developed by researchers at a separate university and is not the focus of the data analysis methods used here. The SEM analysis is performed using manual ASTM methodology and MATLAB. SEM micrographs are captured using a JEOL 7000F field emission SEM. The accelerating voltage was at 20 kV and 10 mm working distance. A total of 18 micrographs are obtained for the included image analysis.

3.6 Early characterization of fabricated samples

Archival data from CB1131 (AFIP6-MkII) and JJ1031 (RERTR-12) gives a baseline of the starting microstructure. The grain size, phase decomposition, and carbide fraction are all investigated. Below, Table 3.3 summarizes the as-fabricated data from report INL/LTD-18-51296 [47]. These are the results from analysis using SEM images. Magnifications of 500X and 5000X are employed to view these features. 500X magnification, however, is the most representative of the actual microstructure. High magnifications will expose a more localized microstructure that is not representative of the rest of the material.

Table (3.3) SEM Characterization of CB1131 and JJ1031 [47]

Sample	Magnification	Light phase (%)	Dark phase (%)	Decomposition phase (%)	Carbide vol. fraction (%)	Mean grain area (μm^2)
JJ1031	500X	59.00	41.00	7.63	2.44	54.13
JJ1031	5000X	n/a	n/a	8.4	0.28	12.53
CB1131	500X	60.17	39.83	14.18	3.95	68
CB1131	5000x	n/a	n/a	4.06	2.65	23.85

The light and dark phase percents are the volume fraction of the micrographs that are banded. An example of this band can be seen in Figure 3.2. The light phase has a low molybdenum concentration, and the dark phases contain the decomposed regions. At 5000X, the light and dark phases are not visible as that level of magnification the bands

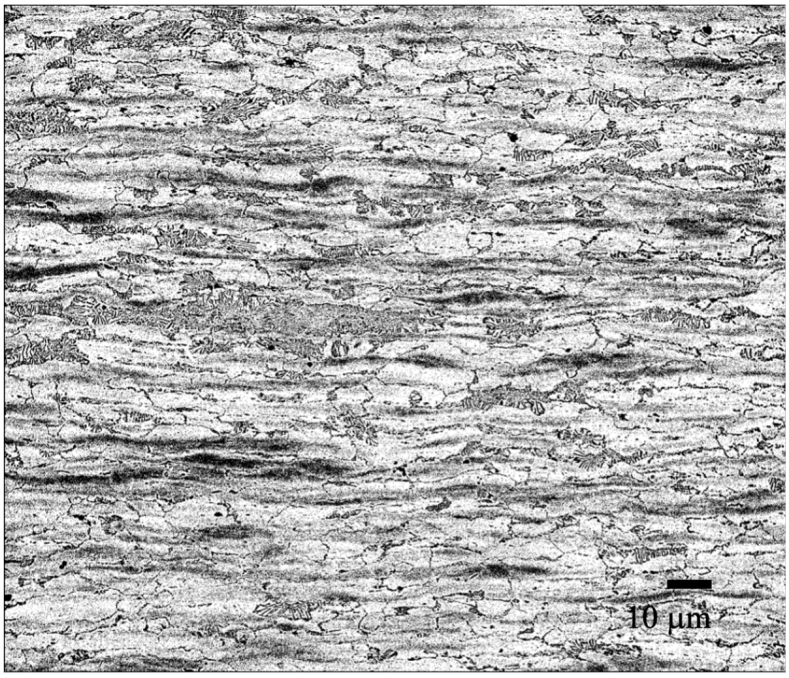

Figure (3.2) Chemical banding observed at 500X, SEM of JJ1031 showing the light and dark phases showing the extent of chemical inhomogeneity affecting the fuel behavior [47].

are no longer visible. CB1131, or the AFIP6-MkII, samples have higher amounts of decomposition and banding. This increase in decomposition and banding is most likely due to the longer time spent at high temperatures during HIP fabrication compared to the RERTR-12 sample.

In a separate analysis, using the ATSM-E562-11 [139] standard point count method, CB1131 was measured to have 100% banding across the surface, and JJ1031 had 88% banding [49]. The amount of molybdenum across the plate is not uniform for either fabricated sample. This inhomogeniety proves problematic due to the early onset of decomposition and grain refinement that may occur due to the low molybdenum content [2, 49, 69, 74, 93, 109]. Robinson et al. [49] present the phase decomposition alongside the banding. The results are about 7.4% decomposed volume fraction in the RERTR sample and about 18% decomposed in the AFIP6-MkII sample [49]. Higher amounts of phase decomposition will allow grain refinement to occur earlier and, therefore, may cause the discrepancies found in the swelling results of the two experiments despite similar fission densities and fabrication.

3.7 Early PIE data

In the irradiated work, OM and SEM micrographs and the proposed image analysis methods measured the porosity, grain size, and the percent of unrefined grains. Four regions are examined within sample L1P755 using OM, the bulge region 1 and 2 and center regions 1 and 2 at two magnifications 20 μm and 50 μm. Three areas, the top, middle, and bottom, of the AFIP6-MkII plate are then examined with OM, as well. The method used to measure

the as-fabricated data is the same for these samples. After the optical examination irradiated samples KGT2144 of AFIP6-MkII and sample L1P755 of RERTR-12 are analyzed using SEM for more detailed microstructure analysis.

3.7.1 Optical results

Table 3.4 gives the final OM results for L1P755. Measured grain sizes in the 50 μm samples are higher than those at 20 μm. The porosity data for both samples is fairly similar with the averages of the two different magnifications, between 22 and 27%. Additionally, the samples are almost fully refined for L1P755. The amount of area that is not is only about 2% at the highest. The grain size differences between the fabricated plates and the irradiated verify this change as well. A decrease from 54 μm^2 to approximately 10 μm^2 was measured.

Table (3.4) Results from the early OM analysis of sample L1P755 [47]

Sample area	Scale Bar Size in Images	Porosity (%)	Mean pore area (μm^2)	Grain size area (μm^2)	non-refined grains (%)	Fission density (10^{21} f/cm^3)
Bulge region 1	20µm	27.29	0.59	n/a	n/a	4.6
Bulge region 2	20µm	26.61	0.6	n/a	n/a	4.6
Center Region 1	20µm	24.68	0.55	8.04	0.8	4
Center Region 2	20µm	25.38	0.55	9.48	2.04	4
Bulge region 1	50µm	26.54	1.83	n/a	n/a	4.6
Bulge region 2	50µm	26.97	1.85	n/a	n/a	4.6
Center Region 1	50µm	23.38	1.89	14.67	1.35	4
Center Region 2	50µm	22.15	1.8	11.64	2.7	4

The optical results for the top, middle, and bottom plane of AFIP6-MkII are given in Table 3.5. In AFIP6-MkII samples, carbides were measured as part of the porosity. This is why the porosity is presented in the form of volume fraction with the carbides. Once the carbides are measured, they are subtracted from the first total to give the porosity. Of the three samples, the largest grain size was at the top. This coincided with the lowest amount of grain refinement, which is expected since larger grains will lead to less grain refinement. The bottom plate exhibited the highest amount of porosity and the highest fission density. Again, this is in line with the expectation that as fission density increases so does the production and growth of FGB.

Table (3.5) Results from the early OM analysis of sample AFIP6-MkII [47].

Plane	Scale Bar Size in Images	Porosity (%)	Mean pore area (μm^2)	Mean porosity w/ carbide phase (%)	Grain size area (μm^2)	non-refined grains (%)	Mean carbide area (μm^2)	Carbide volume fraction (%)	Fission density (10^{21} f/cm^3)
Top	20 µm	20.52	0.55	21.51	34.67	15.65	9.97	0.99	4.5
Middle	20 µm	20.09	0.66	21.18	28.96	5.21	9.74	1.09	4.9
Bottom	20 µm	29.92	1.01	30.83	20.5	1.67	7.73	0.91	4.9
Top	50 µm	19.61	1.75	20.83	39.36	12.74	11.51	1.22	4.5
Middle	50 µm	15.14	1.48	15.65	27.57	5.01	7.73	0.51	4.9
Bottom	50 µm	25.46	2.15	25.97	25.6	1.54	10.59	0.51	4.9

3.7.2 Early SEM analysis

Two samples are studied with the SEM analysis, L1P755 and KGT2144 (AFIP6-MkII). From seven sites on these plates, the microstructural features of porosity, grain size, unrefined grain areas, and carbide volume fraction were obtained. Each is measured at 500X and 5000X magnifications. Below Table 3.6 gives the final results of the two samples at both magnifications.

Table (3.6) SEM results from image analysis of samples L1P755 (KGT2055) and KGT2144 (AFIP6-MkII) [47]

Sample	Mag	Fission density (10^{21}f/cm^3)	Porosity (%)	Mean pore area (μm^2)	Mean pore diameter (μm)	Grain size diameter	Unrefined grain regions (%)	non-refined grain area (μm^2)	Carbide volume fraction (%)
L1P755	500X	5.2	17.88	2.66	1.67	N/A	0.21	14.72	N/A
L1P755	5000X	5.2	20.72	0.12	1.83	8.57	5.11	0.31	N/A
KGT2144	500X	5.1	20.74	3.13	0.34	N/A	1.32	13.89	N/A
KGT2144	5000X	5.1	21.22	0.2	0.42	7.43	16.42	0.55	1.43

Where the carbides volume fraction are not listed, there are no carbides observed in that section of the fuel. At the lower magnification it was also not possible to accurately measure the grain size of the samples so the grain size area is only measured for 5000X. Comparing the SEM results to the optical results shows the differences in measurements that exist when using the same sample but different methods of image collection.

3.7.3 Summary of early optical and SEM results

Between the two experiments, the most considerable difference is between the AFIP6-MkII and RERTR-12 samples were in the starting amount of phase decomposition and the grain sizes. Porosity in the irradiated samples was nearly equal for the OM and SEM analyses. One notable difference is within AFIP6-MkII itself. The measured grain refinement is lower in the top sample of the plate, 85% refined, compared to the bottom plate at almost 100% refined. The grain refinement in the top section AFIP6-MkII also contradicts the theory that phase decomposition leads to higher amounts of grain refinement. RERTR-12 showed lower amount of decomposition in the fabricated microstructure, but was nearly 100% refined after irradiation. The two experiments' differences are not apparent from this cursory analysis of the starting microstructure and irradiated samples. Therefore, further studies are presented next to discuss the differences in porosity and how data collection may be improved compared to that presented above.

3.8 Updated characterization techniques

To meet the needs of the modeling data, more specific and abundant data is required. As explained in Chapter 2, much of the required MM data is required in the form of distributions, as opposed to averages [61, 62]. To understand the best methods in collecting and analyzing, the same material samples were further analyzed using a

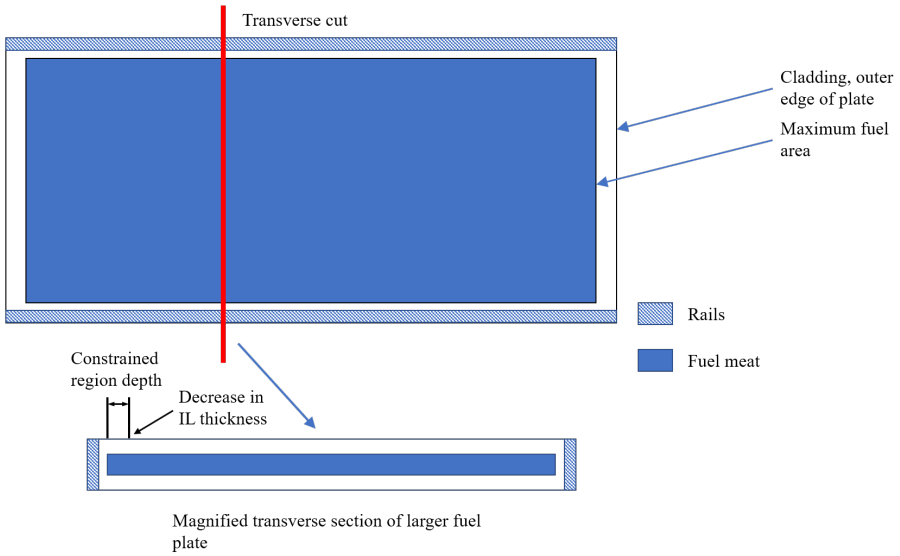

Figure (3.3) Rail region diagram of fuel plate and transverse cut sample illustrating how each AFIP6-MkII and RERTR-12 sample is obtained [127].

newer, standardized image analysis method for measuring porosity developed at the University of Florida by Dr. Charlyne Smith and Dr. Assel Aitkaliyeva [128]. Using the data collected in this new method, a new data analysis method is developed and is presented in the following sections.

3.8.1 Sample description

Three samples from the AFIP6-MkII experiments and one sample from the RERTR-12 experiment are prepared for this work. Each sample is taken as a transverse cut from the original plate. All samples are irradiated face-on to ATR making the irradiations similar and allowing for direct comparison between the two experiments of these samples [73]. Figure 3.3 illustrates how the transverse samples are cut from the larger plate. The samples consist of a U-Mo fuel middle surrounded by the zirconium diffusion barrier and Al cladding, as shown at the bottom of the figure.

The AFIP6-MkII mini-plate samples are KGT2763 (previously 95A), 96A, and 97A and cut from the larger fuel plate. Each mini-plate measures 2.54 by 0.02 cm. Figure 3.4 shows the mini-plate sections in orange. Part b, c, and d in Figure 3.4 are the full micrograph of the three mini-plates. Over the top of the samples, images are the fission densities of each location data was taken. Top, middle, and bottom samples represent varying locations on the large plate and demonstrate the overall plate microstructure. Due to troubles with sample preparations, the top plate, KGT2763, is cut to 0.953 cm [140]. For completeness, the sample was analyzed and included in this analysis, but less data was taken from the smaller sample area and therefore, requires future analysis to understand if the small sample size creates high standard deviation or errors.

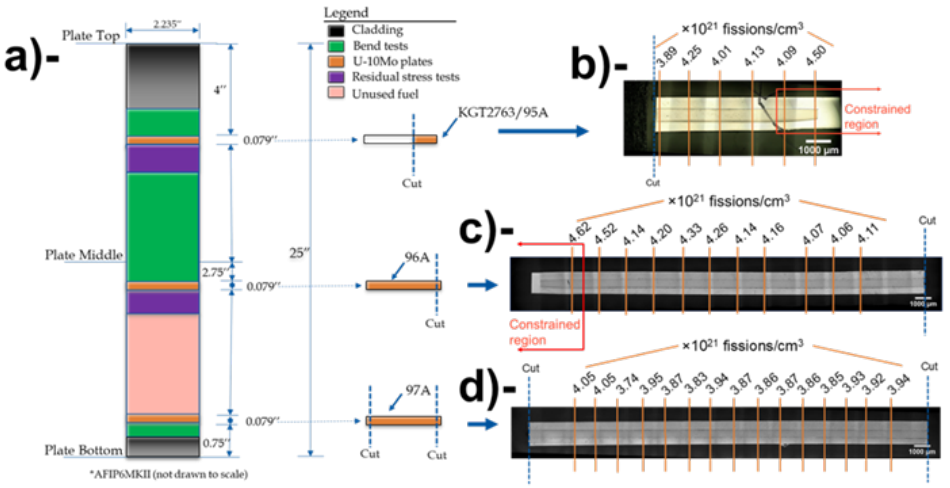

Figure (3.4) AFIP6-MkII full-sized plate illustrating the dimensions of the sample miniplates cut from the top, middle, and bottom of plate [127].

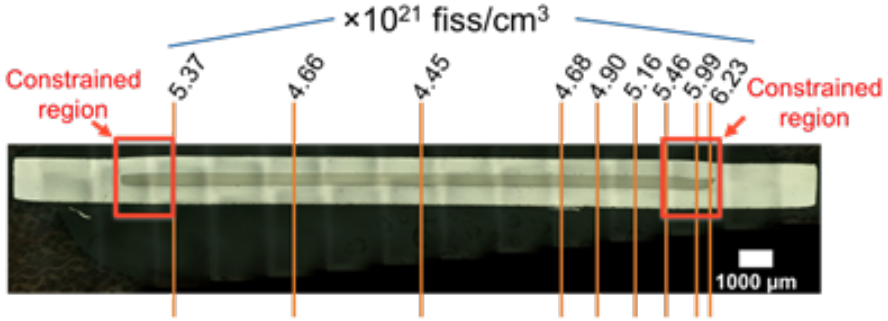

Figure (3.5) Optical micrograph showing the transverse cross-section of L1P755 and the associated fission density for the different test locations [127, 132]

L1P755 is shown in Figure 3.4 and, similar to Figure 3.5, illustrates the fission density at each location studied. Fission densities of L1P755 are higher than those in AFIP6-MkII samples. These differences are considered in later analysis. Along with the fission densities, both figures outline constrained regions at the edges of KGT2763, 96A, and L1P755.

Samples L1P55, KGT2763, and 96A outer edges are constrained by the edge of the fuel cladding and the experimental capsule surrounding the plates' ends. These constrained edges are termed "rail regions" in the remainder of the chapter and illustrated in Figure 3.3. Thickness changes, or the amount of swelling, differ across the plate. AFIP6-MkII and RERTR-12, and metallic fuels in general, exhibit higher amounts of swelling closer to the edge of the fuel plate but not on the edge [44, 62]. The force of the cladding at these locations restricts the fuel growth and causes the behavior to differ from the more central locations on the plate. At high fission densities, it is hypothesized to cause irradiation-assisted creep that produces the nonuniform swelling [47, 62]. This creep-enhanced swelling is separate from the swelling caused by microstructure changes and porosity in the fuel. Applied stresses from

the cladding and fuel interaction will change the behavior on a mechanical and microstructural level. Therefore, areas affected by the constrained rails regions experience uneven stresses and must be quantified to understand the picture of the measured microstructure fully.

Measuring the IL for each sample, including the rail regions, quantifies the areas affected by the rail regions. Swelling measurements decrease drastically at the very edges of the fuel plates, and the IL do not increase in thickness with fission density as is seen in other areas of the plate. There is a decrease in IL thickness where the material is affected by the constrained rail regions. Therefore, the decrease in IL thickness along the transverse cross-section is measured to understand the expected constrained region depths. This distance is about 1 mm in RERTR-12 and 1.5 mm in AFIP6-MkII samples. Data from the rail regions may differ from the data elsewhere. Therefore data in that 1 to 1.5 mm depth may not represent the general fuel microstructure. On sample KGT2763, there are two measurement areas in this rail region on the right-hand side, 95A only contains one, and L1P755 has three on the right side and one measurement location near the constrained area on the left side. In the analysis, these areas are indicated on the respective micrographs. The purpose of calling attention to these areas is to understand what statistical and microstructural FGB differences may exist at certain locations compared to the rest of the measurement locations.

3.8.2 Standardized image analysis method

Back-scattered electron (BSE) SEM micrographs of the mini-plates are taken at the indicated fission density locations from Figures 3.4 and 3.5 to see the FGB, or pores, across the plates. Figures 3.6 through 3.9 show representative micrographs at each fission density, as indicated in the top left of the images. Also, images taken from the rail regions are labeled on the images. The micrographs are presented as they are on the miniplates, moving from left to right. Figures 3.6 to 3.9 are analyzed using the following standard images analysis techniques.

The proposed method of analyzing micrographs from the four samples uses ASTME561 [139], ImageJ, and the automated fission gas pore graphical fission gas pore graphical user interface (FGP-GUI) user interface [141] for mini-plate characterization. The non-refined grain volume fraction of the samples was estimated using the ASTME562 standard, while the FGP-GUI and ImageJ measured the porosity characteristics of the samples. The average porosity, pore size, diameter, and eccentricity were all measured and reported with the FGP-GUI and were verified using the ASTM562 standard method. The University of Florida developed this FGP-GUI technique and verified the methodology independently on RERTR-12 and AFIP-7 samples to automate and standardize porosity image analysis [128].

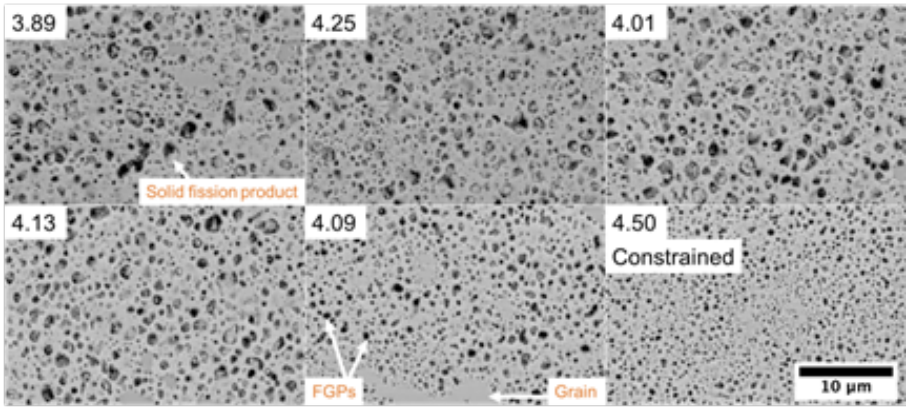

Figure (3.6) Representative BSE micrographs of KGT2763 demonstrating the fission gas pore distribution at different calculated fission densities in units of $\times 10^{21}$ f/cm^3 [127]

3.8.2.1 Image analysis of KGT2763

From Figure 3.6 BSE micrographs of KGT2763 show restricted growth of the FGB clearly when comparing the sample images at 4.5×10^{21} f/cm^3 and the other five fission densities. At the same scale, the observed pores are visibly smaller than those in the non-rail regions. At 3.89×10^{21} f/cm^3, solid fission products are seen decorating the inside of some of the larger pores. The solid fission products are highlighted in the figure. Additionally, the figure brings attention to the intact grains present at 4.09×10^{21} f/cm^3. Grains can be seen in the other two AFIP6-MkII samples as well. These show that grain refinement is undeveloped through all the fuel. Fission densities across the plate are fairly similar but calculated not measured. Errors and uncertainties in the fission density calculation cause the differences in fission densities to be negligible in this case. The analysis below will quantify differences between the various fission density locations and prove the calculated differences important or not.

3.8.2.2 Image analysis of 96A

Mini-plate 96A micrographs are displayed in Figure 3.7. The most notable aspect of these samples is the smaller size of the pores when compared to Figure 3.6. Intact grains are visible at the various sample locations, similar to KGT2763 as well. Overall, the fission density for 96A is higher than in KGT2763. At the constrained, rail region, the FGB do not appear to be as inhibited in their growth as in the previous plate. The pore sizes visually are consistent. The similar pore sizes may be due to the location mini-plate 96A is sampled. It is cut from the middle of the AFIP6-MkII large plate, and the stresses from cladding are lower towards the center of the overall plate. Therefore, the stresses near the top and bottom of the plate may be causing the formation of smaller pores.

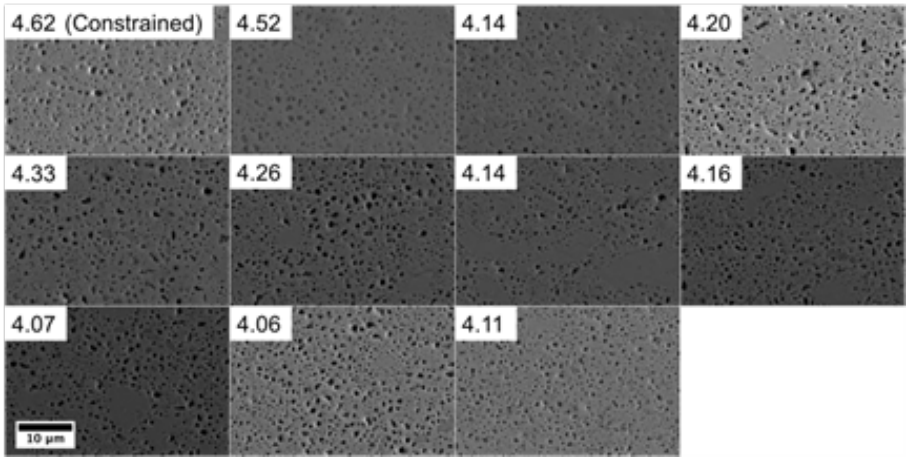

Figure (3.7) Representative BSE micrographs of 96A demonstrating the fission gas pore distribution at different calculated fission densities in units of $\times 10^{21}$ f/cm^3 [127]

3.8.2.3 Image analysis of 97A

Figure 3.8 shows the porosity of the bottom samples of the AFIP6-MkII plate. These samples have the lowest fission density values compared to the others from the same experiment. 97A also is cut from the center of the fuel plate and does not contain any rail regions. Large, intact grains are observed in all of the samples as well. Of the three samples, pores in 97A appear the most uniform from the lack of restriction from rails.

3.8.2.4 Image analysis of L1P755

L1P755 behaved differently from the characterized AFIP6-MkII samples, shown in Figure 3.9. Firstly, it had higher fission densities that caused the growth of larger FGB and pores. Fission density was lowest at 4.45×10^{21} f/cm^3, higher those in 97A, and all but one and two in KGT2763 and 96A, respectively. Interestingly, the FGB at the rail regions appear to grow larger across the plate. These regions contain larger pores compared to toward the center of L1P755 and those seen in AFIP6-MkII samples. The two rightmost rail region pores are the largest, whereas the leftmost rail region samples at 5.46×10^{21} f/cm^3 exhibit the smallest pores in the entire sample. This large pore size at the constrained areas is opposite of observations in the AFIP6-MkII samples. Further studies are required to fully understand the rail region's impacts on the porosity and restricted microstructure evolution.

3.9 Data analysis methods

For the MM work and improving data analysis methods, porosity data was collected and studied here. As previously stated, pores or FGB can be measured in several different metrics; porosity (or pore volume fraction), pore size area, pore diameter, and eccentricity. Pore size area is defined here as the cross-sectional area of the pore. Furthermore, the pore diameter is the average diameter used to calculate the pore size area. Each sample mini-plate

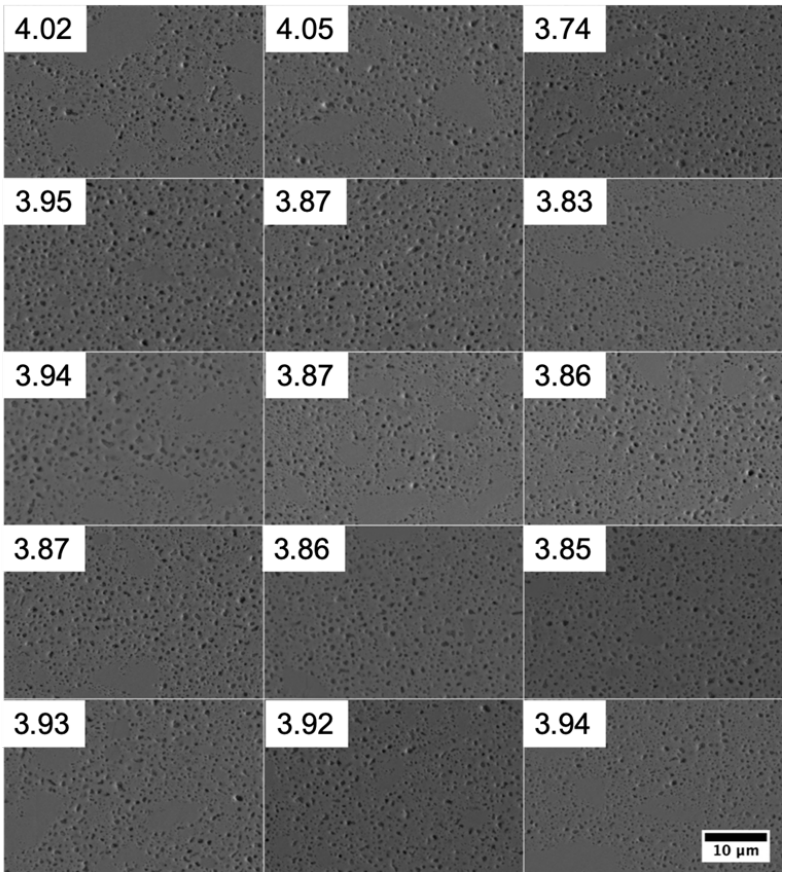

Figure (3.8) Representative BSE micrographs of 97A demonstrating the fission gas pore distribution at different calculated fission densities in units of $\times 10^{21}$ f/cm^3 [127]

measured different numbers of fission density locations and different numbers of pores in the micrographs. This method compares pore data to other microstructural observations and possible connections between these. Python statistical packages and the software R are both used for this data analysis [142, 143].

3.9.1 Summarizing the fundamental relationships of fission density and porosity

Pore measurements dependent on fission density may elucidate the possible causes of the swelling differences shown in Figure 3.1. Four characteristics: porosity, pore size area, pore diameter, and eccentricity, all describe the FGB behavior in the AFIP6-MkII and RERTR-12 samples. The sample mean, median, maximum, and other descriptive statistical values of these pore measurements are found first. The descriptive statistical values used herein include the sample size "n" and the sample mean "$\bar{y}$";

$$\bar{y} = \frac{\Sigma_i y_i}{n} \tag{3.1}$$

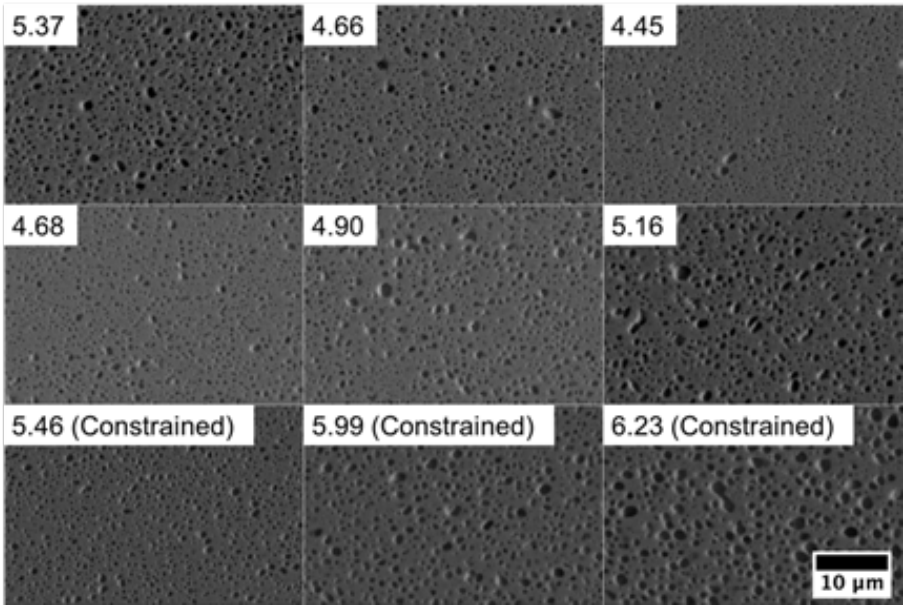

Figure (3.9) Representative BSE micrographs of L1P755 demonstrating the fission gas pore distribution at different calculated fission densities in units of $\times 10^{21}$ f/cm^3 [127]

Linear relationships are the most basic statistical model available for the data. Here the independent variable "x" is the fission density of the sample location and "$\hat{y}$" is the predicted porosity characteristic determined from the intercept $\hat{\beta}_0$ and the slope $\hat{\beta}_1$.

$$\hat{y} = \hat{\beta}_0 + \hat{\beta}_1 x \tag{3.2}$$

$\hat{y}$: pore characteristic

x : fission density

Fitting the data to a linear regression model assumes linearity between the fission density and pore characteristics of the material as well as the independence of the errors [144]. These are both likely untrue because of the complex nature of fuel microstructure evolution and the interconnecting factors impacting the evolution of the fuel. However if a linear relationship exists and may be determined by manipulating the data through transformation, these early analysis steps create a simple, reliable equation for modelers to use in the future.

3.9.2 Data visualization and understanding

Next, in the remaining analysis the dependent variable studied (y) is the pore size area. Unlike the other three pore values of pore diameter, porosity, and eccentricity, the raw data of pore size area were available and collected. To understand the data as whole, boxplots were created for each sample and pore data type. Boxplots and strip plots illustrate the range of the pore size area for each sample and demonstrate if any data outliers exist that may skew the data to be non-representative of the actual physical behavior. Additionally, the boxplots allow for visual com-

parisons between the four samples. Several thousand pore size data points exist for each sample. The information was split into 100 bins; and the sample mean was taken of the data in each bin to make the data more manageable. Data without the rail region samples indicate the effects the constrained areas have on the pore growth.

Understanding the shape and distribution of the data is informative in determining what types of analysis are applicable to describe the behavior of said data. Observing the shape of the pore size data also indicates at what fission density and conditions the FGB behavior may change. Pore size and frequency indicate when other microstructure events like grain refinement will occur based on the fission density and may lead to understanding how FGB relates to other events. Normalized frequency histograms plot the pore size area distribution as a ratio of the whole. Normality, fit to a Gaussian distribution, is visually explored first to understand where 93.75% of the data, or four standard deviations, lies and if there are outliers in the largest pore sizes for each fission density.

3.9.3 Testing normality of pore size area datasets

Visual determination of the dataset distribution is an unreliable test of normality, assuming a normal distribution is a Gaussian distribution. In other words, the null hypothesis tested here is the pore size data is part of a normal distribution. Therefore, a more replicable method for finding the normality of the pore area data will inform future data analysis steps. The D'Agostino and Pearson's test calculates the skewness and kurtosis for the normality of the data. The Python package SciPy calculated these values for this analysis. These tests use a null hypothesis that the data is normally distributed and will determine other statistical methods used to understand the data. Skewness and kurtosis measure the shape of the data and compare it to the expected results of a standard bell curve. Figure 3.10 shows the differences between a skewed, high kurtosis, and normal distribution. As the yellow line in the Figure shows, the skewness, or the symmetry of the distribution, of a normal distribution, is near zero. This means that on either side of the mean value, data is evenly distributed. Any skewness above or below zero indicates a data shape with a curve shifted left or right, this is the black line in the figure. Kurtosis measures the tail shape of the distribution. A value of three is a normal distribution kurtosis. Above three, the tails are long and relate to a sharp peak. This is the grey line in Figure 3.10. Below three is a flat shape with short tails. Below is the more formal definition of the hypothesis test developed to understand the shape of the pore size area data.

H_0: the data arises from a Gaussian distribution

H_a: the data forms a non-Gaussian distribution

Test statistic:

$$X^2 = s^2 + k^2 \tag{3.3}$$

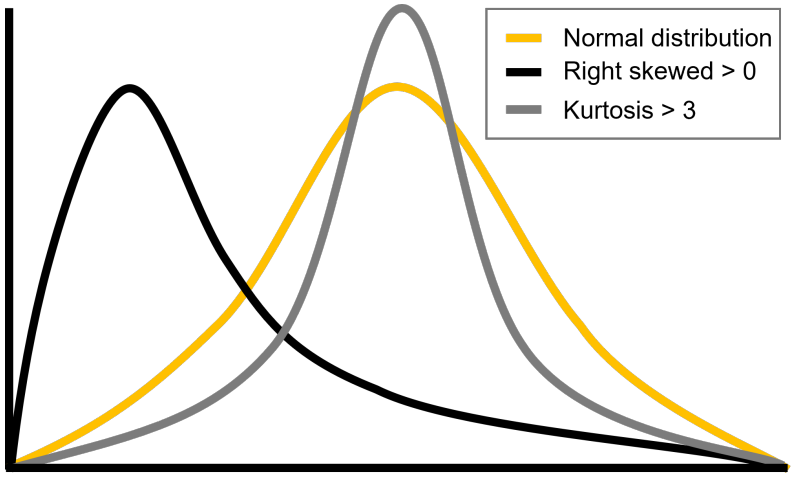

Figure (3.10) Example of a normal distribution compared to a skewed distribution and distribution with high kurtosis, both skew and kurtosis are calculated to determine the normality of pore size data.

SciPy calculates results in the form $s^2 + k^2$ where s and k are the z-scores of the skewness and kurtosis tests, respectively. A Chi-squared probability test produces a p-value that indicates if the significance of the results [143]. If this p-value is less than the significance level, $\alpha = 0.5$, the null hypothesis of normally distributed data is rejected, and the data does not have a normal distribution.

3.9.4 Outlier determination

An important distinction is whether the pore size data represents the overall microstructure or if outliers skew the sample mean and distribution. Pore area outliers were found and removed from the data using Chebyshev's inequality to understand effects on the shape and distribution. This method calculates the z-scores of each data point using equation 3.4 and determines the number of standard deviations away from the mean each point is from the data point value (y), the sample mean ($\bar{y}$), and the standard deviation (σ).

$$\text{z-score} = \frac{y - \bar{y}}{\sigma} \tag{3.4}$$

Chebyshev's inequality instructs that data in a skewed probability distribution will only extend a certain number of standard deviations from the mean. It finds the probability that a data point will exist in a specific range. For a standard deviation 'k' away from the mean, only $1/k^2$ of the data values will fall within that standard deviation. Therefore, any pore size areas that fall outside that chosen standard deviation are considered outliers and not representative of the rest of the sample. The chosen standard deviation here is four, or 93.75% of the pore size data is within four standard deviations of the mean. Meaning, $1/4^2 = 6.25\%$ of the data are out of that range and considered outliers.

3.9.5 Data transformation to achieve normality

If removing the outliers does not normalize the data successfully, data transformations normalize the datasets and ensure each sample compares accurately to the others. Data transformation methods exist that will change a non-normal distribution to a normal one and allow less complex analyses of correlations and relationships between microstructures. This work employs a specific type of power transformation, the Box-Cox transformation method [145]. A Box-Cox transformation converts a non-normal distribution of a dependent variable (pore size area) to a normal distribution using Equation 3.5 and has been successfully applied to positively skewed distributions as a way of creating a normal, Gaussian, distribution [146]. λ is a test variable with any value from -5 to 5, and y is the dependent variable, pore size area. By testing various values of λ within the -5 to 5 range y'(λ) is solved for, and the normality of each y'(λ) is tested at each value of λ. The value of λ that produces the most normal distribution is chosen, and the corresponding y'(λ) is the new, transformed dataset [145].

$$y'(\lambda) = \begin{cases} \frac{y^{\lambda}-1}{\lambda}, & \text{if } \lambda \neq 0; \\ \log(y), & \text{if } \lambda = 0 \end{cases} \tag{3.5}$$

After calculating the appropriate λ value and the new data points, the linear relationship between fission density and pore size area is calculated again. The purpose here is to understand if the transformed data alone creates a fast and straightforward linear relationship. Lastly, the transformed data is used in further tests to understand possible statistical connections between the dependent pore size and the independent fission density.

3.9.6 Analysis of variance (ANOVA) and analysis of covariance (ANCOVA) methods

Possible relationships between the numerous pre- and post-irradiation microstructure data are tested using ANOVA and ANCOVA. ANCOVA is a test measuring the relationships between multiple independent variables and one dependent variable. It looks to see if the behavior of the dependent variable is reliant on more than one other variable in the data. In this case, two independent variables were fission density and the samples. Before the ANCOVA was performed, an ANOVA test was used to understand the relationships between fission density, data location, and porosity. ANOVA tests the impacts an independent variable has on a dependent variable assuming that no other variables are impacting that dependent behavior. The ANOVA may also tell which factor, fission density, or data location has the most impact on the observed porosity.

The relationship between fission density and porosity is supposed proportional; as the fission density increases, so does the porosity. The ANOVA tests if the fission density (independent variable) from this work's data has a significant impact on the porosity (dependent variable) [147]. Since the transformed dataset is normal, this type of

analysis is usable. ANOVAs use an F-value, test statistic, that is a ratio of the variance of means and the variance within a sample population shown in equation 3.6, and p-value to explain the ratio of sample means and individual means within the sample and the significance of the results. If the means are equal or have an F-value of one, the independent variable does not impact the differences between populations. However, a high F-value above the critical point indicates differences in the values are not random and that the null hypothesis cannot be rejected. The method and goals of this test are summarized below.

> H_0: the population means (μ_i) of the different fission density samples are equal:
>
> $$\mu_1 = \mu_2 = ...\mu_i$$
>
> H_a: one or more of the populations means is not equal to the others
> Test statistic: Where s_B^2 is the squared mean between the samples and s_W^2 is the squared mean within the sample [144].
>
> $$\text{F-value} = \frac{s_B^2}{s_W^2} \tag{3.6}$$

To understand the effects of the fission density and the sample itself, i.e. difference in the population means from KGT2763, 96A, 97A, and L1P755 the ANOVA was performed for both independent variables. The sample of each dataset originates from may impact the FGB behavior, and the ANOVA will explore that. For example, there are many aspects in each sample that are not measured here that may affect the FGB such as the chemical homogeneity at the various locations across a sample plate. Therefore, the ANCOVA work is performed for both fission density and sample plate.

The ANCOVA removes the effects of the variance in independent variable, fission density, from the pore data and understands if the sample area still impacts it [147]. The covariate that is controlled, or adjusted, for is the fission density, and the categorical independent variable is the sample or plate identification. This test still determines if any of the means vary from the others, but controls for the effects from both the independent variable and covariate. Therefore, the the analysis is testing if the adjusted means are equal. Below is the official hypothesis test used for this analysis.

H_0: the population means (μ_i'), adjusted for the fission density of each sample, of the sample areas are equal:

$$\mu_1' = \mu_2' = ...\mu_i'$$

H_a: one or more of the adjusted populations means is not equal to the others

Test statistic: Where $s_B'^2$ is the squared mean between the samples and $s_W'^2$ is the squared mean within the sample [144].

$$\text{F-value} = \frac{s_B'^2}{s_W'^2} \tag{3.7}$$

Two assumptions are tested with the ANCOVA; if the independent variables impact each other or if they behave separately. If they are independent of each other, there is no interaction between fission density and the sample areas. An example is if the fabricated microstructure is different in the samples and is causing the porosity differences. However, if the fission density is causing the evolution of another microstructure change that impacts the porosity, like grain refinement, it is not. Further relationships cannot be explored without further data on the other existing microstructures corresponding to each location's porosity. If the area impacts pore growth, there may be underlying effects in the material.

ANOVA and ANCOVA only find if the independent variables, fission density, and measurement location, impact the pore size area. They do not tell what kind of relationship. This type of analysis is important to understand if any connection exists and if it is significant. Further investigations into the relationships are required to produce reliable deterministic models.

3.10 Results and discussion

3.10.1 Summarized data

Average porosity data from all four mini-plates are in Table 3.7. This data is collected from the information available in Appendix A. The highest average fission density for all the samples is in L1P755 at 5.21×10^{21} f/cm^3. Additionally, this sample contains the highest values for all other characteristics along with KGT2763. 97A had the lowest average fission density at 3.91×10^{21} f/cm^3 and the lowest pore characteristic values, as expected. 96A had the second-highest average fission density but pore characteristics most similar to 97A. Of the AFIP6-MkII experiments, KGT2763 has pore sizes 44% higher than 96A and a 37% difference in porosity. KGT2763 is more similar to L1P755 in the microstructure observed than its two sister samples, 96A and 97A. This is unusual because of the higher fission density of L1P755 and that KGT2763 came from the same experimental plate, therefore fabrication and irradiation, as the other two.

Table (3.7) Summarized pore data for RERTR-12 and AFIP6-MkII samples taken from the raw data in Appendix A reproduced from [127].

Sample	Pore area (μm^2)	Pore area S.D.	Porosity (%)	Porosity S.D.	Pore diameter (μm)	Pore diameter S.D.	Eccentricity	Eccentricity S.D.	Fission density (10^{21} f/cm^3)
KGT2763	0.27	0.06	24.24	3.11	0.47	0.08	0.63	0.03	4.14
96A	0.15	0.01	15.04	1.77	0.38	0.01	0.69	0.69	4.24
97A	0.12	0.01	15.49	1.18	0.35	0.01	0.64	0.02	3.91
L1P755	0.25	0.08	25	3.22	0.5	0.07	0.62	0.02	5.21

Scatterplots of the summarized porosity information in Figure 3.11 underscore the differences in fission densities studied as well as the linear relationship between fission density and porosity values. These include linear regression lines and equations. From the Figures, it is clear that the RERTR-12 and AFIP6-MkII samples do not behave the same concerning the fission density. If porosity were only dependent on the fission density of the samples, these would be more alike. Any obvious connections may be elucidated by exploring a possible linear relationship between fission density and porosity values. Based on the strength of the relationships, R^2 values, few samples have a solid connection to the fission density. KGT2763 differs the most of all of the pore data collected. Due to the small sample size and the cutting of the material, there may be unknown causes of the pore dimensions and behavior. Fission density is expected to increase the pore size, porosity, and eccentricity. However, the opposite of that positive relationship exists in Figure 3.11.

3.10.1.1 Porosity versus pore size

Porosity values are inconsistent with location and fission density when comparing all the samples. KGT2763 and L1P755 exhibit the highest levels of porosity, both approximately 25%. The L1P755 porosity is as high as 30%. In comparison, 96A and 97A both had porosity values closer to 15%. Compared with past analysis in Table 3.6, the porosity was slightly higher in the AFIP6-MkII experiments here despite the lower fission density values. The discrepancies between the past porosity results and these porosity results may be due to differences in image analysis of the micrographs used. Standardizing the techniques used would eliminate some of these types of data inconsistencies.

Small FGB will stabilize the material up to a specific fission density that will prevent swelling from increasing while that small FGB are intact [32]. The most swelling is in samples with high porosity and sizeable FGB. This connection between the volume fraction of the FGB and their size is necessary to understanding possible effects of pore size and swelling in a sample. Figure 3.12 shows the relationship of porosity as a function of pore size. All of the samples have a positive relationship between these two factors. There is a small correlation between the two, but it is not strong enough to say that the porosity depends on the pore size for these samples. L1P755 shows the largest changes in porosity and pore size growth, most likely due to the higher fission densities of this sample. In 96A and 97A, the porosity and pore area change is much smaller for the lower fission densities. Figure 3.12 shows the

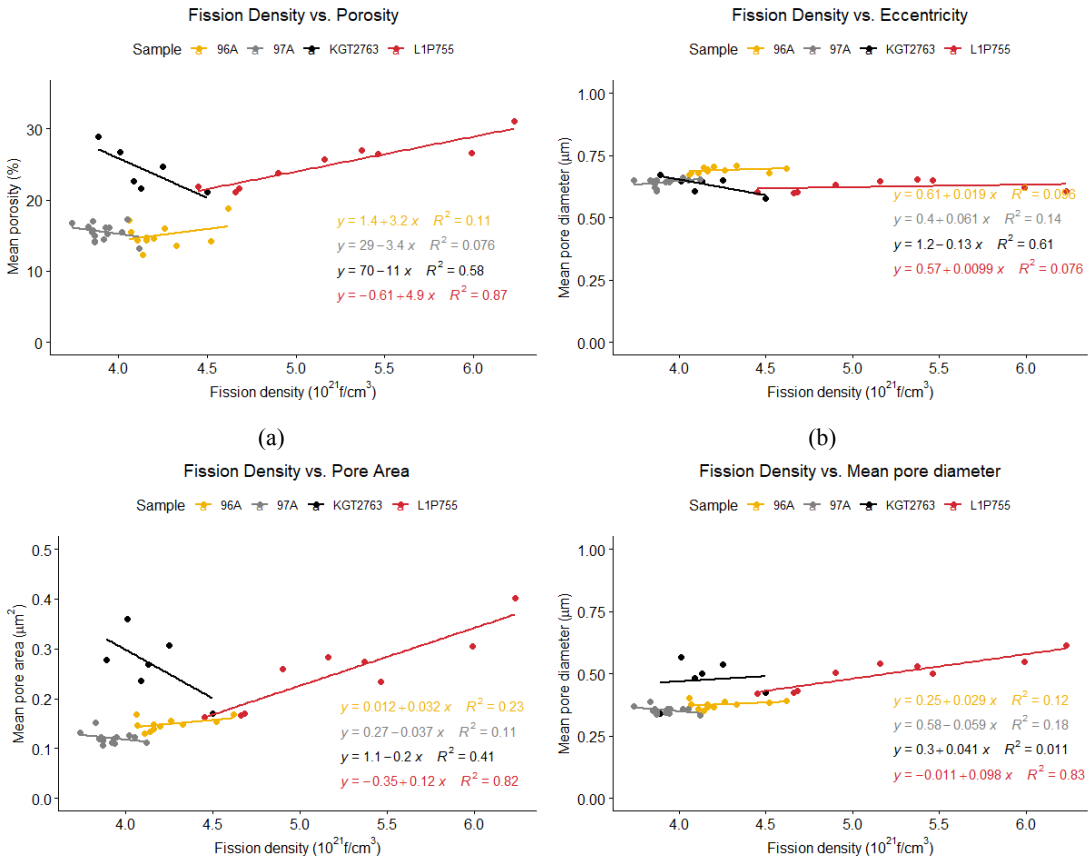

Figure (3.11) Summarized FGB and pore data for AFIP6-MkII and RERTR-12 scatterplots and linear regression dependence on fission density of (a) porosity, (b) eccentricity, (c) pore area, and (d) pore diameter [127].

pore area was less than 0.2 μm^2 and the porosity was less than 20% for 96A and 97A. Therefore, these plates were more dimensionally stable than KGT2763 and L1P755, which had much higher pore size area and porosity values. KGT2763 experienced more changes to the overall pore behavior compared to the other AFIP6-MkII samples. The small sample size may contribute to this, but of the four pore data types explored, it is the most similar to L1P755. The conclusion of this plot is that in samples 96A and 97A the smaller pores and low porosity mean the samples are behaving in a more stable manner, or are not swelling or changing as much as the KGT2763 and L1P755.

3.10.1.2 Eccentricity

Eccentricity was steady across all the samples and did not appear to be heavily affected by the fission density. Of the four samples, the eccentricity was between 0.50 and 0.75, as shown in Figure 3.11b. This measures the shape of the pores and can indicated the crystalline or amorphous behavior of the FGB [148, 149]. A value of one is a more crystalline pore and is more stable [149]. Since the eccentricity does not change drastically with fission density, the pores are not changing shape no matter the number of FGB or the size.

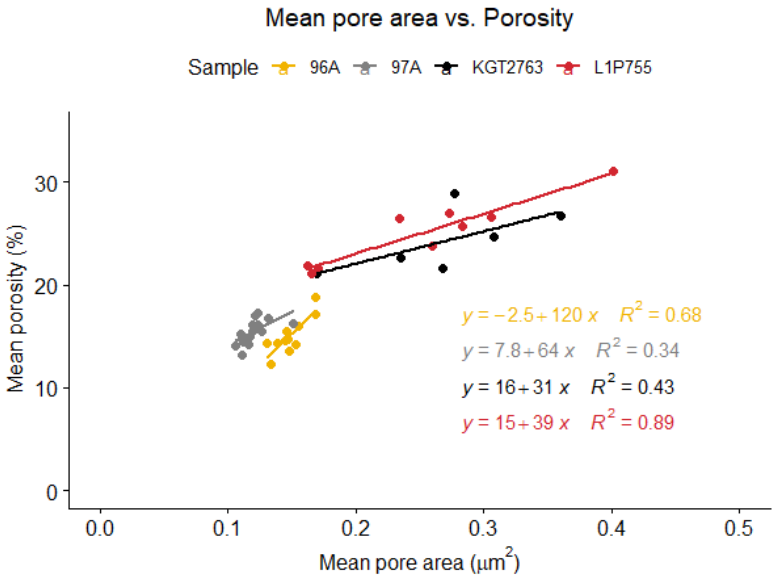

Figure (3.12) Pore size are compared to porosity of the samples used to understand dependency of porosity volume fraction on the pore size area [127].

3.10.2 Pore size area visualization overview

Figure 3.13 is a histogram of all the pore size area data showing the highly skewed and tailed shape of the data. To explore the possibility of the data originating from a normal distribution a Gaussian probability density function (PDF) was plotted over top in yellow. This PDF does not fit the data shape very well. However, the data seems to fit closer to an exponential distribution function, represented by the dashed black line. This visual representation of all the data indicates a normal data distribution does not represent the data and that further work is required to make a manageable linear regression model as well as data analysis using common techniques.

Figure 3.14 is a boxplot and strip plot of the unaltered pore area data. In the boxplot portion is is clear how many outlying data points are present in the data for all the samples, but especially KGT2673 and L1P755. Also, the strip plot data points, in yellow, illustrate how much data was available in each sample dataset and how concentrated the data is near the smaller pore size areas. This high concentration of smaller data points, below 2 μm^2, is also apparent in Figure 3.13. Due to many data points, the main portion of each data set is not comparable. Binning of the data points allows for more easily compared information in this type of plot and is shown in Figure 3.15.

Figure 3.15a is the pore area of binned data, including the rail regions areas discussed previously. KGT2763 has the most extensive range of pore area values with a maximum near 9 μm^2 which is much higher than the next highest value, L1P755 at 5.75μm^2. Comparing KGT2763 and L1P755 to 96A and 97A shows there will likely be fewer outliers in the later samples. No data points fall outside the upper quartiles. The range differences of the samples may be due to the wider fission density ranges in KGT2763 and L1P755 as shown in Table 3.8.

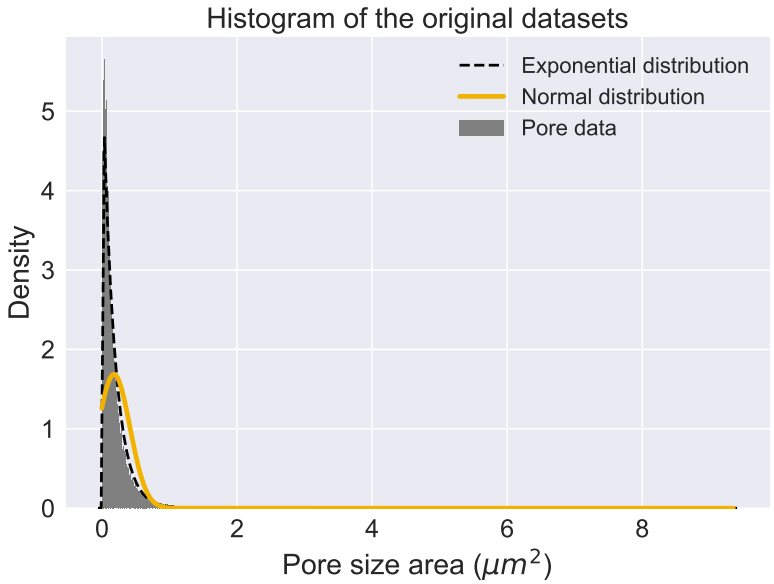

Figure (3.13) Histogram of all the pore size area data in 1000 bins and fit to two common probability distribution functions, exponential and normal (Gaussian). The data is heavily tailed and positively skewed.

Table (3.8) Maximum and minimum fission densities of the AFIP6-MkII and RERTR-12 samples with and without the rail regions included. Reproduced from [127]

Sample	Minimum fission density (10^{21} f/cm^3)	Maximum fission density (10^{21} f/cm^3)	Maximum fission density – no rails (10^{21} f/cm^3)
KGT2763	3.89	4.5	4.25
96A	4.06	4.62	4.52
97A	3.74	4.05	NA
L1P755	4.45	6.23	5.37

Figure 3.15b gives a cursory understanding of how the rail regions of restricted FGB growth change the size of the pores. KGT2763 still shows a significant range and difference from the other three samples. Additionally, L1P755 decreases in the overall pore size area, the opposite of the expected results. If these rail regions are restraining the FGB growth, then the pore areas should have increased when removing the constrained regions from the dataset. The maximum fission density of non-rail regions is smaller than that of the 6.23×10^{21} f/cm^3 in the entire sample. This could be the cause of the increased FGB size. Alternatively, these large pores could be interconnected FGB at rail locations. Further research is required to understand the connections between the rail region constrained growth and the fission density dependence of the FGB.

3.10.3 Data shape and distribution

Figures 3.16 to 3.19 show the data is highly skewed to the right with a bimodal distribution. The histograms use a normalized frequency of the data, making each graph comparable to others from each sample. Above each graph

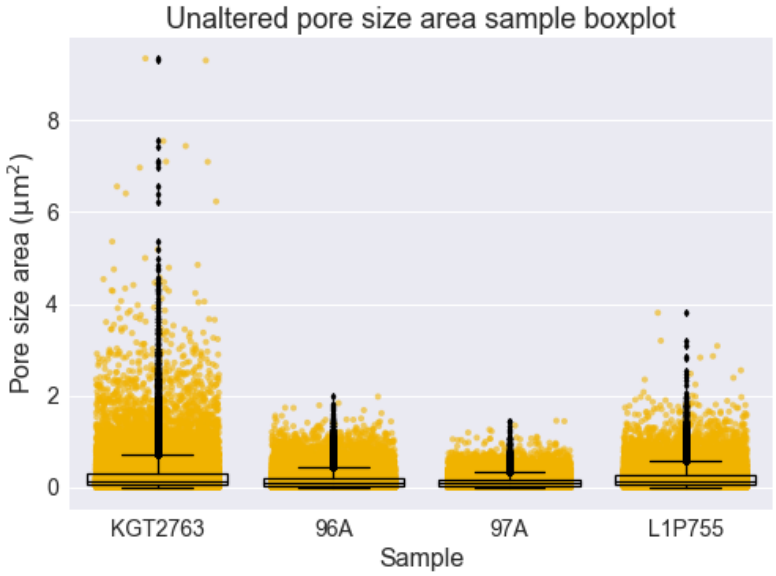

Figure (3.14) Pore size area boxplot of raw data for AFIP6-MkII and RERTR-12 experiments showing the range of pore area data and possible data outliers as well as the strip plot showing (in yellow) the amount of data and the concentration of values below 2 μm^2.

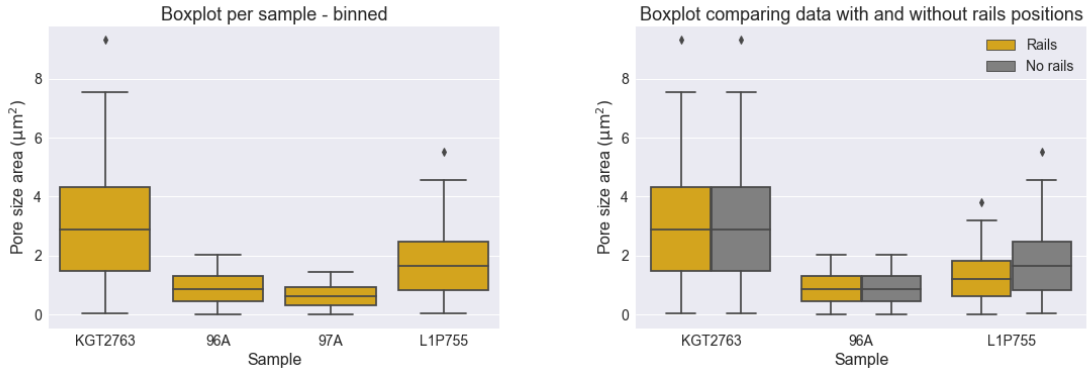

(a) (b)

Figure (3.15) Boxplots of the pore size area data for RERTR-12 and AFIP6-MkII experiments of the binned data (a) and the binned data comparing data with rails and without rails (b) to show how the pore size area is affected when the constrained, rail regions are removed. Adapted from [127].

is the fission density $\times 10^{21}$ f/cm^3. At the far left of each graph is a peak where the smallest FGB are the most prevalent. KGT2763 and L1P755 exhibit the largest peaks at the small pore sizes (high kurtosis). Less distinct peaks are seen for 96A and 97A where the data is more widely distributed across the pore size frequency, or these have lower kurtosis. The limit of the pore size x-axis is set to 2 μm^2 for visual clarity. However, some FGB data fall outside of this range as shown in Figure 3.15 and will be investigated further in Section 3.10.4.

Sample KGT2763 had the most prominent pores and widest data range of any of the samples. It also had a

negative relationship between fission density and porosity. Pores as large as 9μm^2 were found in these samples, and many more were around 3μm^2 size, even at low fission densities. Conversely, notice in Figure 3.16, the y-axis is set a frequency of approximately 30% instead of 20% like the other histograms. This is because of the very high concentration of smaller pores in the KGT2763, so this sample simultaneously had the highest concentration of small pores and the largest pores of all those measured. The highest porosity observed in these samples was 28%. Often large pores and associated with high porosity values. This relationship is associated with the interconnection of FGB, or the merging of two smaller FGB into one large bubble. Previous work predicts the complete interconnection does not occur until about 30% porosity is achieved [150]. Future work will focus on the production of such sizeable FGB and interconnected pores.

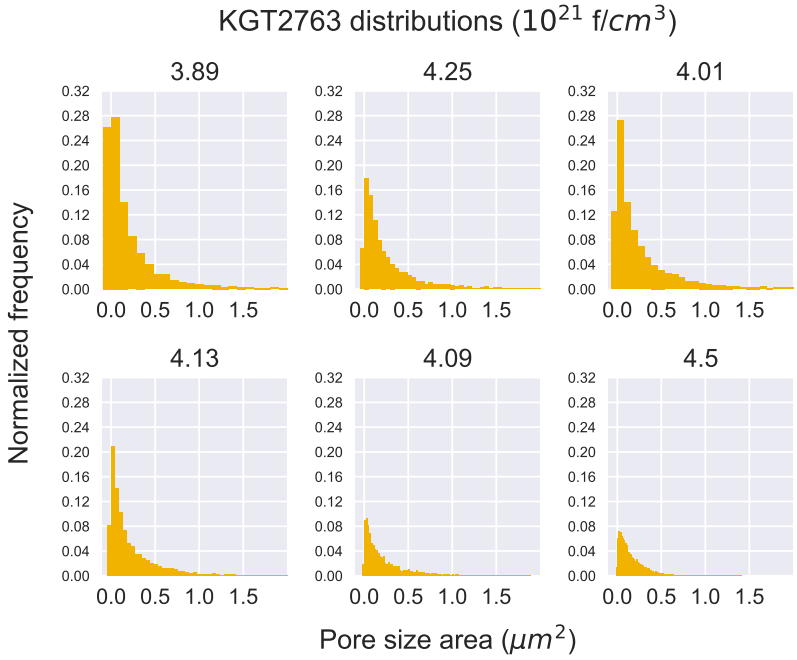

Figure (3.16) KGT2763 pore size area normalized frequency distributions based on the average fission density of each location [127].

Figure 3.17 shows the much smaller pores compared to those of KGT2763. None of the data points extended past 0.7 μm^2 as seen by the tail portion of the frequency distributions. Figure 3.16 demonstrates the larger FGB of the sample with a long tail portion to the right of the graph. 97A and L1P755 were more similar to 96A in this respect.

Sample 97A exhibited the lowest fission densities of the four samples. Therefore, the FGB measured and presented in Figure 3.18 are smaller than in the other samples. The data has less kurtosis and more even distribution.

Grain refinement is expected to begin near 3×10^{21} f/cm^3 and increase the growth of FGB. All of those 97A fission densities exceed this, so it is expected that the pores measured would be more sizable and include a higher porosity.

L1P755 experienced the highest fission densities from RERTR-12. Therefore, larger FGB and higher porosity values are expected. Pores areas near 1 μm^2 were measured in the higher fission density samples. At the rail regions or the last three histograms, there is a high concentration of small FGB. The smaller pores may be due to the constraints from the rails regions as predicted. However, this phenomenon was not observed in the KGT2763 samples.

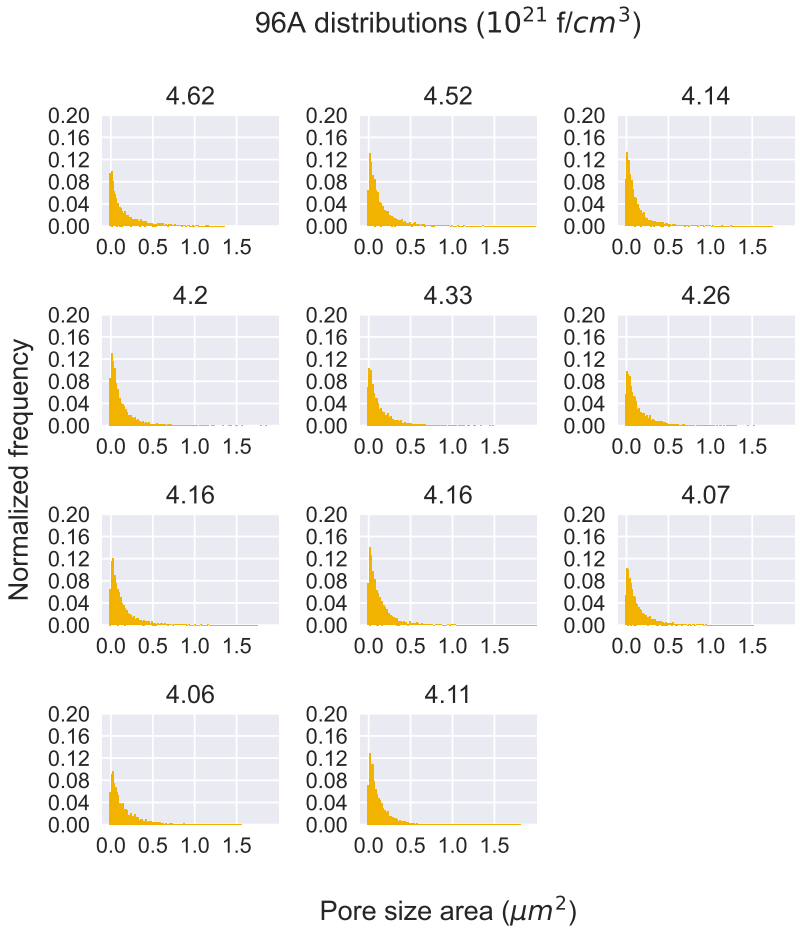

Figure (3.17) 96A pore size area normalized frequency distributions

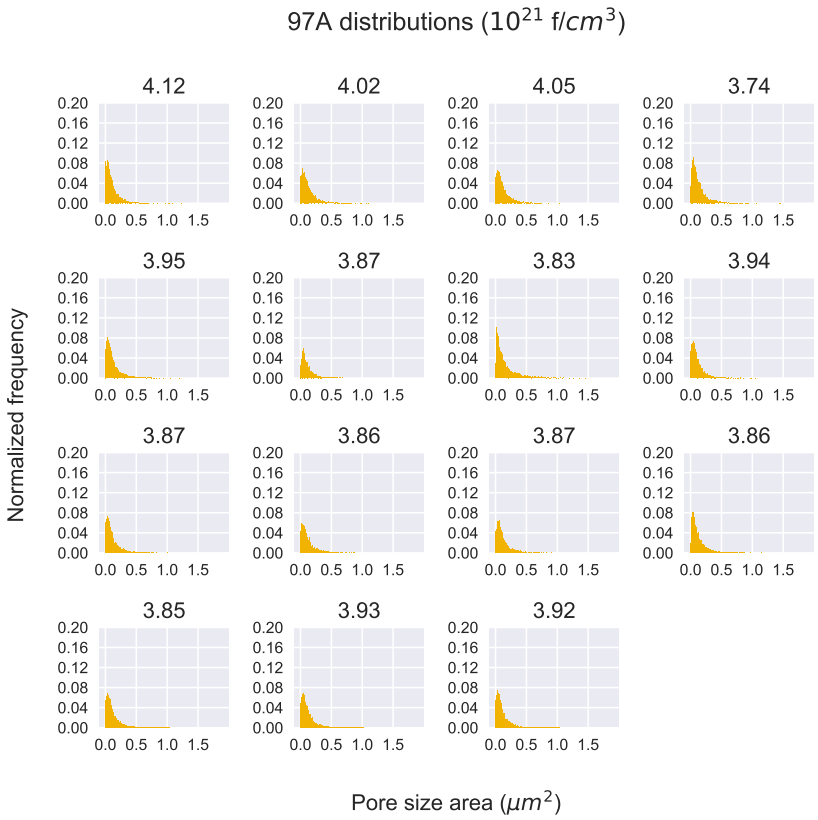

Figure (3.18) 97A pore size area normalized frequency distributions

3.10.3.1 Normality of pore size area data

From the D'Agostino and Pearson's normality tests, the non-normal distribution seen in the previous histograms is confirmed. A non-normal distribution will not always be as visually apparent as in these samples, or the histograms may be misleading. Therefore, using the two more rigorous normality tests is necessary to confirm the data distribution. The tests performed here indicate that transforming the data to create a normal distribution may be useful for further analysis into the pore size area relationship to fission density and other existing microstructures.

3.10.4 Outliers

Table 3.9 shows the data changes if the outliers are removed from KGT2763 sample and fission density 3.89×10^{21} f/cm^3. Approximately 80 data points are excluded, but the mean pore area is not changed drastically due to many data points. The maximum pore size's skewness and kurtosis decrease more drastically. In the raw data, the largest pore is over 9μm^2 compared to the 2μm^2 maxima in the changed data. Most outlying data points will be on the right side of distribution or the larger pore size area from the data shape. Kurtosis decreased from 66.0 to

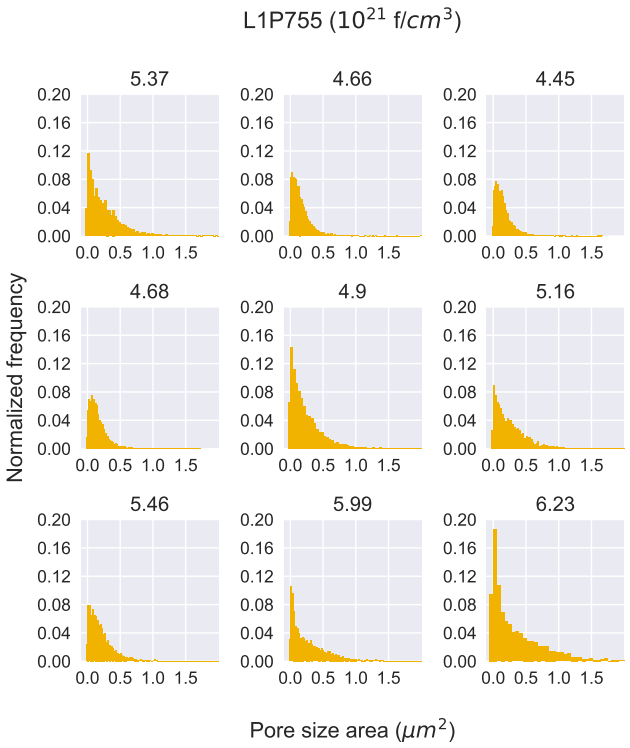

Figure (3.19) L1P755 pore size area normalized frequency distributions

8. This decrease is from the removal of the outliers creating the long tail in the distribution. Skewness decreased from 6 to 2.6; the data shifted to a more even distribution on either side of the mean. Therefore, removing the pore size area data outside of 93.75% of the distribution creates a more normal distribution but does not always create a perfectly normal distribution.

Table (3.9) Raw data comparison to 93.75% of the pore size area data count and distribution information for KGT2763 at a fission density of 3.89×10^{21} f/cm^3

	Raw Data Summary	Outliers Removed
Number of data points (pore count)	7097	7011
Min	0.00074	0.00074
Max	9.34	2.17
Mean (μm^2)	0.277	0.241
Variance	0.231	0.103
Skewness	6.046	2.61
Kurtosis	66	8.04

Determining the outliers of the data is more complicated than just assuming that any data point outside of the 93.75% probability distribution. FGB may exist in these substantial forms due to the interconnection discussed previously. In this work, it is currently unclear if these very large pores are an error of the image analysis processing

or interconnected pores. Without knowing where these outlier data points originate, removing the outlier data without further clarification of the pore interconnection is inadvisable. Also, since removing the outliers did not create a normal data distribution as desired or change the average pore size area substantially, the raw data is used in the following analysis. It is helpful to be aware of the outlier values when analyzing the results to anticipate possible oddities observed in the relationship of the fission density to FGB growth, however.

3.10.5 Data transformations

Python was used to calculate the Box-Cox transformations distributions and solve for the appropriate λ value. The pore size data is combined into one large dataset to find the λ value to use across all samples and fission densities. 0.14 was the calculated λ value based on the combined data. This value for λ is confirmed using the Box Cox normality plot in Figure 3.20a. The values plotted are the tested λ values against the calculated correlation coefficient. The λ closet to one has the strongest correlation to a linear model. Figure 3.20b of the transformed data distribution. The untransformed plot is similar to the distribution of the right-skewed samples seen previously, while the transformed data resembles a normal distribution much more. Skewness decreases from approximately 6 of the untransformed data to 0.015 of the transformed data. And the kurtosis decreased from between 80 and 100 to approximatly 3, the desired value for a normal distribution. Therefore, the Box-Cox transformation did improve the skewness and kurtosis of the data and the data distribution.

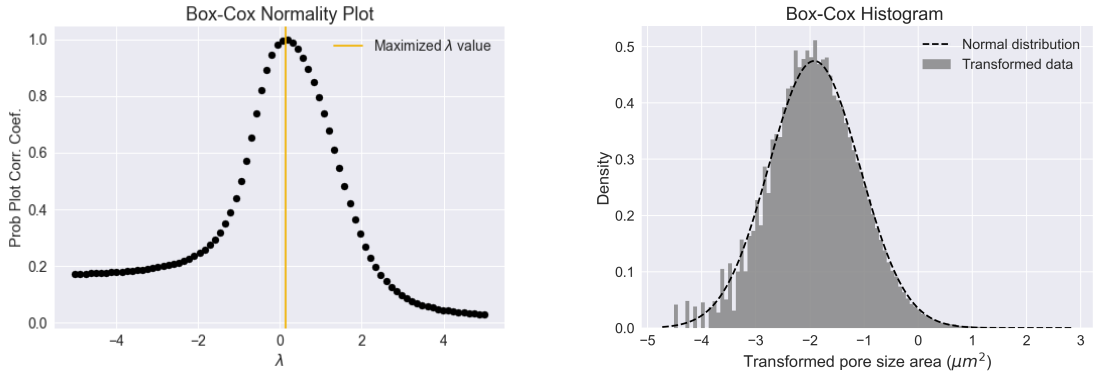

(a) (b)

Figure (3.20) (a) Normality plot of the Box-Cox transformation showing the maximized value of λ (b) transformed pore size area data using the Box-Cox transformation on the combined datasets and a corresponding normal distribution.

As a starting point to understanding the relationship between fission density and pore size area presented here, linear correlations were made. Table 3.10 shows the slope, intercept, skewness, and R^2 of the untransformed and transformed data with and without the rail region datasets. R^2 values increased with the transformed data but were still not near the desired value of one. Skewness, however, improved dramatically after the transformation, as did

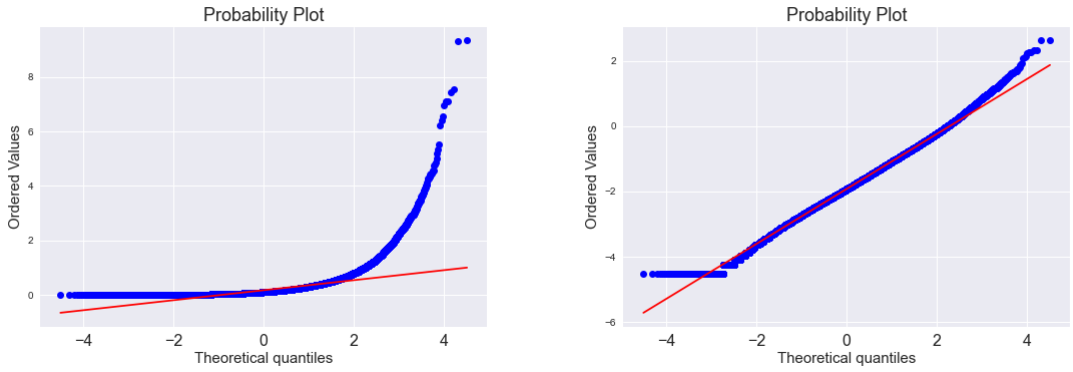

(a) (b)

Figure (3.21) (a) Q-Q plot of the AFIP6-MkII and RERTR-12 pore size area original data (b) transformed pore size area data using the Box-Cox transformation on the combined datasets where the red line is the theoretical, normal distribution and the blue is the data plotted in quantiles [127].

the kurtosis. Because of the lack of fit with the linear model, it is not recommended that a linear relationship be assumed for the transformed data and fission density correlation. This test informs the researchers that further model fitting is required to improve the reliability but was not performed for this analysis.

Table (3.10) Linear relationships and skewness of fission density to pore size area of transformed and untransformed data [127]

Dataset	Slope (m)	y-intercept (b)	R^2	Skew	Kurtosis
Raw data	8.64×10^{-23}	-0.195	0.664	5.89	88.8
Raw data without rails	8.49×10^{-23}	-0.187	0.478	6.65	113
Transformed data	3.03×10^{-22}	-3.22	0.721	0.015	3.29
Transformed data w/o rails	3.63×10^{-22}	-3.46	0.620	0.019	3.38

As the last test of the normality of the transformed data distribution, Q-Q plots are shown in Figure 3.21. Q-Q plots organize and plot the data into their appropriate quantiles, then plot a theoretical, normal distribution with the data [147]. The straight line of the theoretical distribution compares to the plotted data points; if the data aligns closely to the theoretical distribution, the pore size area data belongs to a normal distribution. In Figure 3.21a the untransformed data in blue is not similar to the normal distribution line in red at all. It curves dramatically instead. The transformed data aligns neatly in the center with the theoretical distribution in Figure 3.21b. However, at the ends of the line, the data deviates from it. This means the data is not a perfect normal distribution because of data points near the edges of the distributions. Therefore the Q-Q plot confirms that the transformation successfully made the distribution normal, but not perfectly normal. Some pore size area data points are outside of that normality. Other transformation methods may improve these results and will be studied in future work.

Table (3.11) ANCOVA results from no interaction between fission density and sample [127]

	Sum of squares	Degree of freedom	F-value	p-value	Significance level
Fission Density	0.16758	1	15.186	0.0004068	***
Sample	1.71023	3	51.66	4.00E-13	***
Residuals	0.39726	36			

Significance level codes: “***” 0, “**” 0.001, “*” 0.05, “.” 0.1, blank is not significant

3.10.6 Analysis of variance and analysis of covariance

Using the statistical software R with the transformed dataset, the ANOVA test calculated an test statistic, F-value, of 81.276 and a p-value of less than 0.001. Therefore, the fission density has a significant effect on the means of the pore size area data. Next, an ANOVA of the sample and pore size area was performed. The F-value of 40.336 and a p-value less than 0.001 show that the location impacts the pore size area. However, the sample location is not as impactful as the fission density.

Table 3.11 shows the results for the independent fission density and sample area are all significant ($p<0.001$). Pore size area dependence on the sample area where the pores are measured from (F-value = 51.186, p = 3.99E-13) is more significant than the fission density (F-value = 15.886, p = 0.0004). Therefore, there is something in each area aside from the fission density that is causing the FGB size behavior. This indicates that more work must be done to elucidate what areas affect the porosity in each sample. The independence of the two variables affecting the dependent variable would apply to the differences in starting microstructure or fabrication methods used in each sample section. However, without further information on the starting differences in each location on the plates, independence cannot be assumed certain. Therefore, the effects on the pore size with the interaction of the two variables are shown next.

To explore possible interactions between fission density and sample area on the pore size, another ANCOVA test is included. The results in Table 3.12 show that the F-value and p-value for fission density and sample area are below one, and the results are not significant. This means these two variables have no significant effect on the pore behavior, and if they are reliant on each other, they cannot fully explain the pore size area differences separately. In the row labeled ”fission density and sample,” the results test if the interaction of the two variables explains the differences in the pore size area mean. The F-value is higher, but p is less than 0.05 and a slightly significant result. Therefore, the sample and fission density combination will have to explain the mean differences in the pore size area better than the fission density and sample individually.

ANOVA and ANCOVA analyses are helpful for understanding if the pore size area results are a product of fission density or sample. However, more microstructures present in the samples will affect this performance as well. Comparing the pore data to other variables, such as starting microstructure features in this manner, will

Table (3.12) ANCOVA assuming interaction between fission density and sample [127]

	Sum of squares	Degree of freedom	F-value	P-value	Significance level
Fission Density	0.005731	1	0.6167	0.4379	
Sample	0.075002	3	2.6901	0.06221	.
Fission Density & Sample	0.090575	3	3.2487	0.0341	*
Residuals	0.306687	33			

Significance level codes: “***” 0, “**” 0.001, “*” 0.05, “.” 0.1, blank is not significant

allow for a better understanding of the possible relationships between fission density, microstructure, and pore growth. Data-based models can also be made more precise and reliable by performing more rigorous and data-driven analyses.

3.11 Conclusions

Inconsistencies in microstructure data make comparing different experimental results difficult or unreliable. In the AFIP6-MkII and RERTR-12 samples analyzed here, pores and FGB were explored using a large dataset of the results. By using more complete data distributions as opposed to simplified averages, the behavior can be better understood. The fission densities included in the analysis are not very similar, and the differences in the starting microstructure in the two experiments are not quantified to the level needed to develop more advanced statistical models. Additionally, methods of fission density calculations may be impacting the differences in the swelling and pore behavior [49]. This work is a starting point to defining the statistical methods needed for data analysis.

Relationships between fission density and FGB are explored with ANOVA and ANCOVA analysis of the transformed data sets. From these results, there are underlying mechanisms outside of the fission density causing the change to the swelling and FGB, but without further data, these are not currently determinable. In the future, more detailed data will be collected to more reliably compare the FGB performance and to understand the possible causes of the differences in the AFIP6-MkII and RERTR-12 experiments.

The pore size area of the AFIP6-MkII experiments is approximately 45 to 55 % higher in KGT2673 than in 96A and 97A. 96A was 18% higher in pore area than 97A, even though these all came from the same experimental plate. KGT2763 and L1P755 had the highest porosity values and contained possibly interconnected pores. Further analysis is underway to understand if the observed large pores are an error in the FGP-GUI or interconnection. Differences found in the samples may come from:

- KGT2763 was sheared and much smaller than its other two AFIP6-MkII samples. This causes a much smaller dataset and can contribute to the error in the measurements.
- Rail regions may be inhibiting FGB growth and impacting results in 96A, KGT2763, and L1P755. However, the expected constrained growth was only apparent in the KGT2763 sample. The rail regions had the opposite

effect; the largest pores were observed here.

- In KGT2763, the range of pore sizes was much larger than the other three samples. The large pores may be interconnected, and the previous theory of interconnection not occurring until the porosity reaches 30% is not correct. The temperature may also be affecting these large pore size results.

Further data is required to understand all of these discrepancies and the fuel behavior more clearly. Additionally, to improve the reliability of the data, larger sets of the original data are valuable. More data overall is required for the starting and post-irradiation microstructure to improve current statistical models and U-Mo fuel behavior predictions. In order to provide more data to the microstructure data collection efforts the RUSL experiment will be used for elastic modulus measurements and phase change measurements in-pile. This will provide real time data to the computational scientists necessary for improved models and simulation. The following chapters will focus on this aspects of the research.

Chapter 4: Phase reversion detection and microstructure

To understand phase decomposition impacts on the fuel performance, the following sections will explore the design of an irradiation experiment of a MP-1 U-Mo samples. The RUSL technique is implemented to measure elastic modulus changes in a cantilever material sample that correspond to the crystallographic phases present. Using an updated equation of diffusion, the reverted volume fraction of the starting decomposed phase was is presented and shows the fission rate and temperature conditions designed for the experiment will be sufficient for complete phase reversion in the U-Mo sample. Further explanation of the experiment design and methodology to the calculations is as follows.

4.1 Introduction to phase change measurements

From Table 2.1, MM-1a includes the volume fraction of α and γ phases in the fabricated and post-irradiation microstructure. The need to understand those beginning and ending phases is important because phase decomposition to the $\alpha + \gamma'$ phases will cause the early onset of grain refinement and anisotropic swelling [2, 18, 109]. However, the phase evolution between the beginning and final, post-irradiation phase microstructures is not well quantified. Measuring changes in the material behavior in-pile allows for computational researchers to see real data dependent on time, temperature, and fission conditions [55]. As previously mentioned, phase reversion will occur at a temperature much lower than the eutectoid point of 550°C during irradiation [24, 37, 38]. The actual mechanisms and conditions reversion occurs under are difficult to gather but are important to predicting fuel behavior. Real-time measurements of the evolution may lead to a more thorough understanding of the material behavior during irradiation.

Measurement techniques for material crystallographic phases include TEM [48], EBSD [46] and X-ray diffraction (XRD) analysis [39, 54, 112, 151, 152]. These methods are time-consuming and difficult to perform in situ. Mechanical methods used to determine the phase change occurrence are density [40], electrical resistivity [24, 36, 113, 153–155], and elastic modulus measurements [52]. These tests are more easily performed in-pile and have shown promising results for detecting the phase changes occurring during the irradiation [113, 153]. In this work, the elastic modulus will be used to determine the phase change during an irradiation test in the TREAT.

Schley et al. [55] developed a device that measures the elastic modulus, or elastic stiffness tensor, of a beam of material during irradiation in TREAT at the INL. Originally a copper sample was irradiated and tested, but the next application of RUSL is with a U-Mo sample. By measuring the vibrational frequencies of a beam, the elastic stiffness tenser can be calculated with Young's modulus of elasticity (E) using equation 4.1 [50, 53, 55].

$$f_n = \frac{(\beta_n l)^2}{2\pi l^2}\sqrt{\frac{EI}{\rho A}} \tag{4.1}$$

E is the Young's modulus (GPa), ρ is the material density ($kg\,m^{-3}$), l is the length of the beam (m), A is the cross sectional area (m^2), I is the geometric moment of inertia (m^4), and $\beta_n l$ is a solution to the frequency equation for flexural modes (n) and will be explained in further detail.

The symmetry of a crystalline lattice changes the number of unique elastic tensors of the material and the symmetry of the crystal, and the actual elastic modulus of the lattice. For example, an orthorhombic structure has nine independent elastic constants, where a cubic structure only has three [156]. Therefore, measuring a beam's flexural waves tells of changes in the wave frequency which corresponds to the elastic modulus and the crystal structure [55]. Therefore, during a change in crystallographic structure, the elastic constants of the material also change. A decrease in the elastic modulus should be detectable via a change in the vibrational frequency of the beam if the reactor conditions meet the need to revert the decomposed U-Mo to the cubic γ phase.

The following sections focus specifically on the phase decomposition and mechanical behavior of MP-1 samples of U-Mo, monolithic fuels. MP-1 samples will be tested using this method to determine the ability of RUSL with a fueled specimen to test the real-time temperature and flux conditions phase reversion may occur.

4.1.1 Elastic modulus measurements of U-Mo phase change

Newell measured Young's modulus of α uranium as 187.4 GPa, and the γ U-Mo as 58.6 to 97.0 GPa, with Poisson ratios of 0.21 and 0.35 respectively via the material hardness [54]. Another study by Steiner et al. [52] used the same RUS technique as the RUSL capsule design to compare temperature-dependent elastic moduli to previous studies [52]. This work shows that as the atom percent of molybdenum increases, so does the bulk modulus and Young's modulus and shear modulus do not increase significantly [52]. All of the studies included, however, were exploring the modulus changes based on the increase in temperature, not with an increase in fission density. Little work on the elastic modulus measurements exist based on the irradiation conditions. Two exceptions were Leeser et al. [157], and Schulthess et al. [94].

Leeser et al. [157] showed Young's modulus of α uranium is greater than γ and decreases as the temperature and burn-up increase [12, 157]. The highest amount of burn-up samples showed the lowest elastic modulus and continued to decrease as the temperature exposure increased. In a more recent study by Schulthess et al. [94], measurements from RERTR-12 samples for the elastic constant, strain, and bulk stress agree with the relationship Leeser et al. observed, as the fission density or burn-up increases the elastic modulus of the material decreases [94].

4.2 RUSL measurement technique

As previously mentioned, the RUSL test measures the vibrational frequency of the material beam to detect any microstructural changes. The current RUSL tests were successful at measuring a copper beam specimen's recrystallization in TREAT. However, there has been no test of a fueled specimen in the RUSL apparatus [55,158]. Several considerations are critical to designing the phase reversion experiment to measure the elastic changes in a U-10wt%Mo sample, including the fission rate and temperature where phase reversion occurs, the elastic constants of the different phases of U-Mo, and safety designs for the added neutronic component of a fueled specimen. Therefore, the original RUSL experiment is examined first.

4.2.1 Original RUSL design

Figure 4.1 illustrates the original RUSL design. As the image shows, there are two fiberoptic probes; one is the excitation laser the other, at the free end of the specimen beam, measures the light reflected off the beam back to the light source. The excitation probe heats the specimen and causes optical heating and thermal expansion. The change in light reflected off the sample surface measured by the second optical probe determines the frequency oscillation. The titanium capsule provides a region for the specimen to be clamped in like a cantilever and holds the fiberoptic cables in place, keeping the material contained, away from the reactor environment [55, 158].

The elastic modulus is calculated from the beam vibrations using the Bernoulli-Euler analysis method seen in equation 4.1 [55]. $\beta_n l$ is also known as λ_n which represents the eigenvalues of the natural frequency of the cantilever equation [159]:

$$1 + \cosh(\lambda_n)\cos(\lambda_n) = 0 \tag{4.2}$$

Where the roots of Equation 4.2 are $\lambda_1 = 1.875,\ \lambda_2 = 4.694,\ \text{and}\ \lambda_3 = 7.855$. The calculation of these values and further explanation of the calculations are included in Appendix B.1.

The Young's modulus is calculated from the resonant frequency peaks measured by RUSL. For example, the resonant frequency peaks measured by Schley et al. in the original RUSL test occur at 1188 Hz at the beginning, and 921 Hz after the copper undergoes recrystallization [55]. Figure 4.2 shows these values as measured by the optical fiber method. Using these first mode frequencies in equation 4.1 and solving for the elastic modulus, the values are 118.4 GPa and 70.8 GPa [51]. The Young's modulus decreased by approximately 50 GPa after annealing and recrystallizaiton.Therefore, this method of elastic modulus measurement successfully detected a change in the microstructure.

As a function of temperature, the frequency is plotted from the experiment in Figure 4.3. The frequency drops drastically at a temperature of about 160°C and continues to change more gradually up to the peak temperature. The

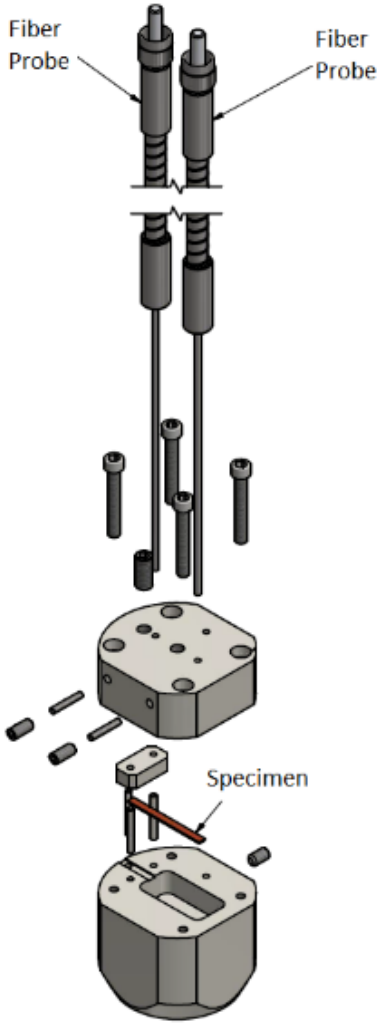

Figure (4.1) Exploded view of the RUSL design from Woolstenhulme et al. [158]. Only one copper specimen is tested in this original experiment with the two fiberoptic cables.

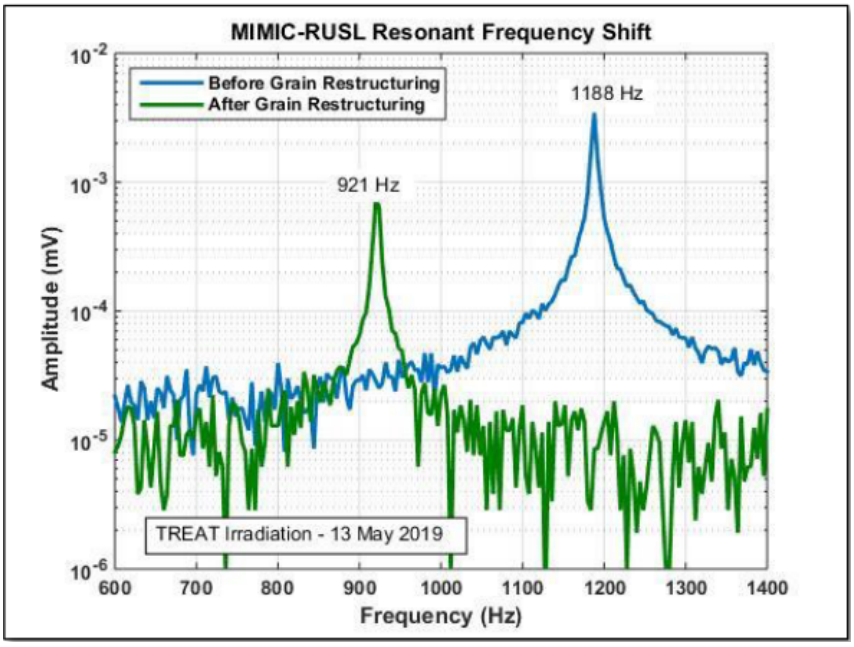

Figure (4.2) Resonant frequency shift during the TREAT irradiation measured by Schley et al. showing the recrystallization of the copper specimen [55].

quick change in frequency is from the grains recrystallizing in the material. As the sample cools, the frequency and grain structure remains constant. The change in frequency is an excellent illustration of a frequency measurement during a RUSL test and what it can explain about the material behavior.

The original RUSL test sampled the frequency every 40 seconds and used a steady-state power in TREAT of 80 kW [55]. While the measurement and design of RUSL were successful, no noticeable difference occurred between the irradiated and furnace-tested specimens. Schley et al. [55] looked at the radiation enhanced diffusion of copper to understand better the possible requirements of irradiation damage and conditions for grain restructuring as a result of radiation. The following work uses similar diffusion and damage calculations to predict and inform the TREAT transient designs in order to see the radiation effects on the MP-1 samples. The following sections explain the theory and calculations required to plan the temperature and transient shapes of the fuel similar to those proposed by the copper experiments in future testing.

4.3 Phase transformation and reversion mechanisms

4.3.1 Phase change mechanisms

Two main methods of phase transformation occur in the material; firstly, the diffusion of the various constituents in the material across boundaries change the chemical composition. The second is the movement of interfaces, or boundaries, that shift atoms in the lattice and assist in the rearrangement to the new phase [160]. Diffusion

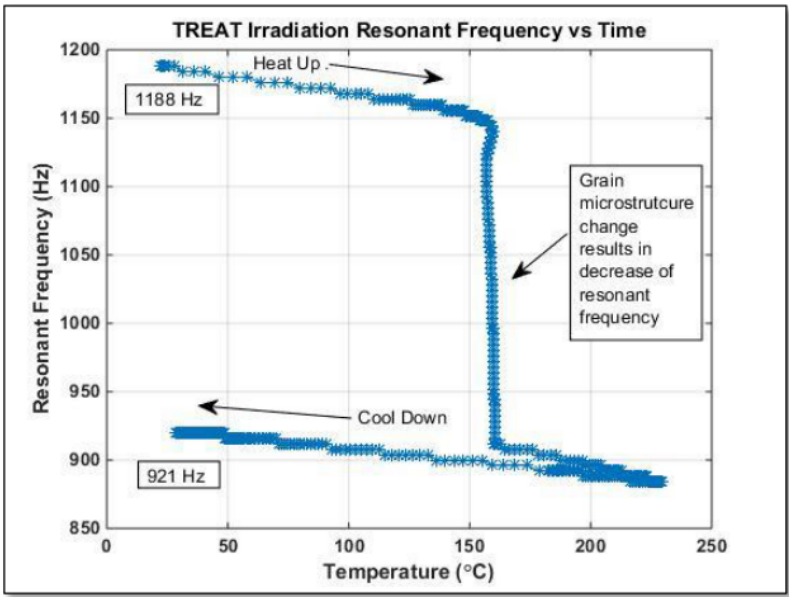

Figure (4.3) Frequency shift of the copper specimen versus the temperature change in the sample showing the change in elastic modulus and microstructure in the copper specimen during TREAT irradiation [55].

and the interface movement are the two controlling factors in the phase transformation [160]. Additionally, the precipitation and dissolution of the phases depend on the diffusivity of the solutes in the "solution" or binary matrix [59]. Recently, a method of determining the fraction of volume transformed in U-Mo fuels was completed by Newell et al. [56]. They used a combination of the JMAK nucleation and growth mechanisms and spherical dissolution model developed by Zuo et al. [59] to understand the kinetics of a thermal phase reversion of decomposed U-Mo. Experiments of the thermal phase reversion agreed well with the combine JMAK and dissolution method. In their work there is included a brief overview of including the irradiation effects on the phase reversion as well and incorporates irradiation induced diffusion coefficients developed by Bleiberg [113] along with the critical fission rate calculation methods explained later created by Willard and Schmitt [37]. The following sections use this proposed method created by Newell et al. [56] along with more recent diffusion calculation and values to understand possible phase reversion volume changes that may occur in the RUSL tests.

4.3.2 Diffusion and phase transformation

For both phase transformation and reversion, the material's change depends on vacancies, interstitials, and defect production, and diffusion through the material. The concentration of vacancies and interstitials is dependent on the energy of the system, and as the energy of the systems increases, these species will move and interact with the surrounding material. Increasing the temperature of the system will increase the internal energy of the material. Similar to this, adding energy via fission fragments and atom collisions will change the internal energy of the lattice as well.

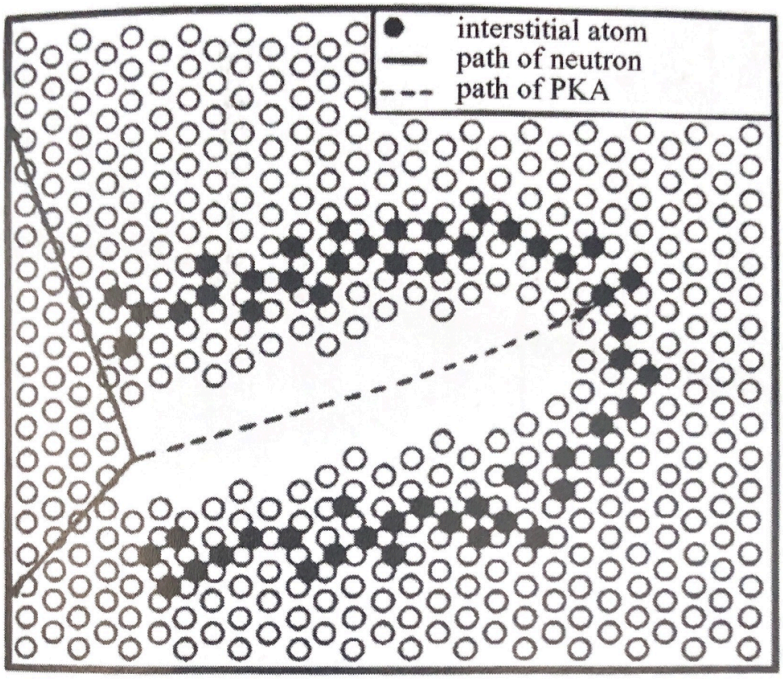

Figure (4.4) PKA interacting with a crystal lattice shows how the interstitial creation occurs around the PKA and disturbs the lattice structure [163].

In a reactor environment, the diffusion of species through a material is controlled by the primary sources of energy addition to the material, temperature, and damage from fission events. Lattice defects are caused by the primary knock-on atom (PKA). These PKA atoms have enough energy to displace surrounding atoms in the lattice forming defects in the lattice that allow for the diffusion of interstitials and vacancies. This process is illustrated in Figure 4.4. It essentially makes the process of diffusion much easier, so diffusion can happen at lower temperatures and more readily [161]. When the atoms are in an ordered arrangement, the material exists in the lowest free energy of a solid. Disorder increases with irradiation, so the free energy increases in the solid [88, 162]. This increase in the free energy of the system enables phase changes through diffusion. Diffusion requires vacant sites in the lattice around the atoms to move into [19]. Vacancy and interstitial production from irradiation create the vacant sites and therefore, diffusion needed to homogenize the mixture of U-Mo to the metastable BCC structure. At the same time, temperature alone is not enough to do that under the reactor temperature conditions. This homogenization helps keep the γ phase present or causes the decomposed phases to revert [38].

Two theories in the literature explain the possible causes of the observed phase reversion, the thermal spike theory and the displacement spike theory. A thermal spike is an area of high energy in the lattice caused by a collision of incoming particles striking the material atoms [19]. From the energy increase melting and annealing occurs, it is proposed this is similar to quenching, so the γ phase will appear after the event [161, 164]. However, Tucker and Senio [165] think that this is not likely because the amount of time the material is held at the temperature

is very short. It is more likely the material will heat up, become energized, and take on the crystal structure of the material around the spike rather than be homogenized by the temperature increase and decrease alone [165]. The interrupted phase could nucleate on its neighbors and change to match the neighboring phase. The thermal spike encourages the defects to increase and diffuse through the lattice.

The displacement spike theory includes the mechanism of the same collision from the thermal spike theory. An incoming particle creates a displacement spike, and the PKA and secondary knock-on atoms result in new vacancies, displacements, and interstitials [19]. The density of the material increases around the displacement spike collapses the structure from the pressure increase, then allows the spike to restructure with the surrounding material. Displaced atoms will move through the material a distance from the spike and can homogenize with the rest of the material [37,38]. Vacancy and interstitial production from irradiation cause the diffusion needed to retain the phase and act similarly to the thermal diffusion [38].

From both theories, the diffusion of species through the material is controlled by temperature and irradiation. This diffusion controls the phase change mechanisms occurring and must be calculated to determine the diffusion changes due to temperature and irradiation conditions. A critical point to the work is that; once the diffusion of the material is known, the possibility of a phase change is predictable. The following section will quantify and explain how diffusion coefficients may be used to predict amount of phase change in the material.

4.4 Predicted phase transformation volumes

Newell et al. [56] created a calculation for determining the fraction of a material changed during phase reversion. Half of the reversion is expected to come from the growth and nucleation of γ phases explained via the JMAK method shown below in equation 4.3 where P is the probability of the volume transforming at any point in the material [56]. The other half of the phase transformation is attributed to the dissolution of particles of $\alpha + \gamma'$ into the γ matrix. Explanations of both mechanisms are below.

4.4.1 JMAK calculation method

JMAK equation of understanding phase transformation kinetics is commonly used to estimate the volume transformation of a crystalline material from one allotrope to another based on the isothermal temperature and time [57, 58]. This method assumes the phase transformation occurs from nucleation and growth reactions [58]. Equation 4.3 is the probability that a point in the matrix is untransformed at the time, t (seconds). This equates to the untransformed volume at that time and is subtracted from 1 to get the transformed phase volume [58].

$$\mathrm{P(t)} = 1 - \mathrm{e}^{-\mathrm{Kt}^{\mathrm{n}}} \tag{4.3}$$

K is the parameters in the growth and nucleation dependent on temperature and n is the JMAK constant assigned the value 4 for continuous nucleation and growth [56]. t is the time component. K is dependent on G and $\dot{N}$ or the growth rate and nucleation rate of the material and is solved for as:

$$K = \frac{4}{3}\pi \dot{N} G^3 \tag{4.4}$$

$\dot{N}$ and G both align with an Arrhenius relationship consisting of pre-exponential factors, $N_o \text{ and } G_o$, and activation energies of $Q_N \text{ and } Q_G$. These were calculated by Newell et al. [56] to both be equal to be 3.0×10^7 $(m^{-3}s^{-1})$ and (m/s) , respectively. The activation energies are $Q_N \text{ and } Q_G$ are equal to 180 kJ/mol [56]. The general from on the Arrhenius equation is:

$$k = A \times e^{\frac{-Q}{RT}} \tag{4.5}$$

$$\dot{N} = N_o \times e^{\frac{-Q}{RT}} \tag{4.6}$$

$$G = G_o \times e^{\frac{-Q}{RT}} \tag{4.7}$$

Which includes the universal gas constant R and the temperature T; A is the pre-exponential factor equal to $N_o \text{ and } G_o$ values stated previously. From this form of the rate equation $\dot{N}$ and G are solved for and included in equation 4.3.

4.4.2 Dissolution method of decomposed particles

The next half of the phase reversion comes from the diffusion and movement of interfaces of already existing phase particles. Zuo et al. [59] developed this analytical, kinetics model of determining phase dissolution with from a modified JMAK method that is derived from "diffusion-controlled transformation theory". It is based on x_e which is the extended volume fraction of the transformation. Essentially, this extended volume fraction of the transformed phase is the amount of the transformed phase that discounts the overlapping areas of the nuclei growth compared to the starting phase volume [58, 59]. The transformed volume equation incorporates the extended volume fraction in the the same form as the traditional JMAK equation.

$$f_t = 1 - e^{-x_e} \tag{4.8}$$

Using two volume equations for the stating volume in the phase and the volume of the transformed area the following equation for x_e is equal to,

$$x_e = \frac{R_o^3 - R^3}{R_o^3} \tag{4.9}$$

where R_o is the beginning particle radius and R is the final particle radius after the dissolution occurs and the particle phase has decreased [59]. In dissolution is controlled by the concentration of the solutes along the interface of the new phase and the matrix it is in for diffusion driven processes [59]. Therefore, the concentration of the phase in all parts of the interface and the size of that interface are needed to understand the dissolution and transformation occurring. The ending particle radius follows the time dependent form of equation 4.10. The derivation and further explanation of the equation is found is Appendix C.

$$R = \sqrt{\frac{k}{\pi}}(R_s - \sqrt{kDt}) + \sqrt{R_s^2 - kDt} \tag{4.10}$$

where D is the diffusion coefficient and t is time. Solving for R will incorporate the diffusion of the material from intrinsic or thermal diffusion (D). However, by replacing the usual interdiffusion coefficient here with an equation for radiation enhanced diffusion the effects of temperature and fission rate on the volume fraction change is possible, and the transformed volume fraction of the new γ can be found [56].

R_s is the steady state dependent particle radius and is equal to

$$R_s = \frac{1}{(1 + \sqrt{k/\pi})} \times R_o \tag{4.11}$$

k is the ratio of three solute concentrations of the phases present. C_e is the concentration of the matrix, C_i is the concentration at the interface of the matrix and the particle, and C_p is the concentration in the particle [56, 59]. Newell et al. [56] assume the concentration of the equilibrium state is dependent on the molybdenum in each phase of the material. In the equilibrium phase, C_e is the γ phase molybdenum concentration in atom percent, C_i the concentration at the solvus line on the phase diagram, and C_p is the amount of molybdenum inside the γ' phase [56]. From these values, k can be calculated with,

$$k = \frac{2\left(C_i - C_e\right)}{C_p - C_i} \tag{4.12}$$

One caveat of this method is, the initial calculation of x_e does not include the interaction between particles and this must be addressed. Initially, the value of x_e or the ratio of the extended transformed volume to the original volume will fall between 0% transformed and 100%, or values of 0 and 1. But if interactions between particles are included the actual limiting factor is from the entire transformation of the phase without the overlapping of particles, or f_t. Using the JMAK method where $V_e = Kt^n$ is fully transformed, or unity, the full extent of the transformation is expressed by Zuo et al. [59] as

$$0 \leq f_t \leq 1 - e^{-1} \tag{4.13}$$

However, this is not completely physically true either, the upper limit of f_t would then be approximately 1.58 which is not possible. The volume of the new phase cannot be larger than the starting phase. Zuo et al. [59] proposes the use of a modifying factor, m, to more accurately describe the transformation taking place [59]. The modified transformation fraction is define as f_{tm} based on a modified time values as well, t_m. Using the integrals of the transformation below in equations 4.14 and 4.15, m is found [59].

$$\int_0^1 df_{tm} = \int_0^{1-e^{-1}} m df_t \tag{4.14}$$

$$m = \frac{1}{1-e^{-1}} \tag{4.15}$$

Therefore, the modified equation of the transformation volume due to dissolution is

$$f_{tm} = m(1-e^{-x_e}) \tag{4.16}$$

By using the above equations and methods as Newell et al. [56] suggests, half of the overall phase reversion occurs from each of method, JMAK and dissolution, the volume fraction of the transformed decomposed phase is calculated as a way of estimating the possible phase reversion undergone in the RUSL experiment. The following sections show the diffusion calculation methods required for the dissolution calculation method to predict the amount of phase reversion occurring in the future RUSL experiments.

4.5 Three diffusion types impacting crystallographic phases

4.5.1 Thermal or intrinsic diffusion (D_T)

In a zero-flux, or non-irradiation, environment the driver of phase change in U-Mo is due to thermal effects or self-diffusion. The movement of vacancies and interstitials will determine the microstructure behavior of the material and the diffusion. Diffusion of these material constituents changes the structure and free energy of the lattice which translates to mechanical, macroscale effects. In unirradiated U-Mo materials, the diffusion of interstitials and vacancies allow for the phase transformation from $\alpha + \gamma'$ to γ and vice versa based on the thermal conditions of the material.

Intrinsic, or self diffusion, is defined using the self-diffusion coefficients experimentally found from Huang et al. [166, 167]. The intrinsic values of uranium and molybdenum from this study are shown in Table 4.1. Using the Arrhenius relationship in equation 4.5 the values are calculated to get the separate intrinsic diffusion values for a standard equation for the two materials. This final diffusion pre-exponential factors and activiation energy values are seen in equation 4.18 and 4.19.

Table (4.1) Intrinsic diffusion measurements from Huang et al. [166] used by Beeler et al. [167]

Temperature (K)	Intrinsic Mo (10^{-13} D_{TMo} (m^2/s))	Intrinsic U (10^{-13} D_{TU} (m^2/s))
1273	1.97	9.93
1173	0.55	3.79
1073	0.17	1.18
973	0.01	0.08
923	0.00	0.03

$$D = D_0 e^{-Q_{sd}/RT} \tag{4.17}$$

D_0 is the frequency factor and Q_{sd} is the self-diffusion activation energy. From this equation and the values found in reference [166], the intrinsic diffusion equations developed by Beeler et al. [167, 168] are in equations 4.18 and 4.19.

$$D_{TU} = (1.28 \times 10^{-5}) \times e^{\frac{-1.76}{kT}} \quad [m^2/s] \tag{4.18}$$

$$D_{TMo} = (1.62 \times 10^{-5}) \times e^{\frac{-1.97}{kT}} \quad [m^2/s] \tag{4.19}$$

These equations are used to determine the thermal diffusion of the uranium and molybdenum in the fuel based solely on temperature conditions. However, in a reactor environment the collisions from fission events will increase the diffusion as well and this must be accounted for and included in the full diffusion calculations.

4.5.2 Radiation enhanced diffusion (D_{RED})

Calculating the radiation enhanced diffusion was performed by Beeler et al. [168] for U-10wt% Mo as part of the USHPRR fuel qualification efforts using a combination of rate theory simulations and molecular dynamics. These two methods ultimately calculated the recombination rate of interstitials and vacancies to solve for the RED coefficients shown in equations 4.20 and 4.21. The defect concentration calculated for the RED diffusion is highly temperature dependent. As the temperature increases so will the defect concentration, but after about 700 K the defect concentration begins decreasing with temperature [168]. Therefore, two equations were made for high and low temperature diffusion in both metals present.

$$D_{URED} = \begin{cases} (1.38 \times 10^{-15}) \times e^{\frac{-0.41}{kT}} \times (5.3 \times 10^{-11}) \times \sqrt{\dot{F}}, & \text{if } T > 700 \text{ K} \\ (1.24 \times 10^{-13} \times e^{\frac{-0.68}{kT}} \times (5.3 \times 10^{-11}) \times \sqrt{\dot{F}}, & \text{if } T < 700 \text{ K} \end{cases} \quad [m^2/s] \tag{4.20}$$

$$D_{MoRED} = \begin{cases} (1.65 \times 10^{-16}) \times e^{\frac{-0.31}{kT}} \times (5.3 \times 10^{-11}) \times \sqrt{\dot{F}}, & \text{if } T > 700 \text{ K} \\ (1.47 \times 10^{-14}) \times e^{\frac{-0.58}{kT}} \times (5.3 \times 10^{-11}) \times \sqrt{\dot{F}}, & \text{if } T < 700 \text{ K} \end{cases} \quad [m^2/s] \tag{4.21}$$

This RED are still dependent on the T, temperature, but also $\dot{F}$, or the fission rate corresponding to the reactor conditions. Therefore, both factors affect the diffusion of species throughout the matrix and will change when the phase reversion occurs. Once the power transient and thermal conditions were developed for the RUSL experiments these values are calculated to understand the conditions of diffusion through the specimen needed to predict the possible phase reversion volume results. The last part of the diffusion due to temperature and radiation is the fully radiation driven diffusion presented next.

4.5.3 Radiation driven diffusion (D_{irr})

Radiation driven diffusion is the mechanism where diffusion is assumed to be dependent on only the fission density of the material. It is based upon the mean-squared displacement of atoms [167, 168]. The calculation for the radiation driven diffusion depends on the energy of fission fragments (170 MeV), 5% of the of that energy is deposited in the lattice, and the fission rate [167]. Values from Beeler et al.'s work [167] are shown below in equations 4.22 and 4.23.

$$D_{Uirr} = (1.97 \times 10^{-41}) \cdot \dot{F} \quad [m^2/s] \quad (4.22)$$

$$D_{Moirr} = (2.01 \times 10^{-41}) \cdot \dot{F} \quad [m^2/s] \quad (4.23)$$

4.5.4 Final diffusion equation for U-10wt% Mo

Finally, the diffusion equations for the uranium and molybdenum are added together to achieve a final diffusion equation based on temperature and fission rate [168]. The calculations result in a peicewise shape at the temperature of 700 K where there if a shift in the slope of the temperature and diffusion results. These are the high temperature systems.

$$D_{U\text{–highT}} = (1.28 \times 10^{-5}) \cdot e^{\frac{-1.76}{kT}} + (1.38 \times 10^{-15}) \cdot e^{\frac{-0.41}{kT}} \cdot (5.3 \times 10^{-11}) \cdot \sqrt{\dot{F}} + (1.97 \times 10^{-41}) \cdot \dot{F} \quad (4.24)$$

$$D_{U\text{–lowT}} = (1.28 \times 10^{-5}) \cdot e^{\frac{-1.76}{kT}} + (1.24 \times 10^{-13}) \cdot e^{\frac{-0.68}{kT}} (5.3 \times 10^{-11}) \cdot \sqrt{\dot{F}} + (1.97 \times 10^{-41}) \cdot \dot{F} \quad (4.25)$$

$$D_{Mo\text{–highT}} = (1.62 \times 10^{-5}) \cdot e^{\frac{-1.97}{kT}} + (1.65 \times 10^{-16}) \cdot e^{\frac{-0.31}{kT}} \cdot (5.3 \times 10^{-11}) \cdot \sqrt{\dot{F}} + (2.01 \times 10^{-41}) \cdot \dot{F} \quad (4.26)$$

$$D_{Mo\text{–lowT}} = (1.62 \times 10^{-5}) \cdot e^{\frac{-1.97}{kT}} + (1.47 \times 10^{-14}) \cdot e^{\frac{-0.58}{kT}} \cdot (5.3 \times 10^{-11}) \cdot \sqrt{\dot{F}} + (2.01 \times 10^{-41}) \cdot \dot{F} \quad (4.27)$$

The three different types of diffusion were calculated to compare the expected dominant diffusion mechanisms are the various experimental temperatures. Each type of diffusion is calculated separately and plotted from 0 to 1200°C at a randomly assigned fission rate of 5×10^{20} f/m^{3}s. As Figure 4.5 illustrates, at various temperatures one type of

diffusion is dominant. For the RED diffusion of U, it dominates the other two types of diffusion between 500 and 650 K. At higher temperatures the thermal diffusion is the dominant type and at lower temperatures the radiation driven diffusion dominates. This is because the energy imparted on the lattice structure from the incoming fission particles do not provide as much energy to the system as the high temperatures do. The incoming fission particles need to interrupt the lattice and produce the proper energy to create the interstitial and vacancy formation for the U-Mo species to migrate and diffuse to form the γ phase. For these purposes when ever the dominant diffusion is primarily dependent of the fission rate the phase reversion is possible.

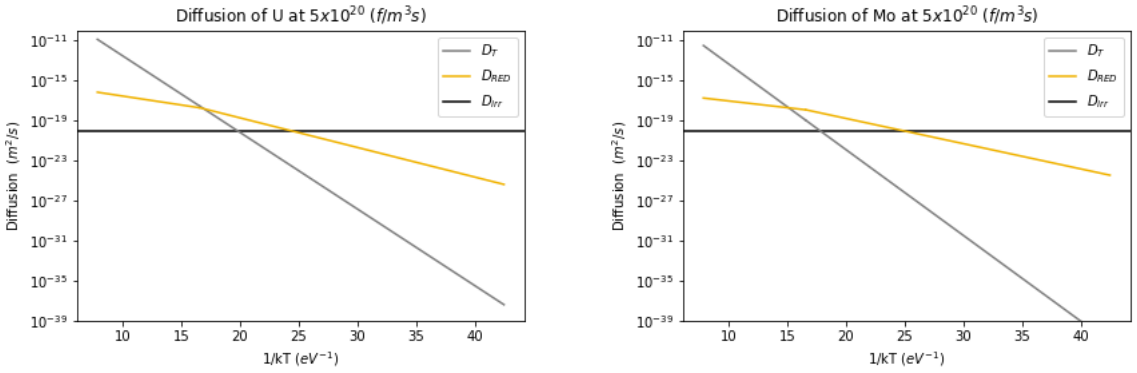

(a) (b)

Figure (4.5) Diffusion results of (a) uranium and (b) molybdenum of intrinsic, RED, and radiation driven diffusion comparing the temperatures in which each type is dominant. At lower temperatures the RED and radiation driven diffusion are dominant.

Knowing the dominant diffusion type is important because it indicates that diffusion from irradiation will control the phase transformation mechanisms. This final value for diffusion of the material is necessary to understanding the temperature and fission rates that phase changes might occur under. The following section explains the methods for calculating a critical fission rate that will cause phase reversion or retention of the ideal γ phase. Finding the critical fission rate where the necessary radiation induced diffusion will overpower the thermal diffusion as defined in Chapter 1 is pivotal to planning the RUSL tests. Critical fission rate approximations determine the necessary temperature and fission rate required to test the theory with the RUSL measurement. Therefore, the critical fission rates are calculated using the methods below to give a baseline for the experimental design.

4.6 Phase reversion critical fission rate

As stated above, the total diffusion in the U-Mo material depends on the combination of intrinsic diffusion, RED, and radiation driven diffusion. At different temperatures and fission conditions, one of the three will be the dominant form of diffusion. Therefore, a critical fission rate exists where the thermal and radiation diffusion mechanisms exist at equilibrium [15, 37, 38]. These conditions determine the phase transformations the material

will undergo or not in the reactor. Therefore, for the RUSL experiment, reactor testing must be planned such that the material is exposed to a high enough fission rate that the dominant diffusion mechanisms are fission enhanced or driven. Calculation of this required fission rate or critical fission rate is explained in the following section.

4.6.1 Early critical fission rate calculations

Willard and Schmitt [37] calculated a theoretical, critical fission rate using thermal diffusion and "irradiation-induced diffusion" of U-Mo fuels [12, 37]. For the purposes here, the "irradiation-induced diffusion" is the combination of the RED and the radiation driven diffusion equation explained above and developed more recently. In these early studies, the critical fission rate exists when the thermal diffusion is equal to the diffusion enhanced diffusion ($D_T = D_R$) [37]. Once the fission rate exceeds the critical value, the radiation conditions drive the phase transformation kinetics, not the thermal conditions. Willard and Schmitt came to this conclusion from the relationship between fission rate and diffusion proposed by Bleiberg based on the volume and number of fission spikes [113]. Bleiberg showed that fission rate and diffusion are directly proportional and verified experimentally two reference values used in the Willard and Schmitt calculations for the radiation-based diffusion in equation 4.28.

$$D_R = \frac{D_{R1}}{CF_1} \cdot CF \qquad [cm^2/s] \quad (4.28)$$

D_{R1} is the reference radiation induced diffusion coefficient $1.4{*}10^{-18}\ cm^2/s$, D_R is the radiation induced diffusion coefficient, CF_1 is the reference critical fission rate $5.25 * 10^{12}$ f/cm^{3}s, and CF is the critical fission rate [37, 113].

Willard uses the thermal diffusion seen in equation 4.29,

$$D_T = D_o e^{-\frac{Q}{RT}} \qquad [cm^2/s] \quad (4.29)$$

where D_o is the diffusion constant, Q is activation energy, R is the universal gas constant, and T is temperature in Kelvin [37]. To solve for the critical fission rate equation 4.28 is set equal to 4.29.This is shown in equation 4.30

$$CF_{exp} = \frac{D_o \cdot e^{-\frac{Q}{kT}}}{2.667 \times 10^{-31}} \qquad [f/cm^3s] \quad (4.30)$$

Willard et al. assumed the pre-exponential factor and activation energy of U-10wt% Mo to be $10^{-}2\ cm^2/s$ and 2.12 eV, respectily [37]. Therefore, equation 4.30 may be simplified to equation 4.31 below.

$$CF_{exp} = 3.75 \times 10^{28} \cdot e^{\frac{-24600}{T}} \cdot (10^6) \qquad [f/cm^3s] \quad (4.31)$$

Equation 4.31 compared well with experimental values obtained from U-10wt% Mo samples irradiated in the

Hallam Nuclear Power Facility. As a part of the PIE, the post-irradiation crystal phases were compared to the starting phases. Figure 4.6 shows the plotted critical fission rate values compared to the measured data points. The equation from Willard and Schmitt showed good agreement between the expected ending fuel phase and where the corresponding temperature and fission rates fell on the critical fission rate line [37].

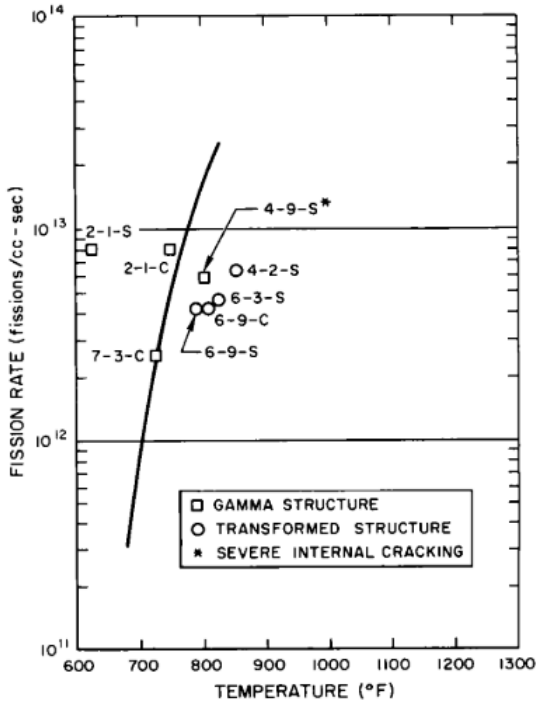

Figure (4.6) The critical fission rate developed by Willard and Schmitt is plotted based on temperature and fission rate. Experimental data points are plotted over this to show the final phases present after irradiation compare to the postulated critical fission rate. Reproduced from [37].

The original RUSL fission rates and temperatures were planned based on this equation for the fission rate. However, to understand if the diffusion coefficients used by Willard and Schmitt were not ideal, the diffusion coefficients calculated previously by Beeler et al. [168] were used to give a more updated critical fission rate equation. The differences in the values are highlighted in later sections, but it is important to note that the TREAT transient power profiles are based on this critical fission rate from Willard and Schmitt [37].

4.6.2 Updated critical fission rate calculations

More recently, the USHPRR developed an equation of the total diffusion due to intrinsic, RED, and radiation driven diffusion of uranium and molybdenum as shown in section 4.5.4 [168]. Each portion of the equation calculates one of the three previously mentioned diffusion mechanisms. By using the Willard and Schmitt [37] method of finding a critical fission rate, a new critical fission rate equation (4.32) was created by setting the intrinsic diffusion (4.18) equal to the RED and radiation driven diffusion equations. Solving for the fission rate produces a

new critical fission rate based on experimental and calculated values from molecular dynamics simulations and phase theory calculations [167, 168]. The newer critical fission rate calculation may improve upon previous work using the Willard and Schmitt [37] fission rate with more recent diffusion coefficients developed with more modern experimental and computational practices.

$$CF_2 = \frac{-\sqrt{4D_T D_{RED}^2 D_{irr} + D_{RED}^4} + 2D_T D_{irr} + D_{RED}^2}{2D_{irr}^2} \qquad [f/m^3 s] \quad (4.32)$$

Equation 4.32 allows for the comparison between the early critical fission rate and newer values for the experimental RUSL results to be understood in more detail. If the elastic modulus measurements differ from the Willard and Schmitt calculation and align more closely to the Beeler et al. based equation, then the RUSL experiment may be considered a validation of the newly developed equation. The reverse of this is also true. The following section compares the two critical fission rate equations to underline the differences and understand possible outcomes in the experiments.

4.6.3 Comparing Willard and Beeler critical fission rates

Initially, the critical fission rate used was from Willard and Schmitt [37], and these values were used to plan the TREAT experiments. However, the calculated values from Beeler et al. [168] are reasonably close to the earlier calculations as shown in Figure 4.7 at lower temperatures and fission rates. As the temperature and fission rate increase, the two begin to deviate from one another more. This is a very large difference as the temperature increases since the scale is logarithmic. As the present the differences in the critical fission rates are not experimentally known, that is the reason for testing this theory with the RUSL method.

From data measured by Willard and Schmitt [37] the data points of irradiated samples that retained or reverted to the γ phase and those that transformed are plotted in Figure 4.6. These points show that the early critical fission rate prediction was accurate at predicting phase reversion of the U-Mo sample. However, to determine if the data points follow the updated critical fission rate, Figure 4.8 shows the γ or transformed phase structure compared to both critical fission rates. The blue γ phase sample points fall below the new critical fission rate except for one reverted sample. The pre-exponential factor and activation energy values used to calculate the thermal diffusion are quite different between the two studies and may account for the difference in critical fission rate.

These two critical fission rate equations inform the experimental planning for the RUSL experiment. Since the necessary fission rates and temperatures are calculated here, the thermal and neutronic models may use these values to determine the experiment's best design and power transient shape. Designing the experiment based on the critical fission rate and proper diffusion coefficients allows for predicting the fuel phase behavior and verifying the accuracy of this critical fission rate.

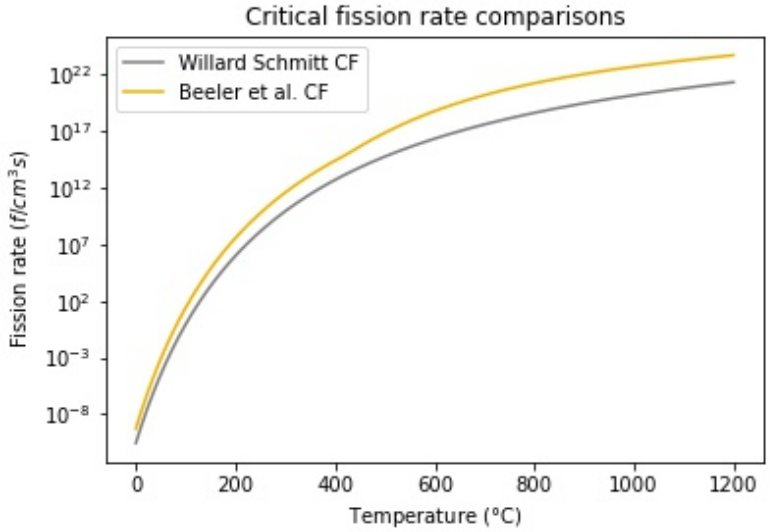

Figure (4.7) Both critical fission rates plotted as a function of temperature. Above the lines the phase reversion or retention is expected. Below the line the phase transformation is likely to occur and above the line phase reversion is likely to occur.

4.7 RUSL experimental design

The original RUSL design is outlined in the Chapter 1. The test design uses a titanium capsule, referred to as the "holder," containing the test specimen and proper fiberoptic cables. After the first iteration of the design, this proposed U-Mo application was modified to account for a fueled specimen, better temperature measurements, and a more complex neutronic environment. The following information explains the purpose of these changes and the analysis performed for the newest design considering the critical fission rate conditions for U-Mo.

4.7.1 Temperature dependence and control

The complicated interconnected temperature and radiation effects on a material make for a difficult measurement method. For example, as a fissile material undergoes fission events, temperature increases in the material, and the two cannot be easily separated to measure the effects of one or the other. Therefore, it is essential to account for both temperature and fission rate to keep the material above or at the desired conditions for phase reversion.

From the critical fission rate equations, the only independent variable is the temperature of the material. So for the RUSL test, a series of temperature values are used to understand the effects of temperature related to the fission rate of the samples. If it were possible to test the same fission rate at the same constant temperatures, that would be ideal. However, irradiating a specimen is more complicated than that. Therefore, the temperatures chosen must be below the eutectoid temperature of U-10wt% Mo to remove the possibility of transforming decomposed regions due to thermal effects. The three starting temperatures chosen are 250°C, 350°C, and 450°C. All of which are

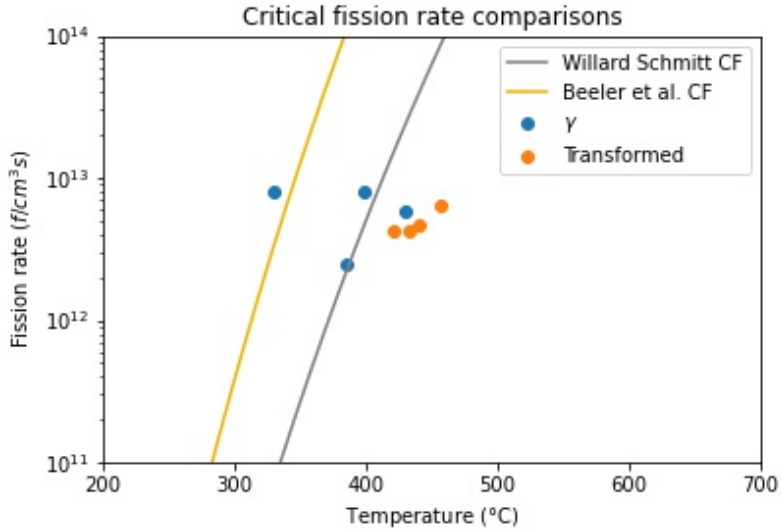

Figure (4.8) Experimental data collected by Willard and Schmitt [37] compared to both critical fission rate equations. These are the same values as displayed in Figure 4.6. The data aligns with the Willard equation but is outside of the Beeler equation.

below the 550˚C eutectoid temperature from the Okamoto phase diagram [35]. 650˚C is the maximum transient sample temperature for safety purposes. By testing the varying temperatures with similar transient shapes, the fission rate effects may be explored in conjunction with the thermal effects.

The samples will be heated before the power transient in the Broad Use Specimen Transient Experiment Rig (BUSTER) heater. Shown in Figure 4.9, the heater module (Figure 4.9b) consists of coiled elements inside of an airtight containment (Figure 4.9a). BUSTER is designed to contain various experimental apparatuses and be interchangeable for these different applications. Additionally, an optional heater is available to add to the containment and heat the experiments as needed. After the specimens are heated to the correct starting temperatures, it is shut off, and the reactor transient may begin.

Each temperature corresponds to one transient run in TREAT. The BUSTER heater increases the sample temperature to the assigned level then the transient run will is completed. Therefore, three separate tests are designed for the holder, RUSL1, RUSL2, and RUSL3. These are scheduled to run sequentially, each, one day in the reactor.

In a perfect world, the tests would keep the temperature the same throughout the irradiation, and the fission rate would remain constant as well. However, this is not physically possible. As the critical fission rate is achieved, the sample heats up. Therefore the fission rate must also increase to keep the material above the critical fission rate value in a positive feedback loop. Each increase in starting temperature requires a higher power to meet the necessary critical fission rate. From these three starting temperatures the critical fission rates required for testing are given in Table 4.2 from equation 4.30. The fission rates listed in Table 4.2 feed into the thermal analysis of the TREAT experiment and determine the reactor power required at each temperature.

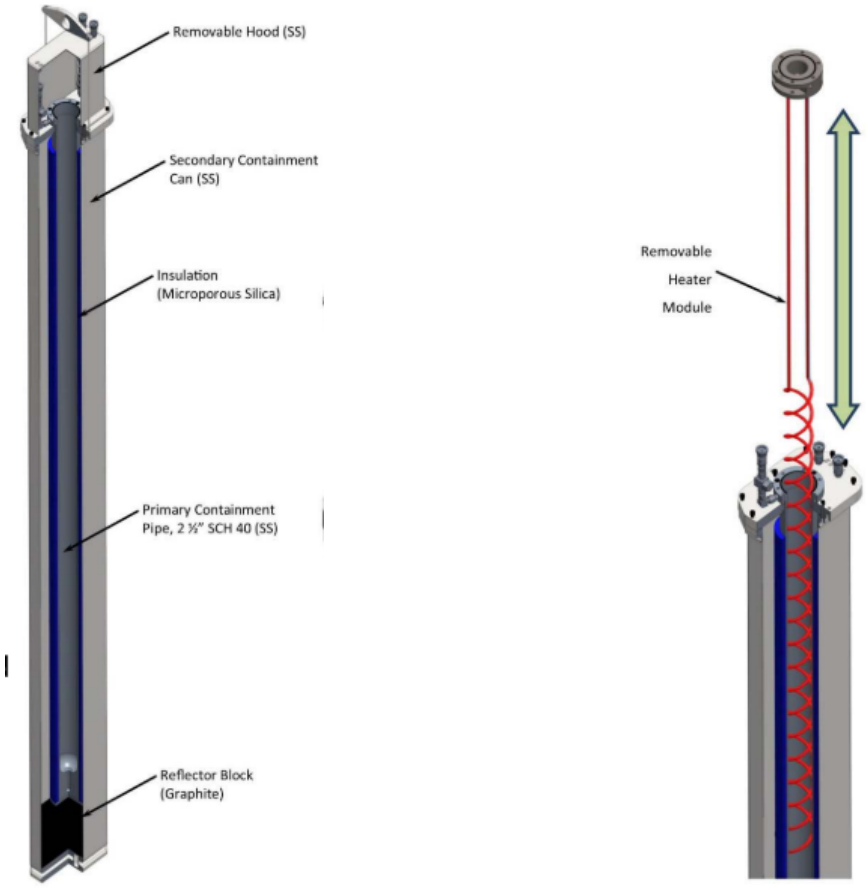

(a) (b)

Figure (4.9) BUSTER canister (a) and BUSTER heater (b) as design for interchangeable TREAT experiments. RUSL used both the canister and the heater for the testing of U-Mo samples. Reproduced from [169]]

4.7.2 Final RUSL holder design

The most significant change to the RUSL holder design for this U-Mo design is a second sample addition used as a ”witness” sample to the actual specimen temperature. This differs from the original RUSL design that only had one specimen to test. Figure 4.10 shows the top sample that is used for the RUS measurement and the lower sample is the witness specimen. A recess for the second U-Mo sample was added to accommodate both samples. In addition, the second sample was added to create a point where thermocouples in the system may detect the actual sample temperature, not only the temperature of the BUSTER heater or outer capsule. Precise temperature monitoring is critical to understanding the material behavior and knowing precisely the temperature and fission rate the U-Mo is exposed to when a measurement is taken. Therefore, the second U-Mo sample placed below the original location has welded thermocouples attached for more accurate temperature readings taken during the TREAT tests.

Table (4.2) Critical fission rates calculated with the Willard and Schmitt [37] equations used for RUSL power transient design

Temperature (°C)	Critical fission rate (f/cm^{3}s)
250	1.4001×10^8
300	8.49×10^9
350	2.66×10^{11}
400	5.005×10^{12}
450	6.269×10^{13}
500	5.663×10^{14}
550	3.915×10^{15}
600	2.169×10^{16}
650	9.980×10^{16}

RUSL U-Mo Samples are taken from leftover mechanical testing samples from MP-1 experiments. It is assumed these samples have a similar microstructure to those measured and reported by Di Lemma et al. [133]. Almost every sample of MP-1 contained decomposed phase regions, and it is assumed, based on the fabrication methods used for standard monolithic fuels, that the amount of decomposition is approximately 15% by volume as found in a study by Park et al. [48]. Therefore, if the phase reversion occurs during the TREAT irradiation, there should be a detectable change in the elastic modulus of the material if the temperature and fission rate are met based on the theory outlined by Willard and Schmitt [37] and Bleiberg [113] and explained in Table 4.2.

The original size of the samples were "dogbone" shapes usually used for tensile testing. However, the samples are cut using electrical discharge machining (EDM) to match the original RUSL length and width of 23.7 mm x 2.0 mm [55]. The samples are of a thickness of approximately 0.64 mm. Several samples pulled from the leftovers are set aside for out-of-pile measurements and testing for assembly of the entire RUSL system as well. Figure 4.11 illustrates the small cantilever beam sample the RUSL design is based around.

Figure 4.10 is the final iteration of the RUSL holder designed by team of scientists and researchers at the INL. The following neutronic and thermal analysis performed requires these dimensions to design the proper TREAT power transients. Subsequently, this design and the critical fission rate values found above are used to meet the needs of the transient power designs.

4.7.3 MCNP design

Predicting the neutronic and irradiation environment is crucial to designing the transient power profiles necessary for TREAT. Monte Carlo N-Particle Transport Code (MCNP) was used to find the k_{eff} and fission rate per MW of the reactor. From early discussions the reactivity ($\%\Delta k/k$ or ρ) must be kept within $0.05\%\Delta k/k$ of previous ATF-SETH neutron equivalent device (NED) TREAT experiments or further safety analysis is required. Essentially, the experiments need to be neutronically equivalent. But to understand the amount of reactivity inserted in the reactor by the addition of the RUSL experiment, equation 4.34 is used. k_2 is the k_{eff} of the reference

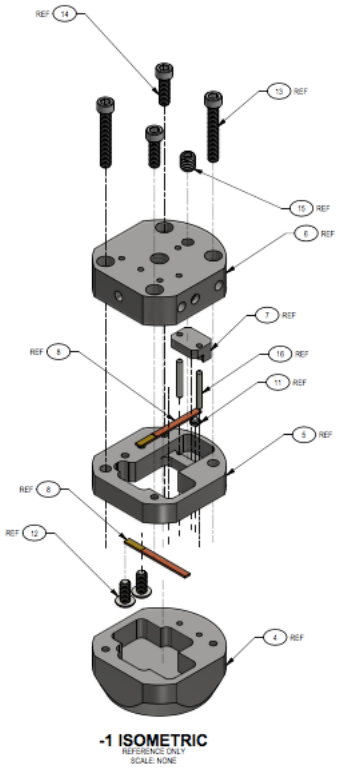

Figure (4.10) Exploded view of the RUSL holder final design. The holder is in three parts that include a clamp to holder the upper cantilever specimen and below this is the lower temperature witness specimen.

NED experiment in TREAT and k_1 is the k_{eff} of the RUSL assembly inserted in the reactor. The k_{eff} value of SETH-NED is 1.00005 [170], assuming the $\%\Delta k/k$ must be less that 0.05% the k_{eff} of the RUSL insertion must not exceed 1.00055.

$$\frac{\%\Delta k}{k} = \frac{k_{eff} - 1}{k_{eff}} \tag{4.33}$$

OR

$$\frac{\%\Delta k}{k} = \frac{k_2 - k_1}{k_1 k_2} \tag{4.34}$$

The second required output of the MCNP analysis is the fission rate tally calculation, referred to as the FM4 tally, used to calculate the constant power coupling factor (PCF). The coupling factor is a constant multiplier value that is used in further thermal analyses based on the power and mass of various elements in the TREAT reactor experiments. This coupling factor is calculated with an F4 multiplier tally that finds the neutron flux per volume in the material. The F4 tally is a particle tracking tally in MCNP used to follow particles as they split or collide with other particles. To determine characteristics like flux or energy deposition, the track length in a volume is used [171]. When a collision occurs, the track calculates the criticality and what occurs during all the events based

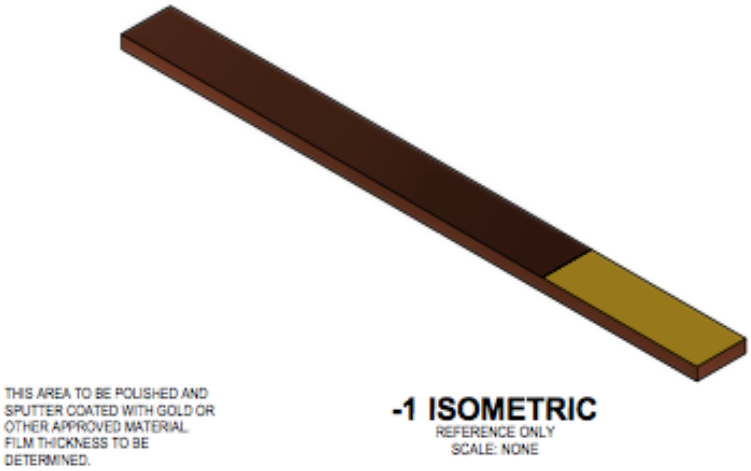

Figure (4.11) One RUSL sample machined from past MP-1 mechanical testing samples. The end is sputter-coated in gold to increase the reflectively.

on the present total cross-sections and probability of an event. F4 tallies describe a "track length estimate of cell flux" or it gives the flux of the desired particle through a material. The multiplier tally is used to convert the regular F4 output to the required fission rate value by multiplying the particles per cm^2 by the atom density and the fission cross-section to normalize the number to particles per volume [171].

Once MCNP completes the analysis of the RUSL design in TREAT the FM4 tally and the $\mathrm{k_{eff}}$ values are retrieved to calculate the PCF. The following equations are used to determine the PCF [172].

$$\mathrm{PCF}\left[\frac{\mathrm{W}}{\mathrm{g-MW_{core}}}\right] = \mathrm{FM4}\left[\frac{\mathrm{f}}{\mathrm{cm^3-sp}}\right] \times \text{source particle}\left[\frac{\text{neutrons}}{\mathrm{s-MW}}\right] \times \nu[\mathrm{cm^3}] \times \mathrm{FCF}\left[\frac{\mathrm{J}}{\mathrm{g-f}}\right] \tag{4.35}$$

$$\mathrm{FCF}\left[\frac{\mathrm{J}}{\mathrm{g-f}}\right] = \frac{\mathrm{Q}\left[\frac{\mathrm{MeV}}{\mathrm{f}}\right] \times \left(\frac{\text{1.602176E–13 J}}{\mathrm{MeV}}\right)}{\mathrm{m[g]} \times \mathrm{k_{eff}}} \tag{4.36}$$

Where Q is the recoverable energy from the fission, m is the mass of the sample, v is the volume of the sample, FCF is the flux conversion factor, and sp is the number of source particles. The source particles are calculated using equations 4.37 and 4.38 where $\bar{\nu}$ is the number of neutrons produced per fission, 2.437 in MCNP.

$$\text{fission reactions}[\frac{\mathrm{f}}{\mathrm{s-MW}}] = \frac{\frac{10^6\mathrm{W}}{\mathrm{MW}} \times \frac{1\mathrm{MeV}}{1.602176\times10^{-13}}}{\mathrm{Q}[\frac{\mathrm{MeV}}{\mathrm{f}}] \times \mathrm{k_{eff}}} \tag{4.37}$$

$$\mathrm{SP}\left[\frac{\mathrm{n}}{\mathrm{s-MW}}\right] = \text{fission reactions} \times \bar{\nu}\left[\frac{\mathrm{n}}{\mathrm{f}}\right] \tag{4.38}$$

4.7.3.1 Early neutronic analysis

The addition of a secondary witness sample in the RUSL holder will increase the amount of fissile material in the reactor environment and therefore increase the reactivity and k_{eff}. To explore the increase in reactivity from the second sample, an MCNP model of the early design was performed. Figure 4.12 shows the RUSL experiment inside the TREAT reactor, and Figure 4.13 is a closer look at the modeled RUSL holder. These early runs of MCNP were performed to understand the starting k_{eff} values to determine design changes required to meet the reactivity limits previously discussed. The sample is placed in the reactor with the control rod positions at 26 inches and ran for the starting RUSL1 temperature of 250°C.

The initial TREAT input deck provided by the INL contained the BUSTER heater and the entire TREAT reactor. After building the RUSL geometry and adding it to the full TREAT model the desired k_{eff} values were obtained.

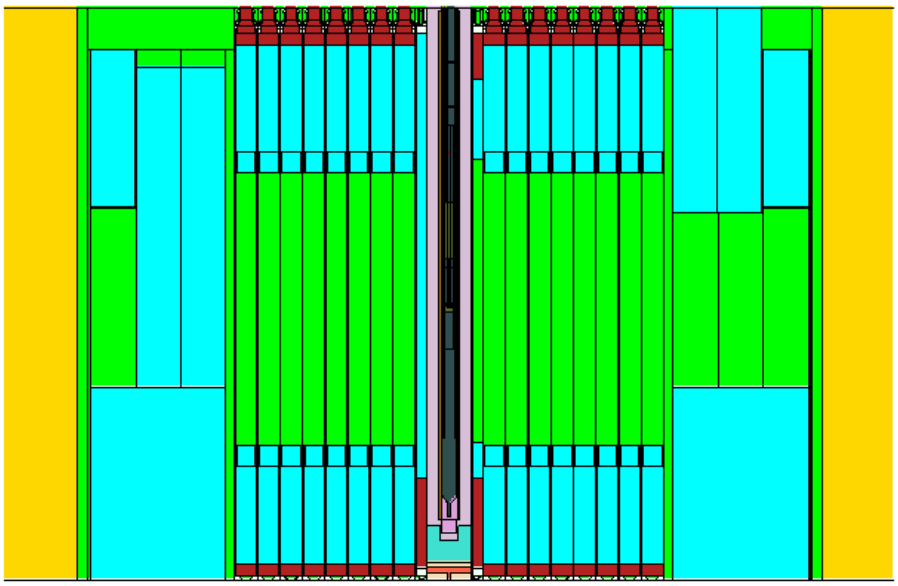

Figure (4.12) Entire TREAT MCNP design with the RUSL holder in the center of the experimental position.

The resulting k_{eff} value and the change in reactivity were 1.00079 and 0.07393%, respectively, determining the amount of reactivity added by the experiment compared to the reference NED value was 0.074%, greater than the required 0.05%. Therefore, an adjustment was required in the assembly design to meet the required design metrics. An idea was proposed to add additional material to the experiment to act as a neutron sync, or "neutron ballast" for the additional reactivity added by the second U-Mo sample. The addition of this device is discussed in the next section in detail. From this point forward, the neutronic analysis was taken over by an analyst at INL as more complex safety calculations must be performed for design review requirements that are outside the scope of this work.

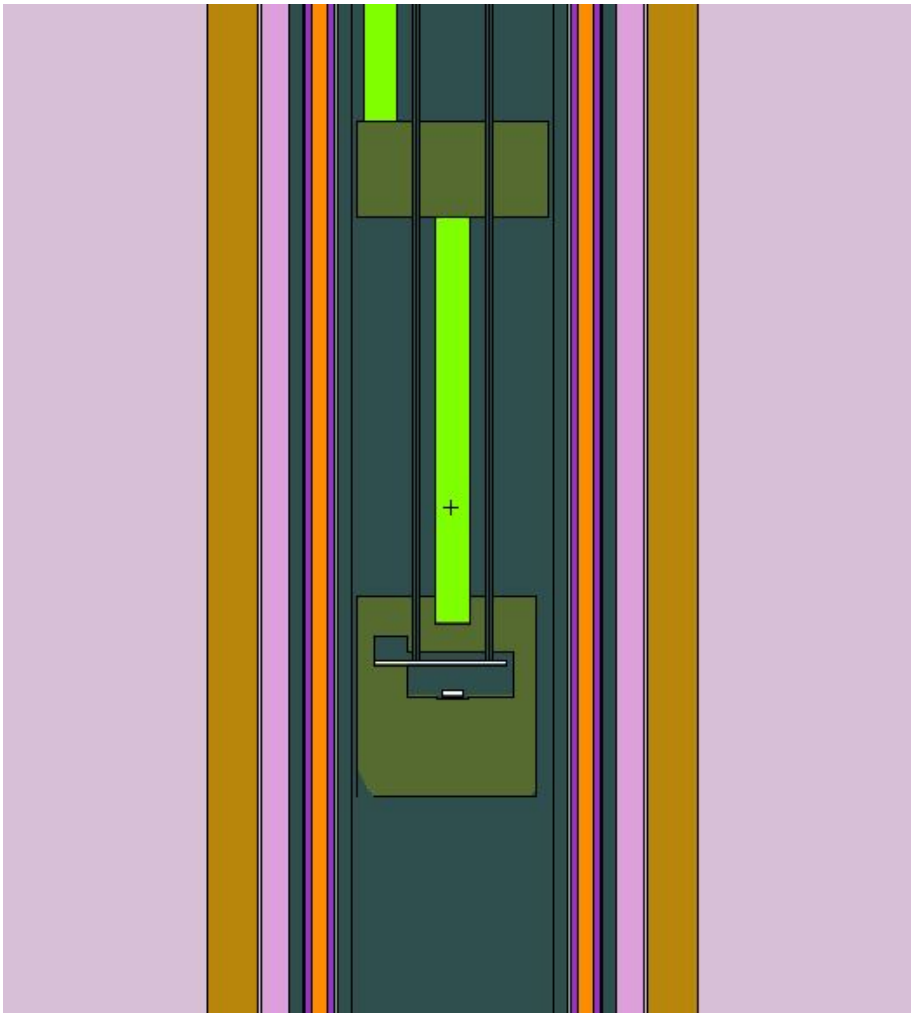

Figure (4.13) Early MCNP model of the RUSL holder inside of TREAT performed to determine the reactivity of the experiment and future design steps.

4.7.3.2 Reactivity adjustments

To achieve the required criticality values, an additional piece of titanium is added to the stainless steel hanger rod holding RUSL. The slug acts as a neutron sync that will absorb some of the additional neutrons created by the U-Mo samples. The ideal size was determined to be about 25 cm long at a diameter of 3.683 cm with two rectangular cuts out of the slug to allow sensor cables to run through the material. The reactivity insertion calculation for this new design was performed and proved to lower the reactivity change to the required 0.05% limit successfully. Shown below in Table 4.3 are the values for the highest and lowest starting temperatures and the associated results.

From these values, the fission rate is calculated based on the thermal analysis. The thermal analysis takes the PCF, models the design, and calculates the temperatures of the samples as well as the required reactor powers. The following section presents the power results determined in the thermal analysis.

Table (4.3) MCNP results from neutronic engineering calculations and analysis report (ECAR) [170]

Temperature (°C)	k_{eff}	Reactivity worth compared to ATF-SETH NED (%Δk/k)	PCF (W/g-MW)	Fission rate/MW
250	1.00047	0.042	7.527	$4.441\,94 \times 10^{12}$
450	1.00045	0.04	7.592	$4.480\,21 \times 10^{12}$

4.7.4 Thermal analysis

Thermal analysis was performed by the INL to ensure all laboratory safety requirements are met. ABAQUS is used to model the experiment with input from the MCNP neutronics calculations. A full explanation of the thermal analysis performed is outside of the scope here and was completed by a thermal analyst at INL.

Results from the analysis given the starting temperatures and required critical fission rates up to 650°C give the final results of the power profile for all three RUSL tests. Each power profile is different due to the amount of energy provided to and absorbed by the U-Mo samples. Vaporization or melting of the samples must be avoided; therefore, the temperatures must stay within the prescribed bounds.

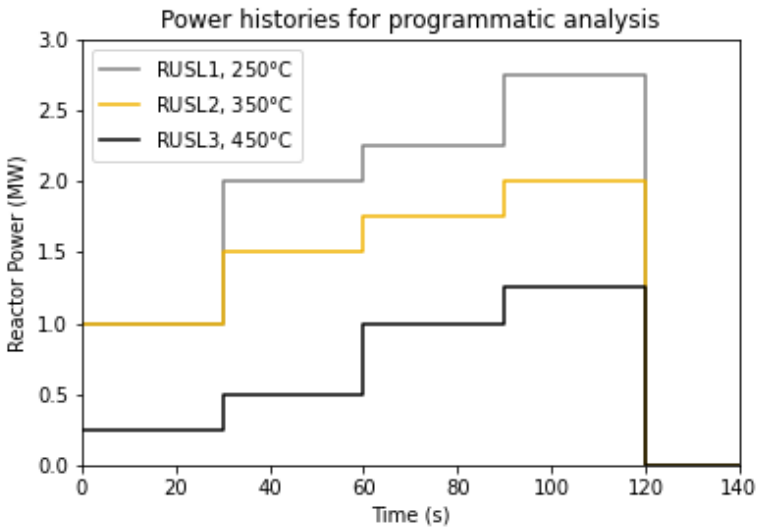

Figure (4.14) Power profile for RUSL for the three experiments

When the PCF calculated using MCNP is multiplied by the mass density of material results in a change of units to per volume, not mass. This value is then multiplied by the reactor power to get the energy generated internally of the piece [173]. The proposed power profiles are shown below in Figure 4.14. Table 4.4 gives the power profiles and the corresponding times of the samples during the modeled transient. For the fiberoptic measurement to be taken accurately, there is a minimum time requirement of 20 seconds.

Table (4.4) Power profiles design for the RUSL transients

Time(s)	Starting temperature (°C)		
	250	350	450
	Reactor power (MW)		
0-29.9	1	1	0.25
30-59.9	2	1.5	0.5
60-89.9	2.25	1.75	1
90-119.9	2.75	2	1.25
120-140	0	0	0

The temperatures of the sample throughout the run increase, as is expected. Figures 4.15 show the shape of the temperature increase in each experiment as well [173]. The temperatures calculated for the two samples are averaged and presented here. To understand the probable fission rate throughout the experiments, the following section uses the temperature, power profile, and fission rate per MW calculations to understand the prevailing fission rate and diffusion methods.

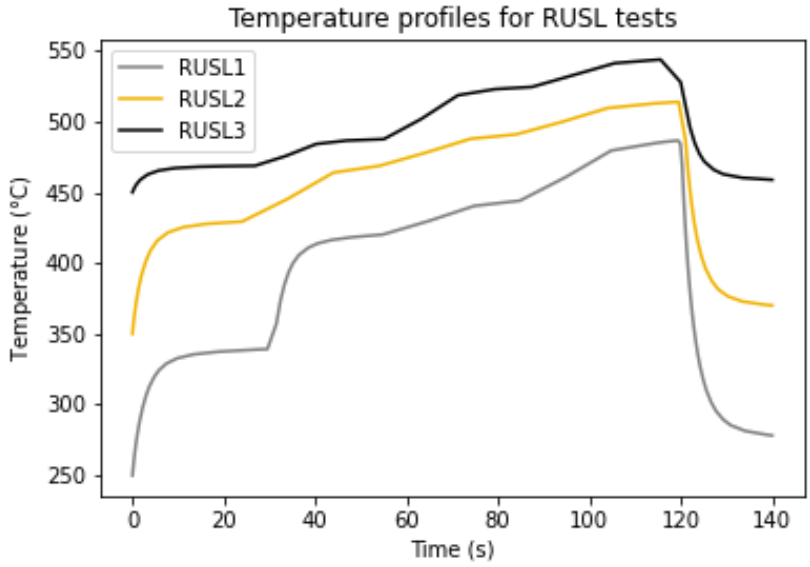

Figure (4.15) Temperature profiles of TREAT transient based on power.

4.8 RUSL analysis results

From all of the above analysis and experimental planning, the expected phase reversion fraction may be calculated to give an estimation of when changes in the RUSL measurements should be observed. This section will first calculate the fission rate throughout each experiment based on the power profiles, temperature, and fission rate per MW core power to find the fission rate. To understand if the actual fission rate will align with the critical fission rate, the two are plotted and indicate if the kinetics from the radiation will dominate the phase changes or thermal

effects. After calculating the fission rate, diffusion values are calculated and compared to more fully understand the drivers of changes in the material. Lastly, the total diffusion values are included in the dissolution calculations to estimate the possible volume change of the decomposed phases throughout the TREAT runs.

4.8.1 Critical fission rate results

Using the Willard and Schmitt [37] and the Beeler et al. [168] methods for calculating a critical fission rate for uranium and molybdenum, a comparison between the actual fission rate and the critical fission rates are given in Figure 4.16. In the first experiment, RUSL1 (Figure 4.16a) the starting temperature is 250°C and the fission rate for the transient, the yellow line, is above the required critical fission rate values for both methods. However, when the samples reach about 325°C for the uranium Beeler values the critical fission rate is above the TREAT fission rate. From the historic Willard values, the critical fission rate is dominant for phase reversion until about 400°C. The highest temperature with the dominant phase reversion fission rate is for the Beeler et al. molybdenum fission rate, up to 450°C. Above this temperature, the fission rate is not high enough in the specimen to expect the radiation enhanced diffusion alone to encourage the γ phase reversion.

In Figure 4.16b, the uranium critical fission rate is higher than the experimental fission rate at all points. In contrast, the Willard and molybdenum values are lower at temperatures of 400°C and 425°C, respectively. For RUSL3, the critical fission rate is above all of the experimental fission rates. Due to the higher temperatures and no cooling ability in the RUSL holder, the power must be kept lower in these tests and does not allow for the achievement of the critical fission rate required by the samples. In RUSL2, the starting fission rate is above the Willard critical fission rate as designed by the early experiment planning.

4.8.2 Diffusion results

The total diffusion from equations 4.24 to 4.27 are plotted in Figure 4.17. At each RUSL experiment, the dominant diffusion species is uranium and is expected to be the driving force of diffusion-related mechanisms in the material of each RUSL test. This observation is especially prevalent in Figure 4.17c where the higher overall temperatures increase the difference between the diffusion of the two species due to the higher values of thermal diffusion in the uranium compared to molybdenum.

To determine the dominant type of diffusion for each experiment, the intrinsic, RED, and radiation driven mechanisms are calculated and shown in Figure 4.5a for uranium. At a constant fission rate of 5×10^{20} f/m^{3}s the irradiation driven diffusion is dominant below 377°C. Between the 273 and 377°C, the RED is dominant. This type of plot and analysis is added with the temperature and fission rate profiles designed for all three RUSL tests for uranium, molybdenum, and the total to understand what form of diffusion is dominant at what points in the experiment.

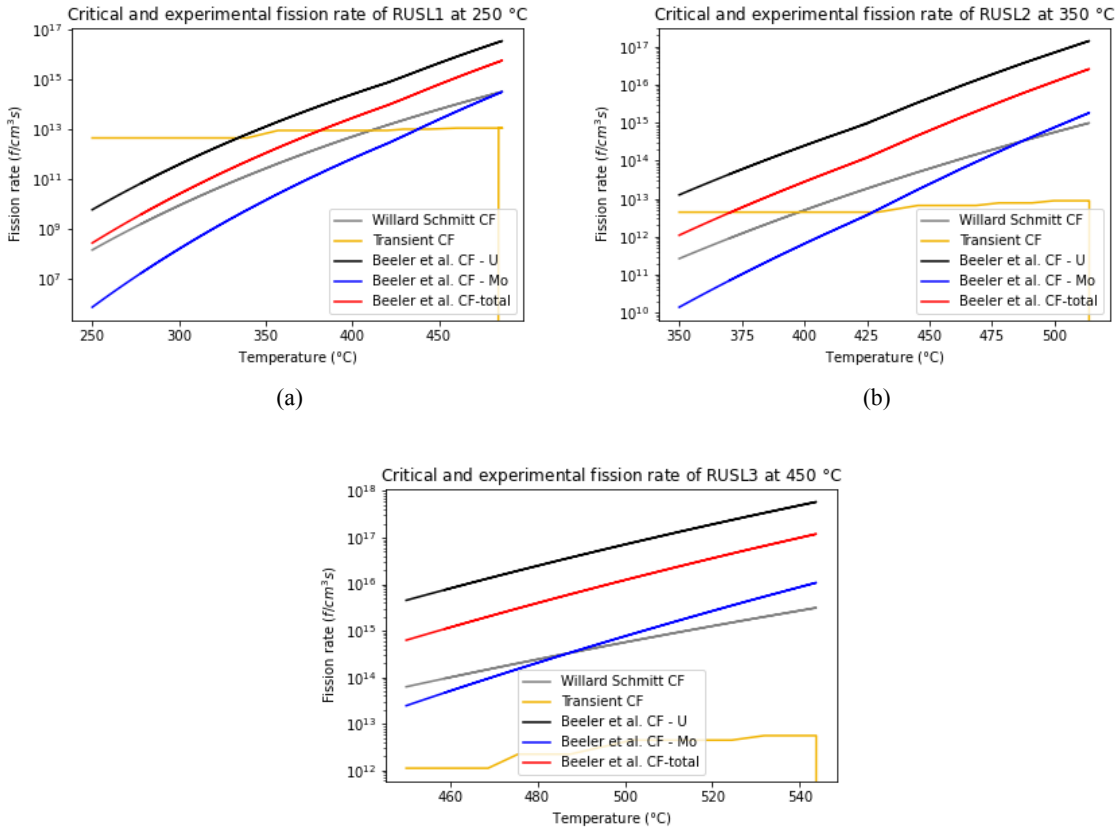

Figure (4.16) Experimental fission rates based on power and temperature designed for the RUSL experiment (yellow line) compared to the Beeler et al. and Willard and Schmitt critical fission rates (black, grey, blue lines) showing where the fission rate is high enough for phase reversion to occur during the irradiation.

All three types of diffusion in Figure 4.18 show which is the primary mechanism for diffusion at each step. The point of this diagram is to compare the U, Mo, and combined diffusion of the specifies to determine which of the diffusion-based mechanisms are dominant and where to expect possible phase reversion to occur based on these values. At the lower temperatures in RUSL1, the RED is the most impactful type of diffusion, but as the temperature increases, thermal diffusion will become the dominant form. In this test for the molybdenum diffusion, the RED is higher than the others for the most extended temperature range. In RUSL2 and 3, the thermal diffusion is dominant for most of the tests except at lower temperatures in the molybdenum diffusion. This is because the higher required power will also increase the testing temperature. However, the thermal kinetics of the phase change in U-Mo is notoriously sluggish. Therefore, if a change is detected in the elastic modulus, it may be due to the increased kinetics from the irradiation rather than the temperature increase over a short amount of time.

The RED coefficients are the highest at the lower temperatures or the RUSL1 experiment power profiles. RED diffusion of molybdenum is dominant to much higher temperatures compared to the uranium values for all three

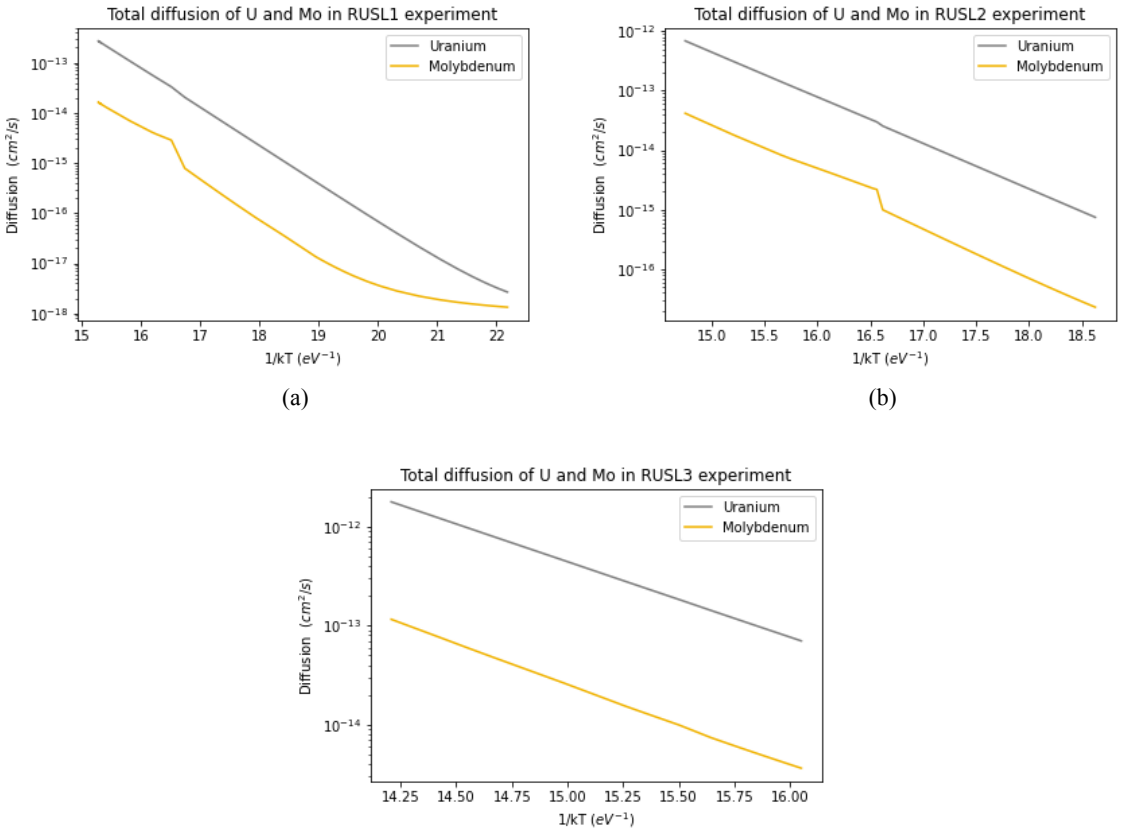

Figure (4.17) Comparison of the total diffusion of uranium and molybdenum based on the RUSL power transients and temperatures starting at a) 250°C, b) 350°C, and c) 450°C.

tests. In RUSL2, the RED coefficient is barely dominant at the lower temperatures, and it is never dominant in the RUSL3 tests. Therefore, in the RUSL3 tests, the thermal diffusion is the theoretical driver of any phase change or elastic modulus changes observed. This is the critical fission rates used to find the power profiles based on the Willard critical fission rate values and diffusion. The newer critical fission rates are higher and may not align with the previously calculated expectations.

4.8.3 Phase reversion fraction results

After the diffusion and experimental fission rates are calculated, the volume fraction of the phase reversion may be calculated using the methods from section 4.4. If the starting volume fraction of the decomposed regions is similar to those measured by Park et al. [48], it will begin at about 15% decomposed, lamellar $\alpha + \gamma'$ phase [48]. Therefore, only 15% of the material is able to transform to the γ phase. According to Newell et al. [56] at 823 K after 36 hours, this amount of reversion occurs isothermally. These results are consistent with experimental results

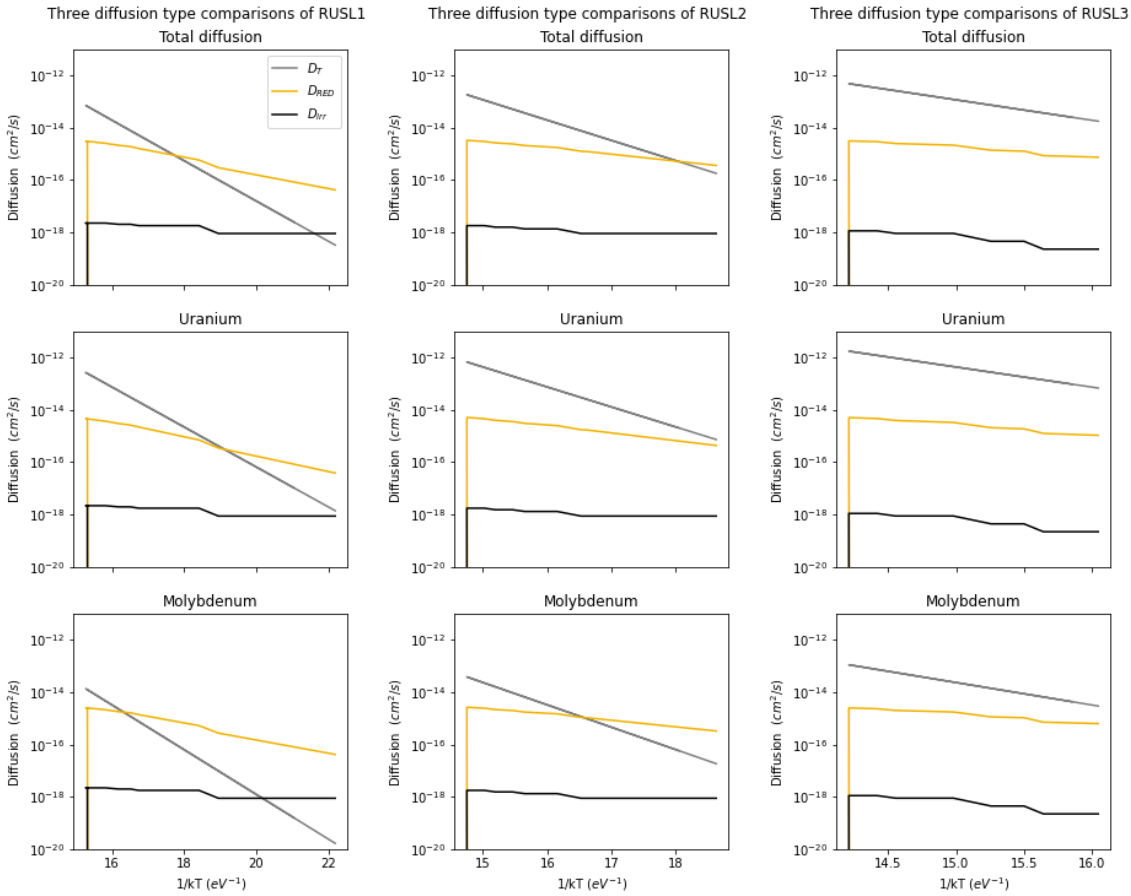

(a) (b) (c)

Figure (4.18) Three diffusion types calculated for uranium, molybdenum, and the total for U-10wt% Mo in RUSL starting at 250, 350, and 450°C. The top line at each temperature and fission density indicate the dominant form of diffusion at that moment.

included in the same study. Combining the dissolution calculation results from Zuo et al. [59] and the temperature-based JMAK method and averaging the two to get a final phase transformation fraction allows the calculation of only isothermal processes, however. This is limiting in that an irradiation experiment does not occur isothermally; even with a constant fission rate, the specimen will increase in temperature as discussed in Section 4.7.1. To mitigate the changing temperature and fission rate, each time step of the experiment is treated as an isothermal event when calculating the volume transformation. In other words, at time zero, the temperature of RUSL1 is 250 °C and constant for 0.0001 seconds. Therefore, the calculated phase transformation fraction results if found from that starting temperature, time duration, and fission rate-dependent diffusion. The next time step is calculated in the same manner using the next temperature and time step and the previously calcualted volume fraction is used as the starting phase volume fraction for this second step. In other words, the change in the starting radius at each time step, R is equal to R_O at the following step needed to calculate the R_S value. The starting decomposed phase is

estimated to be approximately 1 μm. Therefore, volume fraction change is assumed to be additive and is displayed thus in the following plots of the fraction of $\alpha + \gamma'$ transformation using the Newell calculation methods and the RUSL transient design.

As for a fraction of the secondary phase transformation, if the starting phase radius is 1 μm, almost all of the $\alpha + \gamma'$ phase is transformed when only considering the dissolution. Effects due to the JMAK proposed kinetics are much lower due to the brief periods of each section. Therefore, the contribution of this has almost no effect on the phase transformation. From the average of the JMAK and dissolution kinetics Figure 4.19a, 4.19b, and 4.19c for RUSL1, 2 and 3 about 18%, 30%, and 42% of the phase transformation fraction is completed, respectively. The differences in the amount of the decomposed fraction is due to the higher temperatures in the RUSL2 and 3 experiments. The diffusion equation used in the dissolution methods includes thermal as well as radiation affected diffusion. Therefore, at the end of each RUSL test, the volume of the decomposed phase should be partially reverted to the γ phase, and the overall all elastic modulus measurement should decrease during the TREAT irradiation.

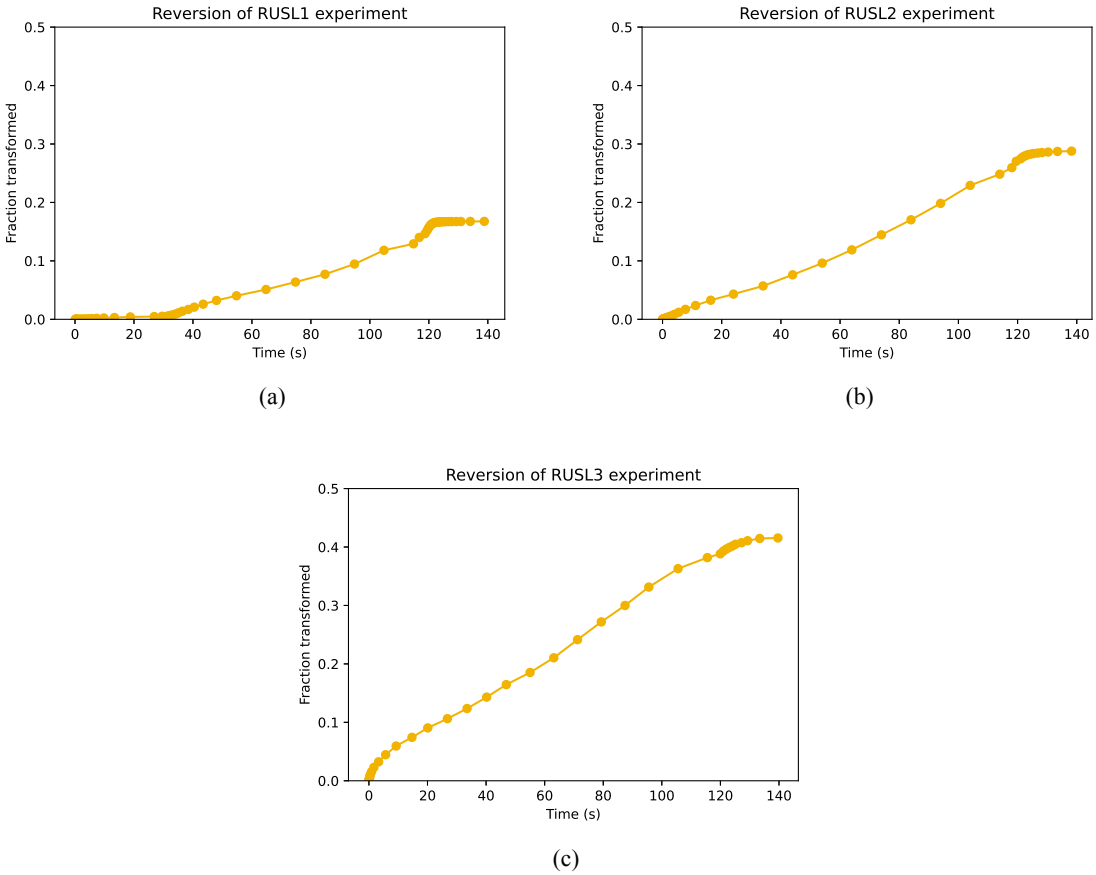

Figure (4.19) Transformation fraction of the decomposed $\alpha+\gamma'$ phase for RUSL1 experiment assuming a starting volume of 15% decomposed phase and a particle size radius of 1μm from the averaged JMAK and dissolution approximation.

The JMAK values are low compared to the dissolution transformation. Therefore, the dissolution calculation is the primary driver of phase reversion it is assumed the phase reversion is primarily dependent on the diffusion coefficients in the dissolution calculations, not only the dependence on time and temperature that is true in the JMAK method. This is important because the resulting temperature and fission rate conditions should theoretically be powerful enough for the phase reversion to occur where temperature effects are insufficient. The time scale of the experiment is so short it is possible the nucleation and growth mechanisms may not have enough time to occur. Therefore, Figure 4.20 shows the volume fraction changes if only the dissolution is controlling the phase reversion of the decomposed phase. The decomposed volume fraction change is almost 80% in RUSL therefore, there may be a higher amount of phase reversion if there is little to no growth or nucleation. This must be confirmed experimentally with RUSL.

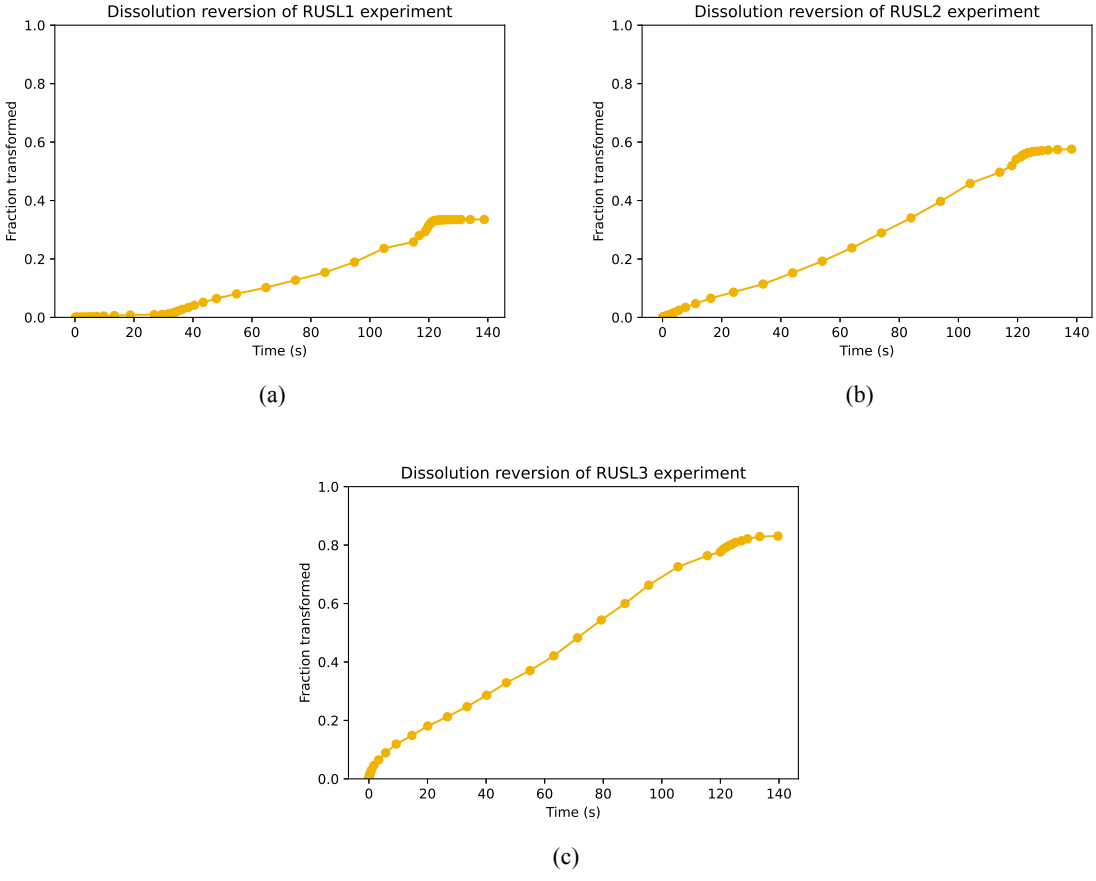

Figure (4.20) Transformation fraction of the decomposed $\alpha+\gamma'$ phase for RUSL1 experiment assuming a starting volume of 15% decomposed phase and a particle size radius of $1\mu m$ from only the dissolution equation.

4.9 Expected TREAT results

Based on the critical fission rate methods of determining the phase reversion possibilities based on the radiation enhanced diffusion, there is a chance a phase reversal may be detected by the increase in elastic stiffness tensor measurements from RUSL. The Young's modulus of the γ U-Mo is lower than the α uranium [12]. Therefore, if the decomposed regions are reverting back to the γ phase the average elastic modulus of the material should be lower.

Based on the total diffusion of the combined uranium and molybdenum the phase transformation is expected to transform approximately half of the decomposed phase present to the cubic phase. This is significant because for the RUSL ultrasonic measurements to detect a change in microstructure there needs to be an anticipated change to the phases present in the material. The actual decomposed volume fraction of the MP-1 samples is not known at this time therefore it is assumed to be similar to other samples of U-Mo fabricated under similar methods [48]. Additionally, the phase transformation increases rapidly after about 70 seconds in each designed experiment. A change in frequency and elastic modulus can then be expected near this time and power.

4.9.1 Experiment limitations

One concern of this experiment is low material damage incurred by the U-Mo samples and the sluggish kinetics of U-Mo. In order to achieve the required critical fission rates, the transient was short, or the samples will quickly overheat. Therefore, the highest amount of power is added to the samples while still keeping it under the maximum 650˚C. From the calculations of critical fission rate, diffusion, and volume fraction transformed, some phase change occurs even at the low damage rates.

The goal of this fueled RUSL experiment is also to test if the RUSL elastic modulus measurement technique will work for a fueled test. Even if the tests are unsuccessful and no change is detected, it will show the method can measure the material properties of a fueled sample and what other factors may be improved upon in future testing, such as the design of a method for cooling the sample.

Chapter 5: Future work

For the included data collection methods and the RUSL measurement techniques, several vital assumptions were made that future study and work may address. Most assumptions included in the work simplify the early designs and test the current theory on phase change reversion for U-Mo fuels. In this chapter, these assumptions are outlined, and future work to address these are explored along with improvements to the ongoing data collection and phase reversion research necessary for qualifying metallic U-Mo fuels for real world applications.

5.1 Data collection method improvements

The current method of collecting data for computational research on U-Mo fuels is time-consuming and ineffective on a large scale. Data available in publications and reports is essential to quantify and disseminate to the computational community; however, communicating data in real-time, collected experimentally, is a much more effective method for transmitting data between groups. This work collected data for microstructure models; however, it only includes data from three experimental campaigns. More data exists collected by independent studies and not as a part of these large fuel campaigns. Firstly, the data requirements must be communicated to all parties involved in this type of research. That is what the purpose of this work has accomplished. However, collecting the data becomes the next challenge once the data needs are expressed and known to the community. Additionally, fission density or fission rate are assumed to be the primary variable that impacts the microstructure changes in the fuel. For example, the ANCOVA performed in Chapter 3 only considers the samples and the fission density of the AFIP6-MkII and RERTR-12 FGB data. However, a complete picture of the fuel behavior would be made possible by collecting accurate temperature profiles of the plates and the starting microstructure. All of the fuel microstructure and treatments the materials undergo can impact the other microstructural evolution throughout fabrication and irradiation. Therefore, the data collected must include temperature, fission conditions, and the starting microstructure to qualify the materials' behavior.

Currently, the team of computational scientists that developed the MM data requirements is working with experimentalists to understand ongoing work that fits under the umbrella of the MM requirements and to get involved with planning future work and understand where overlapping work exists between the two groups. A library of the data collected as a part of this work was provided to the group and will be updated and maintained as more data becomes available. As the quantity of data increases, data collection may also become more specific. For example, the exact location where measurements are taken may be collected and added to the library to connect fission conditions, temperature, and microstructure types. Specifically, "mapping" fuel plates with these three variables before and after irradiation will allow for the direct comparison of the samples before and after irradiation and allows for comparing different locations across the plate. Mapping means defining a coordinate system across the

fuel plate and associating the different variables to the corresponding coordinate on the plate. By doing this, the data collected at each location is then associated with the current microstructure and the fission and temperature conditions existing there. If possible, it would be valuable to continue this work but incorporate the microstructure data measurements taken with the corresponding coordinates on the plate itself to map this information overtop of the temperature and fission density. Much like the mapping of geographic information, this would allow for thorough statistical analysis of the variables and the exploration of connections between the behaviors observed across individual plates and between experiments.

The current method for providing the microstructure data to computational scientists must be made more transparent and reproducible. During the planning of experimental work, the inclusion of the computational data is pivotal to improving model creation and validation. Conversely, the opposite of this is also true. Therefore, experimental researchers must convey how computational methods will improve their work. This is true for not only U-Mo fuels, but the method may be applied to other nuclear materials as well. An feedback loop of data creation and sharing allows for faster and more reliable experimental and computational research for the eventual qualification of U-Mo fuels for the application in research reactors like ATR and HFIR.

5.2 Experimental design changes

5.2.1 Fission rate dependency of RUSL

The most crucial assumption made while designing and planning the LEU-RUSL test is that the phase reversion in the U-Mo microstructure is entirely dependent on the fission rate driven diffusion of species throughout the material. Based on the work by Willard and Schmitt [37] and Bleiberg [113, 153], the relationship between fission rate and the diffusion is proportional, and the experimental evidence showed agreement between these two factors in determining the final phases present in the U-Mo samples. Thus, based on this experimental proof, it is a valid assumption to make. However, no other studies were found that tested this theory experimentally in a reactor environment. Therefore, creating an experiment to explore the relationship between material damage and phase reversion is prudent in future studies. The displacements per atom (DPA) of the experiment is calculated and related to the interstitial and vacancy concentrations in the material. From these values, the comparison can be made of the critical fission rate and the amount of material damage present in U-Mo to determine which value is more telling of the phase reversion and material kinetics.

Additionally, using the fission rate, temperature, and diffusion as the basis for the phase reversion prediction does not include a critical variable, time. Therefore, this method does not predict how long the phase reversion may take or when it is expected to occur during the RUSL irradiations. For this first fueled RUSL test, the theory of the critical fission rate is the primary focus. In other words, is the relationship between the critical fission rate and the

phase change reliable, and does it occur quickly? Or does the phase reversion rely on the time it is irradiated as well? Future experiments need to measure the possible time for phase reversion to start or complete. This may be done in similar RUSL experiments at lower temperatures and longer irradiations. Longer irradiations in the RUSL capsule, however, require more complex heating and cooling system for these tests to prevent overheating of the sample and to keep the temperature and critical fission rates lower than what was done here.

5.2.2 Phase reversion volume fraction estimations

While calculating the expected volume fraction change in the MP-1 samples, several important assumptions were made; the controlling factor of the phase change are 50% nucleation and growth and 50% dissolution, and the samples are 15% decomposed at the start. The decomposition amount aligns well with experiments from U-Mo samples by Park et al. [48] and AFIP6-MkII and RERTR samples [47, 49]. However, one goal of this research is to understand the temperature and irradiation conditions in which the U-Mo phase reversion occurs and the entirety of the fuel is in the cubic γ phase. If these conditions are quantified, then reactor conditions may be designed to maintain that isotropic, ideal phase. Therefore, the starting decomposition of the fuel is no longer important if the decomposed phases may be removed in the reactor before negative effects occur from the $\alpha + \gamma'$ phase. Suppose this proves accurate, and the in-pile γ phase creation is possible. In that case, it is useful to perform the volume transformation calculations for samples with higher decomposition to predict the possibility and required conditions for the phase reversion of a completely decomposed fuel structure. Testing of this theory in a similar RUSL experiment would also be useful for future work.

Now, in addressing the assumption that half of the reversion occurs from phase nucleation and the other half from the dissolution of the decomposed phases into the fuel matrix, studies by Newell et al. [56] support this assumption experimentally. Their work predicted the thermally induced phase reversion with these two assumptions and was corroborated by the experimental results. JMAK equation is a probability-based method for calculation of the nucleation and growth of particles in a material, and the dissolution equation accounts for physical phenomena from the material diffusion [58, 59]. However, the calculations in Chapter 4 deviated from the Newell work in that the volume fraction change calculation was iterative. The JMAK and dissolution methods [58, 59] assume the system is isothermal, the temperature is constant. Therefore, at each temperature and time designed for the TREAT transient, the phase volume fraction was calculated and used as the next beginning phase volume in the following temperature and fission rate. Confirmation of this method requires additional RUSL testing and PIE work to confirm the volume fraction before and after the irradiation using XRD or SEM techniques to measure the phases present. Further PIE analysis is necessary to measure the success of the RUSL technique and to determine if any other underlying microstructure changes are impacting the measured elastic modulus.

5.3 Experimental work

5.3.1 RUSL cooling system

One of the most limiting factors of the current RUSL design and experiment is the lack of a cooling system. As a result, temperature and fission rates are limited by the safety temperatures of the system and the exponentially increasing temperature of the fuel as the irradiation time increases. If future experiments added a cooling system to the BUSTER capsule to keep the samples at a constant, lower temperature, more steady fission rates and powers would be usable. In addition, this allows for better testing of the connection between fission rate, temperature, and phase reversion. A cooling system would also be usable by other testing apparatuses in TREAT. Cooling RUSL may be done by creating a type of natural convection device inside of BUSTER that pushes cooler air over the RUSL capsule. A fan or cooling device may be bulkier and less desirable to add to the system as space is limited inside TREAT. However, using natural convection or a small helical heat exchanger may allow for the proper space in TREAT while maintaining the RUSL experiment at lower temperatures while keeping the fission rate of the irradiation at a steady level. This device also allows for the time-dependent testing of the phase reversion proposed in the previous section.

5.3.2 Elastic modulus and present phases

Due to the different elastic modulus of the various phases of U-Mo, it is assumed that any changes detected in the vibrational frequency in RUSL are results of the phase change. However, there is a possibility that other microstructure changes may influence the change in frequency. The reason to assume the phase change is detected before other microstructures is the required fission rate or time needed for things such as FGB to form during irradiation. Therefore, it is assuming the phase reversion occurs before other fuel behaviors. This is another example where PIE would allow for the comparison of the microstructure and RUSL results. PIE would illuminate any other existing microstructures that may be affecting the RUSL measurement before the phase reversion is detected.

5.3.3 Electrical resistivity measurements

The last assumption to consider is that the changes in vibrational frequency, consequently the elastic modulus, are optimal for measuring the phase changes during irradiation. RUSL proved to be an effective method of detecting recrystallization in copper during a TREAT irradiation and phase changes in uranium-zirconium (U-Zr) fuels in a furnace [51, 174]. It, therefore, is expected it can accurately measure the phase reversion of a U-Mo sample during a TREAT transient. However, other methods for measuring the phase change in a material without time-consuming XRD and microscopy methods exist.

As mentioned in Chapter 4 resistivity has been used in the past to measure the present phases of U-Mo fuels. Another method for measuring the in-pile changes of the U-Mo phases is to detect changes in the electrical current across a sample of the fuel during irradiation. The benefit of this measurement technique over the RUS method is that the actual measurement setup is less sensitive to minor changes and can be more easily assembled. For example, the fiberoptics of the current method accurately measure changes in the material and are very sensitive but susceptible to being disrupted by slight movements of the fiberoptic laser, making it difficult to assemble and move without disturbing the sensors. Additionally, the current RUSL holder design relies on tiny specimen sizes. The use of resistivity may also allow for larger U-Mo samples to measure any phase activity. Using an additional method of phase reversion measurement allows for comparisons between the methods to determine accuracy and ease of use. Therefore, the determination of the best measurement technique would improve upon the current methods and improve the data collected for understand phase reversion in the U-Mo fuels, which will improve the data collected for microstructure modeling and the improvement of computational methods as well as experimental capabilities of TREAT.

5.4 Summary of future work

Future experiments must not only focus on understanding the kinetics of phase reversion in relation to fission rate and temperature, they must also consider the benefits of the data to computational work. Within the currently available microstructure data is compiled and analyzed to give a starting place for the modeling and simulation data collection. The connections between all the microstructure types are qualitatively understood, however a lack of quantitative connections are available in the literature or past experiments. A more intentional data collection approach is needed that incorporates the computational needs with the experimental planning and results. Having the two groups of researchers work more closely together will increase the speed and effectiveness of both focus areas.

Chapter 6: Conclusions

6.1 Computational requirements

This research began by comparing the as-fabricated and PIE microstructure of monolithic AFIP6-MkII and RERTR-12 fuels. From the data collected, analyzed, and presented in Chapter 3 it is clear that there is a relationship between the various microstructures, particularly the FGB, and the fission density the fuel undergoes. However, complex relationships cannot be drawn from the analysis for use in computational models without further information. The purpose of developing more detailed models and predictable relationships between the microstructure, temperature, and irradiation conditions is to collect microstructure data of U-Mo fuels to improve the computational methods. Therefore, the work performed in Chapter 2 increases the understanding of the fuel behavior and collects data for these models in collaboration with the computational researchers. Modeling material properties saves time and money on costly experiments. Access to irradiation facilities that provide necessary neutrons or ions for testing is difficult to come by as well. Therefore, modeling makes these complicated experiments unnecessary and quickens the pace of fuel qualification efforts compared to past experiences. However, for this to become a reality, data used in predictive models must become more reliable and available.

From the included literature review, it is clear there is a lack of microstructure data needed to meet the MM requirements. The missing data areas include the starting microstructure, quantifiable information on the decomposition, carbide volume fraction, and chemical homogeneity. By using the included information as a starting point, the gaps in microstructure data are highlighted and explained so future characterization and PIE work may be performed, keeping in mind these missing computational data.

6.2 RUSL experiment overview

Next, the idea of measuring phase reversion in U-Mo was explored to understand an aspect of the fuel microstructure in more detail and assist in the MM data collection. Using the RUSL method, the vibrational frequency of a U-Mo sample beam is measured by exciting it with a laser and using optical fibers to measure the change in vibration using copper. Phase reversion, or the transformation of the decomposed phase to the γ phase, occurs in U-Mo and other fuel types during irradiation. The elastic constants will change as the crystallographic phase changes in the material. Therefore the measurements of the vibrations will indicate if a phase change occurred during the test. The RUSL work looked to be a proof of concept in using the RUSL technique on a fueled sample, as well as to measure the phase reversion in U-Mo experienced during irradiation. The experimental design for the irradiation in TREAT was performed with the assistance of thermal and neutronic analysts at the INL. Additionally, a novel approach of predicting the volume fraction reversion was employed to understand the possible behavior of

LEU, U-Mo in-pile.

Updating the critical fission rate calculations with the combined radiation driven diffusion and RED values allows for a more modern look at the critical fission rate. Perhaps the diffusion values determined by Beeler et al. [168] better represent the diffusion of uranium and molybdenum through the fuel but may not accurately represent the diffusion needed to predict the phase reversion of the $\gamma + \alpha'$ during irradiation. Based on the data from [37] the Beeler based critical fission rate will overestimate the phase reversion critical fission rate. The results from the RUSL test will determine which method is more accurate and if the phase reversion can be predicted using only the temperature and fission rate. Additionally, combining the radiation caused diffusion values with the combined JMAK and dissolution based phase reversion calculations give new estimations of the possible phase reversion in U-Mo, MP-1 samples. Previous work by Newell et al. [56] accurately predicted the phase reversion in an isothermal experiment system for the U-10 wt%Mo, but this is the first time the updated U-Mo diffusion calculations are used to determine the possible phase reversion in an irradiation environment.

Based on the proposed methods of designing the RUSL experiment and analyses, changes to the MP-1 samples are expected to occur early on during the TREAT power transient. Assuming the decomposed volume of the material is approximately 15% [48], between 15% and 40% of the decomposed regions will revert to the γ phase. Kinetics of particle dissolution and nucleation and growth mechanisms will produce the reverted γ phase from the existing decomposed regions based on the temperature and fission rates planned for the experiment. This novel approach to detecting the elastic modulus changes in a material can be applied to many other nuclear materials and inform computational modeling and simulating fuel behavior for future model and experiment development. Additionally, this is the first time the RUSL device is used with a fueled specimen. By proving the usefulness of RUSL with a nuclear fuel type will allow for further experiments with other types of nuclear fuels and materials.

6.3 Summary of work

From the included work, there is a need and ability to measure the phase change in U-Mo to understand irradiation caused changes in the material. However, as the qualification of this fuel type continues, the computational research requires much more data and experimental support to improve and advance the models. Designing the RUSL experiment with this in mind allows for the collection of the elastic modulus measurements in-situ and tests the hypothesis of the critical fission rates controlling the phase reversion. The final transient irradiations in TREAT will confirm the existence of this critical fission rate as well as test a novel approach to measuring changes to the material during irradiation.

References

[1] D. Wachs, “Reactor conversion,” *Nuclear Engineering International*, Mar. 2010. [Online]. Available: https://www.neimagazine.com/features/featurereactor-conversion

[2] M. Meyer, J. Gan, J. Jue, D. Keiser, E. Perez, A. Robinson, D. Wachs, N. Woolstenhulme, G. Hofman, and Y. Kim, “Irradiation Performance of U-Mo Monolithic Fuel,” *Nuclear Engineering and Technology*, vol. 46, no. 2, pp. 169–182, Apr. 2014. [Online]. Available: https://www.sciencedirect.com/science/article/pii/S1738573315301613

[3] A. Yacout, “Energy Engineering and Systems Analysis Fuel Type: Nuclear Fuel,” 2011. [Online]. Available: www.anl.gov

[4] “Reduced Enrichment for Research and Test Reactors (RERTR),” 2020. [Online]. Available: https://www.rertr.anl.gov/

[5] J. L. Snelgrove, G. L. Hofman, M. K. Meyer, C. L. Trybus, and T. C. Wiencek, “Development of very-high-density low-enriched-uranium fuels,” *Nuclear Engineering and Design*, vol. 178, no. 1, pp. 119–126, Dec. 1997. [Online]. Available: https://linkinghub.elsevier.com/retrieve/pii/S0029549397002173

[6] Y. S. Kim, “3.14 - Uranium Intermetallic Fuels (U–Al, U–Si, U–Mo),” in *Comprehensive Nuclear Materials*. Elsevier, Jan. 2012, pp. 391–422. [Online]. Available: https://www.sciencedirect.com/science/article/pii/B9780080560335001129

[7] T. Wiencek, “Summary report on fuel development and miniplate fabrication for the RERTR Program, 1978 to 1990,” Argonne National Laboratory (ANL), Argonne, IL, Tech. Rep. ANL/RERTR/TM-15, Aug. 1995. [Online]. Available: http://www.osti.gov/servlets/purl/125105-FYIHHn/webviewable/

[8] D. D. Keiser, J.-F. Jue, B. Miller, J. Gan, A. Robinson, P. Medvedev, J. Madden, D. Wachs, C. Clark, and M. Meyer, “Microstructural Characterization of the U-9.1Mo Fuel/AA6061 Cladding Interface in Friction-Bonded Monolithic Fuel Plates Irradiated in the RERTR-6 Experiment,” *Metallurgical and Materials Transactions E*, vol. 2, no. 3, pp. 173–189, Sep. 2015. [Online]. Available: http://link.springer.com/10.1007/s40553-015-0055-8

[9] D. D. Keiser, S. L. Hayes, M. K. Meyer, and C. R. Clark, “High-density, low-enriched uranium fuel for nuclear research reactors,” *JOM*, vol. 55, no. 9, pp. 55–58, Sep. 2003. [Online]. Available: https://link.springer.com/article/10.1007/s11837-003-0031-0

[10] G. Hofman, L. Walters, and T. Bauer, “Metallic fast reactor fuels,” *Progress in Nuclear Energy*, vol. 31, no. 1-2, pp. 83–110, Jan. 1997. [Online]. Available: https://linkinghub.elsevier.com/retrieve/pii/0149197096000054

[11] P. Lemoine and D. Wachs, “High Density Fuel Development for Research Reactors,” in *Global 2007-Advanced Nuclear Fuel Cycles and Systems High density fuel development for Research Reactors*. Idaho National Laboratory, Sep. 2007.

[12] G. Beghi, “Gamma Phase Uranium-Molybdenum Fuel Alloys,” European Atomic Energy Community, Tech. Rep. EUR 4053 e, 1968. [Online]. Available: http://aei.pitt.edu/91386/1/4053.pdf

[13] K. Reeve, “Ceramics as nuclear reactor fuels,” *Ceramurgia International*, vol. 1, no. 2, pp. 59–71, Sep. 1975. [Online]. Available: https://linkinghub.elsevier.com/retrieve/pii/0390551975900083

[14] R. Prabhakaran, “U-Mo Monolithic Fuel for Nuclear Research and Test Reactors,” *JOM*, vol. 69, no. 12, pp. 2529–2531, Dec. 2017. [Online]. Available: http://link.springer.com/10.1007/s11837-017-2612-3

[15] J. Rest, Y. S. Kim, G. L. Hofman, M. K. Meyer, and S. L. Hayes, “U-Mo fuels handbook. Version 1.0,” Argonne National Laboratory (ANL), Argonne, IL (United States), Tech. Rep. ANL-09/31, June 2006. [Online]. Available: http://www.osti.gov/servlets/purl/1335129/

[16] D. E. Janney, J. I. Cole, R. S. Fielding, S. M. Frank, T. Hartmann, T. A. Hyde, D. D. Keiser, J. Kennedy, A. Maddison, R. D. Mariani, S. C. Middlemas, T. P. O’Holleran, B. H. Sencer, and L. N. Squires, “Metallic Fuels Handbook, Part 1: Alloys Based on U-Zr, Pu-Zr, U-Pu, or U-Pu-Zr, Including Those with Minor Actinides (Np, Am, Cm), Rare-earth Elements (La, Ce, Pr, Nd, Gd), and Y,” Idaho National Laboratory, Idaho Falls, ID (United States), Tech. Rep. INL/EXT-15-36520, Aug. 2017.

[17] G. F. Vander Voort, S. R. Lampman, B. R. Sanders, G. J. Anton, C. Polakowski, J. Kinson, K. Muldoon, S. D. Henry, and W. W. Scott Jr, “ASM handbook,” *Metallography and microstructure*, vol. 9, pp. 44 073–002, 2004.

[18] G. L. Hofman and Y. Soo Kim, “A Classification of Uniquely Different Types of Nuclear Fission Gas Behavior,” *Nuclear Engineering and Technology*, vol. 37, no. 4, pp. 299–308, Jan. 2005. [Online]. Available: https://www.researchgate.net/publication/264145541

[19] K. L. Murty and I. Charit, *An introduction to nuclear materials : fundamentals and applications*, 1st ed. Weinheim (Germany): Wiley-VCH, 2013.

[20] Y. S. Kim and G. Hofman, “Fission product induced swelling of U–Mo alloy fuel,” *Journal of Nuclear Materials*, vol. 419, no. 1-3, pp. 291–301, Dec. 2011. [Online]. Available: https://linkinghub.elsevier.com/retrieve/pii/S002231151100794X

[21] G. L. Hofman, M. K. Meyer, and A. E. Ray, “Design of high density gamma-phase uranium alloys for LEU dispersion fuel applications,” in *The 1998 International Reduced Enrichment for Test Reactor Conference*. San Paulo: Argonne National Laboratory, Oct. 1998, pp. 1–13. [Online]. Available: https://www.osti.gov/biblio/11061

[22] Y. Park, J. Yoo, K. Huang, D. Keiser, J. Jue, B. Rabin, G. Moore, and Y. Sohn, “Growth kinetics and microstructural evolution during hot isostatic pressing of U-10wt.% Mo monolithic fuel plate in AA6061 cladding with Zr diffusion barrier,” *Journal of Nuclear Materials*, vol. 447, no. 1-3, pp. 215–224, Apr. 2014. [Online]. Available: https://linkinghub.elsevier.com/retrieve/pii/S0022311514000294

[23] L. N. Kolotova and S. V. Starikov, “Anisotropy of the U–Mo alloy: Molecular-dynamics study,” *The Physics of Metals and Metallography*, vol. 117, no. 5, pp. 487–493, May 2016. [Online]. Available: http://link.springer.com/10.1134/S0031918X16050100

[24] A. Shoudy, W. McHugh, and M. Silliman, “The Effect of Irradiation Temperature and Fission Rate on the Radiation Stability of the Uranium-10 wt.% Molybdenum Alloy,” in *Radiation Damage in Reactor Materials*. Venice: International Atomic Energy Agency, May 1962, pp. 133–162. [Online]. Available: https://inis.iaea.org/search/search.aspx?orig_q=RN:46040590

[25] D. E. Burkes, R. Prabhakaran, T. Hartmann, J.-F. Jue, and F. J. Rice, “Properties of DU–10wt% Mo alloys subjected to various post-rolling heat treatments,” *Nuclear Engineering and Design*, vol. 240, no. 6, pp. 1332–1339, June 2010. [Online]. Available: https://linkinghub.elsevier.com/retrieve/pii/S0029549310001184

[26] S. Van den Berghe, W. Van Renterghem, and A. Leenaers, “Transmission electron microscopy investigation of irradiated U–7wt%Mo dispersion fuel,” *Journal of Nuclear Materials*, vol. 375, no. 3, pp. 340–346, Apr. 2008. [Online]. Available: https://linkinghub.elsevier.com/retrieve/pii/S0022311508000317

[27] A. Glaser, “Monolithic Fuel and High-Flux Reactor Conversion,” in *The 26th International Meeting on Reduced Enrichment for Research and Test Reactors (RERTR)*, Vienna, Apr. 2004. [Online]. Available: https://www.princeton.edu/~aglaser/2004aglaser_monolithic.pdf

[28] S. J. Miller and H. Ozaltun, “Evaluation of U10Mo Fuel Plate Irradiation Behavior via Numerical and Experimental Benchmarking,” in *Volume 6: Energy, Parts A and B*. Houston, Texas:

American Society of Mechanical Engineers, Nov. 2012, pp. 1323–1336. [Online]. Available: https://asmedigitalcollection.asme.org/IMECE/proceedings/IMECE2012/45226/1323/290283

[29] A. Clarke, K. Clarke, R. McCabe, C. Necker, P. Papin, R. Field, A. Kelly, T. Tucker, R. Forsyth, P. Dickerson, J. Foley, H. Swenson, R. Aikin, and D. Dombrowski, "Microstructural evolution of a uranium-10 wt.% molybdenum alloy for nuclear reactor fuels," *Journal of Nuclear Materials*, vol. 465, pp. 784–792, Oct. 2015. [Online]. Available: https://linkinghub.elsevier.com/retrieve/pii/S0022311515300891

[30] Y. S. Kim, G. Hofman, and J. Cheon, "Recrystallization and fission-gas-bubble swelling of U–Mo fuel," *Journal of Nuclear Materials*, vol. 436, no. 1-3, pp. 14–22, May 2013. [Online]. Available: http://dx.doi.org/10.1016/j.jnucmat.2013.01.291

[31] A. M. Casella, D. E. Burkes, P. J. MacFarlan, and E. C. Buck, "Characterization of fission gas bubbles in irradiated U-10Mo fuel," *Materials Characterization*, vol. 131, pp. 459–471, Sep. 2017. [Online]. Available: https://linkinghub.elsevier.com/retrieve/pii/S1044580317309555

[32] J. Gan, B. Miller, D. Keiser, J. Jue, J. Madden, A. Robinson, H. Ozaltun, G. Moore, and M. Meyer, "Irradiated microstructure of U-10Mo monolithic fuel plate at very high fission density," *Journal of Nuclear Materials*, vol. 492, pp. 195–203, Aug. 2017. [Online]. Available: https://linkinghub.elsevier.com/retrieve/pii/S002231151730

[33] S. Jana, A. Devaraj, L. Kovarik, B. Arey, L. Sweet, T. Varga, C. Lavender, and V. Joshi, "Kinetics of cellular transformation and competing precipitation mechanisms during sub-eutectoid annealing of U10Mo alloys," *Journal of Alloys and Compounds*, vol. 723, pp. 757–771, Nov. 2017. [Online]. Available: https://linkinghub.elsevier.com/retrieve/pii/S0925838817323009

[34] N. Overman, S. Jana, D. Field, C. Lavender, and V. Joshi, "An electron backscatter diffraction analysis of grain boundary initiated discontinuous precipitation in U–10Mo," *Journal of Nuclear Materials*, vol. 529, p. 151940, Feb. 2020. [Online]. Available: https://linkinghub.elsevier.com/retrieve/pii/S0022311519310530

[35] H. Okamoto, "Mo-U (Molybdenum-Uranium)," *Binary Alloy Phase Diagrams*, vol. 3, pp. 2682–2683, 1990. [Online]. Available: https://matdata.asminternational.org/apd/viewPicture.aspx?dbKey=grantami_apd&id=10713702&revision=399478#

[36] H. A. Saller, F. A. Rough, and A. A. Bauer, "Transformation Kinetics of Uranium-Molybdenum Alloys," Battelle Memorial Institute, Columbus, OH, Tech. Rep. BMI-957, Oct. 1954. [Online]. Available: https://www.osti.gov/servlets/purl/4376847

[37] R. Willard and A. Schmitt, “Irradiation Swelling, Phase Reversion, and Intergranular Cracking of U-10wt% Mo Fuel Alloy,” Atomics International, Canoga Park, CA, Tech. Rep. NAA-SR-8956, 1965. [Online]. Available: https://digital.library.unt.edu/ark:/67531/metadc860790/m2/1/high_res_d/metadc860790.pdf

[38] M. L. Bleiberg, L. J. Jones, and B. Lustman, “Phase Changes in Pile-Irradiated Uranium-Base Alloys,” *Journal of Applied Physics*, vol. 27, no. 11, pp. 1270–1283, Nov. 1956. [Online]. Available: http://aip.scitation.org/toc/jap/27/11

[39] E. e. Epremian, “Uranium Alloy Newsletter,” Atomic Energy Comission, United States, Tech. Rep., 1956. [Online]. Available: https://www.osti.gov/servlets/purl/4168286

[40] M. L. Bleiberg, J. D. Eichenberg, R. H. Fillnow, and L. J. Jones, “Development and properties of uranium-base alloys corrosion resistant in high temperature water. Part IV - Radiation stability of uranium-base alloys,” Divison of Technical Information Extension, U.S. Atomic Energy Commission, Tech. Rep. WAPD-127(Pt.IV), May 1957. [Online]. Available: http://www.osti.gov/servlets/purl/4326133-IMQAFX/native/

[41] S. Neogy, M. Saify, S. Jha, D. Srivastava, M. Hussain, G. Dey, and R. Singh, “Microstructural study of gamma phase stability in U–9wt.% Mo alloy,” *Journal of Nuclear Materials*, vol. 422, no. 1-3, pp. 77–85, Mar. 2012. [Online]. Available: https://linkinghub.elsevier.com/retrieve/pii/S0022311511010415

[42] E. Pasqualini, A. Robinson, D. Porter, D. Wachs, and M. Finlay, “Fabrication and testing of U–7Mo monolithic plate fuel with Zircaloy cladding,” *Journal of Nuclear Materials*, vol. 479, pp. 402–410, Oct. 2016. [Online]. Available: https://linkinghub.elsevier.com/retrieve/pii/S0022311516304147

[43] V. V. Joshi, E. A. Nyberg, C. A. Lavender, D. Paxton, and D. E. Burkes, “Thermomechanical process optimization of U-10wt% Mo – Part 2: The effect of homogenization on the mechanical properties and microstructure,” *Journal of Nuclear Materials*, vol. 465, pp. 710–718, Oct. 2015. [Online]. Available: https://linkinghub.elsevier.com/retrieve/pii/S002231151530091X

[44] J. Gan, D. Keiser, B. Miller, J. Jue, A. Robinson, and J. Madden, “TEM characterization of irradiated U-7Mo/Mg dispersion fuel,” *Journal of Nuclear Materials*, vol. 494, pp. 380–397, Oct. 2017. [Online]. Available: https://linkinghub.elsevier.com/retrieve/pii/S0022311517304105

[45] D. D. Keiser, J.-F. Jue, J. Gan, B. D. Miller, A. B. Robinson, J. W. Madden, M. Ross Finlay, G. Moore, P. Medvedev, and M. Meyer, “Microstructural characterization of an irradiated RERTR-6 U-7Mo/AA4043 alloy dispersion fuel plate specimen blister-tested to a final temperature of 500 °C,” *Journal of Nuclear Materials*, vol. 488, pp. 100–122, May 2017. [Online]. Available: https://linkinghub.elsevier.com/retrieve/pii/S0022311516310819

[46] S. Jana, N. Overman, T. Varga, C. Lavender, and V. V. Joshi, “Phase transformation kinetics in rolled U-10 wt. % Mo foil: Effect of post-rolling heat treatment and prior γ-UMo grain size,” *Journal of Nuclear Materials*, vol. 496, pp. 215–226, Dec. 2017. [Online]. Available: https://doi.org/10.1016/j.jnucmat.2017.09.030

[47] D. D. Keiser, J.-F. Jue, K. Verner, T. Trowbridge, C. A. Smith, A. Aitkaliyeva, A. B. Robinson, and B. Miller, “Quantitative Image Analysis of AFIP6-MkII and RERTR-12 Fresh Fuel and Irradiated Fuel Fission Gas Bubble and Recrystallized Fraction,” Idaho National Laboratory, Idaho Falls, Idaho, Tech. Rep. INL/LTD-18-51296, 2018.

[48] Y. Park, N. Eriksson, R. Newell, D. Keiser, and Y. Sohn, “Phase decomposition of γ-U (bcc) in U-10 wt% Mo fuel alloy during hot isostatic pressing of monolithic fuel plate,” *Journal of Nuclear Materials*, vol. 480, pp. 271–280, Nov. 2016. [Online]. Available: https://linkinghub.elsevier.com/retrieve/pii/S0022311516306171

[49] A. Robinson, W. Williams, B. Rabin, J.-F. Jue, D. Keiser, and N. Lybeck, “Follow on Investigation of U-Mo Monolithic Fuel Swelling in the AFIP-6 MkII Experiment,” Idaho National Laboratory, Idaho Falls, ID, Tech. Rep. INL/LTD-18-50149, June 2018.

[50] D. H. Hurley, S. J. Reese, S. K. Park, Z. Utegulov, J. R. Kennedy, and K. L. Telschow, “In situ laser-based resonant ultrasound measurements of microstructure mediated mechanical property evolution,” *Journal of Applied Physics*, vol. 107, no. 063510, pp. 1–5, Jan. 2010. [Online]. Available: https://doi.org/10.1063/1.3327428

[51] R. S. Schley, D. H. Hurley, and Z. A. Hua, “Optical fiber technique for in-reactor mechanical properties measurement,” in *AIP Conference Proceedings*, vol. 1511, no. 1. American Institute of PhysicsAIP, Jan. 2013, pp. 1701–1708. [Online]. Available: https://aip.scitation.org/doi/abs/10.1063/1.4789246

[52] M. Steiner, E. Garlea, J. Creasy, A. DeMint, and S. Agnew, “Temperature dependent elastic properties of γ-phase U – 8 wt% Mo,” *Journal of Nuclear Materials*, vol. 500, pp. 184–191, Mar. 2018. [Online]. Available: https://linkinghub.elsevier.com/retrieve/pii/S002231151731231X

[53] I. Ritchie, “Improved resonant bar techniques for the measurement of dynamic elastic moduli and a test of the Timoshenko beam theory,” *Journal of Sound and Vibration*, vol. 31, no. 4, pp. 453–468, Dec. 1973. [Online]. Available: https://linkinghub.elsevier.com/retrieve/pii/S0022460X73802603

[54] R. Newell, “Assessment of Microstructure and Mechanical Behavior of Materials and Phases Observed in Low-Enriched Uranium Monolithic Fuel Plates After Fabrication,” Ph.D. dissertation, University of Central Florida, 2018. [Online]. Available: https://stars.library.ucf.edu/etd/6166

[55] R. Schley, L. K. Aagesen, Z. Hua, and D. Hurley, “Detailed Analysis of RUS Insertion Experiment and Scoping Studies for Performing Next Experiment using an Enriched Fuel Sample,” Idaho National Laboratory, Idaho Falls, ID, Tech. Rep. INL/EXT-19-55962, Sep. 2019.

[56] R. Newell, A. Mehta, D. D. Keiser, and Y. Sohn, “Phase reversion kinetics of thermally decomposed ($\alpha + \gamma'$) phases to γ-phase in U – 10 wt% Mo alloy,” *Journal of Nuclear Materials*, vol. 530, p. 151983, Mar. 2020. [Online]. Available: https://linkinghub.elsevier.com/retrieve/pii/S0022311519303782

[57] M. Avrami, “Kinetics of Phase Change. II Transformation□Time Relations for Random Distribution of Nuclei,” *The Journal of Chemical Physics*, vol. 8, no. 2, pp. 212–224, Feb. 1940. [Online]. Available: http://aip.scitation.org/doi/10.1063/1.1750631

[58] M. Fanfoni and M. Tomellini, “The Johnson-Mehl- Avrami-Kohnogorov model: A brief review,” *Il Nuovo Cimento D*, vol. 20, no. 7-8, pp. 1171–1182, July 1998. [Online]. Available: http://link.springer.com/10.1007/BF03185527

[59] Q. Zuo, F. Liu, L. Wang, C. F. Chen, and Z. H. Zhang, “An analytical model for secondary phase dissolution kinetics,” *Journal of Materials Science*, vol. 49, no. 8, pp. 3066–3079, Apr. 2014. [Online]. Available: http://link.springer.com/10.1007/s10853-013-8009-y

[60] C. Peterson, W. Steele, and S. DiGiallonardo, “Isothermal Transformation Study of Some Uranium-Base Alloys,” Lawrence Livermore National Laboratory (LLNL), Livermore, CA, Tech. Rep. UCRL-7824, Aug. 1964. [Online]. Available: https://www.osti.gov/servlets/purl/4672623

[61] J. Rest, G. L. Hofman, and Y. S. Kim, “Analysis of intergranular fission-gas bubble-size distributions in irradiated uranium-molybdenum alloy fuel,” *Journal of Nuclear Materials*, vol. 385, pp. 563–571, Jan. 2009. [Online]. Available: https://ac.els-cdn.com/S002231150900004X/1-s2.0-S002231150900004X-main.pdf?_tid=a84d6337-1b76-4d39-9f2d-608074dd1c10&acdnat=1547755866_6263c4fa3f4070f1045a0188e8e50ce0

[62] J. Rest, “Evolution of fission-gas-bubble-size distribution in recrystallized U–10Mo nuclear fuel,” *Journal of Nuclear Materials*, vol. 407, no. 1, pp. 55–58, Dec. 2010. [Online]. Available: https://linkinghub.elsevier.com/retrieve/pii/S0022311510002941

[63] B. Ye, J. Rest, Y. S. Kim, G. Hofman, and B. Dionne, “DART Analysis of Irradiation Behavior of U-Mo/Al Dispersion Fuels,” *Nuclear Technology*, vol. 191, no. 1, pp. 27–40, July 2015. [Online]. Available: https://www.tandfonline.com/doi/full/10.13182/NT14-56

[64] H. Zang, D. Yun, K. Mo, K. Wang, W. Mohamed, M. A. Kirk, D. Velázquez, R. Seibert, K. Logan, J. Terry, P. Baldo, A. M. Yacout, W. Liu, B. Zhang, Y. Gao, Y. Du, and J. Liu, "TEM and XAS investigation of fission gas behaviors in U-Mo alloy fuels through ion beam irradiation," *Journal of Nuclear Materials*, vol. 494, pp. 165–171, Oct. 2017. [Online]. Available: https://linkinghub.elsevier.com/retrieve/pii/S0022311516312594

[65] T. Ajantiwalay, C. Smith, D. D. Keiser, and A. Aitkaliyeva, "A critical review of the microstructure of U–Mo fuels," *Journal of Nuclear Materials*, vol. 540, no. 152386, pp. 1–19, July 2020. [Online]. Available: https://doi.org/10.1016/j.jnucmat.2020.152386

[66] M. R. Tonks, D. Andersson, S. R. Phillpot, Y. Zhang, R. Williamson, C. R. Stanek, B. P. Uberuaga, and S. L. Hayes, "Mechanistic materials modeling for nuclear fuel performance," *Annals of Nuclear Energy*, vol. 105, pp. 11–24, July 2017. [Online]. Available: https://linkinghub.elsevier.com/retrieve/pii/S0306454916307423

[67] S. L. Hayes, G. L. Hofman, M. K. Meyer, J. Rest, and J. L. Snelgrove, "Modeling of high-density U-Mo dispersion fuel plate performance," in *International Meeting of Reduced Enrichment of Research and Test Reactors*, San Carlos de Bariloche, Jan. 2002, pp. 1–10. [Online]. Available: https://www.researchgate.net/profile/J_Rest/publication/241959963_Modeling_of_high-density_U-Mo_dispersion_fuel_plate_performance/links/563fd7f508ae8d65c0151250/Modeling-of-high-density-U-Mo-dispersion-fuel-plate-performance.pdf

[68] M. Stan, J. Ramirez, P. Cristea, S. Hu, C. Deo, B. Uberuaga, S. Srivilliputhur, S. Rudin, and J. Wills, "Models and simulations of nuclear fuel materials properties," *Journal of Alloys and Compounds*, vol. 444-445, pp. 415–423, Oct. 2007. [Online]. Available: https://linkinghub.elsevier.com/retrieve/pii/S0925838807001727

[69] S. Hu, D. Burkes, C. A. Lavender, and V. Joshi, "Effect of grain morphology on gas bubble swelling in UMo fuels – A 3D microstructure dependent Booth model," *Journal of Nuclear Materials*, vol. 480, pp. 323–331, Nov. 2016. [Online]. Available: https://linkinghub.elsevier.com/retrieve/pii/S0022311516306808

[70] W. E. Frazier, S. Hu, D. E. Burkes, and B. Beeler, "A Monte Carlo model of irradiation-induced recrystallization in polycrystalline UMo fuels," *Journal of Nuclear Materials*, vol. 524, pp. 164–176, Oct. 2019. [Online]. Available: https://linkinghub.elsevier.com/retrieve/pii/S002231151930457X

[71] B. Ye, J. Rest, and Y. S. Kim, "A Description of the Mechanistic DART-THERMAL Dispersion Fuel Performance Code and Application to Irradiation Behavior Analysis of U-Mo/Al," Argonne National Laboratory, Argonne, IL (United States), Tech. Rep. ANL/GTRI/TM-13/3, Mar. 2013.

[72] Z.-G. Mei, L. Liang, Y. S. Kim, T. Wiencek, E. O'Hare, A. M. Yacout, G. Hofman, and M. Anitescu, "Grain growth in U–7Mo alloy: A combined first-principles and phase field study,"

Journal of Nuclear Materials, vol. 473, pp. 300–308, May 2016. [Online]. Available: https://linkinghub.elsevier.com/retrieve/pii/S0022311516300253

[73] J.-F. Jue, D. Keiser, C. Breckenridge, B. Rabin, G. Moore, A. Robinson, F. Rice, and M. Meyer, "RERTR – 12 Characterization Summary Report," Idaho National Laboratory, Idaho Falls, ID, Tech. Rep. INL/LTD-13-29715, July 2013.

[74] J.-F. Jue, C. Breckenridge, T. Trowbridge, T. O. Holleran, and D. Keiser, "AFIP – 6 MKII Characterization Summary Report," Idaho National Laboratory, Idaho Falls, ID, Tech. Rep. INL/EXT-14-32457, Aug. 2014.

[75] W. Williams, F. Rice, A. B. Robinson, M. Meyer, and B. Rabin, "AFIP-6 MKII Post-irradiation Examination Summary Report," Idaho National Laboratory, Idaho Falls, ID (United States), Tech. Rep. INL/LTD-15-34142, 2015.

[76] F. Rice, W. Williams, A. Robinson, J. Harp, M. Meyer, and B. Rabin, "RERTR-12 Post-irradiation Examination Summary Report," Idaho National Laboratory, Idaho Falls, ID (United States), Tech. Rep. INL/LTD-14-33066, Feb. 2015.

[77] D. D. Keiser, J.-F. Jue, A. B. Robinson, P. Medvedev, J. Gan, B. D. Miller, D. M. Wachs, G. A. Moore, C. R. Clark, M. K. Meyer, and M. Ross Finlay, "Effects of irradiation on the microstructure of U–7Mo dispersion fuel with Al–2Si matrix," *Journal of Nuclear Materials*, vol. 425, no. 1-3, pp. 156–172, June 2012. [Online]. Available: https://linkinghub.elsevier.com/retrieve/pii/S0022311512000177

[78] D. Jadernas, J. Gan, D. Keiser, J. Madden, M. Bachhav, J.-F. Jue, and A. Robinson, "Microstructural characterization of as-fabricated and irradiated U-Mo fuel using SEM/EBSD," *Journal of Nuclear Materials*, vol. 509, pp. 1–8, Oct. 2018. [Online]. Available: https://linkinghub.elsevier.com/retrieve/pii/S0022311518304069

[79] K. H. Kim, D. B. Lee, C. K. Kim, I. H. Kuk, and K. W. Paik, "Characteristics of U 3 Si and U 3 Si 2 Powders Prepared by Centrifugal Atomization," *Journal of Nuclear Science and Technology*, vol. 34, no. 12, pp. 1127–1132, Dec. 1997. [Online]. Available: http://www.tandfonline.com/doi/abs/10.1080/18811248.1997.9733801

[80] M. Meyer, G. Hofman, S. Hayes, C. Clark, T. Wiencek, J. Snelgrove, R. Strain, and K. H. Kim, "Low-temperature irradiation behavior of uranium–molybdenum alloy dispersion fuel," *Journal of Nuclear Materials*, vol. 304, no. 2-3, pp. 221–236, Aug. 2002. [Online]. Available: https://linkinghub.elsevier.com/retrieve/pii/S0022311502008504

[81] J. Gan, D. Keiser, B. Miller, A. Robinson, J.-F. Jue, P. Medvedev, and D. Wachs, "TEM characterization of U–7Mo/Al–2Si dispersion fuel irradiated to intermediate and high fission densities," *Journal of Nuclear Materials*, vol. 424, no. 1-3, pp. 43–50, May 2012. [Online]. Available: https://linkinghub.elsevier.com/retrieve/pii/S0022311512000517

[82] S. Van den Berghe and P. Lemoine, "Review Of 15 Years Of High-Density Low-Enriched Umo Dispersion Fuel Development For Research Reactors In Europe," *Nuclear Engineering and Technology*, vol. 46, no. 2, pp. 125–146, Apr. 2014. [Online]. Available: https://linkinghub.elsevier.com/retrieve/pii/S1738573315301583

[83] B. Miller, J. Gan, D. D. Keiser, A. Robinson, J.-F. Jue, J. Madden, and P. Medvedev, "Transmission electron microscopy characterization of the fission gas bubble superlattice in irradiated U–7 wt%Mo dispersion fuels," *Journal of Nuclear Materials*, vol. 458, pp. 115–121, Mar. 2015. [Online]. Available: https://linkinghub.elsevier.com/retrieve/pii/S0022311514009532

[84] C. R. Clark, N. P. Hallinan, J.-F. Jue, D. D. Keiser, and J. M. Wight, "Monolithic Fuel Fabrication Process Development," in *Research Reactor Fuel Management (RRFM)*, Sofia, Bulgaria, May 2006.

[85] D. M. Wachs, R. G. Ambrosek, G. S. Chang, and M. K. Meyer, "Design and Status of RERTR Irradiation Tests in the Advanced Test Reactor," in *2006 RERTR International Meeting*, Cape Town, 2006.

[86] E. H. Wilson, D. Jaluvka, A. S. Hebden, J. A. Stillman, and L. M. Jamison, "U.S. High Performance Research Reactor Preliminary Design Milestone For Conversion To Low Enriched Uranium Fuel," in *2019 European Research Reactor Conference*. Swemieh: Argonne National Laboratory, 2019. [Online]. Available: https://www.osti.gov/biblio/1515073

[87] K. Huang, Y. Park, D. D. Keiser, and Y. H. Sohn, "Interdiffusion Between Zr Diffusion Barrier and U-Mo Alloy," *Journal of Phase Equilibria and Diffusion*, vol. 33, no. 6, pp. 443–449, Dec. 2012. [Online]. Available: http://link.springer.com/10.1007/s11669-012-0106-0

[88] G. Was, *Fundamentals of Radiation Materials Science*, 1st ed. Berlin, Heidelberg: Springer Berlin Heidelberg, 2007. [Online]. Available: http://link.springer.com/10.1007/978-3-540-49472-0

[89] S. Hu, C. H. Henager, H. L. Heinisch, M. Stan, M. I. Baskes, and S. M. Valone, "Phase-field modeling of gas bubbles and thermal conductivity evolution in nuclear fuels," *Journal of Nuclear Materials*, vol. 392, no. 2, pp. 292–300, July 2009. [Online]. Available: https://linkinghub.elsevier.com/retrieve/pii/S0022311509004334

[90] J. Rest, G. L. Hofman, I. I. Konovalov, and A. A. Maslov, “Experimental and Calculated Swelling Behavior of U-10 wt.% Mo Under Low Irradiation Temperatures,” in *International Meeting on Reduced Enrichment for Research and Test Reactors*. Sao Paulo, Brazil: Argonne National Laboratory, 1998, pp. 1–13. [Online]. Available: https://inis.iaea.org/collection/NCLCollectionStore/_Public/35/040/35040236.pdf

[91] J. Gan, D. D. Keiser, D. Wachs, A. B. Robinson, B. D. Miller, and T. Allen, “Transmission electron microscopy characterization of irradiated U–7Mo/Al–2Si dispersion fuel,” *Journal of Nuclear Materials*, vol. 396, no. 2-3, pp. 234–239, Jan. 2010. [Online]. Available: https://linkinghub.elsevier.com/retrieve/pii/S0022311509009118

[92] A. Robinson, W. Williams, W. Hanson, B. Rabin, N. Lybeck, and M. Meyer, “Swelling of U-Mo Monolithic Fuel: Developing a Predictive Swelling Correlation under Research Reactor Conditions,” *Journal of Nuclear Materials*, vol. 544, p. 152703, Feb. 2021. [Online]. Available: https://linkinghub.elsevier.com/retrieve/pii/S0022311520313118

[93] S. Hu, A. M. Casella, C. A. Lavender, D. J. Senor, and D. E. Burkes, “Assessment of effective thermal conductivity in U–Mo metallic fuels with distributed gas bubbles,” *Journal of Nuclear Materials*, vol. 462, pp. 64–76, July 2015. [Online]. Available: https://linkinghub.elsevier.com/retrieve/pii/S0022311515001865

[94] J. L. Schulthess, W. R. Lloyd, B. Rabin, K. Wheeler, and T. W. Walters, “Mechanical properties of irradiated U-Mo alloy fuel,” *Journal of Nuclear Materials*, vol. 515, pp. 91–106, Mar. 2019. [Online]. Available: https://linkinghub.elsevier.com/retrieve/pii/S002231151831122X

[95] M. Caturla, T. Diaz de la Rubia, and M. Fluss, “Modeling microstructure evolution of f.c.c. metals under irradiation in the presence of He,” *Journal of Nuclear Materials*, vol. 323, no. 2-3, pp. 163–168, Dec. 2003. [Online]. Available: https://linkinghub.elsevier.com/retrieve/pii/S002231150300360X

[96] J. Rest, “A model for the influence of microstructure, precipitate pinning and fission gas behavior on irradiation-induced recrystallization of nuclear fuels,” *Journal of Nuclear Materials*, vol. 326, no. 2-3, pp. 175–184, Mar. 2004. [Online]. Available: https://linkinghub.elsevier.com/retrieve/pii/S0022311504000327

[97] ——, “A model for the effect of the progression of irradiation-induced recrystallization from initiation to completion on swelling of UO2 and U–10Mo nuclear fuels,” *Journal of Nuclear Materials*, vol. 346, no. 2-3, pp. 226–232, Nov. 2005. [Online]. Available: https://linkinghub.elsevier.com/retrieve/pii/S0022311505003016

[98] X. Jian, X. Kong, and S. Ding, “A mesoscale stress model for irradiated U-10Mo monolithic fuels based on evolution of volume fraction-/radius/internal pressure of bubbles,” *Nuclear Engineering and Technology*,

vol. 51, no. 6, pp. 1575–1588, Sep. 2019. [Online]. Available: https://linkinghub.elsevier.com/retrieve/pii/S173857331930066X

[99] J.-F. Jue, D. D. Keiser, B. D. Miller, J. W. Madden, A. B. Robinson, and B. H. Rabin, "Effects of irradiation on the interface between U-Mo and zirconium diffusion barrier," *Journal of Nuclear Materials*, vol. 499, pp. 567–581, Feb. 2018. [Online]. Available: https://linkinghub.elsevier.com/retrieve/pii/S0022311517309455

[100] S. Hu, V. Joshi, and C. A. Lavender, "A Rate-Theory–Phase-Field Model of Irradiation-Induced Recrystallization in UMo Nuclear Fuels," *JOM*, vol. 69, no. 12, pp. 2554–2562, Dec. 2017. [Online]. Available: http://link.springer.com/10.1007/s11837-017-2611-4

[101] C. B. Lee and Y. H. Jung, "An attempt to explain the high burnup structure formation mechanism in UO2 fuel," *Journal of Nuclear Materials*, vol. 279, no. 2-3, pp. 207–215, June 2000. [Online]. Available: https://linkinghub.elsevier.com/retrieve/pii/S0022311500000210

[102] D. Salvato, A. Leenaers, W. Van Renterghem, S. Van den Berghe, C. Detavernier, and J. H. Evans, "The initial formation stages of a nanobubble lattice in neutron irradiated U(Mo)," *Journal of Nuclear Materials*, vol. 529, p. 151947, Feb. 2020. [Online]. Available: https://doi.org/10.1016/j.jnucmat.2019.151947

[103] Y. Miao, K. Mo, B. Ye, L. Jamison, Z.-G. Mei, J. Gan, B. Miller, J. Madden, J.-S. Park, J. Almer, S. Bhattacharya, Y. S. Kim, G. L. Hofman, and A. M. Yacout, "High-energy synchrotron study of in-pile-irradiated U–Mo fuels," *Scripta Materialia*, vol. 114, pp. 146–150, Mar. 2016. [Online]. Available: https://linkinghub.elsevier.com/retrieve/pii/S1359646215300919

[104] R. Collette, J. King, C. Buesch, D. Keiser, W. Williams, B. Miller, and J. Schulthess, "Analysis of irradiated U-7wt%Mo dispersion fuel microstructures using automated image processing," *Journal of Nuclear Materials*, vol. 475, pp. 94–104, July 2016. [Online]. Available: https://linkinghub.elsevier.com/retrieve/pii/S0022311516301015

[105] D. E. Burkes, D. J. Senor, and A. M. Casella, "A model to predict failure of irradiated U–Mo dispersion fuel," *Nuclear Engineering and Design*, vol. 310, pp. 48–56, Dec. 2016. [Online]. Available: https://linkinghub.elsevier.com/retrieve/pii/S0029549316303612

[106] L. Liang, Y. S. Kim, Z.-G. Mei, L. K. Aagesen, and A. M. Yacout, "Fission gas bubbles and recrystallization-induced degradation of the effective thermal conductivity in U-7Mo fuels," *Journal of Nuclear Materials*, vol. 511, pp. 438–445, Dec. 2018. [Online]. Available: https://linkinghub.elsevier.com/retrieve/pii/S0022311518307657

[107] X. Jian, F. Yan, X. Kong, and S. Ding, “Effects of U-Mo irradiation creep coefficient on the mesoscale mechanical behavior in U-Mo/Al monolithic fuel plates,” *Nuclear Materials and Energy*, vol. 21, p. 100706, Dec. 2019. [Online]. Available: http://www.sciencedirect.com/science/article/pii/S2352179119300511

[108] N. Soneda, S. Ishino, A. Takahashi, and K. Dohi, “Modeling the microstructural evolution in bcc-Fe during irradiation using kinetic Monte Carlo computer simulation,” *Journal of Nuclear Materials*, vol. 323, no. 2-3, pp. 169–180, Dec. 2003. [Online]. Available: https://www.sciencedirect.com/science/article/pii/S0022311503003611

[109] B. Beeler, Y. Zhang, and Y. Gao, “An atomistic study of grain boundaries and surfaces in γU-Mo,” *Journal of Nuclear Materials*, vol. 507, pp. 248–257, Aug. 2018. [Online]. Available: https://linkinghub.elsevier.com/retrieve/pii/S0022311518301454

[110] F. G. Di Lemma, J. Burns, J. Madden, A. Winston, A. B. Robinson, J.-F. Jue, D. D. Keiser, and J. I. Cole, “Texture analyses and microstructural evolution in monolithic U-Mo nuclear fuel,” *Journal of Nuclear Materials*, vol. 544, p. 152677, Feb. 2021. [Online]. Available: https://linkinghub.elsevier.com/retrieve/pii/S002231152031285X

[111] Y. S. Kim, J. Park, K. Lee, B. Yoo, H. Ryu, and B. Ye, “In-pile test results of U-silicide or U-nitride coated U-7Mo particle dispersion fuel in Al,” *Journal of Nuclear Materials*, vol. 454, no. 1-3, pp. 238–246, Nov. 2014. [Online]. Available: https://linkinghub.elsevier.com/retrieve/pii/S0022311514005212

[112] W. E. Frazier, S. Hu, N. Overman, C. Lavender, and V. V. Joshi, “Short communication on Kinetics of grain growth and particle pinning in U-10 wt.% Mo,” *Journal of Nuclear Materials*, vol. 498, pp. 254–258, Jan. 2018. [Online]. Available: https://www.sciencedirect.com/science/article/pii/S0022311517311170

[113] M. L. Bleiberg, “Effect of fission rate and lamella spacing upon the irradiation-induced phase transformation of u-9 wt % mo alloy,” *Journal of Nuclear Materials*, vol. 1, no. 2, pp. 182–190, July 1959. [Online]. Available: https://linkinghub.elsevier.com/retrieve/pii/0022311559900510

[114] D. Smirnova, A. Kuksin, and S. Starikov, “Investigation of point defects diffusion in bcc uranium and U–Mo alloys,” *Journal of Nuclear Materials*, vol. 458, pp. 304–311, Mar. 2015. [Online]. Available: https://linkinghub.elsevier.com/retrieve/pii/S002231151401023X

[115] R. Hills, B. Butcher, and J. Heywood, “A study of the effect of cooling rate on the decomposition of the γ-phase in uranium-low molybdenum alloys,” *Journal of the Less Common Metals*, vol. 3, no. 2, pp. 155–169, Apr. 1961. [Online]. Available: https://linkinghub.elsevier.com/retrieve/pii/0022508861900066

[116] R. Hills, B. Howlett, and B. Butcher, “Further studies on the decomposition of the γ phase in uranium-low molybdenum alloys,” *Journal of the Less Common Metals*, vol. 5, no. 5, pp. 369–373, Oct. 1963. [Online]. Available: https://linkinghub.elsevier.com/retrieve/pii/002250886390050X

[117] B. Howlett, A. Eycott, I. Kang, and D. West, “The kinetics of the isothermal decomposition of a gamma-phase uranium - 6 atomic % molybdenum alloy,” *Journal of Nuclear Materials*, vol. 9, no. 2, pp. 143–154, July 1963. [Online]. Available: https://linkinghub.elsevier.com/retrieve/pii/0022311563901302

[118] P. E. Repas, R. Goodenow, and R. F. Hehemann, “Transformation Characteristics Of U-Mo And U-Mo-Ti Alloys,” *Trans. Am. Soc. Metals*, vol. 57, 1964.

[119] Y. Goldstein and A. Bar-Or, “Decomposition of gamma phase in uranium alloys containing 8, 10.8, and 14.3 Wt-percent molybdenum,” *J. Inst. Met.*, vol. 95, pp. 17–21, 1967. [Online]. Available: https://www.scopus.com/record/display.uri?eid=2-s2.0-0009887891&origin=inward&txGid=767cc932c7fb62896f184fb7276b7a69

[120] G. Östberg, M. Möller, and B. Schönntng-Christiansson, “Metallographic study of the transformation of γ phase into (α + γ’) phases in a U-1.6 wt% Mo alloy,” *Journal of Nuclear Materials*, vol. 10, no. 4, pp. 329–338, Dec. 1963. [Online]. Available: https://linkinghub.elsevier.com/retrieve/pii/0022311563901843

[121] G. Östberg and B. Lehtinen, “The γ → γ’ ordering reaction during isothermal transformation of γ in a U-1.6 wt% Mo alloy,” *Journal of Nuclear Materials*, vol. 13, no. 1, pp. 123–124, Jan. 1964. [Online]. Available: https://linkinghub.elsevier.com/retrieve/pii/0022311564900789

[122] J.-F. Jue, D. D. Keiser, C. R. Breckenridge, G. A. Moore, and M. K. Meyer, “Microstructural characteristics of HIP-bonded monolithic nuclear fuels with a diffusion barrier,” *Journal of Nuclear Materials*, vol. 448, no. 1-3, pp. 250–258, May 2014. [Online]. Available: https://linkinghub.elsevier.com/retrieve/pii/S002231151400066X

[123] M. K. Meyer, G. A. Moore, J.-F. Jue, D. D. Keiser, I. Y. Glagolenko, D. M. Wachs, P. E. Murray, A. B. Robinson, F. J. Rice, H. Ozaltun, S. J. Miller, M. A. Okuniewski, B. H. Rabin, H. W. Glunz, and N. J. Lybeck, “Investigation of the Cause of Low Blister Threshold Temperatures in the RERTR-12 and AFIP-4 Experiments,” Idaho National Laboratory, Idaho Falls, ID, Tech. Rep. INL/EXT-12-26500, June 2012.

[124] J.-F. Jue, T. L. Trowbridge, C. R. Breckenridge, G. A. Moore, M. K. Meyer, and D. D. Keiser, “Effects of heat treatment on U–Mo fuel foils with a zirconium diffusion barrier,” *Journal of Nuclear Materials*, vol. 460, pp. 153–159, May 2015. [Online]. Available: https://linkinghub.elsevier.com/retrieve/pii/S0022311515001129

[125] A. B. Robinson, D. M. Wachs, G. S. Chang, and M. A. Lillo, “Summary of ’AFIP’ full sized plate irradiations in the advanced test reactor,” Idaho National Laboratory, Belgium, Tech. Rep. INIS-BE–10K0001, 2010.

[126] A. M. Casella, D. E. Burkes, P. J. MacFarlan, and E. C. Buck, “Determination of the degree of grain refinement in irradiated U-Mo fuels,” *Heliyon*, vol. 4, no. 12, p. e00920, Dec. 2018. [Online]. Available: https://linkinghub.elsevier.com/retrieve/pii/S2405844018308740

[127] K. Verner, C. Smith, D. D. Keiser, A. Aitkaliyeva, B. Beeler, and B. Miller, “AFIP6-MkII and RERTR-12 Porosity Data Collection and Analysis for Modeling and Simulation,” Idaho National Laboratory, Idaho Falls, ID, Tech. Rep. INL/EXT-20-59171, Apr. 2020.

[128] C. A. Smith, D. D. Keiser, B. D. Miller, and A. Aitkaliyeva, “Comparison of manual and automated image analysis techniques for characterization of fission gas pores in irradiated U-Mo fuels,” *Micron*, vol. 119, pp. 98–108, Apr. 2019. [Online]. Available: https://linkinghub.elsevier.com/retrieve/pii/S0968432818304025

[129] Y. S. Kim, G. Hofman, J. Rest, G. V. Shevlyakov, and SSCR RIAR, “Characterization of intergranular fission gas bubbles in U-Mo fuel.” Argonne National Laboratory (ANL), Argonne, IL, Tech. Rep. ANL-08/11, Apr. 2008. [Online]. Available: http://www.osti.gov/servlets/purl/929261-g6VI9V/

[130] Y. S. Kim, G. Hofman, J. Park, H. Ryu, A. B. Robinson, and D. M. Wachs, “Interdiffusion Layer Growth Correlations for U-Mo/Al-Si Dispersion Fuel During Irradiation,” in *33rd RERTR meeting*, Santiago, Chile, 2011.

[131] S. Zhou, R. Jacobs, Y. Zhang, C. Jiang, and D. Morgan, “Combined ab-initio and empirical model for irradiated metal alloys with a focus on uranium alloy fuel thermal conductivity,” *Journal of Nuclear Materials*, vol. 549, p. 152891, June 2021. [Online]. Available: https://linkinghub.elsevier.com/retrieve/pii/S0022311521001148

[132] C. A. Smith, Y. Cui, B. Miller, D. Keiser, A. Zare, and A. Aitkaliyeva, “New approach for measuring interconnectivity of fission gas pores in nuclear fuels from 2D micrographs,” *Journal of Materials Science*, vol. 56, no. 1, pp. 543–557, Jan. 2021. [Online]. Available: http://link.springer.com/10.1007/s10853-020-05368-x

[133] F. G. Di Lemma, T. Trowbridge, C. Brizzee, and J.-F. Jue, “MP - 1 Intermediate Characterization Report Summary,” Idaho National Laboratory, Idaho Falls, ID, Tech. Rep. INL/EXT-18-51367, Sep. 2018.

[134] C. A. Smith, D. D. Keiser, B. D. Miller, and A. Aitkaliyeva, “Microstructural dependence on fuel matrix composition in irradiated U-Mo dispersion fuels,” *Journal of Nuclear Materials*, vol. 550, p. 152943, July 2021. [Online]. Available: https://linkinghub.elsevier.com/retrieve/pii/S0022311521001665

[135] G. Moore, “AFIP-6MKII Fabrication Summary Report,” Idaho National Laboratory, Tech. Rep. INL/LTD-12-27302, 2012.

[136] G. Moore and D. Fox, “RERTR-12 Fabrication Summary Report,” Idaho National Laboratory, Idaho Falls, Idaho, Tech. Rep. INL/LTD-14-33575, 2014.

[137] J.-F. Jue, B. H. Park, C. R. Clark, G. A. Moore, and D. D. Keiser, “Fabrication of Monolithic RERTR Fuels by Hot Isostatic Pressing,” *Nuclear Technology*, vol. 172, no. 2, pp. 204–210, Nov. 2010. [Online]. Available: https://www.tandfonline.com/doi/full/10.13182/NT10-A10905

[138] D. D. Keiser, “Results of the RERTR-6 Experiment Irradiated in the Advanced Test Reactor INL/EX,” Idaho National Laboratory, Tech. Rep., June 2007.

[139] American Society for Testing and Materials, “ASTM E562-11, Standard Test Method for Determining Volume Fraction by Systematic Manual Point Count,” American Society for Testing and Materials, West Conshohocken, PA, Tech. Rep. C, 2011. [Online]. Available: http://www.astm.org/cgi-bin/resolver.cgi?E562-11

[140] D. M. Perez, J. W. Nielsen, G. S. Chang, D. M. Wachs, and N. E. Woolstenhulme, “AFIP-6 Mark II Irradiation Summary Report,” Idaho National Laboratory, Idaho Falls, ID, Tech. Rep. INL/EXT-12-26305, Sep. 2012.

[141] R. Collette, “Fission Gas Pore Analysis GUI User ’ s Manual,” Tech. Rep., 2015.

[142] “R: The R Project for Statistical Computing,” 2020. [Online]. Available: https://www.r-project.org/

[143] “Statistical functions (scipy.stats) — SciPy v1.4.1 Reference Guide,” 2020. [Online]. Available: https://docs.scipy.org/doc/scipy/reference/stats.html

[144] L. Ott and M. Longnecker, *An Introduction to Statistical Methods and Data Analysis*. Brooks/Cole, 2010. [Online]. Available: https://books.google.com/books?id=gAJ8PgAACAAJ

[145] G. E. P. Box and D. R. Cox, “An Analysis of Transformations,” *Journal of the Royal Statistical Society. Series B (Methodological)*, vol. 26, no. 2, pp. 211–252, Apr. 1964. [Online]. Available: http://www.jstor.org/stable/2984418

[146] J. Olivier and M. M. Norberg, “Positively skewed data: revisiting the box-cox power transformation.” *International Journal of Psychological Research*, vol. 3, no. 1, pp. 68–77, June 2010. [Online]. Available: https://revistas.usb.edu.co/index.php/IJPR/article/view/846

[147] R. M. Heiburger and B. Holland, “Statistical Analysis and Data Display: An Intermediate Course with Examples in R (2nd Edition),” *Springer*, 2015. [Online]. Available: http://www.springer.com/series/417

[148] T. Sweijen, S. M. Hassanizadeh, H. Aslannejad, and S. Leszczynski, "The effect of particle shape on porosity of swelling granular materials: Discrete element method and the multi-sphere approximation," *Powder Technology*, vol. 360, pp. 1295–1304, Jan. 2020. [Online]. Available: https://linkinghub.elsevier.com/retrieve/pii/S0032591019307636

[149] A. M. Casella, D. E. Burkes, P. J. MacFarlan, and E. C. Buck, "Characterization of fission gas bubbles in irradiated U-10Mo fuel," *Materials Characterization*, vol. 131, pp. 459–471, Sep. 2017. [Online]. Available: https://linkinghub.elsevier.com/retrieve/pii/S1044580317309555

[150] W. Carmack, D. Porter, Y. Chang, S. Hayes, M. Meyer, D. Burkes, C. Lee, T. Mizuno, F. Delage, and J. Somers, "Metallic fuels for advanced reactors," *Journal of Nuclear Materials*, vol. 392, no. 2, pp. 139–150, July 2009. [Online]. Available: https://linkinghub.elsevier.com/retrieve/pii/S0022311509004103

[151] A. Devaraj, V. V. Joshi, S. Jana, L. Sweet, C. Mcinnis, S. Manandhar, N. J. Lombardo, and C. A. Lavender, "Detecting the Extent of Eutectoid Transformation in U-10Mo," Pacific Northwest National Laboratory, Richland, WA (United States), Tech. Rep. PNNL-SA-120714, Aug. 2016. [Online]. Available: https://www.pnnl.gov/main/publications/external/technical_reports/PNNL-SA-120714.pdf

[152] S. Jana, E. Kautz, A. Schemer-Kohrn, C. Lavender, N. Overman, and V. Joshi, "Eutectoid Transformation in U10Mo Alloy: Effect of Deformation History and Homogenization Heat Treatment," Pacific Northwest National Laboratory, Richland, WA (United States), Tech. Rep. PNNL-28519, Jan. 2019. [Online]. Available: http://www.ntis.gov/about/form.aspx

[153] M. L. Bleiberg, "A Kinetic Study of Irradiation Induced Phase Changes in Uranium-9 w/o Molybdenum Alloy," *Nuclear Science and Engineering*, vol. 5, no. 2, pp. 78–87, June 1959. [Online]. Available: http://www.tandfonline.com/action/journalInformation?journalCode=unse20

[154] H. H. Klepfer and P. Chiotti, "Characteristics of the solid state transformations in uranium," Ames Laboratory, Ames, Iowa, Tech. Rep. ISC-893, June 1957. [Online]. Available: http://lib.dr.iastate.edu/ameslab_iscreports

[155] C. Komar Varela, L. Gribaudo, R. González, and S. Aricó, "Transformation behavior of the γU(Zr,Nb) phase under continuous cooling conditions," *Journal of Nuclear Materials*, vol. 453, no. 1-3, pp. 124–130, Oct. 2014. [Online]. Available: https://linkinghub.elsevier.com/retrieve/pii/S0022311514004012

[156] K. Foster, S. L. Fairburn, R. G. Leisure, S. Kim, D. Balzar, G. Alers, and H. Ledbetter, "Acoustic study of texture in polycrystalline brass," *The Journal of the Acoustical Society of America*, vol.

105, no. 5, pp. 2663–2668, May 1999. [Online]. Available: https://doi.org/10.1121/1.426882http://asa.scitation.org/doi/10.1121/1.426882

[157] D. O. Leeser, F. A. Rough, and A. A. Bauer, "Radiation Stability Of Fuel Elements For The Enrico Fermi Power Reactor," Atomic Power Development Associates, Inc., Detroit, Michigan (United States), Tech. Rep. A/CONF.15/P/622, 1958. [Online]. Available: https://www.osti.gov/biblio/4306566

[158] N. Woolstenhulme, J. Bess, P. Calderoni, B. Heidrich, D. Hurley, C. Jensen, R. Schley, and K. Tsai, "Overview of I2 Irradiation Deployment Activities in TREAT," in *Transactions of the American Nuclear Society*, Minneapolis, Minnesota, June 2019, pp. 280–282. [Online]. Available: http://www.ansannual.org/trans/2019/data/pdfs/207-29084.pdf

[159] S. M. Heinrich and I. Dufour, "Fundamental Theory of Resonant MEMS Devices," in *Resonant MEMS - Fundamentals, Implementation and Application*, 1st ed., O. Brand, I. Dufour, S. Heinrich, and F. Josse, Eds. John Wiley & Sons, 2015, ch. 1, pp. 3 – 28.

[160] X. Liu, H. Li, and M. Zhan, "A review on the modeling and simulations of solid-state diffusional phase transformations in metals and alloys," *Manufacturing Review*, vol. 5, p. 10, July 2018. [Online]. Available: https://doi.org/10.1051/mfreview/2018008

[161] P. R. Roy and D. N. Sah, "Irradiation behaviour of nuclear fuels," *Pramana*, vol. 24, no. 1-2, pp. 397–421, Jan. 1985. [Online]. Available: http://link.springer.com/10.1007/BF02894841

[162] G. Was, "Phase Stability Under Irradiation," in *Fundamentals of Radiation Materials Science*, 2nd ed. New York, NY: Springer New York, 2017, ch. 9, pp. 485–550.

[163] D. Olander, *Fundamental aspects of nuclear reactor fuel elements*, U.S. Department of Energy, Jan. 1976. [Online]. Available: http://www.osti.gov/servlets/purl/7343826/

[164] S. Konobeevskii, N. Pravdyuk, K. Dubrovin, B. Levitskii, L. Panteleev, and V. Golianov, "An investigation of structural changes caused by neutron irradiation of a uranium molybdenum alloy," *Journal of Nuclear Energy (1954)*, vol. 9, no. 1-4, pp. 75–89, June 1959. [Online]. Available: https://linkinghub.elsevier.com/retrieve/pii/0891391959901411

[165] C. W. Tucker and P. Senio, "On the Nature of Thermal Spikes," *Journal of Applied Physics*, vol. 27, no. 3, pp. 207–209, Mar. 1956. [Online]. Available: http://aip.scitation.org/doi/10.1063/1.1722345

[166] K. Huang, D. D. Keiser, and Y. Sohn, "Interdiffusion, Intrinsic Diffusion, Atomic Mobility, and Vacancy Wind Effect in γ(bcc) Uranium-Molybdenum Alloy," *Metallurgical and Materials Transactions A*, vol. 44, no. 2, pp. 738–746, Feb. 2013. [Online]. Available: http://link.springer.com/10.1007/s11661-012-1425-9

[167] B. Beeler, M. W. Cooper, Z.-G. Mei, D. Schwen, and Y. Zhang, "Radiation driven diffusion in γU-Mo," *Journal of Nuclear Materials*, vol. 543, p. 152568, Jan. 2021. [Online]. Available: https://doi.org/10.1016/j.jnucmat.2020.152568

[168] B. Beeler, J. Cole, W. Frazier, Y. Gao, I. Glagolenko, G. Hofman, S. Hu, V. Joshi, C. Lavendar, N. Lombardo, S. Masengale, Z.-G. Mei, A. Oaks, M. Okuniewski, G. Park, K. Verner, A. Yacoutc, B. Ye, and Y. Zhang, "Microstructural-Level Fuel Performance Modeling of U Mo Monolithic Fuel," Idaho National Laboratory, Tech. Rep. INL/EXT-20-58207-Rev 5, 2020.

[169] N. E. Woolstenhulme, "Update on TREAT Restart and Experimental Design Preparations," in *OSU IRP Meeting*. Idaho Falls, ID: Idaho National Laboratory, Nov. 2017. [Online]. Available: www.inl.gov

[170] C. Wilson, "Neutronics Analysis of the ALEU RUSL Experiment in TREAT," Idaho National Laboratory, Idaho Falls, ID (United States), Tech. Rep. ECAR-5403, 2021.

[171] C. J. Werner, "MCNP Users Manual - Code Version 6.2," Los Alamos National Laboratory, Los Alamos, NM, Tech. Rep. LA-UR-17-29981, 2017.

[172] D. M. Wachs, "Neutronics Analysis of the MARCH-SERTTA Capsule," Idaho National Laboratory, Idaho Falls, ID (United States), Tech. Rep. ECAR-4598, 2017.

[173] J. Fishler, "Programmatic and Safety Thermal Analysis of ALEU-RUSL in TREAT," Idaho National Laboratory, Idaho Falls, ID (United States), Tech. Rep. ECAR-5466, 2021.

[174] A. Khanolkar, T. Yao, Z. Hua, C. Dennett, S. Reese, R. Schley, L. He, J. Kennedy, and D. Hurley, "In situ monitoring of microstructure evolution during thermal processing of uranium-zirconium alloys using laser-generated ultrasound," *Journal of Nuclear Materials*, vol. 553, p. 153005, Sep. 2021. [Online]. Available: https://linkinghub.elsevier.com/retrieve/pii/S0022311521002282

[175] G. Waterman, "Boundary Value Problems," in *Ordinary Differential Equations for Engineers and Scientists*. Creative Commons Attribution 4.0, 2017, ch. 5. [Online]. Available: http://math.oit.edu/~watermang/math_321/321book5_18.pdf

[176] D. G. Zill and W. S. Wright, "3.1 Theory of Linear Equations," in *Advanced Engineering Mathematics*. Jones & Bartlett Learning, 2014, ch. 3, pp. 97–195.

[177] M. J. Whelan, "On the Kinetics of Precipitate Dissolution," *Metal Science Journal*, vol. 3, no. 1, pp. 95–97, Jan. 1969. [Online]. Available: https://www.tandfonline.com/doi/abs/10.1179/msc.1969.3.1.95

Appendix A: Pore data of AFIP6-MkII and RERTR-12 experiments

Table (A.1) Summarized pore diameter, porosity, and eccentricity [127]

Fission density (f/cm^3)	Porosity (%)	Porosity S.D.	Diameter (μm)	Diameter S.D.	Eccentricity	Eccentricity S.D.
KGT2763						
3.89	28.907	0.374	0.34	0.003	0.672	0.004
4.25	24.613	0.518	0.538	0.003	0.651	0.005
4.01	26.722	2.627	0.566	0.043	0.646	0.007
4.13	21.581	0.768	0.499	0.02	0.647	0.006
4.09	22.559	0.622	0.481	0.013	0.608	0.007
4.5	21.04	0.54	0.422	0.012	0.578	0.003
96A						
4.62	18.792	0.639	0.391	0.009	0.698	0.009
4.52	14.14	2.055	0.385	0.017	0.68	0.023
4.14	12.269	2.504	0.352	0.03	0.7	0.01
4.2	14.564	0.873	0.366	0.013	0.703	0.003
4.33	13.595	0.606	0.375	0.01	0.707	0.01
4.26	15.955	2.018	0.387	0.036	0.689	0.014
4.16	14.744	2.467	0.376	0.034	0.687	0.004
4.16	14.367	0.814	0.367	0.016	0.695	0.007
4.07	15.447	0.763	0.376	0.006	0.679	0.007
4.06	17.178	0.447	0.402	0.011	0.673	0.001
4.11	14.346	0.82	0.358	0.011	0.679	0.008
97A						
4.12	13.161	1.465	0.333	0.012	0.655	0.004
4.02	15.529	3.37	0.359	0.017	0.662	0.015
4.05	17.323	1.122	0.358	0.011	0.651	0.006
3.74	16.745	3.387	0.368	0.028	0.65	0.007
3.95	16.164	2.407	0.357	0.023	0.65	0.006
3.87	14.075	2.516	0.337	0.006	0.607	0.009
3.83	16.205	1.164	0.386	0.142	0.651	0.006
3.94	15.204	1.306	0.34	0.007	0.642	0.01
3.87	14.171	1.785	0.345	0.006	0.65	0.004
3.86	17.044	1.027	0.356	0.009	0.636	0.011
3.87	14.955	0.869	0.351	0.01	0.615	0.004
3.86	15.687	1.648	0.357	0.019	0.619	0.014
3.85	15.511	2.446	0.351	0.009	0.648	0.005
3.93	16.148	1.263	0.357	0.007	0.645	0.007
3.92	14.393	1.653	0.343	0.013	0.643	0.012
L1P755						
5.37	26.99	1.07	0.528	0.015	0.652	0.014
4.66	21.12	0.55	0.422	0.019	0.6	0.008
4.45	21.83	0.9	0.42	0.026	0.602	0.005
4.68	21.64	0.22	0.43	0.009	0.603	0.008
4.9	23.76	1.25	0.503	0.024	0.63	0.003
5.16	25.65	0.61	0.54	0.011	0.648	0.02
5.46	26.4	1.21	0.5	0.048	0.651	0.01
5.99	26.62	1.47	0.547	0.021	0.62	0.012
6.23	31	0.9	0.613	0.015	0.608	0.006

Table (A.2) Summarized pore size area data [127]

Fission density (10^{21} f/cm^3)	Count	Mean	STD	Min	25%	50%	75%	Max
3.89	7097	0.27690101	0.48021712	0.00073842	0.04504372	0.12257798	0.31309074	9.3439863
4.25	3719	0.30745975	0.40361226	0.00073842	0.07458058	0.16614485	0.37511815	4.78718691
4.01	6039	0.35974873	0.54475604	0.00147684	0.07088847	0.16762169	0.41831581	7.54371456
4.13	5612	0.26797584	0.36005069	0.00147684	0.05759688	0.13956167	0.3426276	4.3345345
4.09	5562	0.23552979	0.25513908	0.00073842	0.05907372	0.14546905	0.31752127	1.87263705
4.5	7200	0.16969727	0.15346777	0.00147684	0.0583353	0.12183956	0.23703332	1.39487831
4.62	5210	0.16789353	0.19866551	0.00073842	0.03027528	0.09451796	0.23241818	1.34761933
4.52	4290	0.15342352	0.17283035	0.00073842	0.03987476	0.09525638	0.20601961	1.97823133
4.14	4293	0.13303508	0.16484922	0.00073842	0.03175213	0.07679584	0.16614485	1.73159854
4.2	4701	0.14421007	0.18277134	0.00073842	0.03322897	0.08048795	0.18017486	1.8364544
4.33	4270	0.14819982	0.17265146	0.00073842	0.03470581	0.08787216	0.19789698	1.47167415
4.26	4795	0.15488819	0.17732571	0.00073842	0.03913634	0.09304112	0.20786567	1.50933365
4.16	4660	0.14727564	0.17305762	0.00073842	0.0376595	0.08934901	0.1882975	1.73676749
4.16	3632	0.13809642	0.15468047	0.00073842	0.03692108	0.08787216	0.18478999	2.03582821
4.07	4918	0.14620056	0.16713089	0.00073842	0.0376595	0.09008743	0.1919896	1.5041647
4.06	2381	0.16791228	0.18663899	0.00073842	0.03987476	0.10190217	0.22595699	1.5418242
4.11	5129	0.13019629	0.14079102	0.00073842	0.03544423	0.08344164	0.17574433	1.80174858
4.12	5871	0.11131148	0.10725627	0.00073842	0.03839792	0.07827268	0.14768431	1.22282609
4.02	5579	0.12614223	0.11778567	0.00073842	0.04652056	0.09304112	0.16688327	1.08991021
4.05	4905	0.12277685	0.11466867	0.00073842	0.04504372	0.08713374	0.16171432	1.03083648
3.74	5909	0.13135294	0.126138	0.00073842	0.0479974	0.09304112	0.1713138	1.45321361
3.95	6100	0.12282141	0.11710372	0.00073842	0.04430529	0.08713374	0.16023748	1.19550449
3.87	4620	0.10590579	0.09116129	0.00073842	0.04356687	0.07901111	0.14103852	0.66900992
3.83	4963	0.15134562	0.16435528	0.00073842	0.04135161	0.09304112	0.20085066	1.45099835
3.94	6429	0.10961925	0.09972006	0.00073842	0.04282845	0.08122637	0.1439922	1.03895912
3.87	5673	0.1157864	0.11152753	0.00073842	0.03987476	0.08122637	0.15359168	0.99982278
3.86	4881	0.12139402	0.11214781	0.00073842	0.04504372	0.08787216	0.15802221	0.87502954
3.87	4459	0.11659029	0.10565303	0.00073842	0.04652056	0.08418006	0.15285326	0.89570534
3.86	5978	0.12163364	0.11473643	0.00073842	0.04356687	0.08639532	0.1609759	1.14012287
3.85	7562	0.11884339	0.11219798	0.00073842	0.04282845	0.0856569	0.15728379	1.03009806
3.93	6109	0.11905256	0.10801908	0.00073842	0.04504372	0.08713374	0.15876063	1.01532963
3.92	5945	0.11221871	0.1043185	0.00073842	0.04209003	0.08048795	0.14768431	1.02566753
5.37	5694	0.27335444	0.26355276	0.00073443	0.07931787	0.20013073	0.38924509	3.08164599
4.66	7357	0.16552846	0.14553055	0.00073443	0.06462937	0.12852432	0.22253068	1.98000896
4.45	7757	0.16230539	0.13996026	0.00073443	0.0653638	0.1277899	0.21518643	1.6539244
4.68	5849	0.17068211	0.14498529	0.00073443	0.0712392	0.13586857	0.22767165	1.71488165
4.9	5403	0.25959718	0.27343457	0.00146885	0.07197362	0.1784652	0.35546155	3.80431989
5.16	4148	0.28276926	0.26397725	0.00146885	0.08813096	0.21298316	0.39603851	2.55139137
5.46	5213	0.23361693	0.22985088	0.00073443	0.08445884	0.17479308	0.30478625	2.32812626
5.99	5025	0.30542567	0.31783487	0.00146885	0.06683265	0.20196679	0.43992039	2.40744413
6.23	4453	0.4014458	0.46402462	0.00073443	0.07417689	0.23354705	0.58533648	5.53168675

Appendix B: Elastic modulus calculations

B.1 Frequency equation of a cantilever beam

The frequency of a cantilever beam's motion is related back to the displacement of the beam y(x,t) and various equations of motion of the system. The displacement of the cantilever beam is described with the fourth-order differential equation. The bending moment, or M(x), of a beam is related to the load per length on the beam w(x) by the relationship [175, 176],

$$\frac{d^2M}{dx^2} = w(x) \tag{B.1}$$

$$M(x) = EI\varkappa \tag{B.2}$$

M(x) can be related back to the curvature, $\varkappa$, of the beam. with the elastic modulus (E) and the geometric moment of inertia (I). When the beam deflection is small ($y'' \approx 0$) $\varkappa$ becomes y" because

$$\varkappa = \frac{y''}{[1 + (y')^2]^{3/2}} \tag{B.3}$$

therefore,

$$\frac{d^2M}{dx^2} = EI\frac{d^2}{dx^2}y'' = EI\frac{d^4y}{dx^4} = w(x) \tag{B.4}$$

This means the fourth-order differential equation of the deflection may calculate the force per unit length of the beam. For the RUSL cantilever however, the force per length is equal to 0 (w(x)=0). Using the transverse force balance equation the shear force derivative plus the distributed force with equal 0.

$$\frac{dV(x)}{dx} + w(x) = 0 \tag{B.5}$$

And the shear force (V(x)) is equal to the lateral acceleration of the beam multiplied by the elemental mass at the portion of the beam or density (ϱ) multiplied with the cross sectional area of the beam (A). This gives the Euler-Bernoulli equation for the free vibration of a beam,

$$\varrho A\frac{\partial^2 y}{\partial t^2} + EI\frac{\partial^4 y}{\partial x^4} = 0 \tag{B.6}$$

Using a similar method the E may be solved for if the lateral displacement, y(x,t) is equated to the form including the natural frequency, ω, and the mode shape associated with the vibrations, $\bar{y}(x)$.

$$y(x,t) = \bar{y}(x,t)\sin\omega t \tag{B.7}$$

$$\frac{\partial^2 \bar{y}}{\partial t^2} = -\omega^2 \bar{y}(x)\sin\omega t \tag{B.8}$$

$$\frac{\partial^2 M}{\partial x} = EI\frac{\partial^2 \bar{y}(x,t)}{\partial x^2} = \bar{y}''''(x)\sin\omega t \tag{B.9}$$

add in the mass of the element and the equation becomes

$$\sin\omega t(EI\bar{y}''''(x) - \rho A\omega^2 \bar{y}(x)) = 0 \tag{B.10}$$

$$\bar{y}''''(x) - \frac{\rho A\omega^2}{EI}\bar{y}(x) = 0 \tag{B.11}$$

Assign a parameter to the dimension variables in the above equation so $\beta^4 = \frac{\rho\omega^2 A}{EI}$ and

$$\bar{y}''''(x) - \beta^4 \bar{y}(x) = 0 \tag{B.12}$$

The ordinary differential equation (ODE) has the solution of

$$\bar{y}(x) = C_1 \cosh Bx + C_2 \sinh Bx + C_3 \cos Bx + C_4 \sin Bx \tag{B.13}$$

For cantilever beams, like the on used in the RUSL measurements, the boundary conditions are found using y(0)=0, the beam is not deflecting at the clamped end, y'(0)=0 there's no curve to the beam with no deflection. Therefore,

$$C_1 + C_3 = 0,\ C_3 = -C_1 \tag{B.14}$$

$$C_2 + C_4 = 0,\ C_4 = -C_2 \tag{B.15}$$

$$\bar{y}(x) = C_1(\cosh Bx - \cos\beta x) + C_2(\sinh Bx - \sin\beta x) \tag{B.16}$$

At the free end length L, y"(L)= 0 because the bending moment at the free end is 0, y"'(L)=0 no shear force at the end either [176].

$$\begin{bmatrix} (\cosh\beta L + \cos\beta L) & (\sinh\beta L + \sin\beta L) \\ (\sinh\beta L - \sin\beta L) & (\cosh\beta L + \cos\beta L) \end{bmatrix} \begin{Bmatrix} C_1 \\ C_2 \end{Bmatrix} = \begin{Bmatrix} 0 \\ 0 \end{Bmatrix} \tag{B.17}$$

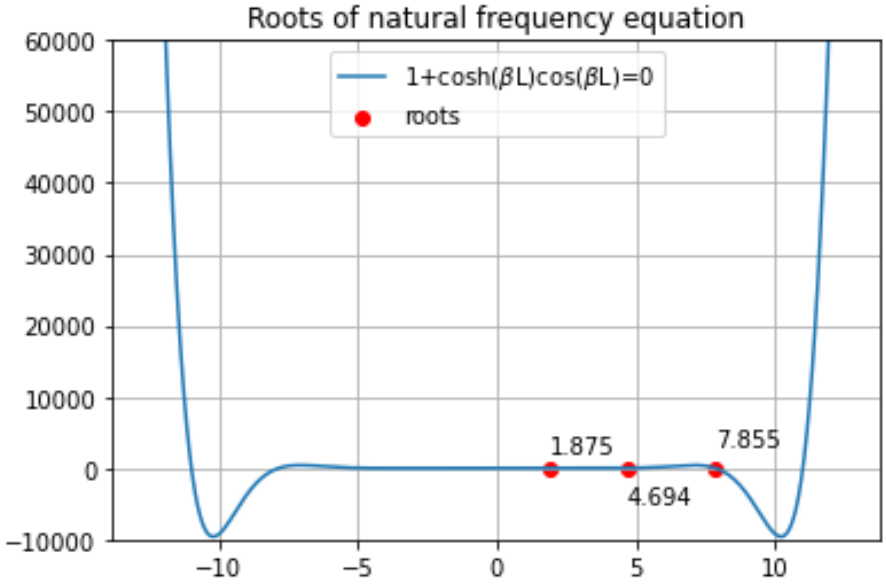

Figure (B.1) Calculation of the roots of the nth mode of the elastic beam vibration

To have non-trivial solutions to the constant vector, the determinate is taken for the matrix, and use trigonometric functions to simplify the equation, the following equation is obtained to calculate the natural frequencies (βl) with the different modes with the boundary value problem above [159]. Figure B.1 was used to solve for the roots of the above equation.

$$1 + \cosh(\beta L)\cos(\beta L) = 0 \tag{B.18}$$

Finally, the frequency of the beam is given by the following equation where the elastic modulus is then solved for and the RUSL elastic modulus measurement may be calculated by substituting βL for ξ.

$$(\beta)^4 = \frac{\rho\omega^2 A}{EI} \tag{B.19}$$

$$(\beta L)^4 = \frac{\rho\omega^2 A L^4}{EI} \tag{B.20}$$

$$\omega^2 = (\xi^4)\frac{EI}{\rho A L^4} \tag{B.21}$$

$$\omega_n = (\frac{\xi_n}{L})^2\sqrt{\frac{EI}{\rho A}} \tag{B.22}$$

The natural frequency (f_n) is ω, the fundamental frequency, divided by 2π, the frequency equation becomes

$$f_n = (\frac{\xi_n}{2\pi L})^2\sqrt{\frac{EI}{\rho A}} \tag{B.23}$$

Appendix C: Dissolution equation calculations

The dissolution of the decomposed particles in the γ matrix depends on the time dependent radius change of the particles. This relationship is represented by the following solute diffusion equation,

$$\frac{\partial C(r,t)}{\partial t} = D \cdot \nabla^2 C(r,t) \tag{C.1}$$

Using the relationship determined by Whelan [59, 177] the rate of the radius change is given by,

$$\frac{dR}{dt} = -\frac{kD}{2R} - \frac{k}{2}\sqrt{\frac{D}{\pi t}} \tag{C.2}$$

$$k = \frac{2(C_\alpha - C_m)}{C_\beta - C_\alpha} \tag{C.3}$$

where D is the diffusion coefficient (cm^2/s), t is time (seconds), k is a ratio of the concentrations of the matrix (C_m), secondary solute (C_β), and the interface (C_α).

Zuo et al. [59] solved this equation analytically with the following method. The change in radius is represented by r_d where R_0 is the radius and R is the transformed radius.

$$r_d = R_0 - R \tag{C.4}$$

At the initial time, t=0, $r_d = 0$, and when the particle is fully dissolved at the end time, $t = t_e$, $r_d = R_0$. Solving for the transformed radius, R,

$$R = r_d - R_0 \tag{C.5}$$

$$\frac{dr_d}{dt} = \frac{kD}{2(R_0 - r_d)} + \frac{k}{2}\sqrt{\frac{D}{\pi t}} \tag{C.6}$$

Zuo separates the equation into the steady state and transient parts. The first half before the addition symbol is steady state and the second half is the transient. The steady state radius can be defined using the starting radius of the transient and steady state as r_t and r_s. After the completion of dissolution, at $t = t_e$, the radii that changed from the two parts are R_t and R_s. This can be expressed as the following equations when $t = 0, r_s = r_t = 0$ and $t = t_e, r_s = R_s, r_t = R_t$.

$$r_s + r_t = r_d \tag{C.7}$$

$$R_s + R_t = R_0 \tag{C.8}$$

Using the steady state and transient parts of equation C.6 the steady state is expressed as the following when $t = 0, r_s = 0$.

$$\frac{dr_s}{dt} = \frac{kD}{2(R_s - r_s)} \tag{C.9}$$

$$r_s = R_s - \sqrt{R_s^2 - kDt} \tag{C.10}$$

For the transient part of the radius change rate,

$$\frac{dr_t}{dt} = \frac{k}{2}\sqrt{\frac{D}{\pi t}} \tag{C.11}$$

$$r_t = \frac{k}{\sqrt{\pi}}\sqrt{Dt} \tag{C.12}$$

Therefore, $R_s$and R_t equal the following equations and the time of dissolution ending,

$$R_s = Rs - \sqrt{R_s + kDt_e} \tag{C.13}$$

$$R_t = \frac{k}{\sqrt{\pi}}\sqrt{Dt_e} \tag{C.14}$$

Solving to the time component gives,

$$t_e = \frac{R_0^2}{kD(1 + \sqrt{\frac{k}{\pi}})^2} \tag{C.15}$$

$$R_s = \frac{1}{(1 + \sqrt{\frac{k}{\pi}})} \cdot R_0 \tag{C.16}$$

To get the relationship between time and the radius of the second phase (R), R_0 is solved for with equation C.16 and added to equation C.5 to solve for R,

$$R = \sqrt{\frac{k}{\pi}}(R_s - \sqrt{kDt}) + \sqrt{R_s^2 - kDt} \tag{C.17}$$